Restricted **SR.15.11335**

Induced seismicity in the Groningen field - statistical assessment of tremors along faults in a compacting reservoir

by

H.M. Wentinck

Shell Global Solutions International B.V., Rijswijk

Further electronic copies can be obtained from the Global Information Centre.

Executive Summary

In this report, we present a statistical model to understand and predict the tremor rates and magnitudes from trends in the past at a local scale following from oil/gas producing reservoirs. The local scale can be a small gas field or a region of several square kilometers of a large field, such as the Groningen field.
The state-driven model supposes that the tremors are generated along the faults in the region of interest. These faults become critically stressed during the compaction of the reservoir in which the reservoir pressure drops. Herewith, the state which triggers the tremors is the mean stress-state along the faults in this region. The model is executed as a Monte Carlo simulation and uses stochastic variables which are related to probabilities that a tremor occurs and that it has a certain magnitude.

The relative likelihood of a seismic fault failure depends on the Weibull distribution function. The tremor rates are normalised to the observed tremor rates using the Poisson probability distribution function. The seismic moments of the tremors follow from a Pareto distribution function, as is commonly done when analysing of natural and man-made induced seismicity.
The model includes that the tremors reduce the mean stress on the faults in proportion to the seismic moment released. The model does not differentiate between a-seismic and seismic fault slip based on field or fault attributes. This could be seen as a shortcoming but we have no clue what this could be, so far.

The model has been applied to 6 relatively small regions in the Groningen field and in the Annerveen and Eleveld fields south of the Groningen field. The model fit parameters have been derived from these regions by comparing the modelled and observed tremors. A sensitivity study has been done and the predictive potential of the model has been explored.

The fit parameters of the model, τ_{fail} and c_{M0} have values which can be understood and constrained from geomechanical calculations. τ_{fail} is a typical mean shear stress along the faults for which the relative likelihood for seismic fault failure substantially increases. c_{M0} relates the mean stress reduction along the faults by the tremors generated by uniaxial compaction.
Remarkable is the high value of the Weibull shape parameter k_W in relation to variations in parameters for rock properties and fault geometry which determine the onset of shear-type fault failure. The Weibull shape parameter determines the period of the transition from no tremors to a constant tremor rate in the case of a constant compaction rate. It's high value may indicate that the tremors are predominantly determined by only a few of these parameters or by another mechanism that differs from a-seismic slip.

The present model cannot reproduce the drastic reduction in the tremor rate in the Eleveld field by a mean field stress relaxation process. This could point to a shortcoming

in the submodel for the stress relaxation or to a shortcoming in the submodel for the generation of the tremors. The latter submodel is driven by the Poisson process and the Weibull distribution probability distribution function for the relative likelihood of a tremor. Presumably, the Poisson process expression which normalises the number of tremors should include a term related to the rate of compaction.

With reservations, we illustrate that the model has some predictive power about tremor rates in a certain region, using the observed tremors in this region in the previous period. In essence, the state-driven model consistently reproduces the gradual onset of the tremor rate followed by a more or less constant tremor rate. Taking a constant and uniform pressure drop over the Groningen field, it must be noted that the model does not capture a small but significant increase in the tremor rate over the last three to four years in the regions around Ten Boer and Loppersum.

We found no correlations between the regional variation of the observed tremor density and the fault dip angle, fault throw and fault azimuth angle in the Groningen field. A remarkable observation is that most tremors with a minimum magnitude of $M = 2.5$ can be associated with faults with high dip angles of about 70° and throws of about 100 m, see Appendix C. These faults could potentially release most of the stored energy from compaction and the imbalance between the field stresses, see Appendix B, §B.2.

We recommend to follow the effects of local gas production reductions in the Groningen field to validate and improve this model, especially in relation to the possible effect of stress relaxation by tremors.
The present model does not differentiate between seismic and a-seismic fault slip because we do not know yet which field or fault attributes are determining here. If this knowledge becomes available, it could be used to constrain the model parameters further.

Table of Contents

Table 0.0.1 : List of frequently used symbols

Symbol	Property	Unit
b	b-value of the Gutenberg-Richter frequency-magnitude law	-
c_{M0}	geometric constant relating seismic moment to stress reduction	Pa/J
c_f	geometric constant relating fault length to fault density in field	-
c_{σ_v}	geometric constant relating vertical stress to mean shear stress	Pa
C_m	uniaxial compaction coefficient	Pa^{-1}
d	constant in the asperity size-frequency relationship	-
D	mean seismic slip distance	m
D_f	mean distance between faults in selected area	m
E	Young modulus of rock	Pa
E_S	seismic energy	J
E_T	liberated gravitational and elastic energy of the system by slip	J
F_{el}	strain-energy or free elastic energy	J
F'_{el}	strain-energy density or free elastic energy density	$\mathrm{J/m}^3$
g	constant of gravitation	$\mathrm{m/s}^2$
h_{res}	reservoir thickness	m
H	poro-elastic constant	-
k_W	shape parameter Weibull distribution	-
K	bulk modulus of rock (drained)	Pa
K_f	bulk modulus of fluid	Pa
K_s	grain modulus	Pa
L	fault length	m
M	Biot modulus	Pa
M_0	seismic moment	J
M	seismic moment magnitude	Richter
M_{llm}	lower limiting seismic moment magnitude	Richter
M_S	surface moment magnitude	Richter
n	integer to identify loading step	-
N	total number of tremors observed or modelled	-
p	fluid pressure in reservoir	Pa
R	typical dimension of the asperity	m
R_{area}	radius of the area of the region under study	m
S	surface area	m^2
S_0	strength of cohesion of rock along fault plane	Pa
SCU	shear capacity utilisation	-
t	time	s
t_{res}	throw at reservoir offset or fault throw	m

Table 0.0.2 : List of frequently used symbols, continued

Symbol	Property	Unit
u, v, w	displacement of rock (x,y,z-direction)	m
V	volume	m^3
W, W_{el}	elastic or strain energy of the system (equal to F_{el})	J
x	value of stochastic variable X	-
X	stochastic variable	-
X_{cen}, Y_{cen}	easting and northing coordinates of the center of the selected region	m
X, Y	x- and y-coordinates or easting and northing coordinates	m
z_{res}	depth of the center of the reservoir	m

Table 0.0.3 : List of frequently used symbols, continued

Symbol	Property	Unit
α	Biot constant	-
α	azimuth angle of fault segment with respect to the north	degree
β	shape parameter for the Pareto probability distribution function	-
γ	stress path coefficient	-
γ	seismic efficiency coefficient	-
δ	dip angle of fault	degree
δp_{fail}	typical change in reservoir pressure for seismic fault failure	Pa
ΔT_q	interevent time or quite period between tremors	s
ϵ_{ik}	components of the strain tensor	m/m
η	failure criterion parameter	-
λ	Lamé constant	Pa
λ	shape parameter for probability distribution functions	-
λ_{PS}	shape parameter for the Poisson probability distribution function	-
μ	friction coefficient	-
μ	shear modulus or Lamé constant	Pa
ν	Poisson ratio	-
ϕ	porosity	-
ϕ	friction angle along fault plane	degree
ρ	mass density of the rock	kg/m^3
σ_{ik}	components of the stress tensor	Pa
σ_h, σ_H	minimum and maximum horizontal field stresses	Pa
σ_n	normal stress on fault plane	Pa
σ_v	vertical field stress	Pa
τ	shear stress on a fault plane	Pa
τ_{fail}	typical mean shear stress on faults for seismic fault failure	Pa
τ_{MC}	shear stress on a fault plane leading to Mohr-Coulomb failure	Pa
θ	complement of dip angle, i.e. $\theta = \pi(90 - \delta)/180$	rad
ζ	fluid displacement per unit volume undeformed rock	m^3/m^3

Table 0.0.4 : List of frequently used symbols, continued

Symbol	Refers to
.....	.....
δ	difference
δ_{ik}	Kronecker delta function
Δ	difference during a tremor
∂	partial derivative
$\sim$	about, roughly
$\approx$	approximately
$\propto$	proportional to
subscripts	
0	initial state or condition or reference condition
1	final state
1,2,3	maximim, medium, minimum principle stresses
area	selected region or area
cen	center of selected area or region
cum	cumulative
el	elastic
h	minimum horizontal field stress
H	maximum horizontal field stress
n	normal component of stress
n	refers to time step n
v	vertical field stress
f	fluid, field or fault
fail	related to a failure leading to a tremor
m	mean value of maximum and minimum principle stresses
min	minimum value
max	maximum value
MC	Mohr-Coulomb failure criterion
ob	overburden
obs	observed value
P	Pareto probability distribution function
PS	Poisson probability distribution function
res	reservoir thickness
rup	rupture of fault
S	seismic energy
T	total energy
ub	underburden
W	Weibull probability distribution function
x, y, z	rectangular coordinate component

Table 0.0.5 : List of frequently used symbols, continued

Symbol	Refers to
.....	.....
superscripts	
0	state just before slip or rupture
1	state just after slip or rupture
$\bar{x}$	mean value of x over a region of interest
$\tilde{x}$	mean value of x during slip or during failure
$\breve{x}$	mean value of x over a fault surface
$'$	per unit volume
$'$	effective stress referring to poro-elastic theory ($\sigma'_{ik} = \sigma_{ik} - \delta_{ik}\alpha\delta p$)
$''$	per unit area
$''$	effective stress referring to rock failure ($\sigma''_{ik} = \sigma_{ik} - \delta_{ik}\delta p$)
$'''$	per unit length

Table 0.0.6 : List of frequently used symbols, continued

Symbol	Refers to
.....	.....
abbreviations	
cdf	cumulative distribution function
ETAS	epidemic type aftershock sequence
LHS	left hand side of the equation
pdf	probability density function
SCU	shear capacity utilisation
UCS	unconfined compressive strength

Chapter 1

Introduction

In general, earthquakes or tremors induced by oil and gas production follow from hydrostatic pressure changes in the field of hydrocarbon extraction. It is assumed that the induced seismicity or tremors result from a sudden slip on pre-existing fault surfaces which are optimally oriented for frictional sliding. Tremors have been reported for a number of fields, see e.g. Grasso (1992) for an overview of about 20 fields where hydrocarbon recoveries induced earthquakes with magnitudes larger than 3 on the Richter scale.

In most reservoirs, total horizontal stresses decrease during hydrocarbon extraction whereas total vertical stresses remain as good as equal. This behaviour has been reported by several authors, see e.g. Mulders (2003) and Roest and Kuilman (1993) and references herein. This differential stress development results from the resistance of the surrounding rock to prevent the reservoir to contract as much as it wants. The differential stresses peak at geometric discontinuities, such as around faults at reservoir offsets.

Currently, the tremor rates in the Groningen field are correlated to the observed reservoir compaction using statistical models and methods, see Bourne et al. (2014) and Bourne and Oates (2014). This work presents another statistical model related to failure mechanics. It supposes that all the tremors originate from seismic fault failure at reservoir offsets. When the fluid pressure reduces during production, the reservoir rock surrounding the faults compacts and the shear stress along these faults change considerably. It is believed that local fault failure and related fault slip is possible when these stresses exceed a certain value, see also e.g. Roest and Kuilman (1993), Mulders (2003), van den Bogert (2015) and Sanz et al. (2015).
It depends on other factors whether this fault slip will develop in a sonic or seismic rock motion and a tremor of significant magnitude and the state-driven model presented here does not explain this[1]. Actually, this model ignores a-seismic slip along faults and the

[1]Any criterion for shear-type failure, such as local or average values of the shear capacity utilisation along faults, are not sufficient to predict the occurrence of a tremor. In general, it depends on both the constitutive equation between shear strength and slip displacement and the elastic stiffness of the surrounding rock if shear-type fault failure leads to unstable rock motion or a tremor, see e.g. Ohnaka

related energy dissipation completely although it will certainly happen. Further, this model does not predict the frequency-magnitude distribution of the seismic tremors and their dependency on the stress. We suppose that the usual, but unknown, heterogeneities or asperities on the fault surface lead, or at least contribute, to this distribution. The observed b-value related to the frequency-magnitude distribution is taken as an input parameter for the model[2].

Assuming a Poisson probability distribution function underlying the observed tremor rates, the tremor rate increases when the stress condition on the faults approaches a critical value according to a Weibull probability distribution function. The model is casted in the form of a Monte Carlo simulation where during small time steps the probability of a tremor to happen is evaluated. Considering only the tremors, or the pure elastic-brittle reponse of the rock, we disregard ductile deformation or other plastic stress relaxations or redistributions, such as following from salt creep. So, the model should be not be used if these stress relaxations or redistributions would significantly alter the observed tremor rate[3] .

The fit parameters or constants in the model are derived from the observed tremors in the regions under study. At the same time, the values of these parameters are constrained by geomechanical calculations. A great deal of the work in this report is about estimating these constraints from the stress conditions in typical faults in the Groningen field using geomechanical calculations, see Appendices A and B.

We have applied the model for 4 regions in the Groningen field and for 2 regions related to the Annerveen and Eleveld fields. In these regions gas production and reservoir compaction have generated a considerable number of tremors over the last decades, see NAM (2013) and references herein. The Annerveen and Eleveld fields are south from the Groningen field but their reservoirs are in the same Rotliegend formation. We suppose that they contain similar faults as the Groningen field, see also Appendix C, Figures C.2.1 and C.2.2 .

The model makes only sense if it has some predictive potential. To explore this potential, we have predicted the tremor rates and magnitudes for the years 2010 - 2014 from the tremors before this period.

(2013), §3.3.

[2]We have concluded not to make use of the so-called dynamic sliding block models. While such models are useful to understand qualitatively some aspects of seismological data, they are difficult to fit to specific data sets and to use them as a basis for quantitative predictions. Also, they are not useful to model dynamic rupturing processes. For the same reason, we do not consider to use the so-called Dynamic Lattice Network Models or other discrete element fracture codes which are frequently applied to model the subsonic fracture processes in heterogeneous materials. So far, we don't use results from rupture modelling. Applied to faults in compacting reservoirs, this work has just been started by Shell SGS-I and under contract by TNO (the Netherlands).

[3]Such a conclusion may follow when validating this model against other observed data.

The model and the probability functions used are explained in Chapter 2. It is used to analyse the observed tremors from the Groningen field in Chapter 3. The predictive potential of the model is discussed in §3.7.
The present results depend to some extend on subjective judgements and a rigorous statistical analysis of the results still must be done. We realise that the present model is not unique to explain the present tremor rates, see also the work of Bourne and Oates (2014). Also, we realise that the parameters used can be further constrained by other geomechanical modelling and experimental data. We recommend to improve the model using statistical methods to compare the results with the observed data.

Chapter 2

Model

2.1 Assumptions and equations

2.1.1 Assumptions

In the field, faults at reservoir offsets have various dip angles and throws and herewith are exposed to different stresses under reservoir compaction. Reservoir heterogeneities, such as variations in the reservoir compaction coefficient or gradients in the hydraulic pressure, may contribute to these differences. Extensive geomechanical modelling of the Groningen field by Sanz et al. (2015) indicates that field stresses along the faults substantially vary over the field. This holds also for local stress conditions around micro-cracks in a rock sample under a triaxial loading. As for this rock sample, we suppose that for a region of several square kilometers in the field the stress conditions along a considerable number of these faults can be represented by a single stress condition. We assume that in a region of this size, the other field variables, such as the reservoir and other rock properties and the reservoir pressure changes, are about uniform[1].

In this model we ignore a-seismic relaxation or redistribution of stress by plastic deformation, e.g. along faults. Also, stress effects from salt creep in the overburden are not considered. In relation to the generation of tremors, the rock behaves as a pure 'elastic-brittle' medium. Further, we assume

- Changes in the mean stress condition or stress state along the faults are only driven by the reservoir pressure and the energy release by the tremors.
- The relative likelihood of seismic failure along a fault or a tremor is given by a Weibull probability distribution function. This state variable is the change in the mean stress when compared to a failure stress value.

[1]The last qualitative statement is subjective. In this work, it means that we disregard variations in these properties over the region of interest, unless explicitly mentioned.

- The fault segments respond independently to the mean stress in the region of interest. Aftershock effects on the tremor rate from nearby tremors are ignored, see also §2.1.3 and §3.6.
- The mean stress on the faults reduces in proportion to the gravitational and elastic energy released by the tremors. The latter is proportional to the total seismic moment of the tremors in the region of interest, see below.
- The frequency-magnitude relationship for the tremors follows from a Pareto probability distribution function.

2.1.2 Stress state

Take that the reservoir compaction is fairly uniform in the region of interest. Discretising the time t in small equal time steps δt, the uniaxial effective vertical stress σ'_v in the reservoir away from faults changes during a time step n as[2]

$$\delta\sigma'_{v,n} = -\alpha\delta p_n. \tag{2.1.1}$$

$\delta p_n = p(t_n) - p(t_{n-1})$ [Pa] is the change in the reservoir pressure during time step n. α [-] is the Biot constant of the reservoir rock. The relation between the Biot constant and the uniaxial compaction coefficient C_m [Pa^{-1}] of the reservoir rock is given in Appendix A, §A.1. Since $\alpha > 0$, the effective vertical stress increases when the reservoir pressure decreases and $\delta p_n < 0$.

The mean shear stress on faults in the region of interest $\bar{\tau}$ changes during time step n as[3]

$$\delta\bar{\tau}_n = c_{\sigma_v}\delta\sigma'_{v,n} - \delta\bar{\tau}_{rup,n}. \tag{2.1.2}$$

c_{σ_v} [-] is a geometrical constant which relates the effective vertical stress away from the faults to the mean shear stress on the faults. It depends on the geometry around the reservoir offset, such as the fault throw and fault dip. This value is of order 1 for the faults of interest, see Appendix B, §B.1. The last term in Eq. (2.1.2) accounts for the mean shear stress reduction in the region due to tremors during time step n. $\delta\bar{\tau}_{rup,n}$ is

[2]The deformation of the reservoir rock approximates one of uniaxial compaction already at a distance a few times the reservoir thickness away from the faults, see Appendix B, §B.1 or van den Bogert (2015). The ' is used to denote the effective stress as defined in poro-elasticity. Other conventions and notations are explained in Appendix A, §A.1.

[3]In the reservoir at a reservoir offset, the shear stress along the fault varies strongly and even changes sign. For this reason we regard the mean of the absolute shear stress as a measure of the stress state of the fault instead of the mean of the shear stress. To simplify notations, we omit the || symbol to denote the absolute value of a property where it does not lead to confusion. When determining the mean value, we consider in the region of interest the surface S of all faults with at least on one side reservoir rock. The mean value of a property x, $\bar{x}$ is calculated from integrating x over S and dividing this value by the area of S.

proportional to the total seismic moment released by the tremors during this time step, see §2.2,

$$\delta\bar{\tau}_{rup,n} = c_{M0}(\bar{\tau}) \sum_{i=1}^{N(n)} M_{0,i}. \tag{2.1.3}$$

The summation is over the $N(n)$ tremors during time step n. c_{M0} [Pa/J] is a parameter which relates a reduction in the mean shear stress on the faults to the released energy by the tremors, see §2.2. In general, it may depend on the mean shear stress on the faults. After time step n, the mean shear stress on the faults is given by

$$\bar{\tau}_n = \bar{\tau}_0 + c_{\sigma_v}\sigma'_{v,n} - \bar{\tau}_{rup,n}. \tag{2.1.4}$$

$\bar{\tau}_0$ [Pa] is the mean initial shear stress on the faults before gas production and reservoir compaction. $\sigma'_{v,n} = -\alpha(p_n - p_0)$ is the effective uniaxial vertical stresss due to the reduction of the reservoir pressure from p_0 to p_n. $\bar{\tau}_{rup,n}$ is the mean stress reduction due to tremors up to time step n. For c_{M0} is constant,

$$\bar{\tau}_{rup,n} = c_{M0} \sum_{i=1}^{N_n} M_{0,i}. \tag{2.1.5}$$

N_n is the total number of tremors in the region up to time step n.

2.1.3 The relative likelihood of a tremor

The relative likelihood of a tremor in the field depends on the mean stress state in the region of interest but also on the rock and fault properties and the fault geometry, such as the throw of the reservoir offset or fault throw, the dip angle of the fault and the size distribution of the asperities at which stress accumulates before rupturing. In general, these properties are poorly known just as they are poorly known in industrial brittle materials or natural rocks under a triaxial test at a much smaller length scale. From arguments explained in §2.5, we suppose that the relative likelihood of a tremor can be described by a Weibull probability distribution function. The relative likelihood of a tremor depends on the following evaluation

$$X > 1 - \exp(-\eta^k). \tag{2.1.6}$$

The dimensionless variable η [-] is a loading parameter leading to rock failure and a tremor. The load is driven by the pressure drop in the reservoir δp. k [-] is a distribution shape parameter. The value of the stochastic variable X follows from a random sample taken from a uniform probability distribution in the interval [0,1] at each time step n. If X is larger than the value of the expression on the RHS of Eq. (2.1.6), a tremor occurs.

Regarding that a region in the field contains a considerable number of faults with different throws and dip angles, it is at this stage sufficient to use a simple expression for η.

We use[4]

$$\eta_n = \frac{\bar{\tau}_n - \bar{\tau}_0}{\tau_{fail}}, \tag{2.1.7}$$

where τ_{fail} [Pa] is a fit constant to the observed data. The mean initial stress $\bar{\tau}_0$ is subtracted from the mean stress. Herewith, the stochastic variable η concerns only a change in the conditions, as is usually done when using the Weibull distribution function to determine the relative likelihood of failure. To generate about the same amount of tremors as observed in the region of interest, we multiply for each time step the relative likelihood of a tremor from the Weibull probability distribution function with another probability. This probability follows from the Poisson probability distribution function for the occurrence of tremor in the time interval related to the time step taken[5]. For small time steps and short time intervals, similar tremor rates are obtained by using a uniform distribution function to determine the probability of a tremor in this time interval, see also §2.4. We ignore that the tremor rate is influenced by aftershocks from nearby tremors[6].

The time reduces to a parameter which defines the stress condition. The time step taken time step δt should be shorter than the shortest interevent time observed in the region of interest. Further, the load on the system should hardly change during a time step. In this case, the probability for the occurrence of a tremor is proportional to the frequency of evaluating the probability by Eq. (2.1.6). The latter probability is controlled by the Poisson distribution.

[4]If the stress reduction by tremors could be disregarded on forehand, we could equally well use $\eta_n = \delta p_n / \delta p_{fail}$, see also Appendix A, §A.3.
One may relate η to a change in the so-called shear capacity utilisation (SCU) of faults. The shear capacity utilisation compares the stress state along a fault or in a rock with the Mohr-Coulomb failure criterion, see Appendix A. However, such a relation is not straightforward. The stresses which form the basis of the calculation of the shear capacity utilisation vary considerably along the fault at a reservoir offset, see Appendix B. Further, it depends on distinct other factors whether a local excess of the shear capacity utilisation and followed by local subsonic slip of rock mass will develop into a sonic or seismic motion of rock mass and a significant tremor. These factors are the reduction of frictional resistance along the faults with slip, the distance over which this happens and the stress state and stiffness of the surrounding rock.

[5]Otherwise, the value of the time or loading step would have an artificial effect on the value of the fit parameter τ_{fail}. In particular, for smaller time steps and more frequent evaluations of the probability of failure, the probability for the occurrence of a tremor would automatically increase.
Bourne et al. (2014) and Bourne and Oates (2014) also use the Poisson distribution to model the tremor rate and call the shape parameter or intensity factor λ the intensity function. The main difference with their work is that the intensity function is replaced by the Weibull probability distribution function for fault failure and that there is an effect of stress reduction by the tremors generated, see also §2.4. At this stage, there are no fundamental principles which would favour one model above the other. Both models are phenomenological. The outstanding issue remains to identify the best field parameters which determine the relative likelihood of an tremor.

[6]Bourne and Oates (2014) apply Ogata's epidemic type aftershock (ETAS) model to modify the log-likelihood of the time-ordered sequence of observed events at the scale of the Groningen field. Although the inclusion of afterschocks has an effect on the tremor rate, we ignore it at this stage of model development to minimise the number of fit parameters.

For c_{M0} constant, we could combine Eqs. (2.1.4), (2.1.5) and (2.1.7) to minimise the number of fit parameters and express η_n as

$$\eta_n = -\frac{p_n - p_0}{\delta p_{fail}} - \frac{c_{M0}}{\tau_{fail}} \sum_{i=0}^{N_n} M_{0,i}, \tag{2.1.8}$$

where

$$\delta p_{fail} = \frac{\tau_{fail}}{\alpha c_{\sigma_v}}. \tag{2.1.9}$$

δp_{fail} [Pa] is the typical change in the reservoir pressure at which tremors are about to start.

2.1.4 Frequency-magnitude-relation-of-tremors

We have at least two options to complete the model. The first (extreme) one is that the magnitude of the tremor completely correlates with the time passed after the last seismic event and the related increase of the stress state. The second option, which we follow, is that the magnitude of the tremor or its seismic moment is an independent stochastic variable. Its value follows from a random sample from a predescribed probability distribution function. In accordance with the Gutenberg-Richter frequency-magnitude law observed for natural earthquakes, we use the Pareto probability distribution function for the seismic moments. In §2.3, we explain how the frequency-magnitude relationship may be related to the size distribution of asperities (or slip barriers) in the fault.

Taking that the magnitude of the tremor does not correlate with the probability of a tremor, we take the risk that the first tremors release an amount of energy which largely exceeds the potential and elastic energy stored around the faults in the reservoir by the field stress and by reservoir compaction. It must be verified afterwards that this does not happen. For the Groningen field, tremors start to appear after a considerable amount of energy is stored in the field by compaction and this possibility is remote.

For convenience, the Poisson, Weibull and Pareto probability distribution functions are explained in §2.4 and §2.5.

2.2 Energy release by tremors and mean stress reduction

2.2.1 Liberated energy, slip and stress

The magnitude of a tremor from a shear-type rupture can be expressed by its seismic moment M_0 as introduced by Aki (1966), i.e.

$$M_0 = \mu D S. \tag{2.2.1}$$

S [m^2] is the surface area that slipped. D [m] is the mean slip distance over this area and μ [Pa] the shear modulus of the rock[7]. The liberated gravitational and elastic energy (or the total energy) of the system by seismic slip E_T [J] can be expressed as, see Udias et al. (2014), §1.5 and Appendix B, §B.2,

$$E_T = \tilde{\tau} DS. \tag{2.2.2}$$

$\tilde{\tau}$ is the mean value of the shear stress over the slip surface during slip[8]. Combining Eqs. (2.2.1) and (2.2.2),

$$E_T = \frac{\tilde{\tau}}{\mu} M_0. \tag{2.2.3}$$

Defining the seismic efficiency coefficient γ [-] as the ratio between the seismic energy E_S [J] and the total release of energy E_T, i.e. $\gamma \equiv E_S/E_T$, the seismic energy relates to the seismic moment as

$$E_S = \gamma \frac{\tilde{\tau}}{\mu} M_0, \tag{2.2.4}$$

or, using Eq. (2.2.1),

$$E_S = \gamma \tilde{\tau} DS. \tag{2.2.5}$$

In general, $\tilde{\tau} \ll \mu$ and herewith $E_S \ll M_0$.

Another expression is given by Scholz (2002), §4.2. In reasonable approximation, according to Scholz (2002), Eq. 4.7 and in the notations of this report,

$$E_S = \frac{1}{2} \Delta\tau DS. \tag{2.2.6}$$

$\Delta\tau = \tau^0 - \tau^1$ is the (apparent) stress drop over the fault during rupturing. τ^0 and τ^1 are the shear stresses over the fault just before and after rupture, respectively. According to Scholz (2002), Eq. 4.5, the release of energy is in the notations of this report given by Eq. (2.2.3). The seismic efficiency becomes

$$\gamma = \frac{E_S}{E_T} = \frac{\Delta\tau}{2\tilde{\tau}}. \tag{2.2.7}$$

[7]One derivation of this expression is given by Ohnaka (2013), §5.2. The total moment of the shear stress over the interval $-\eta < x < \eta$ over a volume element of $x \times 1 \times 1$ m about the z-axis just before slip is given by, see also Figure 2.2.1 ,

$$\int_{-\eta}^{\eta} y \frac{\partial \tau^0_{yx}}{\partial y} dy = \Big[y\tau^0_{yx} \Big]_{-\eta}^{\eta} - \int_{-\eta}^{\eta} y\tau^0_{yx} = -\int_{-\eta}^{\eta} \mu \frac{\partial u^0}{\partial y} dy = -\mu\big(u_{+\eta} - u_{-\eta}\big),$$

since the term between the rectangular brackets is zero. Immediately after slip, the seismic moment over the same volume element is

$$\int_{-\eta}^{\eta} y \frac{\partial \tau^1_{yx}}{\partial y} dy = \Big[y\tau^1_{yx} \Big]_{-\eta}^{\eta} - \int_{-\eta}^{\eta} y\tau^1_{yx} = -\int_{-\eta}^{\eta} \mu \frac{\partial u^1}{\partial y} dy = -\mu\big(u_{+\eta} - u_{-\eta} - D\big).$$

The difference between the seismic moments before and after slip is equal to μD for this volume element.

[8]The following notations are used. $\tilde{x}$ is the mean value of x during slip. $\bar{x}$ is the mean value of x over the surface or rock volume in the region of interest.

According to McGarr (1999), the stress drop $\Delta\tau$ over the fault during rupture is for natural earthquakes in general about an order of magnitude smaller than the mean stress over the fault. According to geomechanical modelling, the mean shear stress over faults in the reservoir of the Groningen field is after compaction of the order 10 MPa, see Appendix B. So, the expected stress drop on this basis would be of the order 1 MPa[9]. However, according to Udias et al. (2014) $\gamma > 0.25$ for shallow tectonic earthquakes or for brittle failure. In this case, the stress drop would be larger.

Take that the fault would fail over the complete reservoir heigth and the mean slip distance D is of the order of the absolute value of the change in the reservoir thickness by uniaxial compaction, i.e. $D \sim |\delta h_{res}|$. According to Eq. (2.2.5), the seismic energy release per unit length fault E_S''' [J/m] would be

$$E_S''' \sim \gamma \tilde{\tau} h_{res} \delta h_{res}. \tag{2.2.8}$$

Disregarding heat production during seismic slip and the attenuation of the seismic waves by the surrounding rock, take a conservative value for the seismic efficiency $\gamma = 1$. Take a relative small remaining shear stress. So, the mean shear stress during the rupture of the complete fault in the reservoir is $\tilde{\tau} \sim \bar{\tau}/2$.
Herein, $\bar{\tau} = \tau_0 + c_{\sigma_v} \alpha \delta p$ and τ_0 depends on the dip angle of the fault and the horizontal stress, see Appendix B, Tables B.1.2 and B.1.3 . Disregarding τ_0 with values of several MPa's, using $c_{\sigma_v} = 0.5$, see Appendix B, §B.1, $\gamma = 1$, $\alpha = 0.7$, $h_{res} = 200$ m, $\delta h_{res} = C_m \alpha \delta p =$ - 0.3 m at 25 MPa pressure drop, we obtain $\tilde{\tau} = \bar{\tau}/2 \sim 4$ MPa and $E_s''' = \gamma \tilde{\tau} h_{res} \delta h_{res} \sim 0.2$ GJ/m. This amount of energy is of the same order as the amount that follows from geomechanical calculations if we ignore the elastic energy stored in the rock by the field stresses, see Appendix B, §B.2, Table B.2.3 .

Taking for $\mu = 4$ GPa, the related seismic moment per meter fault is $M_0''' = \mu/(\gamma\tilde{\tau}) E_S''' \sim 0.2$ TJ/m for $\gamma = 1$. A related rupture over a fault length of 1 km would lead to a tremor with a seismic moment of $M_0 \sim 200$ TJ, equivalent to a moment magnitude $M \sim 3.6$

[9]This is in line with an analysis of the tremors in the Groningen field by Kraaijpoel and Dost (2013), Table 2. They derive from the seismic signals and using Brune's model that the stress drop is in the range 0.4 - 1.7 MPa for tremors with magnitudes in the range 2.9 - 3.5.
It is less than a value for the stress drop of 3 MPa used to predict the ground motions from the tremors in Groningen area, see Bommer et al. (2015).

Suppose that the tremors evolve from a slip motion in a circular plane. According to Scholz (2002), Eq. 4.30, the radius of this plane r_{slip} is about

$$r_{slip} \sim \left(\frac{7}{16} \frac{M_0}{\Delta\tau} \right)^{1/3}.$$

For a stress drop $\Delta\tau = 1$ MPa, a tremor with a magnitude 3.6 Richter and a seismic moment $M_0 \sim 200$ TJ, $r_{slip} \sim 400$ m, would correspond to a slip area of about 0.5 km^2. Considering an average reservoir thickness of 200 m, this would suggest that ruptures of these magnitudes would considerably penetrate into the underburden and/or that the stress drop is larger.

Richter.

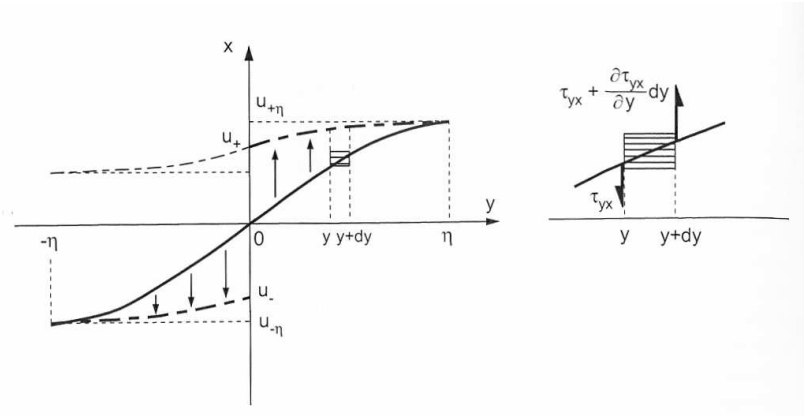

Figure 2.2.1 : The reduction of seismic moment by slip along a fault under shear stress. The x-axis follows the fault plane in the xz-plane. The y-axis is perpendicular to the fault plane and the shear stress over the fault is generated by a relative motion of the rock in the x-direction at $y = -\infty$ and $y = \infty$. η denotes the distance between the fault plane and a point beyond which $\partial u/\partial y \approx 0$ holds. The solid and dash-dotted lines show the displacement of the rock u in the x-direction before and after slip, respectively. The arrows show the displacement by slip of the rock on both sides of the fault. The right small figure shows the shear forces acting on a volume element located between y and $y + dy$. Figure copied from Ohnaka (2013), Figure 5.19.

2.2.2 Reduction in the mean shear stress along the faults in the region of interest by tremors

According to Molnar (1983), the cumulative reduction of the strain tensor $\epsilon_{jk,cum}$ [-] in a rock volume V [m^3] with multiple faults by N tremors in this volume is given by [10]

$$\epsilon_{jk,cum} = \frac{1}{\mu V} \sum_{i=1}^{N} M_{0,i,jk}. \tag{2.2.9}$$

$M_{0,i,jk}$ [J] is the seismic moment tensor component jk related to tremor i. For a set of more or less parallel faults in volume V, the mean shear stress released along these faults by tremors is

$$\bar{\tau}_{rup} = c_{M0} \sum_{i=1}^{N} M_{0,i}. \tag{2.2.10}$$

$c_{M0} = 1/(cV)$ [Pa/J] or [m^{-3}] is a constant where c is a geometrical constant $0 < c < 1$. We have assumed that the shear modulus μ of the rock surrounding the fault remains constant and that the mean shear stress along the faults is in proportion to the cumulative

[10] For long waves and/or long source-receiver distances the volume V is effectively a point source and V can be considered a system of couples located at a point, say the center of V. The moment tensor is equal to the integral of the moment density over V. For an effective point source, the moment tensor components M_{pq} [J] are, see Aki and Richards (2009), §3.4,

$$M_{pq} = \int c_{pqrs} \epsilon_{rs} dV.$$

c_{pqrs} [Pa] is the elasticity tensor and ϵ_{rs} [-] is the change in the strain tensor (we use the summation convention for terms with the same indices). For shear collapse in a homogeneous isotropic body of volume V with non-zero transformational strain components $\epsilon_{13} = \epsilon_{31}$, the moment tensor is

$$\boldsymbol{M} = 2\mu V \epsilon_{13} \begin{pmatrix} 0 & 0 & 1 \\ 0 & 0 & 0 \\ 1 & 0 & 0 \end{pmatrix}.$$

This expression is equivalent to one for fault slip except that the seismic moment M_0 is given by $M_0 = 2\mu\epsilon_{13}V$. Vice versa, $\epsilon_{13} = M_0/(2\mu V)$.
For a group of tremors in a seismic volume V small compared to the wavelength of the tremor, a cumulative change in the strain in this volume may be more meaningful than a cumulative slip. For this reason Kostrov (1974) suggested to sum the moments of a group of tremors in a given volume V and sharing the same source mechanism to find the total change in strain in this volume. For the previous example of shear collapse in a homogeneous isotropic body of volume V, the cumulative change in strain $|\epsilon_{cum}|$ in volume V is

$$|\epsilon_{cum}| = \frac{1}{2\mu V} \sum_{i=1}^{N} M_{0,i}.$$

This expression is used by Bourne et al. (2014) where the strain is generated in the reservoir by compaction. The underlying assumption of this expression is that the domain of integration is irrotational. However, for systems with multiple faults this is in general not true. Molnar (1983) shows that the expression of Kostrov (1974) should be multiplied by a factor 2.

shear strain in the surrounding reservoir rock, i.e. $\bar{\tau}_{rup} = c\mu|\epsilon_{cum}|$.

The remaining task is to define the relevant fault system and/or relevant related rock volume V. Ignoring the underlying assumption of this expression that the seismic wavelength and source-receiver distance are large compared to the typical dimension of the considered volume V, and taking $V = S_{area}h_{res}$ where S_{area} is the area of the region of interest and h_{res} is the reservoir thickness,

$$c_{M0} = \frac{1}{cS_{area}h_{res}}. \tag{2.2.11}$$

For a reservoir thickness of 200 m and for a region of interest with a radius of 5 km, h_{res} = 200 m and S_{area} = 78 km^2 and V = 1.6 10^{10} m^3. For c = 1, c_{M0} = 6 10^{-11} [Pa/J] and this value should be seen as an underlimit for c_{M0}. The reduction of the mean shear stress over all faults in the region of interest by a tremor can also be derived from an energy balance during a rupture, see Appendix B, §B.3. We obtain a c_{M0} value of similar order. In general, c_{M0} is larger for smaller regions. c_{M0} is also larger for a lower fault density or for a lower density of seismic active faults and for a smaller stress reduction over the fault during rupture, see Appendix B, §B.3.

2.2.3 Relation with observations

To compare the seismic moments M_0 generated by the model with the observed moment magnitudes of the tremors M [Richter], we use the following relation between M and M_0[11], see for example Udias et al. (2014), §1.4 or Scholz (2002), §4.3,

$$M = \frac{2}{3}\log_{10} M_0 - 6.1. \tag{2.2.12}$$

[11]The value of the moment magnitude M is derived from the seismic moment M_0 under the hypothesis of a constant stress drop during rupture that satisfies the empirical relations between the surface wave magnitude M_S, the epicentral distance Δ and the energy radiated as seismic waves E_S. M_S, and herewith E_S, are corrected for inelastic attenuation and the geometric spreading of these waves.
The surface wave magnitude M_S relates to the energy radiated as seismic waves E_S and to the seismic moment M_0 as, according to Udias et al. (2014), §1.4

$$\log_{10} E_S = 1.5M_S + 4.8 \quad \text{and} \quad log_{10}M_0 = 1.5M_S + 4.8 - \log_{10}\left(\frac{\gamma\tilde{\tau}}{\mu}\right).$$

γ [-] is the seismic efficiency coefficient and $\tilde{\tau}$ [Pa] is the change in the shear stress along the fault during slip, see also §2.2. Combining these expressions yields Eq. (2.2.4), i.e. $E_S = \gamma\tilde{\tau}/\mu M_0$.

Moment magnitudes M are not routinely calculated for small earthquakes or tremors and most national seismograph networks report some variation of the local magnitude of the observed tremors. For several tremors KNMI has calculated the moment magnitudes and shows that the moment magnitude and the local magnitude are equivalent above M $\sim$ 3. For smaller moment magnitudes, the moment magnitudes seem to be somewhat larger than the local magnitudes. In this report we disregard this difference.

This relationship has been developed for natural earthquakes which primarily originate from shear-type failure along fault planes.

2.3 Relation between frequency-magnitude relationship and the asperity distribution

The Gutenberg-Richter frequency-magnitude relationship, as observed for natural earthquakes, agrees with a Pareto probability distribution function with a value $\beta \sim 2/3$. These earthquakes are generated along faults which are loaded by a constant far field shear stress. The cumulative number of earthquakes with magnitudes equal or greater than M is according to the Gutenberg-Richter frequency-magnitude relationship,

$$N(M) \propto 10^{-bM}. \tag{2.3.1}$$

Using $\beta = 2/3b$, the constant $b \sim 1$. In terms of the seismic moment M_0, using $M \propto 2/3 \log_{10} M_0$, this number is

$$N(M_0) \propto M_0^{-\frac{2}{3}b}. \tag{2.3.2}$$

According to Ohnaka (2013), Chapter 6.5, one explanation of this relationship originates from the distribution of so-called asperities or geometric heterogeneities on the fault surface. These asperities form the barriers or areas of resistance to rupture or slip. Only when the stress is sufficient to break an asperity on the fault surface (in case of intact rock) or move the rock over this asperity (in the case of an existing slipping fault), the tremor is generated. In the simplest case, the asperity can be characterised by one length scale R [m]. The size distribution of the asperities (or surface roughness) follows in many cases a power law. The number of asperities equal or greater than R are

$$N(R) \propto R^{-d}, \tag{2.3.3}$$

where d is the fractal dimension. Take that the so-called breakdown displacement of frictional resistance D_c [m] is proportional to the size of the asperity, i.e. $D_c \propto R$ and that the seismic moment M_0 is proportional to D_c^3. Inserting these relations into Eq. (2.3.3),

$$N(M_0) \propto M_0^{-\frac{1}{3}d}, \tag{2.3.4}$$

From comparing Eqs. (2.3.2) and (2.3.4), the size distribution of asperities is consistent with the observed tremors if

$$b = \frac{d}{2}. \tag{2.3.5}$$

Commonly, the fractal dimension of rock surface $d \sim 2$, which is consistent with observed b-values for natural earthquakes.

2.3.1 Other b-values

b-values can differ from 1, see also §3.4. Also, the b-value can vary over time under non-stationary or transient conditions. At a small scale, Scholz (1968) demonstrated that microfracture events during rock deformation experiments also follow the Gutenberg-Richter law and that the b-value decreases when the stress on the rock is increased. This relationship can be described by a statistical model of fracture growth. A decrease in the b-value is often observed before failure in both tension and compression tests in laboratory rock fracture experiments. The b-value linearly relates to stress intensity factor $b = c_1 - c_2 K$ where c_1 and c_2 are constants and K is a stress intensity factor. The stress intensity increases with fracture length and herewith the b-value decreases when fractures lengthen and unite. This occurs just before bulk failure.
Another example is a massive fracking operation in a geothermal project. In a few cases the b-value of the tremors decreased over time when the hard rock was fracked by injecting large amounts of fluid into the rock around the geothermal well. In the geothermal projects in Soultz-sous-Forets (France) and Basel (Switzerland), the b-value decreased also with the distance from the injection well, see Vlcek et al. (2014). This may be a consequence of an increasing stress build-up around a continuous increasing infiltrated rock volume.

Tormann et al. (2015) have analysed the b-values of earthquakes along a 1000 km long section of the subducting Pacific Plate beneath central and northern Japan since 1998. The b-values vary spatially and mirror the tectonic regime. Low b-values, indicative of high stress, occur where the subducting and overriding plates are strongly coupled. Parts of the plate interface which ruptured during the 2011 Tohoku-oki earthquake were highly stressed in the years leading up to the earthquake. High b-values, indicative of low stress, occur in locations characterized by deep magma chambers.
High b-value anomalies are also observed when volcanoes become active. An increase in the pore fluid pressure reduces the effective stress around the magma chamber allows for more slip on existing fractures, rather than the creation of new fractures. This creates a larger proportion of small events, leading to an increase in the b-value.

Low b-values are also observed at a much larger scale in north of Sweden, see Korja et al. (2015). Intraplate earthquakes and tremors evolve from stress changes along faults following from the rebound of Scandinavia after the last period of glaciation. Since the melting of the 3 km thick icecap in Scandinavia 20000 years ago, Scandinavia raised 0.5 - 0.8 km. A further raise of about 50 - 100 m is expected. In relation to the tremors in the Groningen field, we observe that large isolated areas (with a length scale of a few hundred km) with tremors and earthquakes are found but much smaller than the total area of deformation by glaciation which is of a length scale of a few thousends km. Assuming that faults are everywhere in the crust of Scandinavia, regional variations in rock and fault properties may play a role here.

It is not always clear whether heterogeneities along faults, which are related to ruptures of different magnitudes, are of geometric origin. In fact, a-seismic slip or less seismic active slip zones along subduction zones, like along the coast of Japan, may be correlated with the subduction of very rough landscapes with subsea mountains while other more geometrically smooth subduction zones produce the largest earthquakes, see e.g. Wang et al. (2015). Earthquakes in these areas are correlated to a patchwork of significant local stress drops and increases while the average stress drop over a whole area may be quite moderate.

According to laboratory experiments, the b-value of acoustic emissions decreases linearly with the difference between the largest and the smallest principle stress, $\sigma_1 - \sigma_3$. Scholz (2015) shows that this may also hold for earthquakes. Using a frictional strength model for stresses in the continental lithosphere combined with earthquake b-values measured as a function of depth in a wide variety of tectonic regions, Scholz finds $b = 1.23 \pm 0.06 - (0.0012 \pm 0.0003)(\sigma_1 - \sigma_3)$ where the stress difference $\sigma_1 - \sigma_3$ is in MPa[12].

It cannot be excluded that aforementioned relations hold in a qualitative sense also along the faults in a compacting reservoir. Further, even if the size distribution of asperities or rupture barriers or other strength heterogeneities[13], such along the fault plane would contribute to a b-value ~ 1, the stress over the fault increases for the first time after a very long period because of reservoir compaction. At the start of stress build-up, large tremors are relatively less likely and deformation energy due to compaction still must be added. In a later phase of stress build-up, more deformation energy is available, there is more stress difference and larger tremors become possible with a decreasing b-value as a consequence.

Considering all above, it is not strange that we observe lower b-values in regions with many tremors in the Groningen field than in regions with less tremors.

In this report, we disregard a possible decrease of the b-value over time. Such a trend is hard to derive from the relative small number of tremors. We refer to Harris (2015) for an analysis about a b-value development over time in the Groningen field.

[12]For subduction zones, he finds that the b-value correlates linearly with the slab pull force and with the net reduction of plate interface normal force, both of which also indicate a negative linear relation between b value and differential stress.

[13]Other strength heterogeneities could be related to the various materials in the fault zone. We expect patches in the fault plane of various areal dimensions containing layers of aeolian or fluvial sandstones mixed with carbonates, anhydrites and clays. The sand grains will be poorly or strongly cemented depending on the burial history, the influence of hydrothermal water flows and the aforementioned materials in the fault. This all may lead to patches which give more or less stable local fault slip, see also the remarks in Roest and Kuilman (1993).

2.4 Pareto, Weibull and Poisson probability distributions

For convenience, we explain in this section the probability functions used and in the notations of this report. They can be found in many textbooks as wells as in the Wikipedia. The probability density function (pdf) $f(x)$ describes the relative likelihood that a stochastic variable X has a particular value x. The area under the pdf $f(x)$ is unity. The stochastic variables we use are continuously distributed and can take all possible values. Another way of presenting the same information is in the form of a cumulative distribution function (cdf) $F(x)$, which gives the probability that the stochastic variable has a value less than or equal to the selected value. So, $F(x)$ is the integral of the corresponding pdf $f(x)$. The ordinate at $F(x)$ on the pdf is equal to the area under the pdf $f(x)$ to the left of x. The 'expected' value of the stochastic variable X is the value for which $df(x)/dx = 0$.

2.4.1 Pareto distribution

The Pareto (or Bradford) probability distribution function is usually applied to model the distribution of wealth, communities, companies and money transfers or the relative use of words in a text. It is also used to describe the frequency-magnitude (or frequency-seismic-moment) relationship of natural and manmade induced earthquakes or tremors, see e.g. Vere-Jones et al. (2005). The Pareto pdf and cdf f_P and F_P are defined by the parameters x_{min} and β, i.e. for $x > x_{min}$

$$f_P(x; x_{min}, \beta) = \frac{\beta}{x_{min}} \left(\frac{x_{min}}{x} \right)^{\beta+1} \quad \text{and} \quad F_P(x; x_{min}, \beta) = 1 - \left(\frac{x_{min}}{x} \right)^{\beta}. \tag{2.4.1}$$

The probability that the stochastic variable X is less or equal to x is given by $P(X \leq x) = F_P$. The probability that X exceeds x is $P(X > x) = 1 - F_P$ or

$$P(X > x) = \left(\frac{x_{min}}{x} \right)^{\beta}. \tag{2.4.2}$$

Applying the Pareto distribution to the distribution of seismic moments, the pdf and cdf are given by, for $M_0 > M_{0,min}$,

$$f_P(M_0; M_{0,min}, \beta) = \frac{\beta}{M_{0,min}} \left(\frac{M_{0,min}}{M_0} \right)^{\beta+1} \quad \text{and} \quad F_P(M_0; M_{0,min}, \beta) = 1 - \left(\frac{M_{0,min}}{M_0} \right)^{\beta}. \tag{2.4.3}$$

$M_{0,min}$ is the observed or relevant minimum seismic moment and β is a shape parameter. To obtain the Gutenberg-Richter frequency-magnitude law, $\beta \sim 2/3$.

2.4.2 Weibull distribution

The Weibull distribution function is frequently applied to describe the lifetime distribution of products, the distribution of wind forces, droplet and particle size distributions, to analyse point load tests on rock core, describe the heterogeneous distribution of microfractures in natural materials or to analyse other systems with many similar components (such as a chain). The idea that a system with many similar components will fail when the weakest component fails has led to widespread use of this distribution in industrial reliability analysis. The Weibull probability density function of the stochastic variable X is for $x \geq 0$

$$f_W(x;\lambda,k) = \frac{k}{\lambda}\left(\frac{x}{\lambda}\right)^{k-1}\exp\bigl(-(x/\lambda)^k\bigr). \tag{2.4.4}$$

$k > 0$ [-] is the Weibull shape parameter and $\lambda > 0$ is a scale parameter of the distribution. The related cumulative Weibull distribution function is a stretched exponential function. For $x \geq 0$,

$$F_W(x;\lambda,k) = 1 - \exp\bigl(-(x/\lambda)^k\bigr)\bigr). \tag{2.4.5}$$

If the stochastic variable X is a 'time-to-failure', the Weibull probability density distribution gives a distribution for which the failure rate is proportional to a power of time[14].

In the model, $\tau_{fail} = \lambda$ is the Weibull scale parameter, $\eta = (\bar{\tau} - \bar{\tau}_0)/\tau_{fail} = x/\lambda$ and $k_W = k$ the Weibull shape parameter.

2.4.3 Poisson distribution

The Poisson distribution is actually a discrete probability function. Usually, it is applied to stochastic variables which count the number of events in a certain time period, certain distance, area or volume. Examples are related to radioactive decay, the number of cars which pass a cross road, the number of typing errors in a page, the amount of telephone calls in a day, the number of dead animals on a road and the number of WEB server calls per day. The Poisson distribution is also used to explain the time sequence of earthquakes or tremors when a fault fails under a constant loading rate generated by far field tectonic

[14]The shape parameter k is that power plus one, and so this parameter can be interpreted as follows. A value of $k < 1$ indicates that the failure rate decreases over time. This happens if there is in this context a significant 'infant mortality', or defective items failing early and the failure rate decreasing over time as the defective items are weeded out of the population.
A value of $k > 1$ indicates that the failure rate increases with time. This happens in this context if there is an 'aging' process, or parts that are more likely to fail as time goes on. A value of $k = 1$ indicates that the failure rate is constant over time. This might suggest that random external events are causing mortality, or failure. In this case, the Weibull distribution function reduces to the exponential distribution function or the Poisson distribution. For high values of k, the Weibull cumulative distribution function shows a sharp transition.

motions. According to the Poisson distribution, the probability that exactly n events take place, where n is an integer (0,1,2,...), is given by

$$P(X = n; \lambda) = \frac{\lambda^n}{n!} \exp(-\lambda). \tag{2.4.6}$$

X is the stochastic variable counting the number of events and λ is a shape parameter with a value related to the subject to be analysed. The expected number of events in that same interval is where the probability has a maximum, i.e. where $dP/dn = 0$. At this maximum, also the logarithm of P, $\log P$ has a maximum. Using Stirling's approximation, for large n, $d \log P/dn \approx n \log \lambda - n \log n$ and the expected value of n in the selected interval is λ.

For a steady process under constant conditions, the expected value of n is proportional to the size or length of the interval selected and herewith the shape parameter λ. Considering a process in time, the Poisson distribution can be rewritten as

$$P(X = n; \lambda t) = \frac{(\lambda t)^n}{n!} \exp\big(-\lambda t\big). \tag{2.4.7}$$

The Poisson distribution function describes the number of events in a unit time interval and the shape parameter λ refers to a probability per unit time. Eq. (2.4.7) is frequently generalised to describe Poisson processes where conditions slowly vary over time and λ becomes a function of time too. In particular, this generalisation is applied to explain the tremors following from manmade stress changes in the subsurface, see Bourne et al. (2014).

The probability of no events in the time interval $[0, t]$ is according to Eq. (2.4.7),

$$P(X = 0; \lambda t) = \exp\big(-\lambda t\big). \tag{2.4.8}$$

Eq. (2.4.7) can also be seen as the probability density function f_{PS} of the stochastic variable X. Calling the first event to take place a 'failure', the related time-to-failure follows from inserting $n = 1$ into Eq. (2.4.7). For $t \geq 0$,

$$P(X = 1; \lambda t) = f_{PS}(x; \lambda t) = \lambda t \exp\big(-\lambda t\big). \tag{2.4.9}$$

Replacing λt by x/λ, we see that Eq. (2.4.9) is identical to the related expression for the Weibull distribution, Eq. (2.4.4) for $k = 1$.

For small intervals with a low probability for the occurrence of an event, the shape parameter $\lambda \ll 1$ according to Eq. (2.4.6). In good approximation, only the first few terms of $P(X = n; \lambda)$ in Eq. (2.4.6) do matter. They are

$$P(X = 0; \lambda) = \exp(-\lambda), \quad P(X = 1; \lambda) = \lambda \exp(-\lambda) \quad \text{and}$$

$$P(X = 2; \lambda) = \frac{\lambda^2}{2} \exp(-\lambda)... \tag{2.4.10}$$

Taking only the first two terms and using that for $\lambda \ll 1$, $\exp(-\lambda) \approx 1 - \lambda$, we have in good approximation

$$P(X = 0; \lambda) \approx 1 - \lambda \quad \text{and} \quad P(X = 1; \lambda) \approx \lambda(1 - \lambda) \approx \lambda. \tag{2.4.11}$$

In this case, similar tremor rates can be expected when taking a sample from the Poisson distribution function or from a uniform distribution function. The use of the latter can be compared with throwing a dice each time step and where throwing of e.g. number six leads to a failure. For the studies in this report, we found no significant differences in the results using one or the other.

Bourne and Oates (2014) call the shape parameter or intensity factor λ the intensity function. This function is related to the reservoir compaction, the reservoir compaction rate and a term related to Ogata's aftershock model. Disregarding the aftershock model term and the space dependency, λ is according to Bourne and Oates (2014), Eq. 19,

$$\lambda = \beta_0 \dot{c}(1 + \beta_1 c) \exp(\beta_1 c). \tag{2.4.12}$$

β_0 [s/m] and β_1 [1/m] are constants, $c = c(t)$ [m] is the reservoir compaction and $\dot{c} = \partial c(t)/\partial t$ [m/s] is the reservoir compaction rate. Since the compaction rate in the Groningen field has been approximately constant over the period of interest, λ can be approximated as

$$\lambda \approx \beta_2(1 + \beta_1 c) \exp(\beta_1 c), \tag{2.4.13}$$

where β_2 [1/m] is a constant. For a small time interval δt, the probability of one tremor is approximately

$$P_{n=1,\delta t} = \lambda \delta t \approx \beta_2(1 + \beta_1 c) \exp(\beta_1 c)\delta t. \tag{2.4.14}$$

For $\beta_1 c \gg 1$, $P_{n=1,\delta t} \propto c \exp(\beta_1 c)$. According to the present model, the probability for one tremor in the same small time interval δt is

$$P_{n=1,\delta t} = \left(1 - \exp(-\eta^k)\right) \times \lambda_{PS} \delta t. \tag{2.4.15}$$

The first term expresses the relative likelihood of tremor due to fault failure depending on the variable η. In the absence of stress relaxation by tremors, η is proportional to the change in the reservoir pressure and herewith to the reservoir compaction c. The Poisson shape parameter λ_{PS} is here a normalisation constant to match the number of modelled tremors to the number of observed tremors. Both expressions for $P_{n=1,\delta t}$, Eqs. (2.4.14) and (2.4.15), lead in a certain range of reservoir pressures or reservoir compaction to a steep or 'exponential' increase in the probability of a tremor in the time interval δt under a constant compaction rate.

2.5 Application of the Weibull distribution for the probability of tremors

Originally, Weibull explained the statistical nature of the failure of brittle materials assuming a weakest link. Later, Weibull's weakest link theory has been applied to explain

scale effects in laboratory measured rock properties. Nowadays, the Weibull distribution is used to calculate how many products of a single series have failed in a certain period and under a certain load[15]. This phenomenological distribution function is also used to calculate the probability of failure of a system with many similar components. The fact that all products or components are not exactly equal but vary in strength and dimensions may lead to this distribution, see also Appendix A.

In general, these observations lead to a phenomenological understanding of the effects of heterogeneity on the failure of natural materials. Small material heterogeneities influence the development of the fracture process zone by affecting fracture growth and fracture coalescence and may lead to a Weibull distribution for the probability of macroscopic failure[16]

Instead of describing a failure process of heterogeneous materials over time under a constant load caused by subsonic micro-fracture growth and coalescence over time, we apply the Weibull distribution function at a much larger scale and for a different reason[17]. Zooming out, we consider the whole reservoir rock in the region of interest as a heterogeneous macroscopic body. The heterogeneities at the larger scale follow from the system of faults or fault segments with different dip and azimuth angles, different throws and local variations in the horizontal stress, in the compaction modulus and in the rock strength parameters.

We suppose that, in general, the faults react independently on the mean stress in the region generated by the reduction of the pressure in the reservoir. This is a fair assumption for the Groningen field where the mean distance between the mapped faults exceeds the length of the disturbed stress zone around a fault. This zone is confined within a distance of a few times the reservoir thickness[18]. Herewith, the area of significant deformation around faults at reservoir offsets is a fraction of the area of the compacting

[15]It is used to characterise the lifetime distribution of granular materials, such as catalyst particles used in cat crackers. Another example is the lifetime distribution of light-bulbs, see Timmer (2000). They fail because of the evaporation of the tungsten wire and reactions between tungsten and little amounts of oxygen. Preferably these processes occur at grain boundaries. The filament fails by brittle fracture when it becomes too weak from thinning. The motion of dislocations towards the grain boundaries could further contribute to the weakening of the grain boundaries.

[16]This application of the Weibull distribution should not be confused with another related application of the Weibull distribution. The Weibull distribution is also used to populate rock with microscopic heterogeneous fracture networks in numerical models for three dimensional rock failure. The related finite element simulations underscore the significant influence of microcrack length statistics, see for example Cai (2012). However, it may be well possible that other distribution functions for microscopic properties could also lead to a Weibull probability of failure at a macroscopic scale.

[17]Actually, subsonic and plastic rock degradation may lead to the formation of a nucleation site of sufficient dimensions for a tremor along the fault. The description of this process is outside the scope of the present work.

[18]At this stage, we cannot exclude that seismic waves generated by a tremor of sufficient energy cause fatigue-like damage on nearby faults. This still should be sorted out.

reservoir.
When faults could be regarded as isolated or independent features in the field, stress relaxations by tremors in one fault smooth out over the entire region. If true, we expect that a tremor has almost no direct effect on a particular stress condition in one of the surrounding faults.

Further, we suppose that the physical barriers for failure do not change with time and that the frictional resistance to overcome these barriers does not change in another way than by the load. This all means that the probability of a tremor (or a local failure) in this system and the related tremors in a given time interval only depend on the mean load which is a result the initial stress, the change in the reservoir pressure and the tremors generated so far. Herewith, the time reduces to a parameter defining the stress condition.

We cannot proof that the Weibull probability function can be applied for this system. One argument to use it follows from observed temporal distributions of natural earthquake occurrences. According to Ohnaka (2013), §7.1, quasi-periodic earthquake occurrences can be observed when a large fault is in a critically stressed state under a quasi-steady condition defined by a constant tectonic force at large distance from the fault over sufficient time. After an earthquake and a sudden (partial) reduction of the subsurface stress, the mean load on the fault builds up at a constant rate until the next main earthquake occurrence. The distribution of the time-to-failure, or the interevent time, can be described by a Weibull distribution. The mean interevent time corresponds with the time in which the mechanical load builds up over the fault before a major earthquake takes place.
A naturally loaded fault differs only in geometrical aspects from the system of independent faults loaded by the compacting reservoir, we consider. The physical process of loading a system with weak elements is the same. So, we see no fundamental physical reason why the Weibull distribution function could not be applied for the faults in the compacting reservoir. Further, for small tremor-rich regions in the Groningen field of a few square kilometers, we observe also a tendency to a similar quasi-periodic behaviour, see §3.6.

Chapter 3

Application of the model to the seismic activity in the Groningen, Annerveen and Eleveld fields

3.1 Field data

The model has been applied to analyse the tremors in the Groningen, Annerveen and Eleveld fields following from compaction by gas production. No earthquakes have been recorded before production[1]. The reservoir pressure before production was about 35 MPa, at about hydrostatic. We expect no major subsurface stresses other than the usual field stress and those induced by reservoir compaction. The anisotropy in the horizontal field stress is small. Approximately, $\sigma_{h,0} = \sigma_{H,0}$[2].

The $\sim$ 40 x 40 km Groningen field has numerous faults with various reservoir offsets and fault dips. The reservoir thickness varies from about 100 m in the south-east to about 300 m in the north-west and the reservoir compaction has varied over the period 1964 - 2008 from 0.15 m in the south-east of the field to about 0.25 m in the center of the field. The mean uniaxial compression coefficient C_m is of the order 10^{-4} MPa^{-1}. More data is given in Appendix C, §C.1. The Annerveen and Eleveld fields are smaller. The Annerveen field is $\sim$ 17 km in east-west direction and $\sim$ 3 km in north-west direction. The Eleveld field is $\sim$ 3 km in east-west direction and $\sim$ 5 km in north-west direction[3]. Both fields contain also faults, see Appendix C, §C.2.

[1] Tremors in hydrocarbon fields in the Netherlands have only be observed after a pressure depletion exceeding 10 MPa, see van Eijs et al. (2006).

[2] Extensive modelling of Sanz et al. (2015) indicates that this oversimplifies the stresses on the faults in the field. The stresses vary according to reservoir, fault and overburden geometry.

[3] For more data about the Eleveld field, we refer to Roest and Kuilman (1993) and Roest and Kuilman (1994).

3.2 Tremor data

The tremor data used originates from the Koninklijke Nederlands Meteorologisch Instituut in the Netherlands (KNMI) as can be found in tables available from the KNMI www.knmi.nl WEB site. The data we have used is given in Appendix D, Tables D.0.2 - D.0.21 . The tables contain the name of the town/village of the hypocenter of the tremors, the date/time of the tremors, the easting and northing X and Y [km] coordinates of the hypocenters and the magnitude of the tremors M [Richter]. For the data from january 1960 to december 2014, the X and Y locations of the hypocenters of the tremors have been calculated from the longitude and lattitude data as provided by the KNMI. The elapsed time in terms of days has been calculated from the data by using that an average year has 365.25 days.

The tables contain about 1000 tremors. However, the network of seismometers has been designed to detect and locate tremors in the Groningen field above magnitudes of $M = 1.5$ and was only fully operational after 1994. This means that not all tremors before 1995 have been captured. Excluding data before 1995 and with magnitudes below $M = 1.0$, about 700 tremors remain. The distribution of tremors is not uniform over the Groningen field and also the frequency-magnitude relationship derived in the regions of interest varies somewhat. Figure 3.3.1 shows the tremors and identified faults in and around the Groningen field.
In plots showing this relationship, all earthquakes with a magnitude above a lower limit are counted and the base-10 logarithm of this count N is shown as a function of the lower limiting magnitude M_{llm}. For increasing M_{llm} there are less and less tremors with magnitudes above this limit. So, these plots can be seen as a cumulative distribution functions (or cdf) when reading it from right to left[4]. Taking various periods and parts of the field the b-value in the Gutenberg-Richter law $logN = a - bM_{llm}$ varies in the range $0.8 < b < 1$, see below. The related constant β in the Pareto probability distribution for the frequency-magnitude relationship is in the range $0.5 < \beta < 0.66$[5].

The hypocenters of a number of tremors are away from the plotted faults. Still, we assume that most if not all tremors are fault related for the following reasons. Firstly, not all the faults that can be derived from seismics have been included in the fault data file. Moreover, it can be argued a number some faults have not been identified by seismics. From a statistical analysis of the frequency of appearance faults with different fault throws, it can be expected that a considerable number of faults with throws in the range 30 - 70 m have not been found, see Mallik (2015). So, the shown set of faults is incomplete.

[4]We can reproduce Pijpers (2014a), Figure 2. In particular, we can derive from the same data, i.e. from the whole field in the period 1995 - 2012, the Gutenberg-Richter law $logN = a - bM_{llm}$ with a slope of $b \sim 1$, consistent with the value reported by Dost et al. (2012). The match with the observed data is for the range $1.1 < M_{llm} < 3.1$. For lower limiting magnitudes, the observed number of tremors is less than expected from the Gutenberg-Richter law. This deficit of observed tremors is expected from the limited sensitivity of the seismometer network

[5]From $N \propto 10^{-bM}$, $M_0 \propto 10^{3/2M}$ and $N \propto M_0^{-\beta}$, we obtain that $\beta = 2/3b$.

On the other hand, many or a significant number of the faults presented here may slip non-seismically or don't slip at all. Herewith, the typical distance and length of seismic active faults in the regions of interest is uncertain.
The second reason is that the location of the observed tremors is not accurately known. It may even exceed the 500 m uncertainty circle around the designated location, as claimed by the KNMI[6].

3.3 Regions of interest

We have analysed 6 regions around Loppersum, Ten Boer, Lageland, Woudsbloem, Annen and Eleveld. These regions have most tremors, see also Figure D.0.1 in Appendix D. Annen and Eleveld are the villages above the Annerveen and Eleveld fields which are located south of the Groningen field.
We have included the Annerveen and Eleveld fields because the reservoirs are in the same Rotliegend rock as in the Groningen field but the reservoir pressure reductions over time have been quite different in these fields. In the selected west part of the Annerveen field, the main reservoir pressure reduction from 35 MPa to 5 MPa took place in the period before 1995. In the Eleveld field, the main reservoir pressure reduction took place in the period before 2005[7]. In the Annerveen field the tremors started after the main gas production. Most tremors are observed in the period 1995 - 2014 when the reservoir pressure slowly declined from about 5 MPa to about 1 MPa[8]. Herewith in contrast, the tremor rate decreased in the Eleveld field after the reservoir pressure reduction rate in the largest south block decreased, i.e. after 2005.

The default radius of the area of the regions, R_{area} is 5 km. The lower limit of the magnitude is varied using $M = 1$ and 1.5 noting that not all tremors of magnitudes below $M = 1.5$ have been measured by at least three seismometers in the Groningen field. For the region around Loppersum, we repeated the calculations also for a lower limit of the magnitude $M = 0.5$. Table 3.3.1 shows the field data used in the model. Figure 3.3.2 shows the tremors and part of the faults in the regions of interest in more detail. Larger figures for the regions round Loppersum, Ten Boer, Woudsbloem and Lageland are shown in Appendix D, Figures D.0.2 - D.0.5 . Remembering that the shown fault set is incomplete, the mean distance between the fault segments in the regions of interest is

[6]According to Kraaijpoel and Dost (2013), the typical accuracy of the localisation of the tremors is in the order of 1 km in the horizontal plane.

[7]The Eleveld field has three blocks, from south to north B, B1 and B2, see Appendix C §C.2. According to NAM ELV-101 and ELV-102 well data, the reservoir pressure in the south and largest 4×3 km^2 B block decreased from about 38 MPa to about 3 MPa over the period 1975 - 2005, and initially at a somewhat higher rate. In june 2009, the reservoir pressure in the ELV-101 well was about 2 MPa. The reservoir pressure in the center block B1 of about 2 - 3 km^2 reduced from 1996 - 2014 from 38 MPa to 20 MPa. The reservoir pressure in the north block B2 of about 2 - 3 km^2 reduced from 2008 - 2014 from 38 MPa to 5 MPa.

[8]According to NAM data, this holds for the ANN, WTD, WVD and ZLV wells. The pressure drop in the ANS and ZLN wells is somewhat slower.

of the order of 1 km.

For the Groningen field, we take that the reservoir pressure during gas production is uniform and starts to decline in 1970 at a constant rate for the entire field up to the end of 2014. We disregard local non-uniformities in the reservoir pressure and temporal deviations from a constant pressure decline. In particular, we disregard that the production around Loppersum has been reduced since early 2014. For the Annerveen and Eleveld fields, we have used other pressure reduction rates, see Table 3.3.1 . Note that these fields have been depleted much faster and that the main pressure depletion stopped long before 2014. For the Eleveld field, we use the reservoir pressure development of the largest block B. This simplification has consequences for the fit parameters derived, see also §3.6.
We ignore possible effects of salt creep during gas production on the stresses on the faults and ignore variations in the compaction rate over the Groningen, Annerveen and Eleveld fields.

Table 3.3.1 : Default input parameters for 6 regions of interest. Values for the regions around Ten Boer, Lageland, Woudsbloem, Annen (Annerveen field) and Eleveld are the same as for Loppersum if they are not repeated in these columns. The region around Eleveld includes the three reservoir blocks B, B1 and B2 of the Eleveld field. We use the reservoir pressure development of the largest block B.
The mean fault distance between the seismic active fault segments is only an indicative number. It is used to determine constaints on the fit parameter c_{M0} related to stress relaxation along the faults.

Property	Symbol	Unit	Lop	TenB	Lag	Wou	Ann	Ele
.....	.....	.....	.....	.....	.....	.....	.....	.....
X-coord. of center of region	X_{cen}	km	244	250	242	248	244	235
Y-coord. of center of region	Y_{cen}	km	598	591	585	578	566	553
radius of area	R_{area}	km	5	5	5	5	5	5
mean fault distance	D_f	km	1.2	1.3	1.1	1.0	NA	NA
start year	t_0	Y/M	1960/01					
end date	t_1	Y/M	2015/01					
time step	δt	day	4					
initial pressure	p_0	MPa	35				35	38
'halfway' pressure	p_x	MPa					5	3
final pressure	p_1	MPa	10				1	3
start date pressure drop	$t_{p,0}$	Y/M	1970/01				1973/01	1975/01
date halfway pressure drop	$t_{p,x}$	Y/M					1995/01	2005/01
end date pressure drop	$t_{p,1}$	Y/M	2015/01				2014/01	2014/01
min. magnitude tremors	M_{min}	Richter	1.0/1.5					
min. seism. mom. tremors	$M_{0,min}$	TJ	0.045/0.25					
max. magnitude tremors	M_{max}	Richter	4.0					
max. seism. mom. tremors	$M_{0,max}$	TJ	1400					

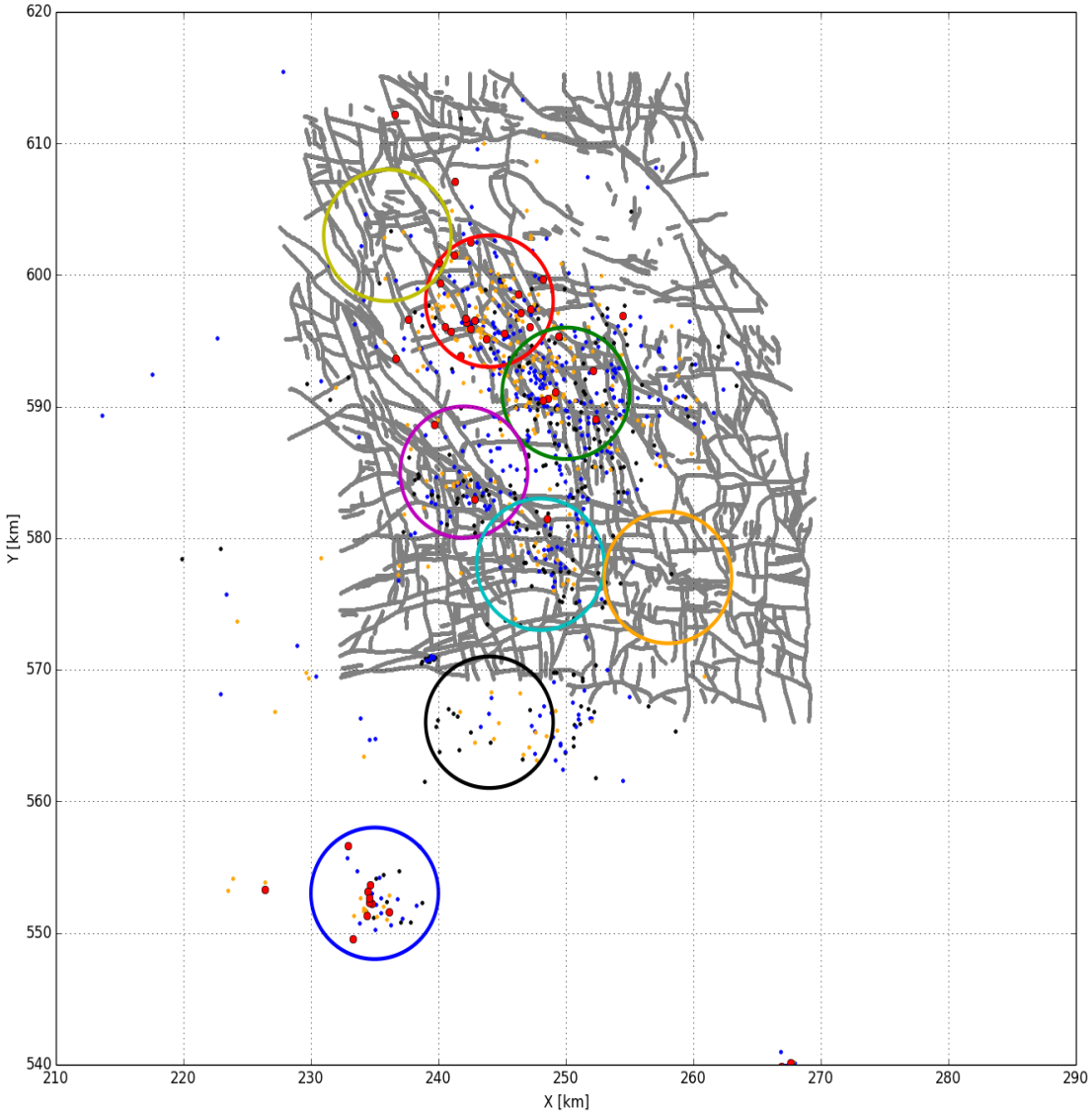

Figure 3.3.1 : Faults and hypocenters of tremors in the Groningen field according to KNMI and NAM data. The faults are shown as grey lines. The regions of interest are shown by circles of 5 km radius, Loppersum (red), Ten Boer (green), Lageland (magenta), Woudsbloem (cyan), Scheemda (orange), Usquert (yellow), Annerveen (around Annen) (black) and Eleveld (blue). The hypocenters of the tremors are shown by the coloured dots. The colors correspond to the magnitude of the tremors in the following ranges on the scale of Richter: black for $0.5 \leq M < 1$, blue for $1.0 \leq M < 1.5$, orange for $1.5 \leq M < 2.5$ and red for $2.5 \leq M < 4$. Note that not all faults with throws less than about 80 m and tremors below $M = 1.5$ have been captured.

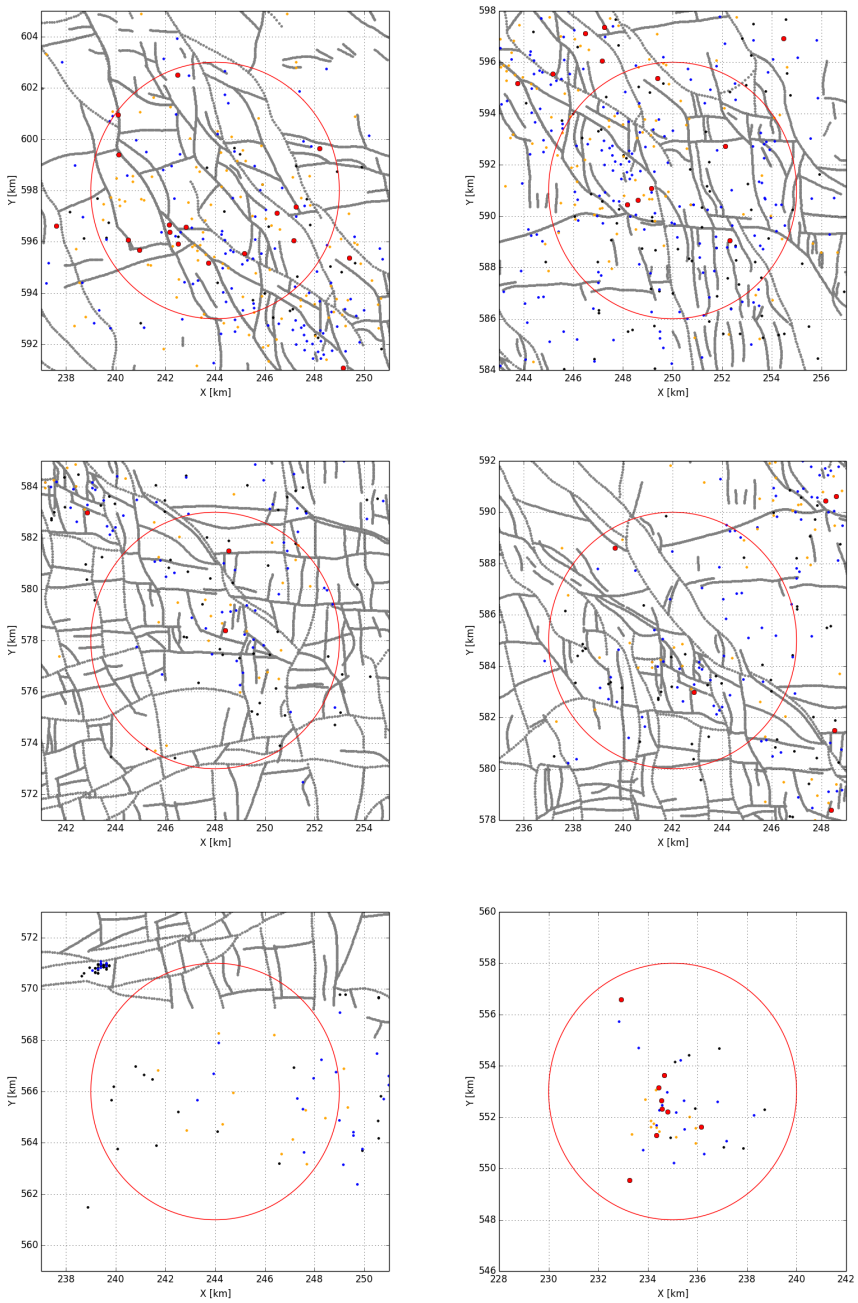

Figure 3.3.2 : Faults and hypocenters of tremors in the Groningen field according to KNMI and NAM data. The faults are shown as grey lines. The regions of interest are shown by red circles of 5 km radius, Loppersum (left-top), Ten Boer (right-top), Lageland (left-center) and Woudsbloem (right-center), Annerveen (around Annen) (left-bottom) and Eleveld (right-bottom). For the regions around Annen and Eleveld the fault data is not shown. The hypocenters of the tremors are shown by the coloured dots. The colors correspond to the magnitude of the tremors in the following ranges on the scale of Richter: black for $0.5 \leq M < 1$, blue for $1.0 \leq M < 1.5$, orange for $1.5 \leq M < 2.5$ and red for $2.5 \leq M < 4$. Note that not all faults with throws less than about 80 m and tremors below $M = 1.5$ have been captured. Larger figures for these regions are shown in Appendix D.

3.4 Results

The default number of time steps taken to simulate the period 1960 - 2015 is 5000. This corresponds with a time step of about 4 days. This time step is small enough to reproduce the tremor rate of tremors with a magnitude $M \geq 0.5$ in the regions of interest.

The number of Monte Carlo simulations to fit the model with the observed data is 50[9]. From these simulations, we calculate the mean number and the standard deviation of the modelled number of tremors as a function of time. The Gutenberg-Richter b-values of the frequency-magnitude distribution of the tremors in the regions of interest are the same as those derived from the observed tremors in these regions[10]. The values are obtained using the *curve_fit* routine of Python which is based on the least square error method applied to the frequency lower limit magnitude relation.
The b-value is assumed to be constant over the whole period of gas production and reservoir compaction. We disregard a possible decrease of the b-value over time because a possible trend is hard to derive from the relative small number of tremors. According to Harris (2015), there is no statistical evidence for changing b-values over time. Note that there is no fundamental reason to expect a constant b-value for systems which deform non-steadily, such as a compacting reservoir, see also §2.3.1.
The width of the bins to derive the b-value is in all cases 0.3 M. The magnitude intervals somewhat vary from case to case, see the tables. Taking the lower limit of the magnitude interval, we acknowledge that the network of seismometers could have missed tremors below $M = 1.5$. Taking the upper limit, we acknowledge that the deviation between the observed number of tremors and the statistically expected number can be large for a small number of tremors, as has been illustrated by Harris (2015), Figure 1[11].
To suppress extreme large magnitudes using low b-values, the maximum accepted magnitude is taken M = 4. In practice, this constraint is only effective for b-values of 0.7 - 0.8 and in combination with stress relaxation by tremors, i.e. for significant values of c_{M0}.

The standard deviation in the estimation of the b-value is considerable for small numbers of tremors, see Harris (2015) for a rigorous determination of the b-values and the uncertainties herein. When there are about 100 tremors, we estimate a standard deviation in the b-value of about 0.1. For about 30 tremors, we estimate a standard deviation of about 0.15[12]. Low numbers of tremors are obtained when the regions produce only a few

[9] In fact, 10 - 20 simulations would also be sufficient to make a good fit to the observed data.

[10] Determining the b-value from the observed data, the last tremor was not used.

[11] This figure shows that the error term is large for a small number of tremors when the number of bins in the histograms is more than 5. Considering the same subjective limits, Harris (2015), Eq. A.14 gives practically the same b-values.

[12] According to Harris (2015), Eqs. A.44 and A.45, the standard deviation in the determination of the b-value is $\sigma_b = \sigma_{\log N}/\Delta M$. $\sigma_{\log N}$ is the standard deviation in the number of tremors in the bins with respect to a straight line. $\Delta M = \sqrt{\sum_{k=1}^{N}(M_k - \bar{M})^2} \sim \bar{M}$ is a measure for the magnitude range over which the b-value is determined. $\bar{M}$ is the mean value of the magnitude range. The summation is over all magnitude bins M_k where $k = 1, .., n$. For an uncertainty of about 1.5 tremors in the bins for the

tremors or for small regions of interest or when the lower magnitude limit is high.
For the regions around Lageland, Woudsbloem and Annen (Annerveen field) with a moderate number of tremors, the observed b-values are higher than 1. For the regions with many tremors, the observed b-values tend to be lower. For the region around Loppersum, b ~ 0.85. These lower values agree with the b-value derived from tremors observed by the geophones in two deep observation wells in Stedum and Zeerijp near Loppersum. For the region around Ten Boer, b ~ 1 for $M \geq 1.0$ for an area with a radius of 5 km around the center. It drops to about b ~ 0.6 for smaller areas around the center, see §3.5 below. For the region around Eleveld, we derive a low b-value of about 0.7. Harris (2015) obtains similar b-values for the regions around Loppersum and Ten Boer, using a more rigorous maximum likelihood method which gives more weight to the lower magnitudes.

We ignore variations in the reservoir compaction rate over the Groningen field, in contrast with Bourne and Oates (2014). Also, we ignore variations in the geometric constant relating vertical stress to the mean shear stress on the faults. So, we take constant values for α and c_{σ_v}, i.e. $\alpha = 0.7$ and $c_{\sigma_v} = 0.5$. As a consequence, variations in the shape parameter of the Poisson process λ_{PS} or variations in the typical mean stress on faults for seismic failure τ_{fail} (or typical reservoir pressure change for seismic failure $\delta p_{fail} = \tau_{fail}/(\alpha c_{\sigma_v})$) highlight differences in reservoir compaction or in fault properties in the different regions of interest.
We also ignore that the three blocks B, B1 and B2 in the Eleveld field have been produced differently. The effect of the different reservoir pressure reductions in these blocks is discussed in §3.6.

Firstly, we show the results of the model supposing that the tremors generated hardly reduce the mean stress state, i.e. if $c_{M0} = 0$. A more physical correct condition of a non-negligible, finite stress relaxation by tremors is discussed in §3.6 below. The derived fit parameters are given in Tables 3.4.2 and 3.4.3 .
Table 3.4.1 shows the sensitivities of the fit parameters on the value of the time step δt and the minimum magnitude M_{min} for the region around Loppersum. The time step δt has a marginal effect on the Weibull parameter k_W and the typical failure pressure change δp_{fail}. For larger time steps, the observed short interevent times are not captured. For smaller areas around the center, similar parameters are derived.
The observed tremors are reasonably well spread over the region around Loppersum. For the areas with radii 5, 4, 3 and 2 km, the number of tremors with $M \geq 1.0$ are 136, 107, 66 and 28, respectively. This corresponds with about 1.7, 2.1, 2.2 and 2.1 tremors per km^2. There is a systematic north-south gradient in the number of tremors which may explain why the tremor density of the 5 km radius region is smaller, see §3.6.
Tables 3.4.2 and 3.4.3 show that variations in τ_{fail} are moderate for the regions investigated. Actually, there is a positive correlation between the fit parameters τ_{fail} and λ_{PS}. Increasing the first fit parameter, the second one must also increase to maintain the same

higher magnitudes, which we observe for these numbers of tremors, $\sigma_{\log N} \sim 0.2$ and a mean magnitude $\bar{M} = 2$, $\sigma_b \sim 0.15$.

fit with little or no effect on the Weibull distribution shape parameter k_W.
For $M_{min} \geq 1$, the Weibull distribution shape parameter k_W is in the range 6 - 7 and the typical pressure change for failure δp_{fail} in the range 16 - 20 MPa. The value of this parameter is quite robust against variations in the parameters τ_{fail} and λ_{PS}. Although the onset of the tremor rate could be somewhat influenced by the installment of the network of seismometers in the Groningen field, the value of the Weibull shape parameter k_W is remarkably high in relation to possible variations in fault properties leading to Mohr-Coulomb shear-type failure. According to §A.3 in Appendix A, Table A.3.1 , the mechanical properties with an effect on shear-type fault failure should on average vary less than about 10% to obtain such a high value for k_W.

The value of the minimum magnitude M_{min} has hardly an effect on the fit parameters. For the other regions of interest, we choose two minimum magnitudes, $M_{min} = 1$ and $M_{min} = 1.5$. The default value for the radius of the region of interest is $R_{area} = 5$ km. We observe that the area of the region has no significant effect on k_W and δp_{fail}. The Poisson shape parameter λ_{PS} which is used to normalise the tremor rate is roughly in proportion to the number of tremors. In most cases $\lambda_{PS} \ll 1$. The Poisson probability distribution function to normalise the tremor rates could have been replaced by a uniform probability distribution function.

Figures 3.4.1 - 3.4.12 show the results for the regions of interest for $M_{min} = 1$ and $M_{min} = 1.5$. They show the number of tremors over time, the reservoir pressure and stress state over time, the distribution of interevent times and the Gutenberg-Richter frequency-magnitude relationship.
For the Loppersum and Ten Boer regions, the modelled mean number of tremors show a small but distinct difference with the observed number in the last three years, i.e. from 2012 - 2015. While the modelled number almost constantly increases with time, the observed number tends to increase somewhat faster in this period. Another, but opposite clear difference is observed for the region around Eleveld where the reservoir pressure reduction in block B after 2005 almost has stopped. In this case, the modelled number of tremors steadily increases while the observed ones increase at a significantly lower rate. This observation has been used to calibrate or constrain the value of the stress relaxation factor c_{M0} in §3.6 below.
The typical mean shear stress on faults for seismic fault failure τ_{fail} for the Annerveen field is considerably higher than for the other fields. This is a consequence of the observed tremor rate. Tremors started after 1995 when most of the reservoir pressure drop in the field had occurred. It is not clear yet which field or fault attribute is responsible for this. The modelled tremor rate of a single simulation scatters around the mean value similarly as the observed tremor rate. Whether there is a statistical significant difference in the scattering around the mean tremor rate between the modelled and the observed tremors is still outstanding. To the eye, the interevent time histograms show no systematic differences.

A first attempt to identify an explicit effect of reservoir compaction in the regions of interest on the numbers of tremors or on the cumulative seismic moment generated by these tremors $M_{0,cum}$, is to compare these quantitities with the mean subidence in these regions over a considerable period of time. For the Groningen field, the mean subsidence in a region is a reasonable proxy or surrogate for the mean reservoir compaction in the same region. We have used the subsidence data over the period 1972 - 2008, see Appendix C. In this period, the reservoir pressure in the Groningen field decreased roughly uniformly over the field from about 35 MPa to about 12 MPa. In the model, the number of tremors strongly depends on the parameter λ_{PS} for constant Weibull shape parameter k_W and mean shear stress for seismic failure τ_{fail}. Disregarding variations in k_W and τ_{fail}, Table 3.4.4 shows that λ_{PS} somewhat correlates with the number of tremors.

For the regions of interest, we do not observe a clear proportionality between the mean subsidence, the number of tremors, the cumulative seismic moment of these tremors or the parameter λ_{PS} which determine the tremor rate. Further, we note that the mean subsidence in the regions around Usquert and Scheemda in the same period 1972 - 2008 are 13 and 14 cm, respectively. The regions hardly produce tremors. Regarding the subsidence data, we would have expected more tremors in these regions.
It seems that other factors, such as fault properties and rock material, are important too. But, this statement requires firstly a more thorough analysis whether the lack of proportionality is statistically relevant regarding the small number of tremors. So far, we have not identified from the fault property histograms in Appendix C a fault property which can be correlated to the number of tremors.

Table 3.4.1 : Fit parameters for the region around Loppersum obtained for various time steps, minimum tremor magnitudes and areas around the center. The stress relaxation parameter $c_{M0} = 0$.

δt	M_{min}	R_{area}	N_{obs}	λ_{PS}	k_W	b	δp_{fail}
day	Richter	km	-	-	-	-	MPa
.....	.....	.....	.....	.....	.....	.....	.....
2	0.5	5	154	0.045	6	0.85	16.6
4	0.5	5	154	0.091	5	0.85	16.6
2	1.0	5	136	0.040	6	0.83	16.6
4	1.0	5	136	0.080	6	0.83	16.6
8	1.0	5	136	0.160	6	0.83	16.6
16	1.0	5	136	0.320	6	0.83	16.6
4	1.0	4	107	0.064	6	0.83	17.0
4	1.0	3	66	0.038	6	0.83	17.0
4	1.0	2	28	0.016	6	0.83	16.6
4	1.5	5	82	0.053	6	0.83	16.6

Table 3.4.2 : Fit parameters for 6 regions of interest. The time step $\delta t = 4$ days, minimum magnitude $M = 1.0$, radius of area $R_{area} = 5$ km, stress relaxation parameter $c_{M0} = 0$. The minimum and maximum magnitudes used to determine the b-value from the observed tremors are listed seperately. They somewhat vary from region to region, depending on the number of tremors, see also the related figures.
The b-value and the Pareto distribution shape parameter β are dependent, $\beta = 2/3b$. This holds also for the fit parameters τ_{fail} and δp_{fail}. τ_{fail} is calculated from δp_{fail} using typical values $\alpha = 0.7$ and $c_{\sigma_v} = 0.5$.

Property	Symbol	Unit	Lop	TenB	Lag	Wou	Ann	Ele
.....	.....	.....	.....	.....	.....	.....	.....	.....
Number of observed tremors	N_{obs}	-	136	160	67	55	20	38
Min. magn. to fit GR law	$M_{min,GR}$	Richter	1.5	1.5	1.6	1.4	1.4	1.5
Max. magn. to fit GR law	$M_{max,GR}$	Richter	3.5	3.3	2.8	2.8	2.4	3.0
Pareto distr. shape parameter	β	-	0.55	0.67	0.8	0.8	0.8	0.47
Gutenberg-Richter b-value	b	-	0.82	1.0	1.2	1.2	1.2	0.7
Poisson distr. shape parameter	λ_{PS}	-	0.080	0.11	0.043	0.038	0.011	0.017
Weibull distr. shape parameter	k_W	-	6	7	7	6	7	7
typ. pressure change for failure	δp_{fail}	MPa	17	18	19	18	30	19
mean shear str. for seism. fail.	τ_{fail}	MPa	5.8	6.3	6.8	6.4	10.4	6.8

Table 3.4.3 : Fit parameters for 6 regions of interest. The time step $\delta t = 4$ days, minimum magnitude $M = 1.5$, radius of area $R_{area} = 5$ km, stress relaxation parameter $c_{M0} = 0$. The minimum and maximum magnitudes used to determine the b-value from the observed tremors are listed separately. They somewhat vary from region to region, depending on the number of tremors, see also the related figures.
The b-value and the Pareto distribution shape parameter β are dependent, $\beta = 2/3b$. This holds also for the fit parameters τ_{fail} and δp_{fail}. τ_{fail} is calculated from δp_{fail} using typical values $\alpha = 0.7$ and $c_{\sigma_v} = 0.5$.

Property	Symbol	Unit	Lop	TenB	Lag	Wou	Ann	Ele
.....	.....	.....	.....	.....	.....	.....	.....	.....
Number of observed tremors	N_{obs}	-	82	60	19	24	11	22
Min. magn. to fit GR law	$M_{min,GR}$	Richter	1.5	1.5	1.6	1.4	1.4	1.5
Max. magn. to fit GR law	$M_{max,GR}$	Richter	3.5	3.3	2.8	2.8	2.4	3.0
Pareto distr. shape parameter	β	-	0.55	0.67	0.8	0.8	0.8	0.47
Gutenberg-Richter b-value	b	-	0.83	1.0	1.2	1.2	1.2	0.7
Poisson distr. shape parameter	λ_{PS}	-	0.053	0.043	0.016	0.018	0.007	0.010
Weibull distr. shape parameter	k_W	-	6	7	7	6	7	7
typ. pressure change for failure	δp_{fail}	MPa	17	18	19	19	30	19
mean shear str. for seism. fail.	τ_{fail}	MPa	6.0	6.3	6.8	6.8	10.4	6.8

Table 3.4.4 : Mean subsidence in the period 1972 - 2008, the number of tremors N, the cumulative seismic moment of the observed tremors $M_{0,cum}$ and the fit parameters λ_{PS} and τ_{fail} for the 6 regions of interest for $M_{min} = 1.5$.
The observed subsidence is for the Groningen field a reasonable proxy for the reservoir compaction. This is not true for the smaller Annerveen and Eleveld fields. For the Eleveld field, the calculated reservoir compaction is 0.1 - 0.14 m, see Roest and Kuilman (1993). Taking $\delta_z = 0.12$ m, the ratio $-1000 \times \delta_z / N_{obs} \sim 6$.
The ratio's between the number of observed tremors, cumulative seismic moment, the selected model parametes of all tremors and the mean subsidence between 1972 and 2008 substantially differ for the regions of interest. Similar differences in the ratio's would remain after subtracting a constant treshold value for the subsidence (or reservoir compaction). The ratio $\times N_{obs}/\lambda_{PS}$ varies moderately considering that δp_{fail} and k_W do not vary much (except for the Annerveen field).

Property	Symbol	Unit	Lop	TenB	Lag	Wou	Ann	Ele
.....	.....	.....	.....	.....	.....	.....	.....	.....
Mean subsidence	δ_z	m	-0.26	-0.25	-0.21	-0.16	-0.07	NA
Number of observed tremors	N_{obs}	-	82	60	19	24	11	22
Cum. seism. moment, $M_{min} = 1.5$	$M_{0,cum}$	TJ	0.029	0.010	0.0014	0.0026	0.0010	0.0061
Cum. seism. moment, $M_{min} = 1.0$	$M_{0,cum}$	TJ	0.031	0.012	0.0024	0.0031	0.0012	0.0063
$-1000 \times \delta_z / N_{obs}$		m	3	4	12	7	7	NA
$-0.001 \times \delta_z / M_{0,cum}$, $M_{min} = 1.5$		m	1	2.5	15	6	7	NA
Poisson distr. shape parameter	λ_{PS}	-	0.053	0.043	0.016	0.018	0.007	0.010
$0.001 \times N_{obs}/\lambda_{PS}$		-	1.5	1.4	1.2	1.3	1.7	2.2

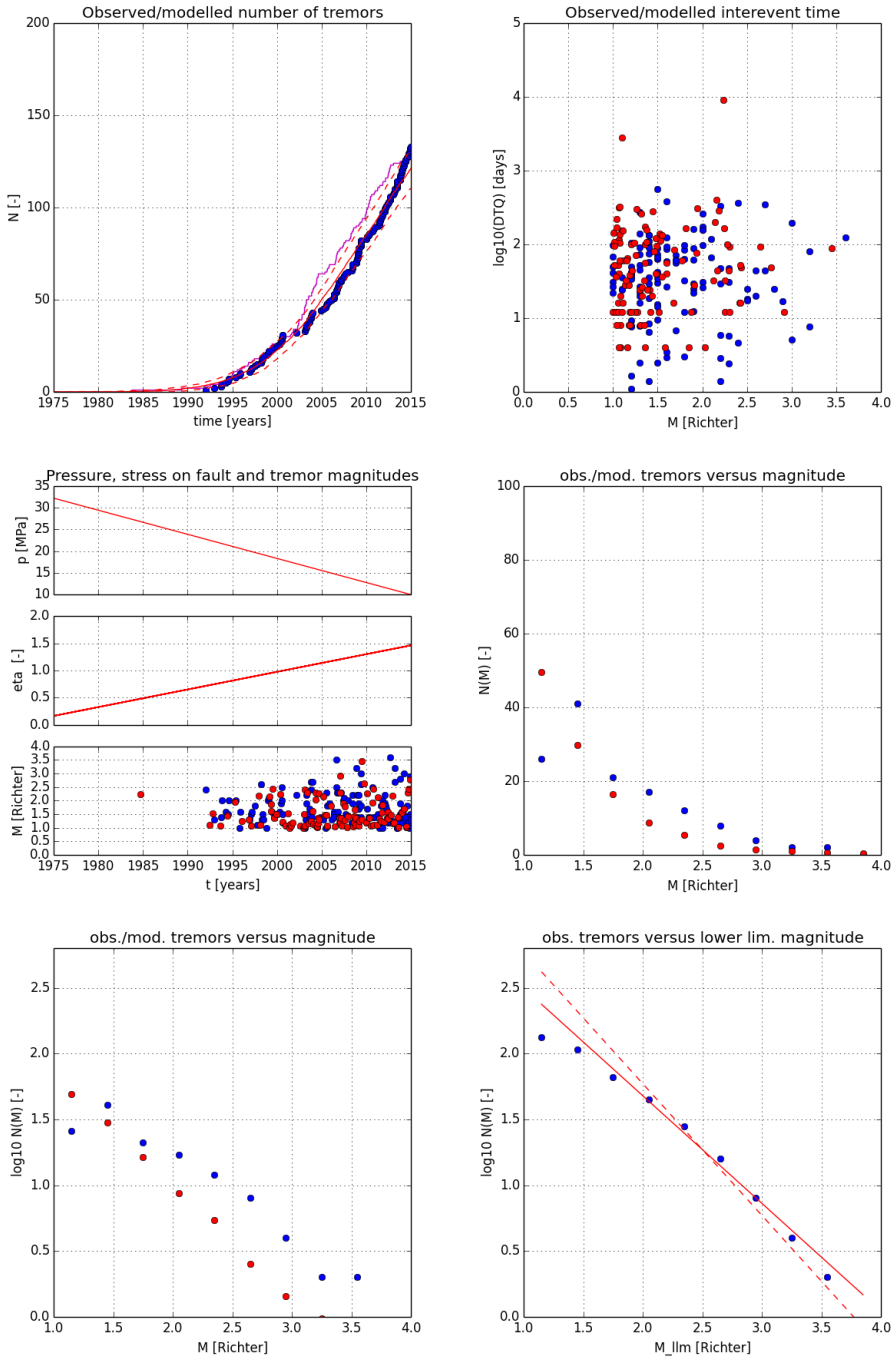

Figure 3.4.1 : Observed (blue dots) and modelled (red dots, lines) tremors around Loppersum, $M_{min} = 1.0$, $c_{M0} = 0$. Top-left: number of observed and modelled tremors as a function of time. Red solid line shows mean value of 50 simulations. Red dashed lines show $\pm$ one standard deviation from the mean value. Purple solid line shows one simulation. Top-right: interevent times versus magnitude M. Center-left: reservoir pressure, mean stress $\bar{\tau}$ and tremors versus time. Center-right: pdf of number of tremors versus magnitude. Bottom-left: cdf of number of tremors versus lower limiting magnitude M_{llm}. Bottom-right: cdf of log of number of tremors versus lower limiting magnitude M_{llm}. Dashed line $b = 1$.

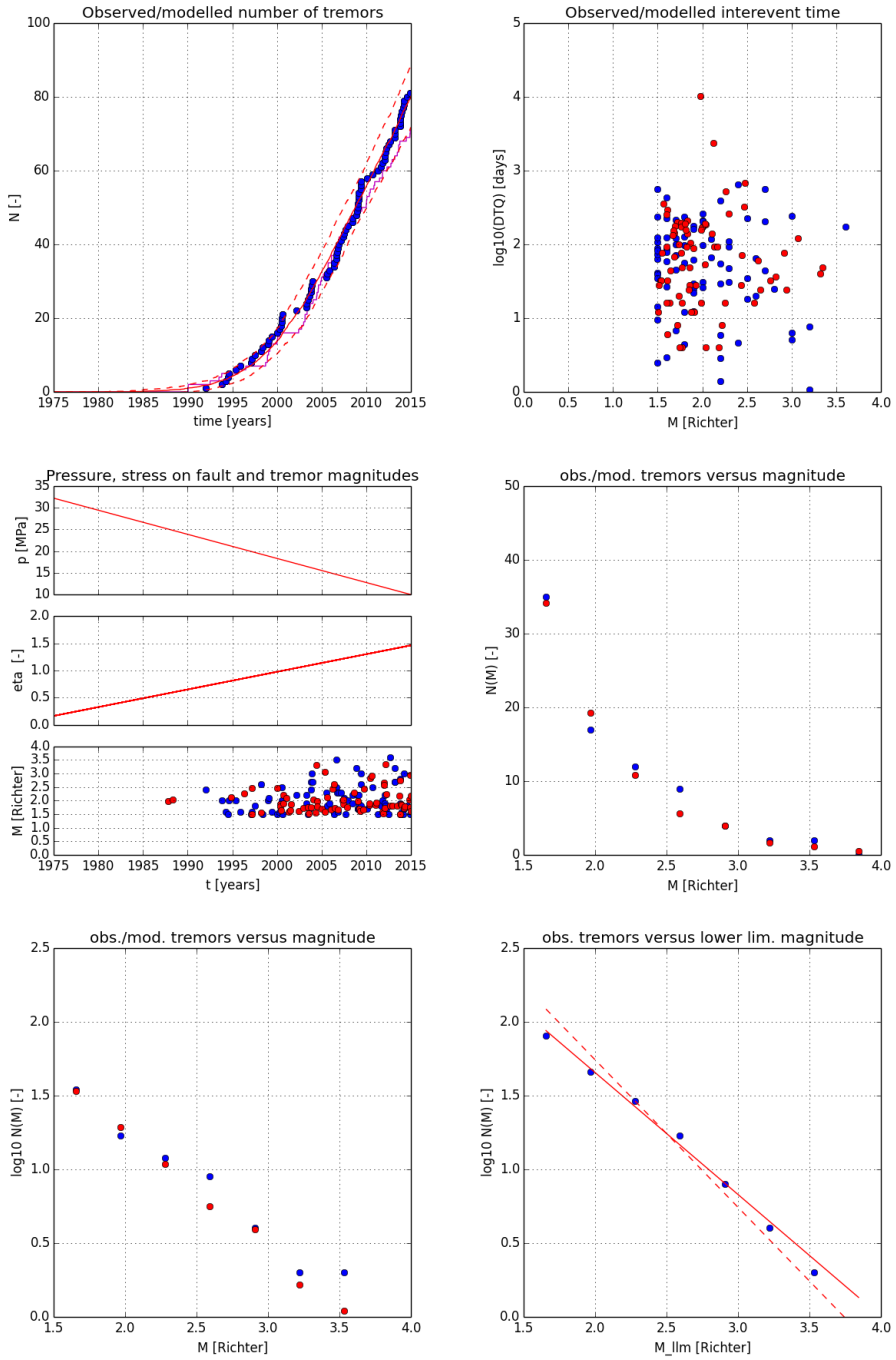

Figure 3.4.2 : Observed (blue dots) and modelled (red dots, lines) tremors around Loppersum, $M_{min} = 1.5$, $c_{M0} = 0$. Top-left: number of observed and modelled tremors as a function of time. Red solid line shows mean value of 50 simulations. Red dashed lines show $\pm$ one standard deviation from the mean value. Purple solid line shows one simulation. Top-right: interevent times versus magnitude M. Center-left: reservoir pressure, mean stress $\bar{\tau}$ and tremors versus time. Center-right: pdf of number of tremors versus magnitude. Bottom-left: cdf of number of tremors versus lower limiting magnitude M_{llm}. Bottom-right: cdf of log of number of tremors versus lower limiting magnitude M_{llm}. Dashed line $b = 1$.

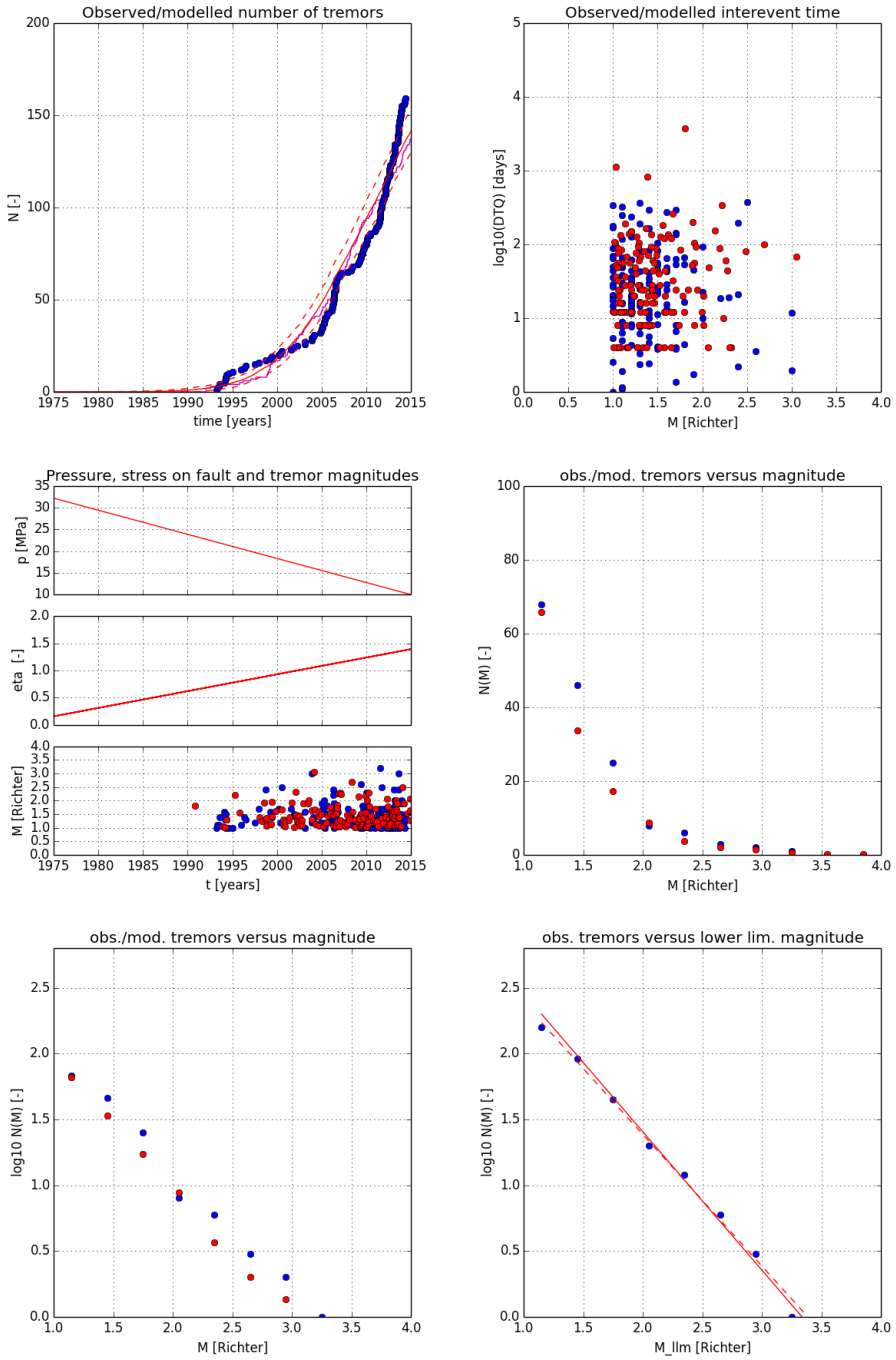

Figure 3.4.3 : Observed (blue dots) and modelled (red dots, lines) tremors around Ten Boer, $M_{min} = 1.0$, $c_{M0} = 0$. Top-left: number of observed and modelled tremors as a function of time. Red solid line shows mean value of 50 simulations. Red dashed lines show $\pm$ one standard deviation from the mean value. Purple solid line shows one simulation. Top-right: interevent times versus magnitude M. Center-left: reservoir pressure, mean stress $\bar{\tau}$ and tremors versus time. Center-right: pdf of number of tremors versus magnitude. Bottom-left: cdf of number of tremors versus lower limiting magnitude M_{llm}. Bottom-right: cdf of log of number of tremors versus lower limiting magnitude M_{llm}. Dashed line $b = 1$.

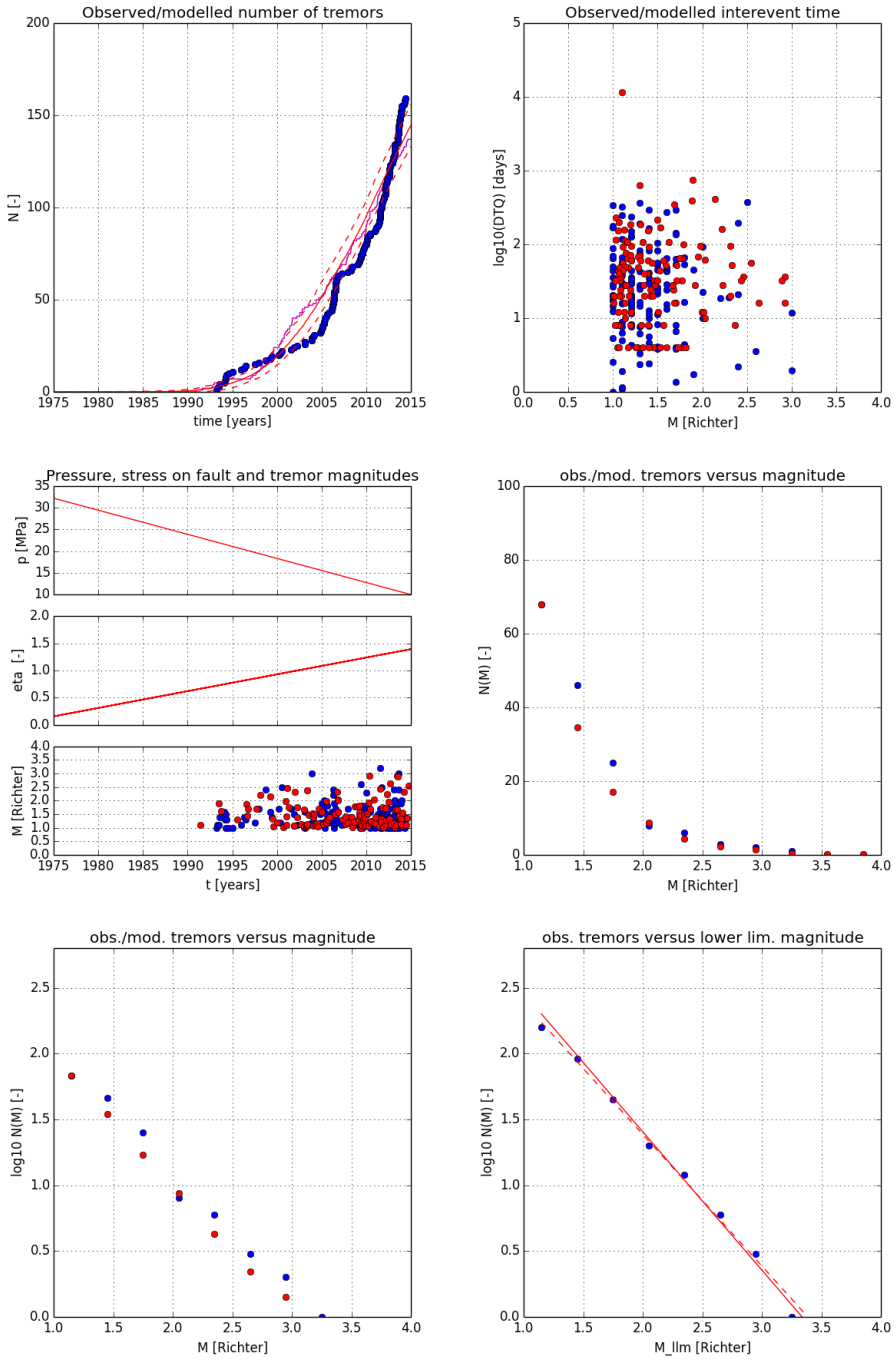

Figure 3.4.4 : Observed (blue dots) and modelled (red dots, lines) tremors around Ten Boer, $M_{min} = 1.5$, $c_{M0} = 0$. Top-left: number of observed and modelled tremors as a function of time. Red solid line shows mean value of 50 simulations. Red dashed lines show $\pm$ one standard deviation from the mean value. Purple solid line shows one simulation. Top-right: interevent times versus magnitude M. Center-left: reservoir pressure, mean stress $\bar{\tau}$ and tremors versus time. Center-right: pdf of number of tremors versus magnitude. Bottom-left: cdf of number of tremors versus lower limiting magnitude M_{llm}. Bottom-right: cdf of log of number of tremors versus lower limiting magnitude M_{llm}. Dashed line $b = 1$.

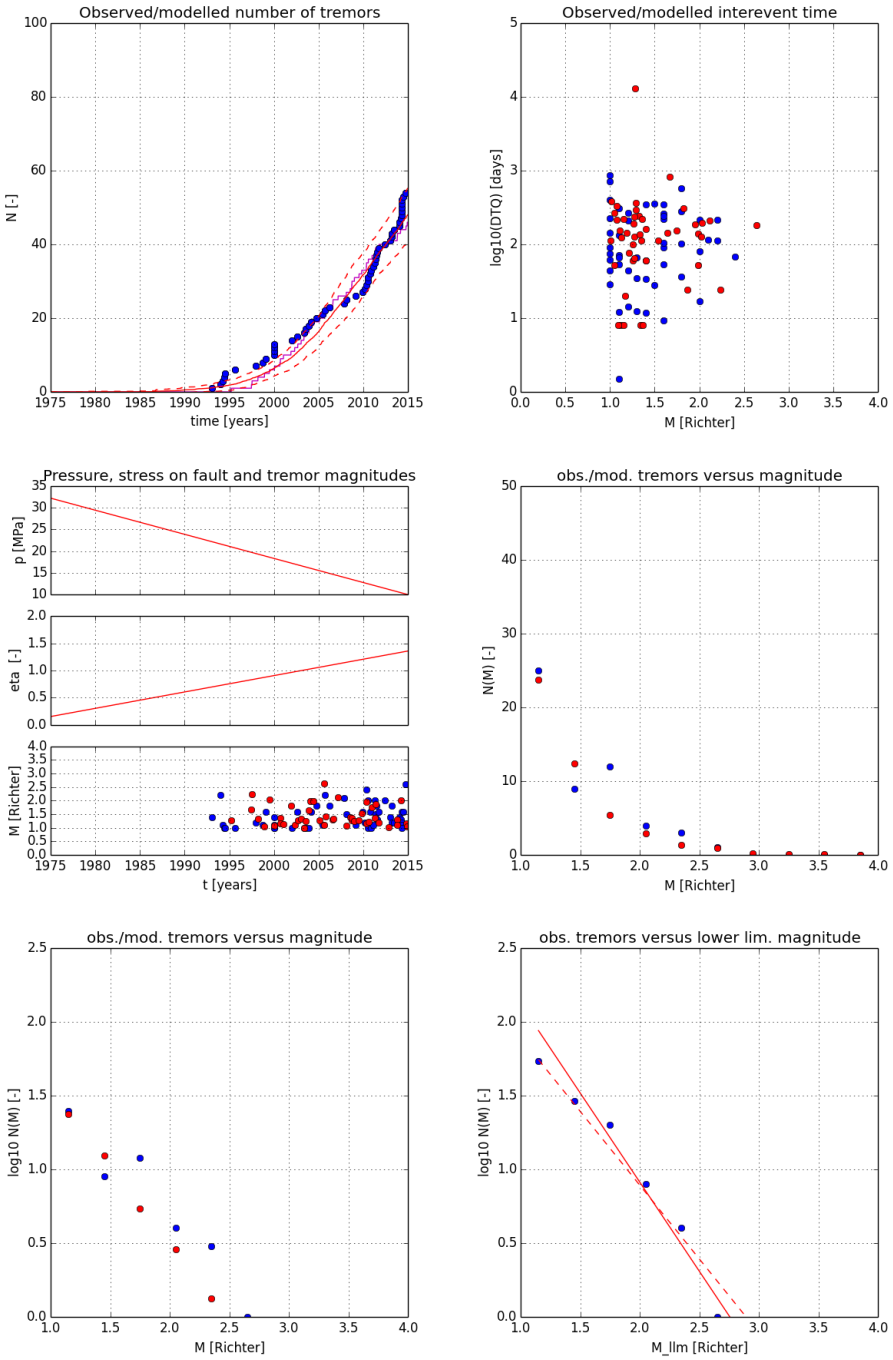

Figure 3.4.5 : Observed (blue dots) and modelled (red dots, lines) tremors around Woudsbloem, $M_{min} = 1.0$, $c_{M0} = 0$. Top-left: number of observed and modelled tremors as a function of time. Red solid line shows mean value of 50 simulations. Red dashed lines show $\pm$ one standard deviation from the mean value. Purple solid line shows one simulation. Top-right: interevent times versus magnitude M. Center-left: reservoir pressure, mean stress $\bar{\tau}$ and tremors versus time. Center-right: pdf of number of tremors versus magnitude. Bottom-left: cdf of number of tremors versus lower limiting magnitude M_{llm}. Bottom-right: cdf of log of number of tremors versus lower limiting magnitude M_{llm}. Dashed line $b = 1$.

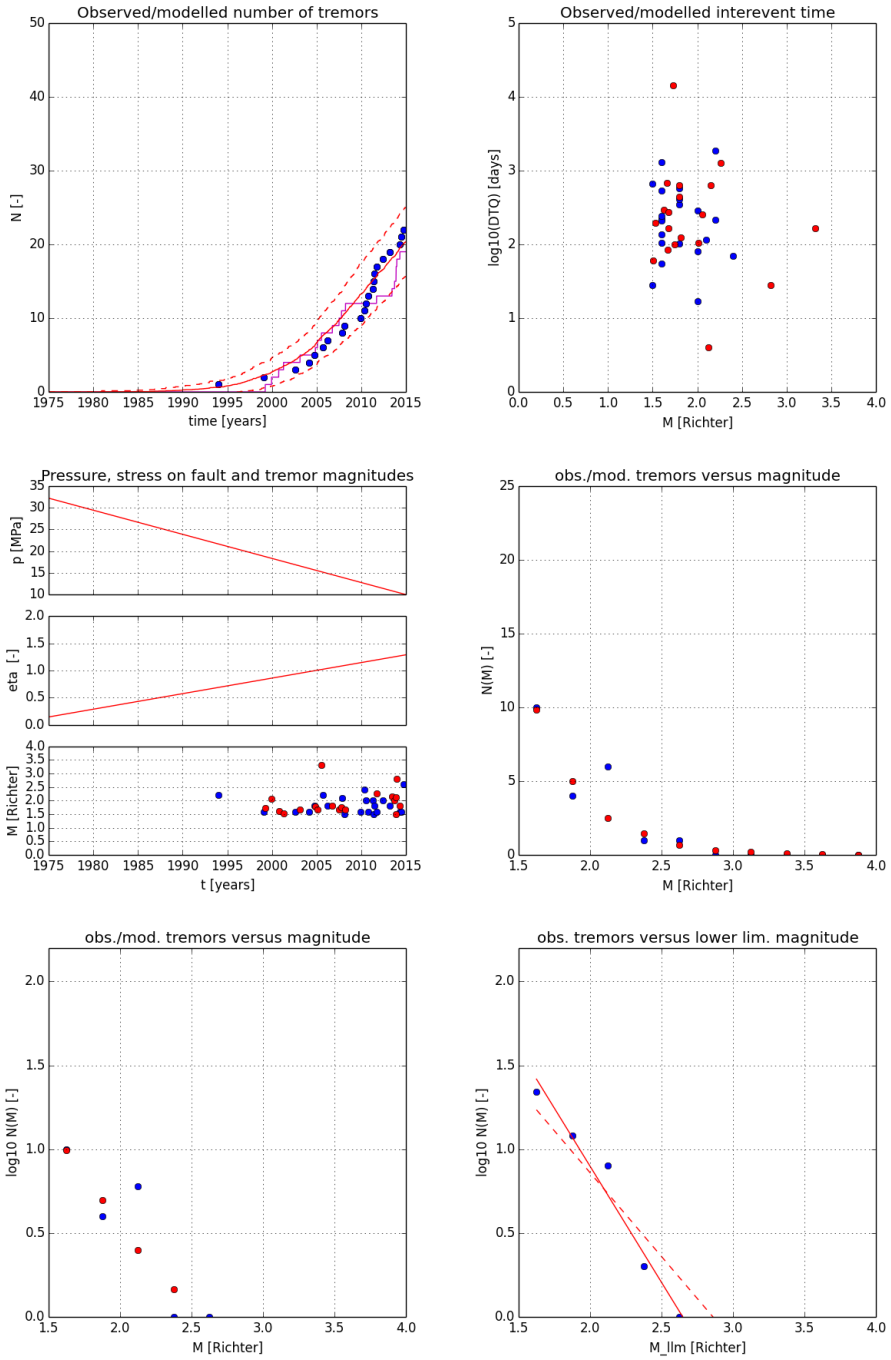

Figure 3.4.6 : Observed (blue dots) and modelled (red dots, lines) tremors around Woudsbloem, $M_{min} = 1.5$, $c_{M0} = 0$. Top-left: number of observed and modelled tremors as a function of time. Red solid line shows mean value of 50 simulations. Red dashed lines show $\pm$ one standard deviation from the mean value. Purple solid line shows one simulation. Top-right: interevent times versus magnitude M. Center-left: reservoir pressure, mean stress $\bar{\tau}$ and tremors versus time. Center-right: pdf of number of tremors versus magnitude. Bottom-left: cdf of number of tremors versus lower limiting magnitude M_{llm}. Bottom-right: cdf of log of number of tremors versus lower limiting magnitude M_{llm}. Dashed line $b = 1$.

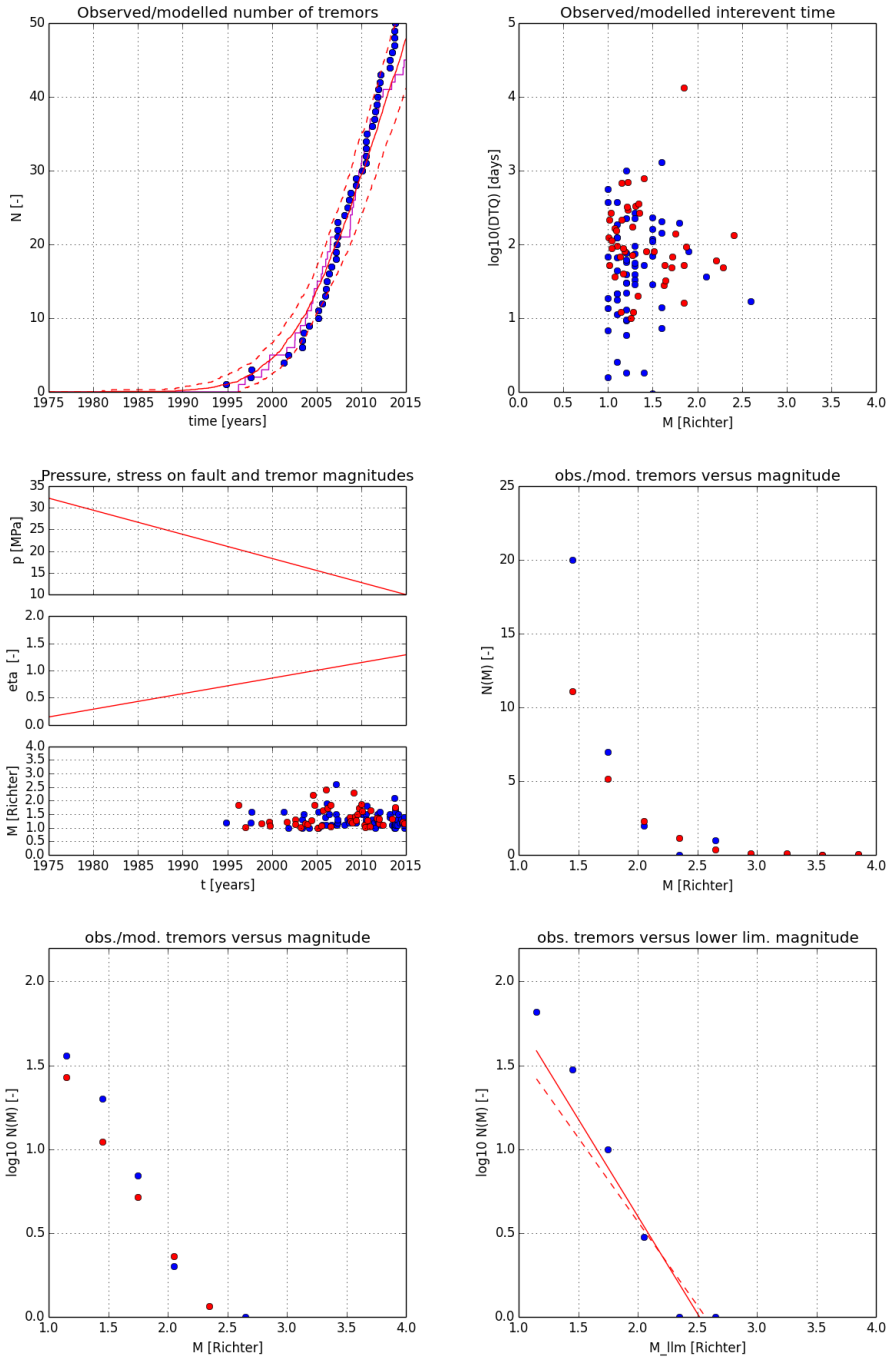

Figure 3.4.7 : Observed (blue dots) and modelled (red dots, lines) tremors around Lageland, $M_{min} = 1.0$, $c_{M0} = 0$. Top-left: number of observed and modelled tremors as a function of time. Red solid line shows mean value of 50 simulations. Red dashed lines show $\pm$ one standard deviation from the mean value. Purple solid line shows one simulation. Top-right: interevent times versus magnitude M. Center-left: reservoir pressure, mean stress $\bar{\tau}$ and tremors versus time. Center-right: pdf of number of tremors versus magnitude. Bottom-left: cdf of number of tremors versus lower limiting magnitude M_{llm}. Bottom-right: cdf of log of number of tremors versus lower limiting magnitude M_{llm}. Dashed line $b = 1$.

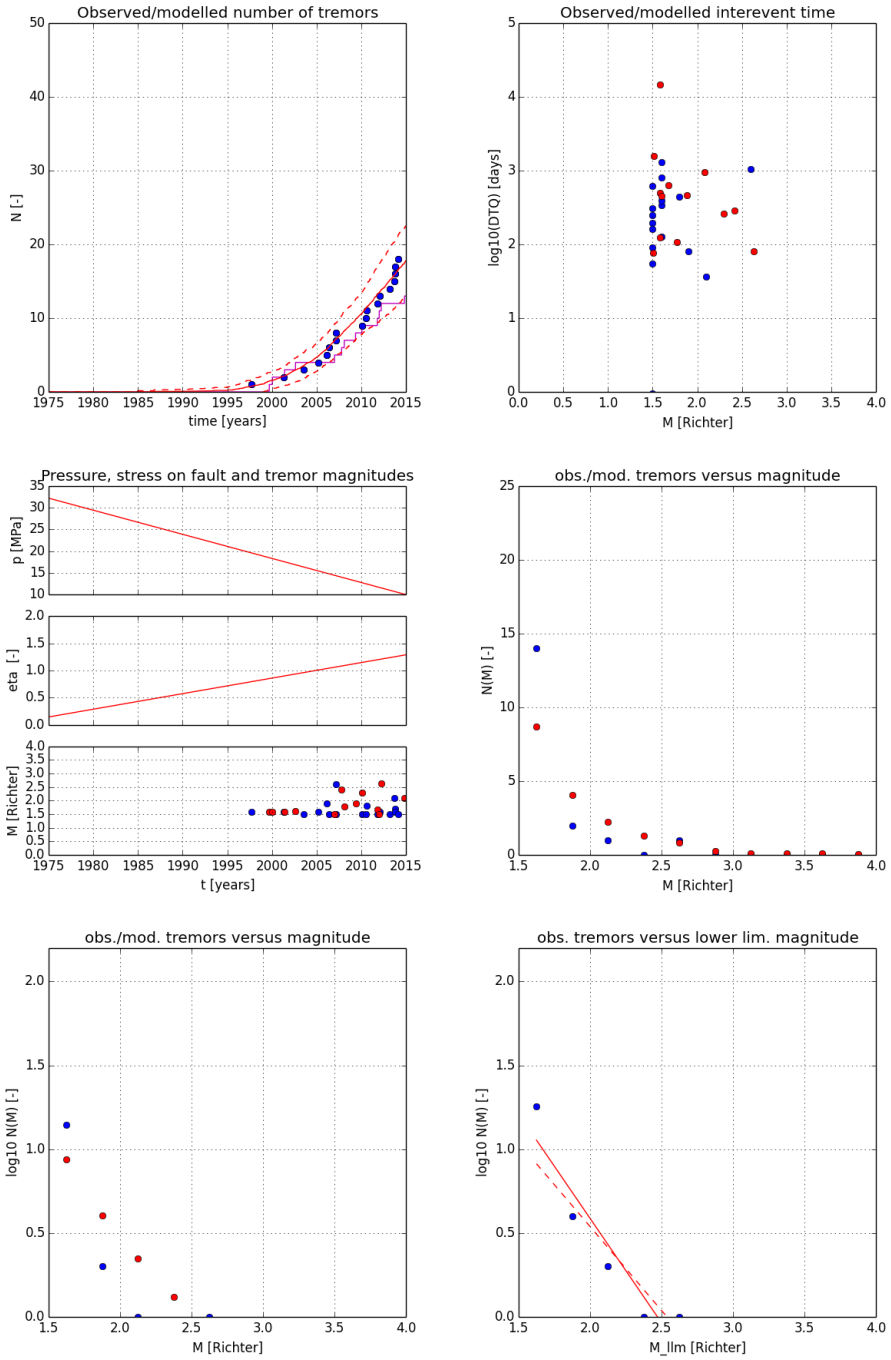

Figure 3.4.8 : Observed (blue dots) and modelled (red dots, lines) tremors around Lageland, $M_{min} = 1.5$, $c_{M0} = 0$. Top-left: number of observed and modelled tremors as a function of time. Red solid line shows mean value of 50 simulations. Red dashed lines show $\pm$ one standard deviation from the mean value. Purple solid line shows one simulation. Top-right: interevent times versus magnitude M. Center-left: reservoir pressure, mean stress $\bar{\tau}$ and tremors versus time. Center-right: pdf of number of tremors versus magnitude. Bottom-left: cdf of number of tremors versus lower limiting magnitude M_{llm}. Bottom-right: cdf of log of number of tremors versus lower limiting magnitude M_{llm}. Dashed line $b = 1$.

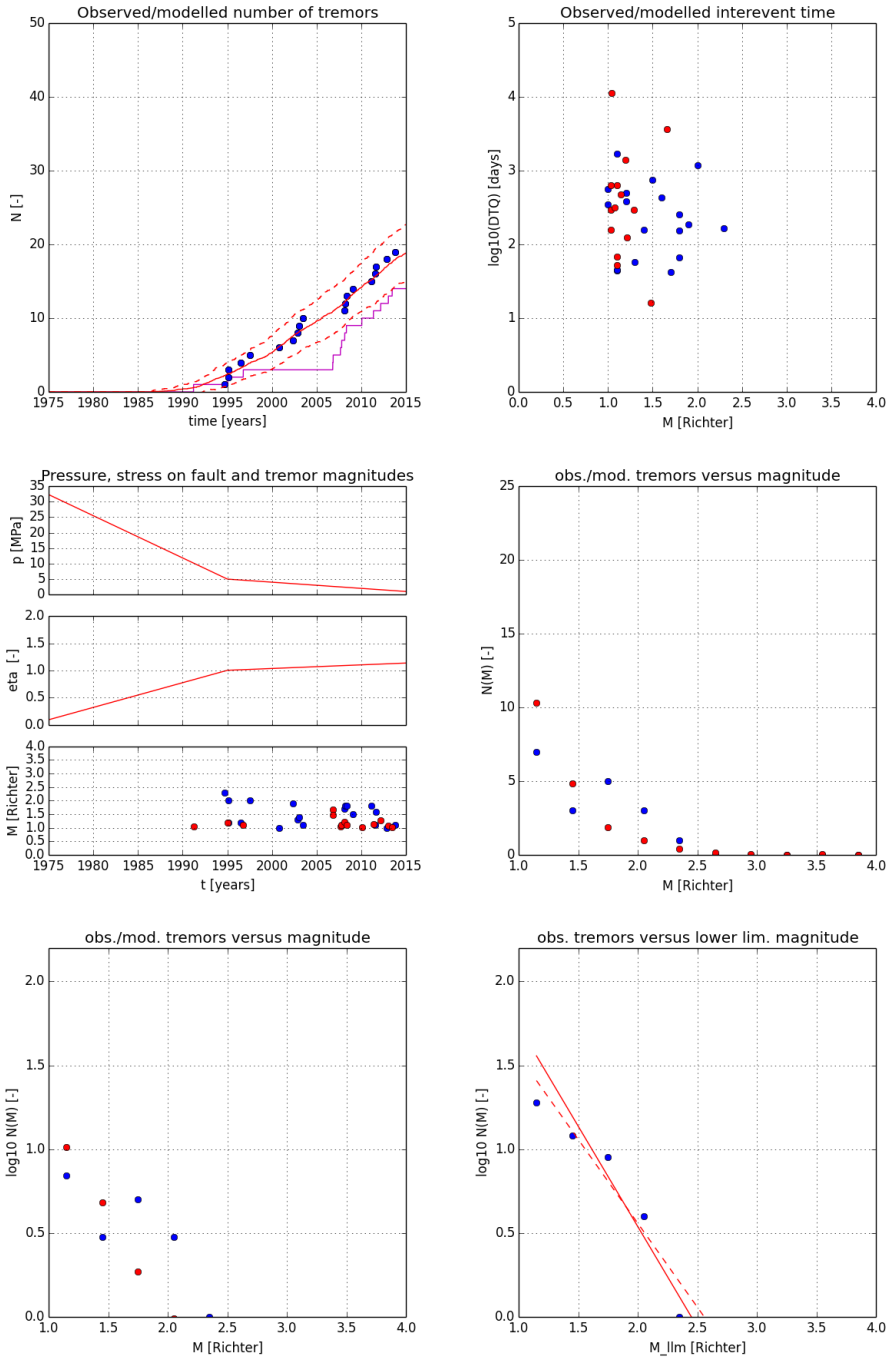

Figure 3.4.9 : Observed (blue dots) and modelled (red dots, lines) tremors around Annen in the Annerveen field, $M_{min} = 1.0$, $c_{M0} = 0$. Top-left: number of observed and modelled tremors as a function of time. Red solid line shows mean value of 50 simulations. Red dashed lines show $\pm$ one standard deviation from the mean value. Purple solid line shows one simulation. Top-right: interevent times versus magnitude M. Center-left: reservoir pressure, mean stress $\bar{\tau}$ and tremors versus time. Center-right: pdf of number of tremors versus magnitude. Bottom-left: cdf of number of tremors versus lower limiting magnitude M_{llm}. Bottom-right: cdf of log of number of tremors versus lower limiting magnitude M_{llm}. Dashed line $b = 1$.

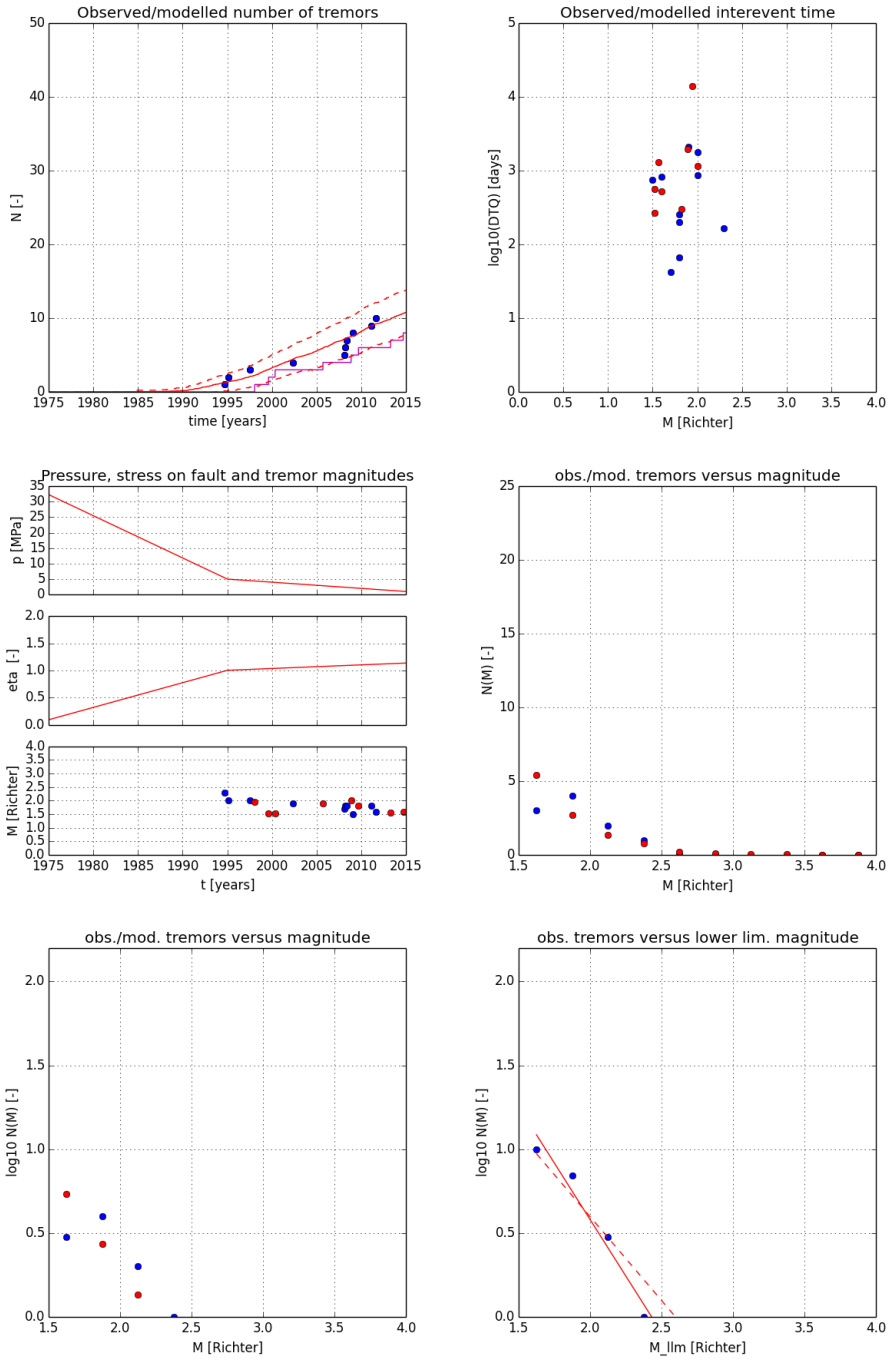

Figure 3.4.10 : Observed (blue dots) and modelled (red dots, lines) tremors around Annen in the Annerveen field, $M_{min} = 1.5$, $c_{M0} = 0$. Top-left: number of observed and modelled tremors as a function of time. Red solid line shows mean value of 50 simulations. Red dashed lines show $\pm$ one standard deviation from the mean value. Purple solid line shows one simulation. Top-right: interevent times versus magnitude M. Center-left: reservoir pressure, mean stress $\bar{\tau}$ and tremors versus time. Center-right: pdf of number of tremors versus magnitude. Bottom-left: cdf of number of tremors versus lower limiting magnitude M_{llm}. Bottom-right: cdf of log of number of tremors versus lower limiting magnitude M_{llm}. Dashed line $b = 1$.

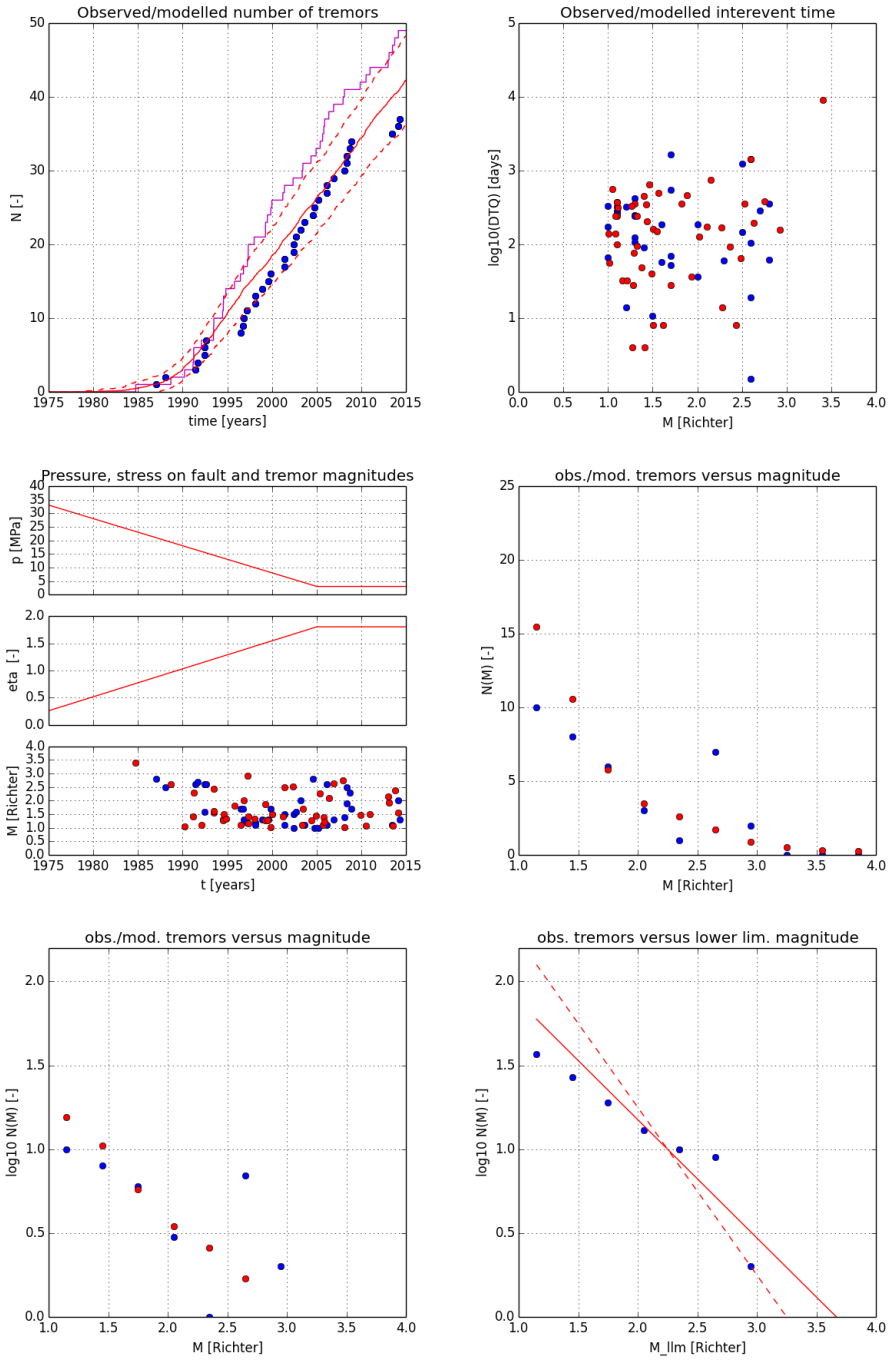

Figure 3.4.11 : Observed (blue dots) and modelled (red dots, lines) tremors around Eleveld, $M_{min} = 1.0$, $c_{M0} = 0$. Top-left: number of observed and modelled tremors as a function of time. Red solid line shows mean value of 50 simulations. Red dashed lines show $\pm$ one standard deviation from the mean value. Purple solid line shows one simulation. Top-right: interevent times versus magnitude M. Center-left: reservoir pressure, mean stress $\bar{\tau}$ and tremors versus time. Center-right: pdf of number of tremors versus magnitude. Bottom-left: cdf of number of tremors versus lower limiting magnitude M_{llm}. Bottom-right: cdf of log of number of tremors versus lower limiting magnitude M_{llm}. Dashed line $b = 1$.

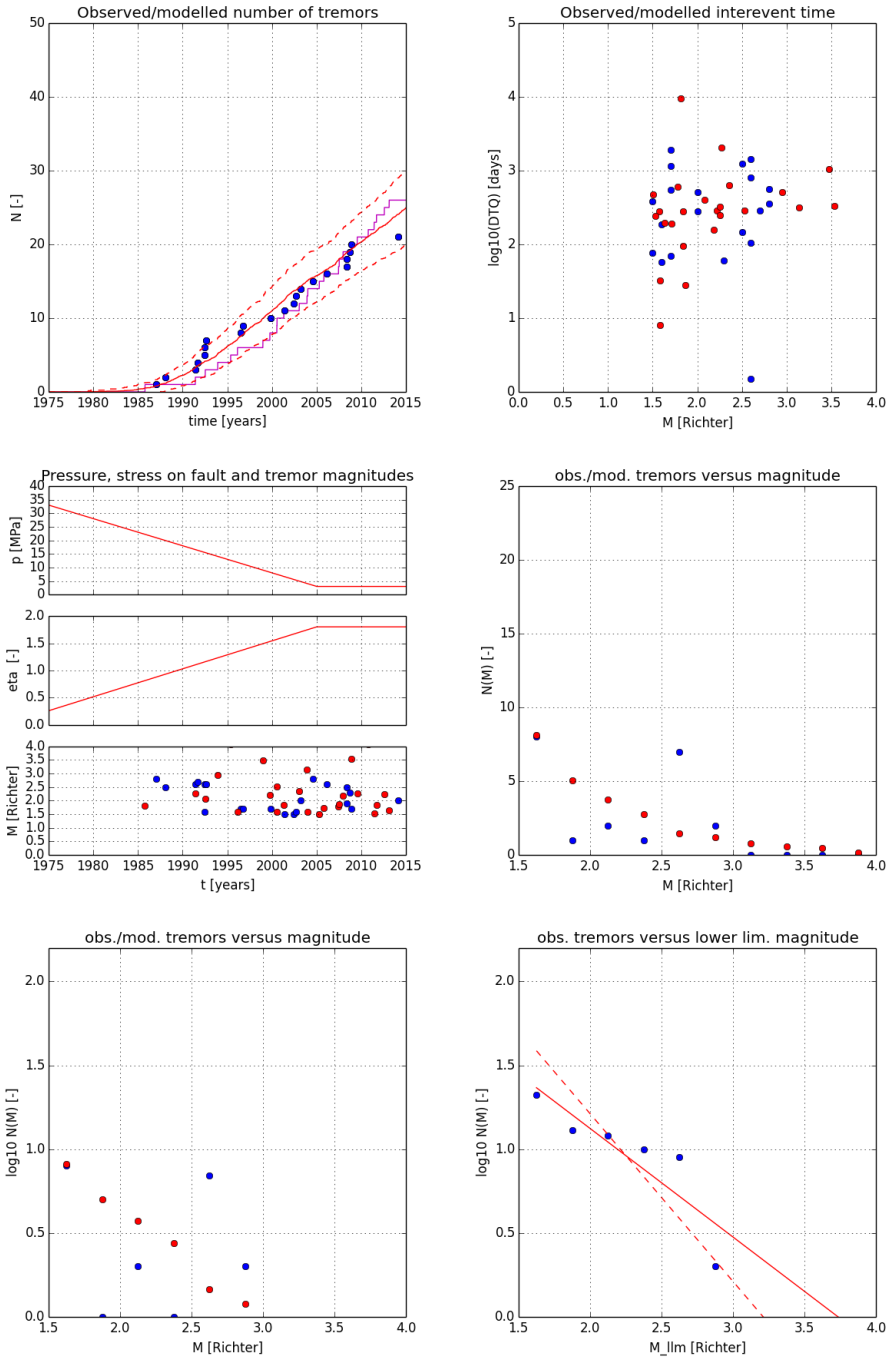

Figure 3.4.12 : Observed (blue dots) and modelled (red dots, lines) tremors around Eleveld, $M_{min} = 1.5$, $c_{M0} = 0$. Top-left: number of observed and modelled tremors as a function of time. Red solid line shows mean value of 50 simulations. Red dashed lines show $\pm$ one standard deviation from the mean value. Purple solid line shows one simulation. Top-right: interevent times versus magnitude M. Center-left: reservoir pressure, mean stress $\bar{\tau}$ and tremors versus time. Center-right: pdf of number of tremors versus magnitude. Bottom-left: cdf of number of tremors versus lower limiting magnitude M_{llm}. Bottom-right: cdf of log of number of tremors versus lower limiting magnitude M_{llm}. Dashed line $b = 1$.

3.5 The effect of the size of the region

In this section, the effect of the size of the region of interest is shown for the region around Ten Boer. The effect of the size of the region in the Eleveld field in relation to the gas production and the reservoir pressure reduction in the three blocks B, B1 and B2 in the field is discussed in §3.6. The tremor rate in around Ten Boer is comparable but about 15% higher than around Loppersum. The areas have radii of 5, 4, 3 and 2 km and have the same center. The tremor density is reasonably constant for these areas, see Table 3.5.1 . It is somewhat lower for the largest area with a radius of 5 km, like around Loppersom.

Keeping the Weibull shape parameter $k_W = 7$, the mean shear stress on the fault for seismic failure $\tau_{fail} = 6.3$ MPa and the stress relaxation factor $c_{M0} = 0$ constant, λ_{PS} scales with the number of observed tremors. In contrast with the region around Loppersum, the b-value of the Gutenberg-Richter frequency-magnitude relationship is about 1 for the larger regions with radii of 4 and 5 km. For the two smaller regions, the b-value decreases considerably to lower values. We repeat that also the uncertainty in these values is considerable because of the small numbers of tremors, i.e. the standard deviation is about $\pm$ 0.15 for about 30 tremors. A similar trend has been observed by Harris (2015) using the more robust maximum likelihood method.

Figure 3.5.1 and 3.5.2 show the number of tremors versus time, the interevent times versus tremor magnitude and the frequency-magnitude relationship for these areas for $M_{min} = 1.0$ and 1.5. The interevent times tend to cluster in a range 100 - 1000 days for the smaller regions although this is difficult to judge from the small number of tremors. Using a value $c_{M0} = 0$ and not allowing for a stress relaxation by tremors, the model cannot reproduce this clustering of interevent times. Rather, the modelled distribution of interevent times would shift to a larger mean interevent time.

Table 3.5.1 : Fit parameters for the region around Ten Boer for various areas around the same center. The stress relaxation parameter $c_{M0} = 0$, the mean shear stress on the faults for seismic failure $\tau_{fail} = 6.3$ MPa, the Weibull shape parameter $k_W = 7$ and the time step δt is 4 days for all cases.

M_{min}	R_{area}	N_{obs}	N_{obs}/A_{area}	λ_{PS}	b
Richter	km	-	km^{-2}	-	-
.....	.....	.....	.....	.....	.....
1.0	5	160	2.0	0.11	1.0
1.0	4	120	2.4	0.086	1.0
1.0	3	73	2.5	0.052	0.83
1.0	2	32	2.5	0.022	0.6
1.5	5	60	0.8	0.043	1.0
1.5	4	47	0.9	0.033	1.0
1.5	3	28	1.0	0.020	0.83
1.5	2	14	1.0	0.009	0.6

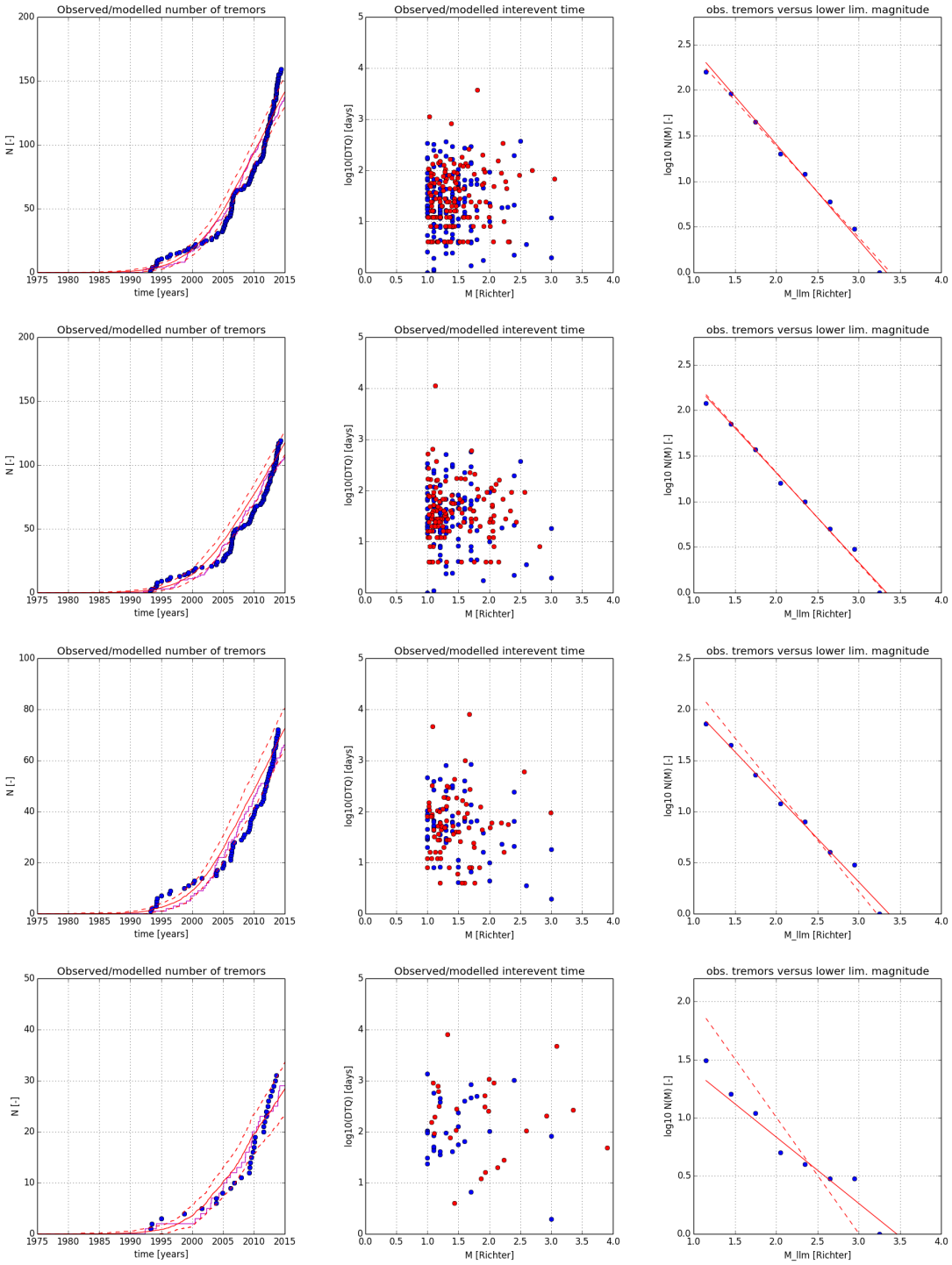

Figure 3.5.1 : Observed (blue dots) and modelled (red dots, lines) tremors in region around Ten Boer for various areas. $M_{min} = 1.0$, $c_{M0} = 0$, $c_{\sigma_v} = 0.4$, $k_W = 7$ and δt is 4 days for all cases. From top to bottom, areas with a radius R_{area} of 5, 4, 3 and 2 km. Left: number of tremors versus time. Solid line shows mean value of 50 simulations. Red dashed lines show ± one standard deviation from the mean value. Purple solid line shows one simulation. Center: interevent times versus magnitude M. Right: cdf of log of number of tremors versus lower limiting magnitude M_{llm}. Dashed line $b = 1$.

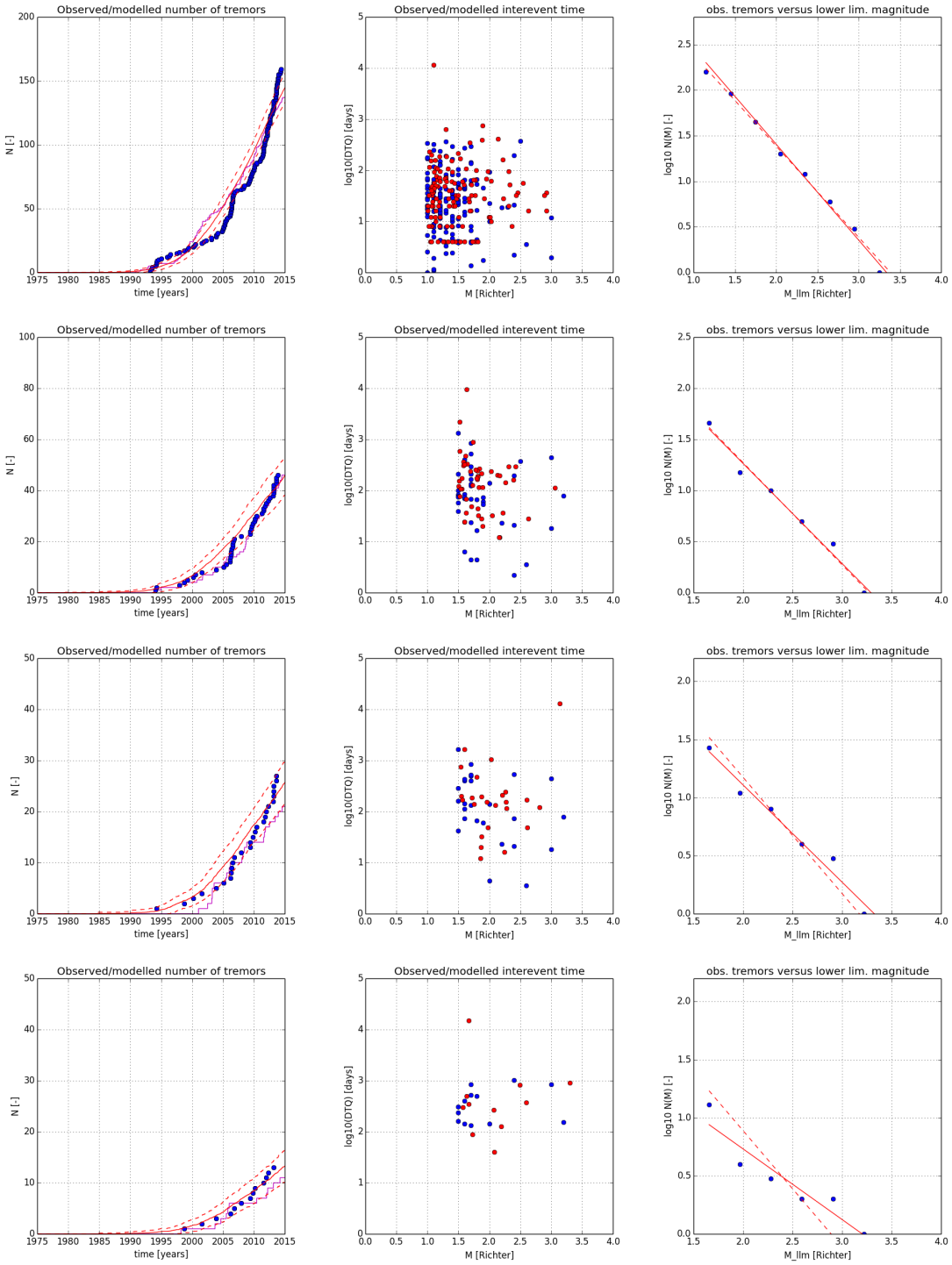

Figure 3.5.2 : Observed (blue dots) and modelled (red dots, lines) tremors in region around Ten Boer for various areas. $M_{min} = 1.5$, $c_{M0} = 0$, $c_{\sigma_v} = 0.4$, $k_W = 7$ and δt is 4 days for all cases. From top to bottom, areas with a radius R_{area} of 5, 4, 3 and 2 km. Left: number of tremors versus time. Solid line shows mean value of 50 simulations. Red dashed lines show $\pm$ one standard deviation from the mean value. Purple solid line shows one simulation. Center: interevent times versus magnitude M. Right: cdf of log of number of tremors versus lower limiting magnitude M_{llm}. Dashed line $b = 1$.

3.6 The effect of the stress relaxation parameter c_{M0}

Using this model without stress relaxation by tremors, the tremor rate would not decline if the applied stress related to the pressure drop would remain constant. Such a condition is not physical because the gravitational and elastic energy flows away from the region with the tremors in the form of seismic waves. Qualitatively, this decline is opposed to the effect of Ogata's epidemic type aftershock sequence (ETAS) model on the tremor rate, see Ogata (1998)[13]. Since the regions of interest are relatively small and the spatial clustering effect can hardly be identified if present, we assume that the aftershock effect is included in the expression for the tremor rate.

The stress relaxation term can be used to model the reduction of tremors when the reservoir pressure reduction stops in a certain region. Vice-versa, the observations can be used to constrain or calibrate the parameter c_{M0} in the stress relaxation term of Eq. (2.1.4). This could be done for the Annerveen and Eleveld fields where the reservoir pressure reduction hardly changes after gas production over a significant period of time.
The tremors in the Annerveen field started after 1995, i.e. after the period of the main gas production. They are observed in the period 1995 - 2014 when the reservoir pressure slowly declined from about 5 MPa to about 1 MPa. Having no tremors before 1995 and not too many in the period 1995 - 2014 makes it difficult to constrain the parameter c_{M0} unambiguously, see also §3.6.2 below. In the Eleveld field most of the tremors occur during production and the tremor rate declines hereafter.

3.6.1 Eleveld field

The Eleveld field has three blocks, from south to north B, B1 and B2, see Appendix C §C.2. According to NAM ELV-101 and ELV-102 well data, the reservoir pressure in the largest 4×3 km^2 B block decreased from about 38 MPa to about 3 MPa in the period 1975 - 2005, and initially at a somewhat higher rate. In june 2009, the reservoir pressure

[13]This effect has been applied by Bourne and Oates (2014) to analyse the tremors in the Groningen field. They derive that the likelihood of tremors is about inversely proportional with the distance between the tremors to the power 2 and with the time to the power 1.5 and exponentially increases with the magnitude of the tremors. The effect is important for interevent times of less than a few days and a distance between the hypocenters of the tremors less than a few kilometers. According to Bourne and Oates (2014), Figure 11, the aftershock productivity is about 0.2 for tremors with a magnitude $M \leq 2$ and about 1 for tremors with a magnitude $M \sim 3$.
Considering that the frequency-magnitude relation of the aftershocks follows the Gutenberg-Richter law with a b-value of about 1, most of the aftershocks following from the few big tremors are small. The main effect of using Ogata's aftershock model would be a higher mean tremor rate with some spatial and temporal clustering of the tremors with respect to a uniform spatial distribution and a Poisson distribution in time, respectively.
It is not clear whether Ogata's model can be applied to a system of many, more or less equivalent, faults with a mutual distance similar or less than the typical triggering distance in the aftershock model. Stress redistributions in a dense fault system may be quite different from stress redistributions around a single dominating fault exposed to a tectonic stress.

in the ELV-101 well was about 2 MPa. The reservoir pressure in the center block B1 of about 2 - 3 km^2 reduced from 1996 - 2014 from 38 MPa to 20 MPa. The reservoir pressure in the north block B2 of about 2 - 3 km^2 reduced from 2008 - 2014 from 38 MPa to 5 MPa.
The tremor rate in the whole Eleveld field after the reservoir pressure reduction in the largest south block B significantly reduces after 2005 despite that in the smaller blocks B1 and B2 the reservoir pressure still reduces substantially.

According to §2.2 and Appendix B, §B.3, the lower limit for c_{M0} is of the order 0.1 kPa/TJ for a region of interest with a radius of 5 km, if all faults in the database would be seismically active.
This value for c_{M0} has no effect on the tremor rate in the Eleveld field. For a much larger value $c_{M0} = 3$ kPa/TJ, the stress relaxation term has an effect on the tremor rates. Typical results are shown for the Eleveld field in Figures 3.6.1 and 3.6.2 for $M_{min} = 1.0$ and $M_{min} = 1.5$, respectively. The only difference between the parameters used for these simulations and those used for the previous simulations with $c_{M0} = 0$ kPa/TJ is the value for the shape parameter of the Poisson distribution[14].
For $M_{min} = 1.5$, the fit to the observed data improves somewhat by including a non-zero c_{M0} after the production stops. For $M_{min} = 1.0$, a possible improvement is less clear. Actually, the decrease in the observed tremor rate is more abrupt.

Since the region around Eleveld includes three blocks B, B1 and B2 with different reservoir pressure reduction rates, we have repeated the calculation for the Eleveld field using a region that covers only the B block in the south. The easting and northing X and Y coordinates of the center of the selected region are 235 km and 551.5 km, respectively. The radius of the region is only 1.5 km to use only the tremors in the B block and exclude tremors from the other blocks.
Figure 3.6.3 shows that there are no tremors in this block after 2005 when the reservoir pressure reduction rate becomes practically nihil. A similar substantial reduction in the tremor rate is observed in the so-called "zone central" around Loppersum after a gas production stop in this region early 2014, see Pijpers (2014b)[15]. On the other hand, we don't see a substantial reduction in the tremor rate in the Annerveen field after 1995 when the reservoir pressure slowly decreased from 5 MPa to 1 MPa.

Table 3.6.1 shows the parameters used to fit the tremor data in the whole Eleveld field (blocks B, B1 and B2) and in block B in the Eleveld field for $c_{M0} = 3$ kPa/TJ. The Weibull shape parameter k_W and the typical mean shear stress on faults for seismic fault failure τ_{fail} are larger than for the whole field refecting the sharp onset of the tremors in this block.

[14]For $M_{min} = 1.0$ and $M_{min} = 1.5$, $\lambda_{PS} = 0.019$ and $\lambda_{PS} = 0.013$, respectively.
[15]It is not the purpose of this work make a judgement about the statistical significance of this reduction in this relative short period.

The present model cannot reproduce the drastic reduction in the tremor rate in block B in the Eleveld field using a mean field stress relaxation process. Assuming that this tremor rate reduction is an essential feature of the underlying process generating the tremors in compacting reservoirs, we may conclude that

- The submodel for generating the tremors, using the Weibull probability distribution function for the relative likelihood of a tremor the Poisson probability distribution function to normalise the tremor rate, is incomplete. It could be proposed to include a function which depends on the loading rate or to incorporate the loading rate effect in the Poisson shape parameter, λ_{PS} as in Eq. (2.4.12)[16]. If the stress strate would be frozen (supposing that creep is absent) there are no tremors.
  This function would have no effect on the tremor rate under an almost constant loading rate. This condition applies to the Groningen field where the reservoir pressure almost constantly reduced during many years.

- The submodel for the reduction of the tremor rate by stress relaxation from tremors is not correct. However, since the observed tremors do not to line up next to each other along a single fault but appear all over the region on different faults, it is not obvious to identify a plausible physical mechanism that could do this.

3.6.2 Other fields

The effect of the stress relaxation parameter c_{M0} with values of the same order is shown for all regions of interest in Table 3.6.2 . The simulations are for $M_{min} = 1.0$ and for an area with a radius $R_{area} = 5$ km. To obtain similar fits, λ_{PS} must be about 10 - 20% higher than the values in Table 3.4.2 . The Poisson distribution shape parameter λ_{PS} normalises the number of modelled tremors to the observed number of tremors. If reservoir compaction continues at a steady state, a possible effect of stress relaxation on the tremor rate can be masked by a higher value for λ_{PS}.

The effect of stress relaxation becomes more explicit when modelling tremors in a smaller region. Since the value c_{M0} scales with the inversely with the area, see Appendix B, §B.3, we anticipate to increase the value of c_{M0}. Figure 3.6.4 shows the results for $c_{M0} = 0$, 20, 50 and 500 kPa/TJ. The Weibull distribution shape parameter k_W is comparable but slightly larger, i.e. 7 instead of 6. The latter value has been derived for the region around Loppersum with a radius of 5 km, see Tables 3.4.3 and 3.4.3 . Using $c_{\sigma_v} = 0.5$, the other parameters are $\tau_{fail} = 6.3$ MPa and $\delta p_{fail} = 18$ MPa. The b-value is taken the same as for the larger region around Loppersum, i.e. b = 0.8.
The number of tremors reduces with increasing c_{M0}. For the highest value $c_{M0} = 500$ kPa/TJ, the mean shear stress on the faults in the region reduces after a large tremor so

[16] In the context of this model, the latter option means that the tremor rate normalisation depends now on the loading rate while the relative likelihood of a tremor as determined by the Weibull probability distribution function remains the same. It is as if you don't throw the dice when you are not loading or less often when the loading rate is reduced.

much that after this tremor the probability of failure according to the Weibull distribution becomes very small and the tremor rate becomes practically zero. For the two smaller values for c_{M0}, the tremor rates seem comparable and fits are reasonable. For $c_{M0} = 50$ kPa/TJ, the fit is less convincing.

3.6.3 Loppersum field

We have repeated these calculations for 9 small regions around Loppersum, using $c_{M0} = 20$ kPa/TJ. All regions have a radius $R_{area} = 1.5$ km and an area of ~ 6 km^2. One region is centered around the original center. The centers of the other 8 regions are 2 km west, north-west, north, north-east, east, south-east, south and south-west of this center. The distance between the centres of the north-west, north-east, south-east and south-west to the original center is $2\sqrt{2} \sim 3$ km.

The shape parameter of the Poisson distribution λ_{PS} must be varied to match the number of modelled tremors to the observed ones, see Table 3.6.3 . λ_{PS} is larger south of Loppersum where there are more tremors. The other parameters are the same for all small regions. The systematic and substantial north-south gradient in the number of tremors may be a reason why the Weibull distribution shape parameter k_W is somehat higher for the smaller regions than for the larger region around Loppersum.

Figure 3.6.5 shows that for all small regions reasonable fits can be derived using the same fit parameters, except λ_{PS}. Table 3.6.3 shows that the fault data in all 9 regions is about similar and cannot explain the systematic increase of the tremor rate in the south. An increasing subsidence (and related reservoir compaction) towards the south correlates with an increasing tremor rate to the south. Other observations are

- The observed interevent times ΔT_q for the smaller regions tend to cluster in the range 100 - 1000 days, see Figure 3.6.6 . This tends toward a more quasi-perodic behaviour which is also observed for natural earthquakes under a constant loading rate, see Ohnaka (2013), §7.1.
- The combination of a low b-value of 0.7 and a stress relaxation parameter exceeding $c_{M0} = 3$ kPa/TJ leads, at least for Eleveld, to a small but significant probability that during a single Monte Carlo simulation the tremors are killed in an early phase of reservoir compaction. If the present model for stress reduction would be valid, this may indicate that the low b-value develops over time.

Table 3.6.1 : Fit parameters for whole Eleveld field (blocks B, B1 and B2) and block B in the Eleveld field. c_{M0} = 3 kPa/TJ.

Blocks	M_{min}	R_{area}	N_{obs}	λ_{PS}	k_W	b	τ_{fail}
-	Richter	km	-	-	-	-	MPa
.....	.....	.....	.....	.....	.....	.....	.....
B+B1+B2	1.0	5	38	0.018	7	0.7	6.8
B+B1+B2	1.5	5	22	0.013	7	0.7	6.8
B	1.0	1.5	23	0.018	10	0.7	8.6
B	1.5	1.5	14	0.010	10	0.7	8.6

Table 3.6.2 : Fit parameters for 6 regions of interest. The time step $\delta t = 4$ days, minimum magnitude $M = 1.0$, radius of area $R_{area} = 5$ km. The stress relaxation parameter c_{M0} = 1.5 and 3 kPa/TJ.
The b-value and the Pareto distribution shape parameter β are dependent, $\beta = 2/3b$. This holds also for the fit parameters τ_{fail} and δp_{fail}. τ_{fail} is calculated from δp_{fail} using typical values $\alpha = 0.7$ and $c_{\sigma_v} = 0.5$.

Property	Symbol	Unit	Lop	TenB	Lag	Wou	Ann	Ele
.....	.....	.....	.....	.....	.....	.....	.....	.....
Number of observed tremors	N_{obs}	-	136	160	67	55	20	38
Min. magn. to fit GR law	M_{min}	Richter	1.5	1.6	1.6	1.4	1.4	1.5
Max. magn. to fit GR law	M_{max}	Richter	3.5	3.3	2.8	2.8	2.4	3.0
Pareto distr. shape parameter	β	-	0.55	0.67	0.8	0.8	0.8	0.47
Gutenberg-Richter b-value	b	-	0.82	1.0	1.2	1.2	1.2	0.7
Poisson distr. shape parameter	λ_{PS}	-	0.11	0.17	0.047	0.043	0.012	0.018
Weibull distr. shape parameter	k_W	-	6	7	7	7	7	7
mean shear str. for seism. fail.	τ_{fail}	MPa	5.8	6.3	6.6	6.4	10.4	6.8
stress relaxation parameter	c_{M0}	kPa/TJ	1.5	3	3	3	3	3

Table 3.6.3 : The number of tremors, the shape parameter λ_{PS} and fault data (mean and standard deviation) for the 9 small regions around Loppersom.
The fault data listed are the mean fault throw $\bar{t}_{res}$, the mean fault dip $\bar{\delta}$ and the standard deviation of these properties in the region of interest, i.e. $\sigma_{t,res}$ and σ_{δ}.

Region	N	λ_{PS}	L_f	D_f	$\bar{t}_{res}$	$\sigma_{t,res}$	$\bar{\delta}$	σ_{δ}
		-	km	km	m	m	degree	degree
Center	12	0.0092	13	1.1	48	48	71	24
W	10	0.011	14	1.0	52	43	67	24
NW	9	0.0067	12	1.1	32	23	71	26
N	12	0.0092	16	0.9	50	53	74	22
NE	8	0.0059	12	1.2	45	54	68	25
E	17	0.019	16	0.9	49	45	73	25
SE	19	0.021	13	1.1	51	39	75	23
S	29	0.029	13	1.1	41	31	75	14
SW	19	0.019	16	0.9	31	22	68	22

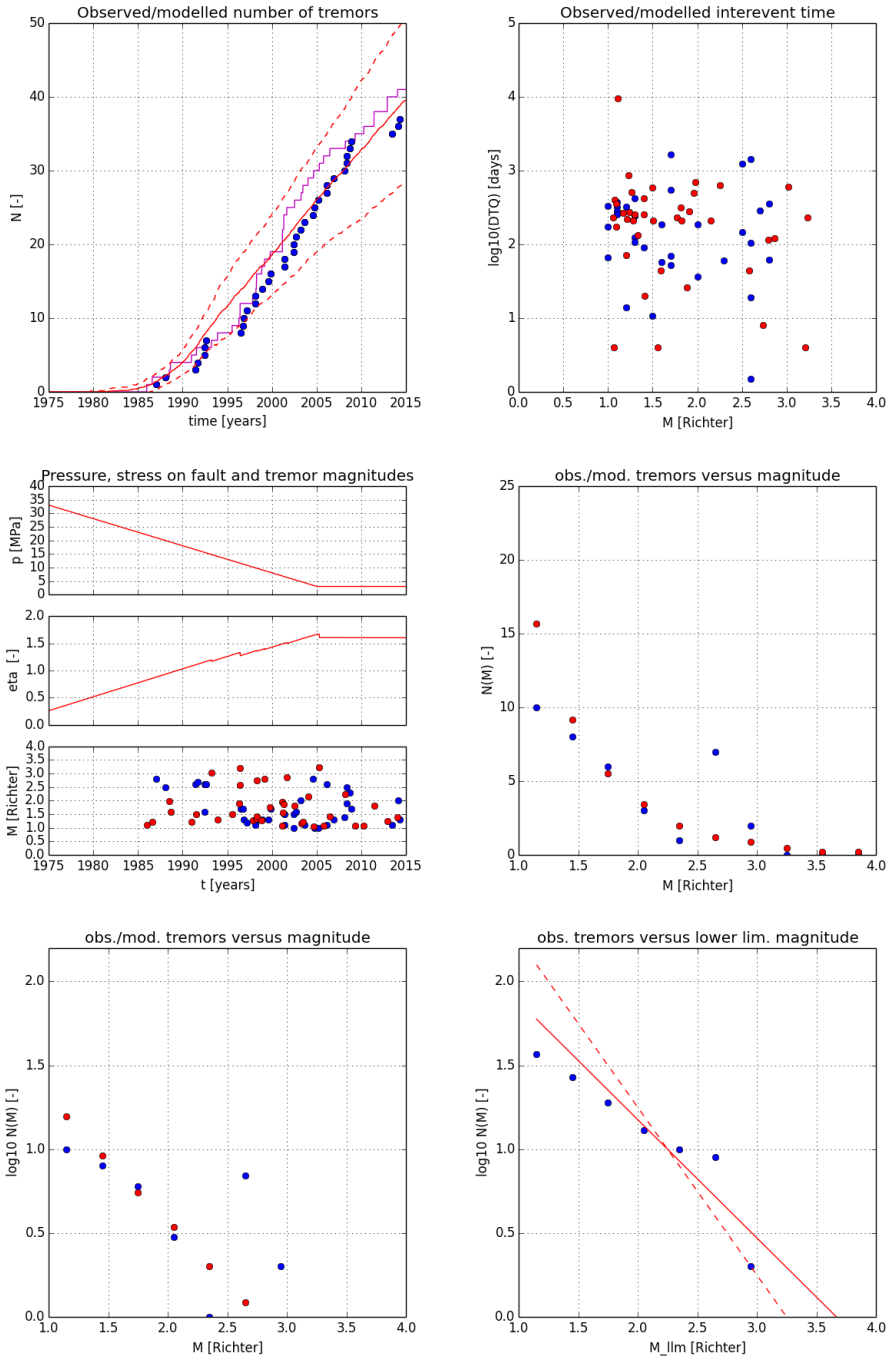

Figure 3.6.1 : Observed (blue dots) and modelled (red dots, lines) tremors in the Eleveld field (all blocks, B, B1 and B2), $M_{min} = 1.0$, $c_{M0} = 3$ kPa/TJ. Top-left: number of observed and modelled tremors as a function of time. Red solid line shows mean value of 50 simulations. Red dashed lines show $\pm$ one standard deviation from the mean value. Purple solid line shows one simulation. Top-right: interevent times versus magnitude M. Center-left: reservoir pressure, mean stress $\bar{\tau}$ and tremors versus time. Center-right: pdf of number of tremors versus magnitude. Bottom-left: cdf of number of tremors versus lower limiting magnitude M_{llm}. Bottom-right: cdf of log of number of tremors versus lower limiting magnitude M_{llm}. Dashed line $b = 1$.

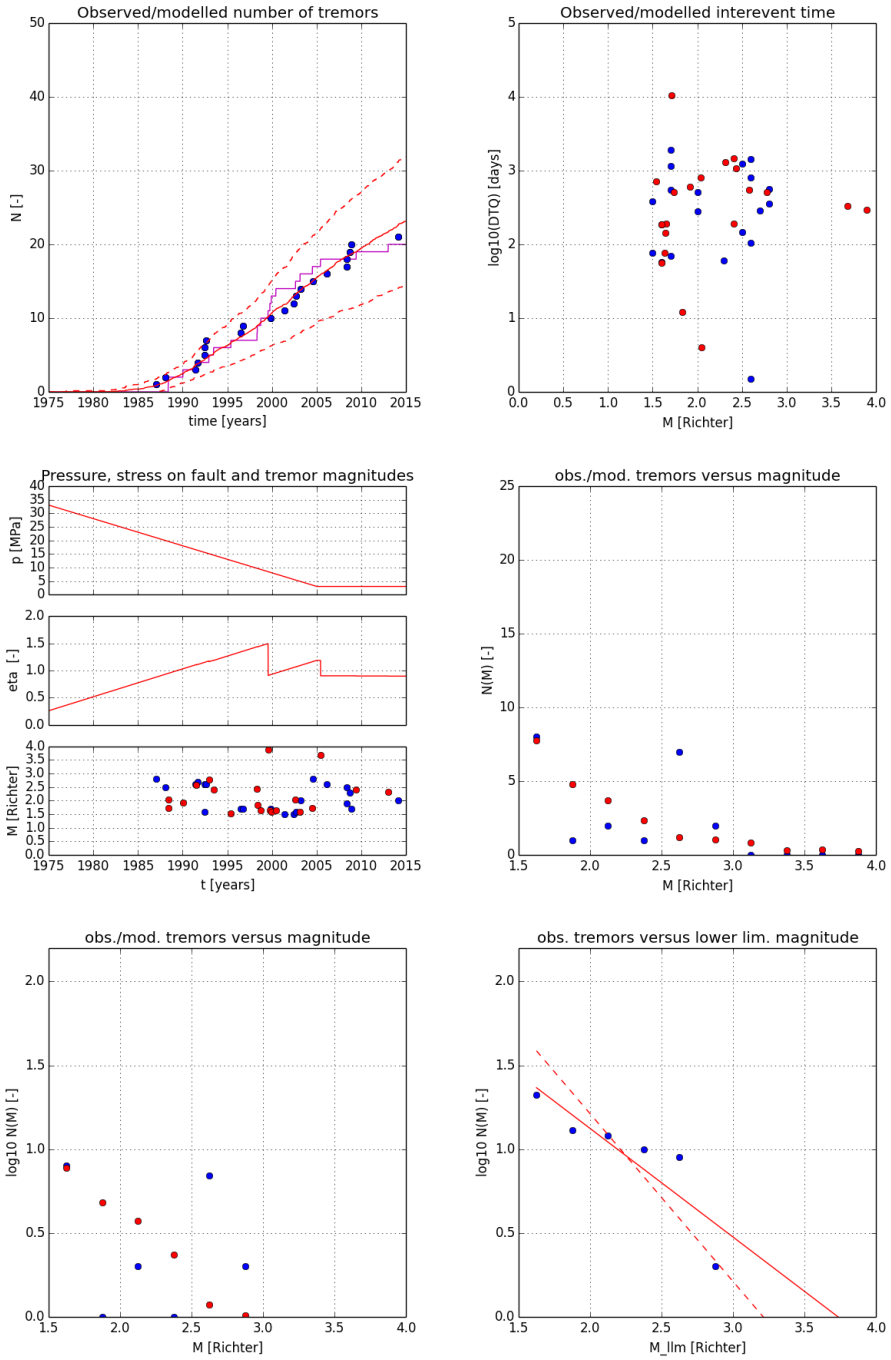

Figure 3.6.2 : Observed (blue dots) and modelled (red dots, lines) tremors in the Eleveld field (all blocks, B, B1 and B2), $M_{min} = 1.5$, $c_{M0} = 3$ kPa/TJ. Top-left: number of observed and modelled tremors as a function of time. Red solid line shows mean value of 50 simulations. Red dashed lines show $\pm$ one standard deviation from the mean value. Purple solid line shows one simulation. Top-right: interevent times versus magnitude M. Center-left: reservoir pressure, mean stress $\bar{\tau}$ and tremors versus time. Center-right: pdf of number of tremors versus magnitude. Bottom-left: cdf of number of tremors versus lower limiting magnitude M_{llm}. Bottom-right: cdf of log of number of tremors versus lower limiting magnitude M_{llm}. Dashed line $b = 1$.

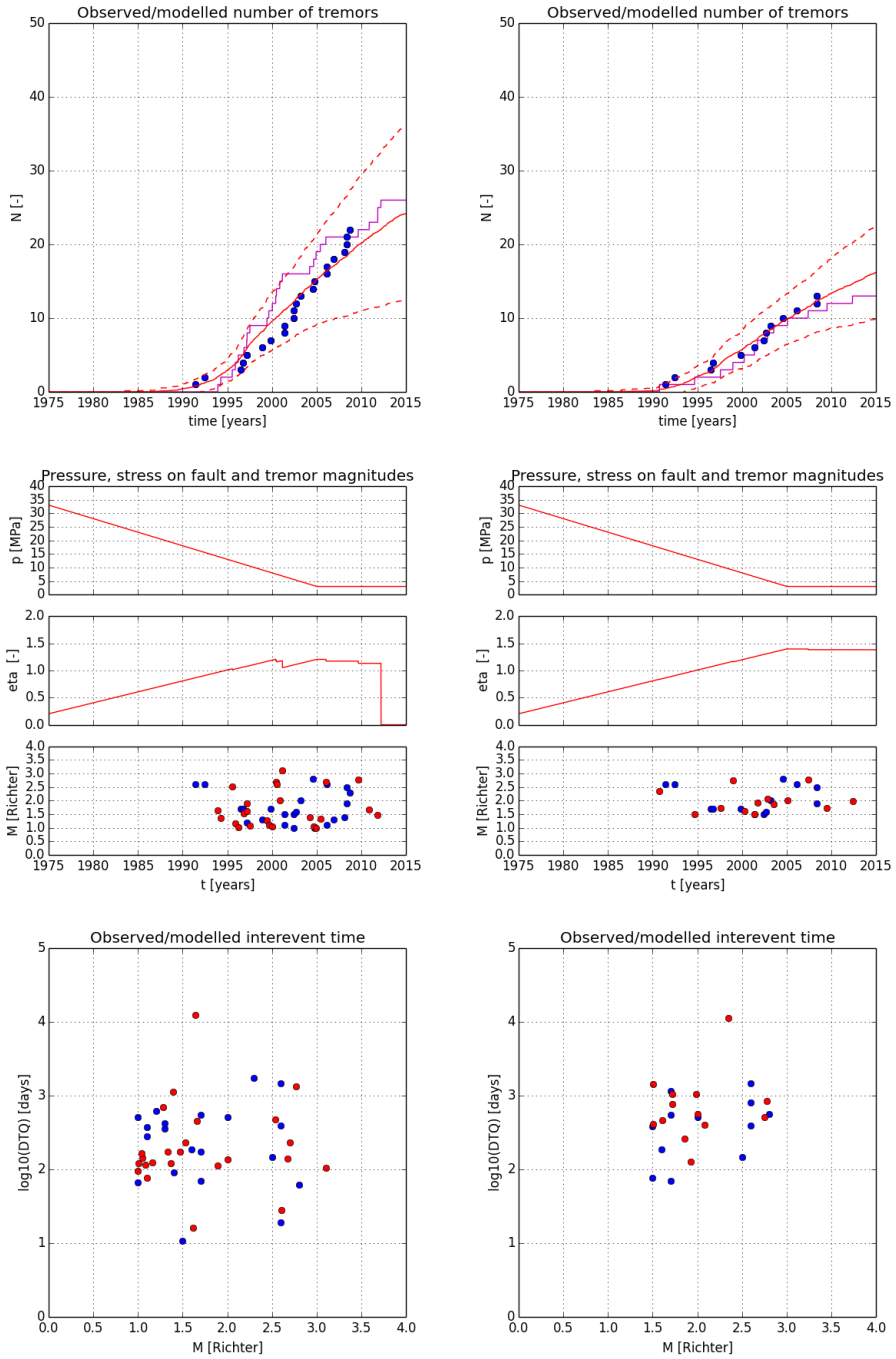

Figure 3.6.3 : Observed (blue dots) and modelled (red dots, lines) tremors in the south block B of the Eleveld field, $M_{min} = 1.0$ (left) and $M_{min} = 1.5$ (right), $c_{M0} = 3$ kPa/TJ. Top: number of observed and modelled tremors as a function of time. Red solid line shows mean value of 50 simulations. Red dashed lines show ± one standard deviation from the mean value. Purple solid line shows one simulation. Center: reservoir pressure, mean stress $\bar{\tau}$ and tremors versus time. Bottom: interevent times versus magnitude M.

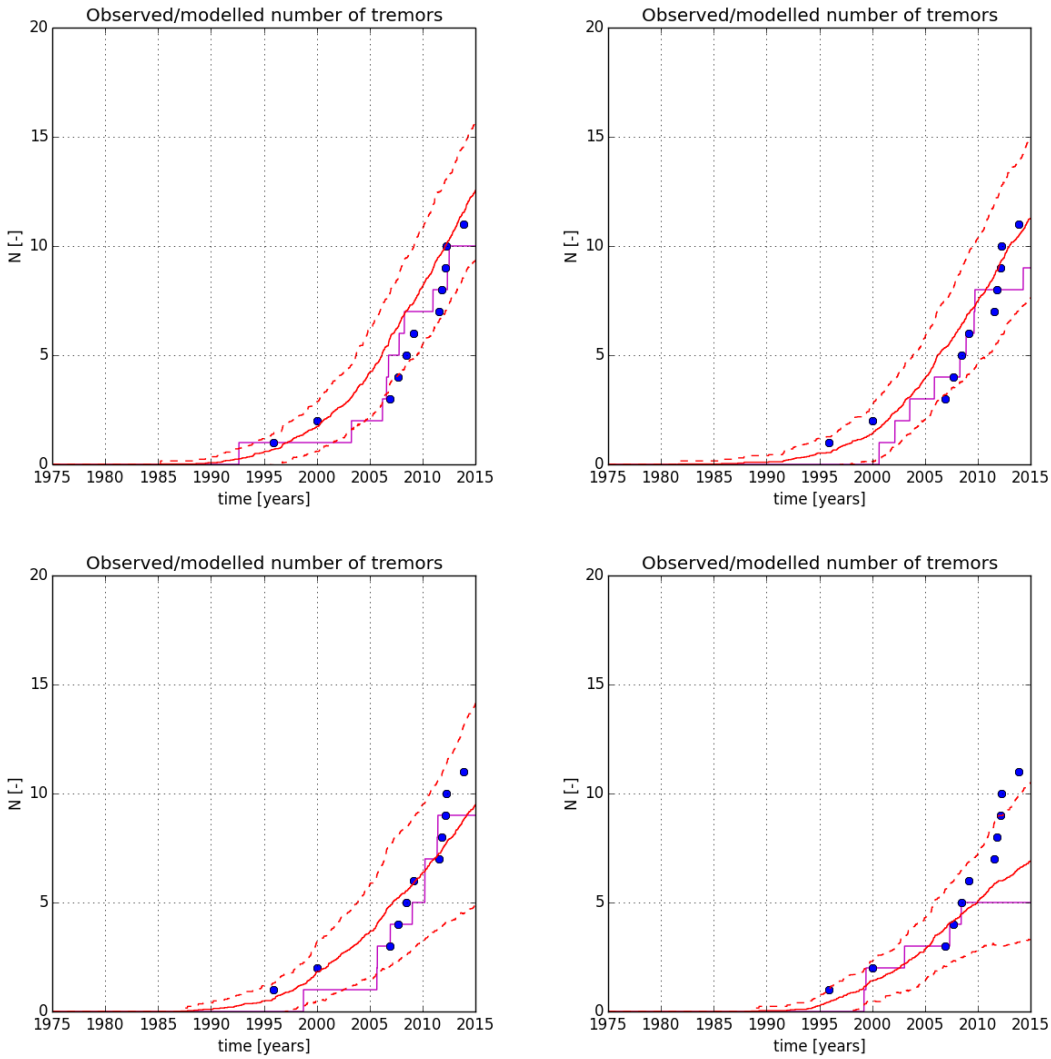

Figure 3.6.4 : Observed (blue dots) and modelled (red and purple lines) number of tremors around Loppersum in region of 1.5 km radius. The effect of the parameter c_{M0}. In the order top-left, top-right, bottom-left and bottom-right: $c_{M0} = 0$, 20, 50 and 500 kPa/TJ. Red solid line shows mean value of 50 simulations. Red dashed lines show $\pm$ one standard deviation from the mean value. Purple solid line shows one simulation.

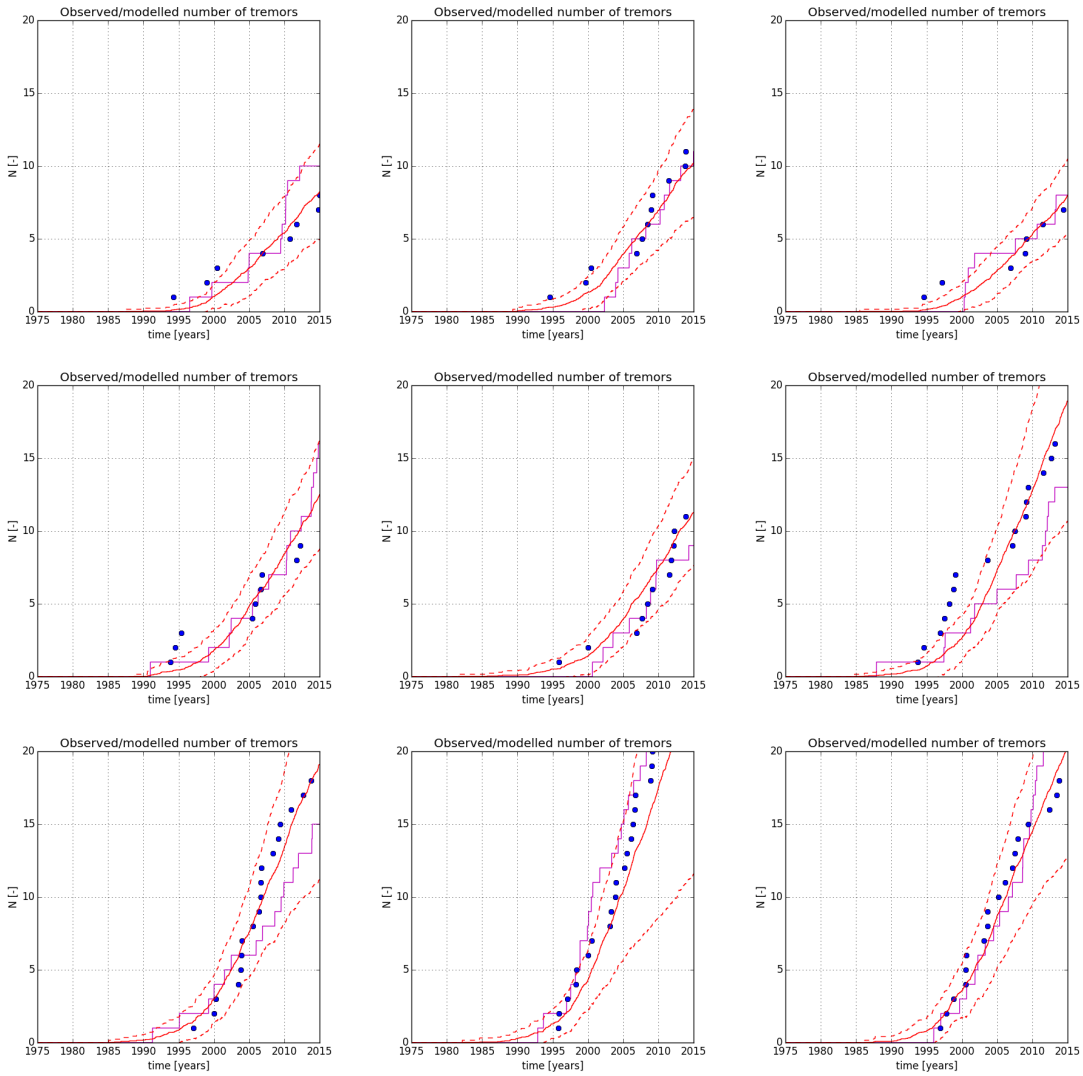

Figure 3.6.5 : Observed (blue dots) and modelled (red and purple lines) number of tremors around Loppersum in regions of 1.5 km radius, located W, NW, N, NE, E, SE, S and SW from the center. The figures are ordered clock-wise according to these directions. M_{min} = 1, c_{M0} = 20 kPa/TJ. Red solid line shows mean value of 50 simulations. Red dashed lines show ± one standard deviation from the mean value. Purple solid line shows one simulation.

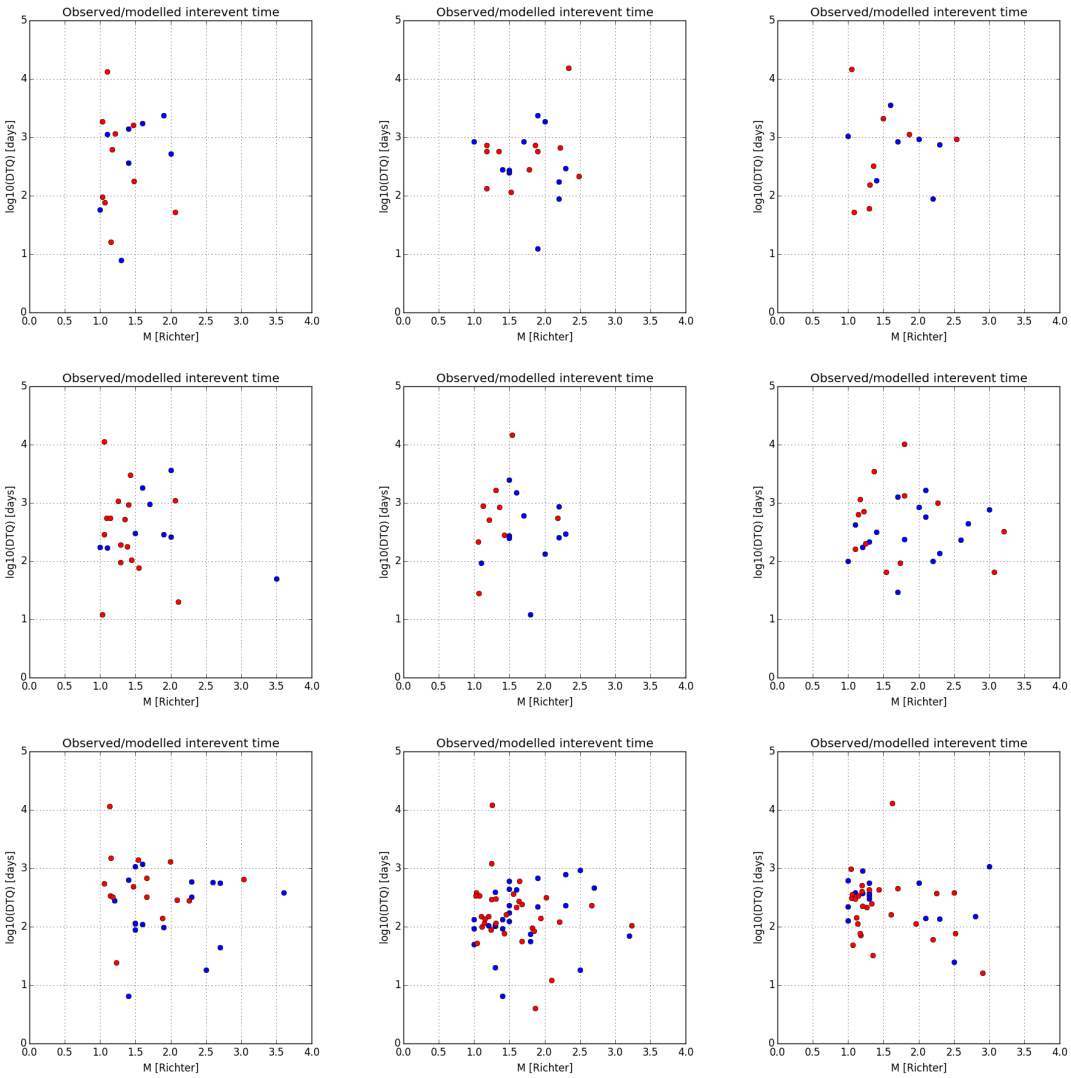

Figure 3.6.6 : Observed (blue dots) and modelled (red dots) interevent time between tremors around Loppersum in regions of 1.5 km radius, located W, NW, N, NE, E, SE, S and SW from the center. The figures are ordered clock-wise according to these directions. $M_{min} = 1$, $c_{M0} = 2$ kPa/TJ.

3.7 Predictive potential of the model

In general, the present model predicts for a wide range of parameters similar trends for the development of tremor rate. After the start of the gas production and reservoir compaction and after a quiet period, tremors appear and the tremor rate increases until a more or less steady tremor rate develops. At least, this holds for the mean tremor rate following from a number of simulations. When the observed tremor data includes the onset of tremors and a part of more or less steady tremor rate, fits can be made relatively easily. In this case, an estimate can be made about the tremor rate in the future when the pressure reduction and related compaction rate don't change.

We have shown that the stress relaxation term in the model does not satisfactorily explain the strong observed decline of the tremor rate in the Eleveld field. For the other regions, a possible effect of the stress relaxation term is masked by tuning the shape parameter for the Poisson distribution λ_{PS}. This parameter normalises the number of modelled tremors to the number of observed tremors. At this stage, the present stress relaxation term cannot be used with confidence to predict tremor rates following from alternative production scenarios.

With this reservation, we show in Figure 3.7.1 that the model could have estimated the tremor rates $M_{min} \geq 1.0$. in the regions around Loppersum and Ten Boer for the period 2010-2015 from the tremor rate data before this period. The regions have a radius of 3 km. We disregard the stress relaxation effect and use $c_{M0} = 0$ and assume that the pressure decline is constant over this period. The predictions are reasonable although the small but significant increasing tremor rate in the region around Ten Boer (and may be also in the region around Loppersum) in the period 2010 - 2014 is not captured by the model.
We recognise that a single tremor rate simulation may differ from the mean tremor rate, see for example the purple solid lines in 3.7.1 . At the same time, we note that the present model cannot explain the increase of the observed tremor rate with time when taking a constant pressure reduction rate.

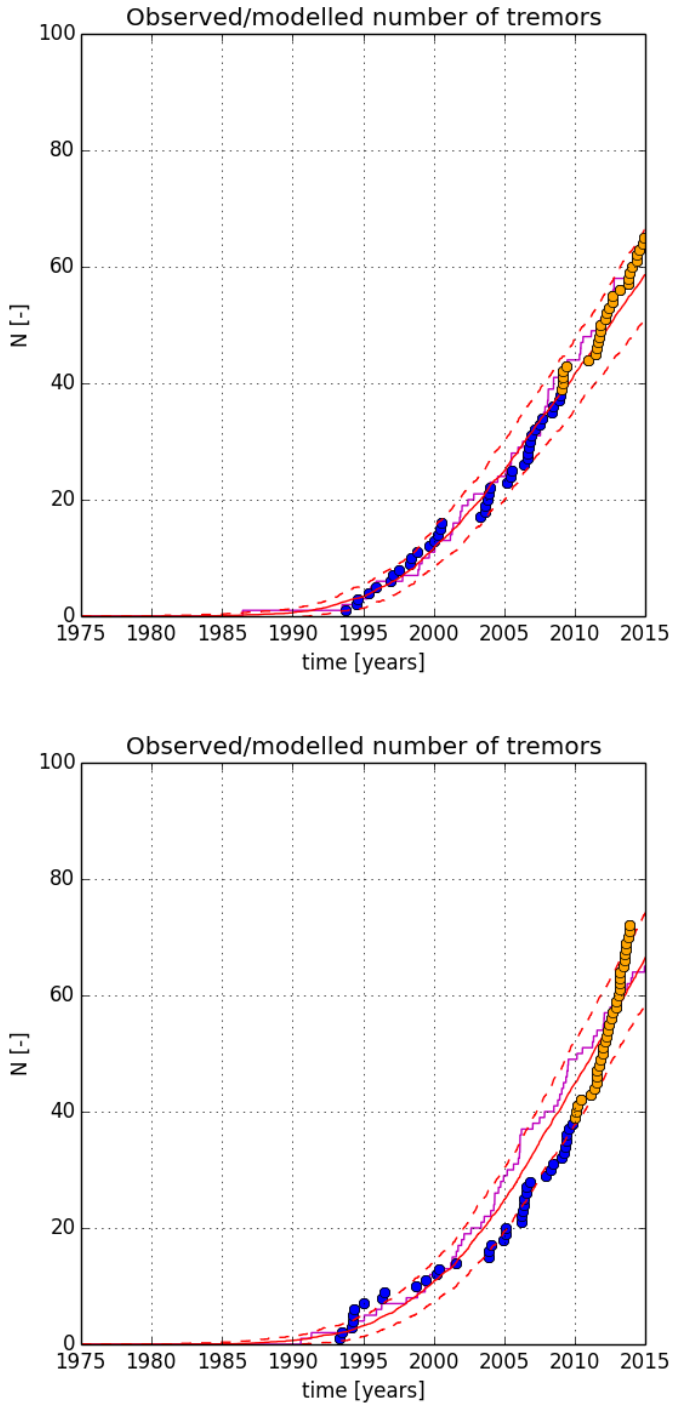

Figure 3.7.1 : Observed (blue dots) and modelled (red dots, lines) tremors around Loppersum (top) and Ten Boer (bottom), $M_{min} = 1.0$, $c_{M0} = 0$. Radius of region $R_{area} = 3$ km. Number of observed and modelled tremors as a function of time. The blue dots are the observed tremors used for the predictions, the orange dots are the observed tremors in the period 2010 - 2014. Red solid line shows mean value of 50 simulations. Red dashed lines show ± one standard deviation from the mean value. Purple solid line shows one simulation.

Chapter 4

Discussion

The model presented in this work can reasonably reproduce the observed tremors in a number of regions in the Groningen field and around Annerveen and Eleveld. The values of the fit parameters makes sense in a geomechanical context. The modelled tremor rate of a single simulation scatters around the mean modelled value like the observed tremor rate. To the eye, the interevent time histograms looks also similar. Whether there is a statistical significant difference between the observed and modelled tremors must still be sorted out.

The Weibull shape parameter k_W determines the transition period from no tremors to a constant tremor rate in the case of a constant compaction rate. Recognising that the onset of the observed tremor rate could be influenced by the installment of the network of seismometers, it is remarkable that this shape parameter is relatively high in relation to possible variations in fault properties which determine Mohr-Coulomb shear-type failure. According to §A.3 in Appendix A, Table A.3.1 , the mechanical properties with a potential effect on shear-type failure should by average vary less than about 10% to obtain the derived high values for k_W. These high values may indicate that only a few fault or rock properties really matter in the production of tremors or other fault or rock properties are responsible for this.

With the model and parameter values used, a possible stress relaxation effect could almost be completely masked unless reservoir compaction stops over sufficient time, such as in the region around Eleveld. For the other regions, fits to the observed tremor data made with $c_{M0} = 0$ can be 'repaired' by increasing the value of the Poisson shape parameter λ_{PS} which normalises the number of modelled tremors to the observed number of tremors. The present model cannot reproduce the drastic reduction in the tremor rate in the south block of the Eleveld field by a mean field stress relaxation process. This points to a shortcoming in the submodel for the stress relaxation or to a shortcoming in the submodel for the generation of the tremors. The latter submodel is driven by the Poisson process and the Weibull distribution probability distribution function for the relative likelihood of a tremor. The problem could be 'solved' by introducing a Poisson shape parameter λ_{PS}

which depends on the loading rate.

With reservations, we have illustrated that the model has some predictive power about tremor rates in a relative small region, using the observed tremors in this region in the previous period. Assuming a constant pressure reduction rate, the model does not capture a small but significant increase in the tremor rates in the last years in the regions around Ten Boer and Loppersum and, as said before, the adrupt reduction of the small tremors when gas production stops.

We recommend to follow the effects of local gas production reductions in the Groningen field to validate and improve this model, especially in relation to a possible effect of stress relaxation by tremors and to apply the model to other gas fields which have produced tremors during gas production. Examples are gas fields in North West Germany and Dutch gas fields in other reservoir formations, such as in the Buntsandstein around Roswinkel and in the Zechstein carbonate around Emmen.

We recognise that the present model does not differentiate between seismic and a-seismic fault slip. We do not know yet which field or fault attributes are determining here. If this knowledge becomes available, it could be used to further constrain the input parameters for the model.

Chapter 5

Acknowledgements

I heartily thank Chris Harris, Peter van den Bogert, Rob van Eijs and Stephen Bourne for reviewing this work and for all their useful comments. I thank Onno van der Wal from NAM for giving me the field data.

Bibliography

Aki, K., and Richards, P. G., "Quantitative Seismology", University Science Books, 2009.

Aki, K., "Generation and Propagation of G Waves from the Niigata Earthquake of June16, 1964. Estimation of Earthquake Movement, Released Energy and Stress-Strain Drop from G Wave Spectrum", Bulletin Earthquake Research Institute, 44, 23–88, 1966.

Bierman, S. M., and Kraaijeveld, F., "Regularised Direct Inversion to Compaction in the Groningen Reservoir using Measurements from Optical Leveling Campaigns",, Technical Report SR.15.11194, Shell Global Solutions International, 2015.

Biot, M. A., "Mechanics of Deformation and Acoustic Propagation in Porous Media", Journal of Applied Physics, 33, 1482–1498, 1962.

Bommer, J. J., Stafford, P. J., Edwards, B., Ntinalexis, M., and Dost, B., "Groningen Seismic Hazard and Risk Assessment Model - Development of Version 1 GMPEs for Response Spectral Accelerations and for Strong-Motion Durations",, Technical Report Draft version 4 March 2015, Imperial College London, United Kingdom, 2015.

Bourne, S. J., and Oates, S. J., "An Activity Rate Model of Induced Seismicity within the Groningen Field, draft",, Technical report, Nederlandse Aardolie Maatschappij. Assen, The Netherlands, 2014.

Bourne, S. J., Oates, S. J., van Elk, J., and Doornhof, D., "A Seismological Model for Earthquakes Induced by Fluid Extraction from a Subsurface Reservoir", J. Geophys. Res. Solid Earth, 119, 8991–9015, 2014.

Cai, M., "Rock Mechanics: Achievements and Ambitions", CRC Press, 2012.

Dake, L. P., "Fundamentals of Reservoir Engineering", Elsevier, Amsterdam, 1978.

Dost, B., Goutbeek, F., van Eck, T., and Kraaijpoel, D., "Monitoring Induced Seismicity in the North of the Netherlands: status report 2010,",, Technical Report Scientific Report WR 2012-03, Koninklijke Nederlands Meteorologisch Instituut, the Netherlands, 2012.

Fjaer, E., Holt, R. M., Horsrud, P., Raaen, A. M., and Risnes, R., "Petroleum related Rock Mechanics in Developments in Petroleum Science, 2nd edition 53", Elsevier, Amsterdam, 2008.

Grasso, J. R., "Mechanics of Seismic Instabilities Induced by the Recovery of Hydrocarbons", Pure and Applied Geophysics, 139, 507–534, 1992.

Harris, C. K., "Maximum Likelihood Estimates of b-Value for Induced Seismicity in the Groningen Field",, Technical Report SR.15.XX, Shell Global Solutions International, 2015.

Hoek, E., and Brown, E. T., "Practical Estimates of Rock Mass Strength", Int. J.of Rock Mechanics and Mining Sc., 34, 1165–1186, 1997.

Hoek, E., "Practical Rock Engineering", rocscience.com, 2006.

Hol, S., van der Linden, A. J., Zuiderwijk, P. M. M., and Makurat, A. H., "Long-term Compaction Behavior of Permain Sandstones - An Investigation into the Mechanisms of Subsidence in the Dutch Wadden Sea", ARMA 15-618, 2015.

Korja, A., Uski, M., Koskinen, P., Lund, B., Grigull, S., Nironen, M., Kosonen, E., and Högdahl, K., "Observations on Intraplate Seismicity in Central Fennoscandia",, Technical report, EGU Conference april 2015 Vienna, 2015.

Kostrov, V. V., "Seismic Moment and Energy of Earthquakes, and Seismic Flow of Rocks", Izv. Acad. Sci. USSR Phys. Solid Earth, 1, Eng. Transl., 23–44, 1974.

Kraaijpoel, D., and Dost, B., "Implications of Salt-related Propagation and Mode Conversion Effects on the Analysis of Induceed Seismicity", Journal of Seismology, 17, 95–107, 2013.

Mallik, J., "Map Based Fault Slip Risking for the Groningen Gas Field",, Technical Report EP201501207022, Nederlandse Aardolie Maatschappij B.V., 2015.

McGarr, A., "On Relating Apparent Stress to the Stress Causing Earthquake Fault Slip", Journal Geophysical Research - Solid Earth, 104, 3003–3011, 1999.

Molnar, P., "Average Regional Strain due to Slip on Numerous Faults of Different Orientations", Journal of Geophysical Research, 88, 6430–6432, 1983.

Mulders, F. M. M., "Modeling of Stress Development and Fault Slip in and around Producing Gas Reservoirs",, Technical Report Ph.D. Thesis, Delft University of Technology, Netherlands, 2003.

NAM, "Aanbieding Winningsplan Groningenveld",, Technical Report Letter to the Minister of Economic Affairs, 29 nov. 2013, Nederlandse Aardolie Maatschappij, 2013.

Ogata, Y., "Space-time Point-Process Models for Earthquake Occurrences", Ann. Inst. Statist. Math., 50, 379–402, 1998.

Ohnaka, M., "The Physics of Rock Failure and Earthquakes", Cambridge University Press, 2013.

Pijpers, F. P., "Significance of Trend Changes in Ground Subsidence in Groningen",, Technical Report Phase 0 Report 1, CBS Statistics Netherlands, the Netherlands, 2014.

———, "Significance of Trend Changes in Ground Subsidence in Groningen",, Technical Report Phase 0 Report 2, CBS Statistics Netherlands, the Netherlands, 2014.

Roest, J. P. A., and Kuilman, W., "Geomechanische Analyse van de Lichte Aardschokken in het Eleveld Reservoir",, Technical report, Technical University Delft, The Netherlands, 1993.

Roest, J. P. A., and Kuilman, W., "Geomechanical Analysis of Small Earthquakes at the Eleveld Gas Reservoir", SPE paper, pages 573–580, 1994.

Sanz, P. F., Lele, S. P., Searles, K. H., Hsu, S. Y., and Garzon, J. L., "Geomechanical Analysis to Evaluate Groningen Production Scenarios",, Technical Report 20150209, ExxonMobil Upstream Research Company Houston, TX, 2015.

Scholz, C. H., "The Frequency-Magnitude Relation of Microfracturing in Rock and its Relation to Earthquakes", Bulletin of the Seismological Society of America, 58, 399–415, 1968.

Scholz, C. H., "The Mechanics of Earthquakes and Faulting, 2^{nd} edition", Cambridge University Press, 2002.

Scholz, C. H., "On the Stress Dependence of the Earthquake b-value", Geophysical Research Letters, 42, 13991402, 2015.

Timmer, D. H., "An Analysis of the Reliability of an Incandescent Light Bulb", Quality Engineering, 13, 299–305, 2000.

Tormann, T., Enescu, B., Woessner, J., and Wiemer, S., "Randomness of Megathrust Earthquakes implied by Rapid Stress recovery after the Japan Earthquake", Nature Geoscience, 8, 152–158, 2015.

Udias, A., Madariaga, R., and Buforn, E., "Source Mechanisms of Earthquakes - Theory and Practice", Cambridge University Press, 2014.

van den Bogert, P. A. J., "Impact of Various Modelling Options on the Onset of Fault Slip and Fault Slip Response using 2-Dimensional Finite-Element Modelling",, Technical Report SR.15.11455, Shell Global Solutions International BV, 2015.

van Eijs, R., and Valencia, K., "Minimum Horizontal Stress Information in the Groningen Field (Rotliegendes Formation)",, Technical Report EP201301200514, Shell Internation Exploration and Production, 2014.

van Eijs, R. M. H. E., Mulders, F. M. M., Nepveu, M., Kenter, C. J., and Scheffers, B. C., "Correlation between Hydrocarbon Reservoir Properties and Induced Seismicity in the Netherlands", Engineering Geology, 84, 99–111, 2006.

Vere-Jones, D., Ben-Zion, Y., and Zúniga, R., "Statistical Seismology", Birkhäuser, 2005.

Vlcek, J., Fischer, T., and Dorbath, C., "B-value Mapping of Injection-induced Earthquakes and Earthquake swarms",, Technical report, EGU Conference april 2015 Vienna, 2014.

Wang, K., Brown, L., Gao, X., and Bilek, S., "Rupture and Creep Behaviours of Subduction Interface Controlled by Fault Zone Heterogeneity",, Technical report, EGU Conference april 2015 Vienna, 2015.

Appendix A

Failure condition for a fault

Appendix A.1 Stress changes in the reservoir due to isotropic elastic deformation

The compaction of a large reservoir approximates uniaxial compaction at a distance a few times the reservoir thickness from the fault. For $\sigma_h = \sigma_H$ [Pa] and for an isotropic uniform poro-elastic rock, the change in the horizontal effective stress σ'_h [Pa] relates to the vertical effective stress σ'_v [Pa] as[1]

$$\sigma'_h = \frac{\nu}{1-\nu}\sigma'_v. \tag{A.1.1}$$

The vertical strain ϵ_v [-] relates to the vertical effective stress as

$$\epsilon_v = \frac{1}{E}\frac{(1+\nu)(1-2\nu)}{1-\nu}\sigma'_v. \tag{A.1.2}$$

E [Pa] is the Young modulus and ν [-] is the Poisson ratio of the drained rock. The change in the effective poro-elastic stress is $\sigma' = \sigma - \alpha(p - p_0)$ where $\alpha = 1 - K/K_s$ [-] is the Biot constant. Since the overburden load on the reservoir remains constant and $\sigma_v = 0$,

$$\sigma'_v = \sigma_v - \alpha(p - p_0) = -\alpha(p - p_0). \tag{A.1.3}$$

For a pressure reduction, $(p - p_0) < 0$ and $\sigma'_v > 0$. The effective vertical stress increases. According to Eq. (A.1.1), the effective horizontal stress σ'_h also increases. Using the

[1]For isotropic uniform poro-elastic rock under uniaxial compression, the following strain stress equations apply, see also Fjaer et al. (2008), §12.2. For $\sigma_h = \sigma_H$, we have for the horizontal and vertical strains, ϵ_h and ϵ_v,

$$E\epsilon_h = \sigma'_h - \nu(\sigma'_h + \sigma'_v) \quad \text{and} \quad E\epsilon_v = \sigma'_v - 2\nu\sigma'_h.$$

For uniaxial compaction $\epsilon_h = 0$. Substituting this into the first expression, we obtain Eqs. (A.1.1) and (A.1.2).

geomechanical sign convention, it means that the reservoir rock is compressed in all directions under uniaxial compression.

Combining Eqs. (A.1.2) and (A.1.3),

$$\epsilon_v = -C_m\alpha(p-p_0) \quad \text{where} \quad C_m = \frac{1}{E}\frac{(1+\nu)(1-2\nu)}{1-\nu} \quad \text{or} \quad C_m = \frac{1}{3K}\frac{1+\nu}{1-\nu}. \tag{A.1.4}$$

Using the general relation betweeen the Young modulus E, Poisson ratio ν and bulk modulus K, i.e. $E = 3K(1-2\nu)$, the compaction coefficient C_m relates to the Biot constant α as

$$C_m = \frac{1}{3K}\frac{1+\nu}{1-\nu}. \tag{A.1.5}$$

C_m [Pa^{-1}] is the uniaxial compaction coefficient. For a pressure reduction, $p-p_0 < 0$ and $\epsilon_v > 0$, consistent with the geomechanic notation that a positive strain means shrinkage. The total horizontal stress changes as, using Eqs. (A.1.1) and (A.1.3),

$$\sigma_h = \sigma_h' + \alpha(p-p_0) = \gamma(p-p_0) \quad \text{where} \quad \gamma = \frac{1-2\nu}{1-\nu}\alpha(p-p_0). \tag{A.1.6}$$

The horizontal stress decreases when the reservoir pressure reduces. The change in the effective horizontal stress in relation to poro-elasticity can be written as

$$\sigma_h' = \sigma_h - \alpha(p-p_0) = \gamma'(p-p_0) \quad \text{where} \quad \gamma' = -\frac{\nu}{1-\nu}\alpha. \tag{A.1.7}$$

The change in the effective horizontal stress in relation to rock failure changes can be written as

$$\sigma_h'' = \sigma_h - (p-p_0) = \gamma''(p-p_0) \quad \text{where} \quad \gamma'' = \gamma - 1. \tag{A.1.8}$$

For $\nu = 0.25$ and $\alpha = 0.7$, the stress path coefficients are $\gamma = 0.46$, $\gamma' = -0.23$ and $\gamma'' = -0.54$. Note that in the literature other sign conventions can be used. For a pressure reduction, $p-p_0 < 0$ and $\sigma_h'' > 0$. The effective horizontal stress in relation to failure increases under uniaxial compaction.
For a rock not constrained by other boundary conditions (such as an over- or underburden), the stress condition with respect to rock failure becomes more favourable in all directions. For stress conditions along faults at reservoir offsets, this is not the case, see Appendix B. Further, non-vertical faults have a non-zero initial shear stress τ_0. The normal stress σ_n and shear stress τ on a two-dimensional fault plane under a dip angle δ [degree] with the vertical axis relate to the horizontal field stress σ_h and vertical field stress σ_v as, see e.g. Fjaer et al. (2008), §1.1,

$$\sigma_n = \frac{1}{2}\big(\sigma_h + \sigma_v\big) + \frac{1}{2}\big(\sigma_h - \sigma_v\big)\cos(2\theta), \tag{A.1.9}$$

and

$$\tau = \frac{1}{2}\big(\sigma_v - \sigma_h\big), \tag{A.1.10}$$

where $\theta = \pi(90 - \delta)/180$ [rad]. Similar relations hold for the effective stresses.

In the following, we use the geomechanical convention that the stress and strain are positive under compression and negative under extension. Variables at an initial or reference condition have the subscript 0. Changes in stress and strain with respect to the initial or reference condition are given by the symbols themselves. Variables after pressure step n have the subscript n. The change in the effective stress in relation to poro-elasticity theory is defined as $\sigma' = \sigma - \alpha(p - p_0)$ where σ is the change in the total stress[2]. Large changes in the pore pressure are denoted as $p - p_0$. The change in the effective stress in relation to rock failure is defined as $\sigma'' = \sigma - (p - p_0)$. According to Fjaer et al. (2008), §2.6, this is the relevant parameter for a change in the stress condition in relation to rock failure.

Appendix A.2 Shear capacity utilisation

Considering ongoing geomechanical analysis of faults at reservoir offsets, see van den Bogert (2015) and Sanz et al. (2015), we may relate the failure criterion parameter η [-] to the so-called shear capacity utilisation (SCU) of the fault. The shear capacity utilisation is a quantity which expresses the stress state of the fault relative to the fault strength. The fault strength is usually expressed in terms of Mohr-Coulomb shear-type failure[3].
We recall that the local or average values of the shear capacity utilisation of faults or any other criterion for local shear-type failure are not sufficient to predict the occurrence of a tremor. In general, it depends on both the constitutive equation between shear strength and slip displacement and the elastic stiffness of the surrounding rock if shear-type fault failure leads to unstable rock motion or a tremor, see e.g. Ohnaka (2013), §3.3.

The shear capacity utilisation can be formulated in two ways. The first one, which is also used by van den Bogert (2015) in relation to the failure of a predefined weak plane in a competent rock, such as a fault or a fracture, is in the notations of this report

$$SCU_n = \frac{\tau_n}{\tau_{MC,n}}. \tag{A.2.1}$$

[2]This notation preserves the symbol Δ for changes in displacements, strain and stress during an tremor.

[3]The Mohr-Coulomb shear-type failure criterion is the result of average rock behaviour while at the micro-scale, rock material is exposed to all kind of micro-stresses. Herewith, the shear capacity utilisation makes only sense for rock volumes larger than the so-called representative elementary rock volume for which also other macroscopic rock properties, such as the rock Young modulus and the Poisson ratio, are well defined.
If there are microfractures in the rock at all length scales, a representative rock volume cannot be assigned. In this case, one may define the representative elementary volume from a variability criterion. In this case, strength parameters, and herewith the Mohr-Coulomb criterion, become scale dependent.
At a much larger scale a dense fault system could be regarded as an integral part of the rock determining its mechanical properties. It depends on the length scales of the problem whether a fault can be regarded as a separate mechanical identity or as an integral part of the rock

$\tau_n = \tau_0 + \tau$ [Pa] is the shear stress after depletion. τ_0 and τ are the initial shear stress and the change in the shear stress along the predefined fault plane. The subscript 'n' refers to the stress state after pressure depletion step n. $\tau_{MC,n}$ [Pa] is the shear stress after depletion for which Mohr-Coulomb shear-type fault failure can be expected, i.e.

$$\tau_{MC,n} = S_0 + \sigma''_{n,n} \tan\phi. \tag{A.2.2}$$

$\sigma''_{n,n} = \sigma''_{n,0} + \sigma''_n = \sigma''_{n,0} + \sigma_n - (p_n - p_0)$ [Pa] is the normal effective stress on the fault after depletion. $\sigma''_{n,0} = \sigma_{n,0} - p_0$ [Pa] is the initial normal effective stress on the fault. The strength of cohesion S_0 [Pa] is a measure for the force of cohesion and ϕ is the angle of internal friction in the fault zone. For $SCU \sim 1$, shear-type failure can be expected.

The second formulation for the shear capacity utilisation, which is frequently used for the failure of intact rock, is

$$SCU_n = \frac{\sigma''_{1,n} - \sigma''_{3,n}}{2(\sigma''_{m,n} + S_0/\tan\phi)\sin\phi}. \tag{A.2.3}$$

Herein, $\sigma''_{1,n} = \sigma''_{1,0} + \sigma''_1$, $\sigma''_{3,n} = \sigma''_{3,0} + \sigma''_3$ and $\sigma''_{m,n} = \sigma''_{m,0} + \sigma''_m$. $\sigma''_{m,0} = (\sigma''_{1,0} + \sigma''_{3,0})/2$ is the average of the initial largest and smallest principal effective stresses $\sigma''_{1,0}$ and $\sigma''_{3,0}$, respectively. $\sigma''_m = (\sigma''_1 + \sigma''_3)/2$ is the average of the change in the largest and smallest principal effective stresses σ''_1 and σ''_3, respectively. The expression is explained in Figure A.2.1 .

Expression Eq. (A.2.3) can be used to analyse the stress condition along an imaginary plane under a dip in a compacting reservoir. For equal horizontal field stresses σ_h and σ_H, the azimuth angle of the fault with respect to the south-north direction is irrelevant and the stress condition of the rock is two-dimensional. Take that the largest and smallest principle effective stresses after pressure depletion are equal to $\sigma''_{1,n} = \sigma''_{1,0} + \sigma''_1 = \sigma''_{v,n}$ and $\sigma''_{3,n} = \sigma''_{3,0} + \sigma''_3 = \sigma''_{h,n}$, respectively. The stress changes due to reservoir depletion are calculated in the next section. The corresponding shear and normal effective stresses τ_n and $\sigma''_{n,n}$ along this plane are

$$\sigma''_{n,n} = \frac{1}{2}\big(\sigma''_{h,n} + \sigma''_{v,n}\big) + \frac{1}{2}\big(\sigma''_{h,n} - \sigma''_{v,n}\big)\cos 2\theta \quad \text{and} \quad \tau = \big(\sigma''_{v,n} - \sigma''_{h,n}\big)\cos\theta\sin\theta. \tag{A.2.4}$$

θ is the dip angle of the plane with the vertical axis. These expressions are explained in Figure A.2.2 , see also Fjaer et al. (2008), §1.1.

Substituting these expressions for the shear stress and the normal effective stress into Eqs. (A.2.1) and (A.2.2) leads to a different expression for the shear capacity utilisation than Eq. (A.2.3). The reason is that both expressions for the shear capacity utilisation refer to different physical conditions. The first one refers to a stress condition along a

predefined weak plane with designated strength properties defined by S_0 and ϕ. The second one refers to the stress condition along an imaginary plane in an intact rock with uniform strength properties defined by the same variables S_0 and ϕ.

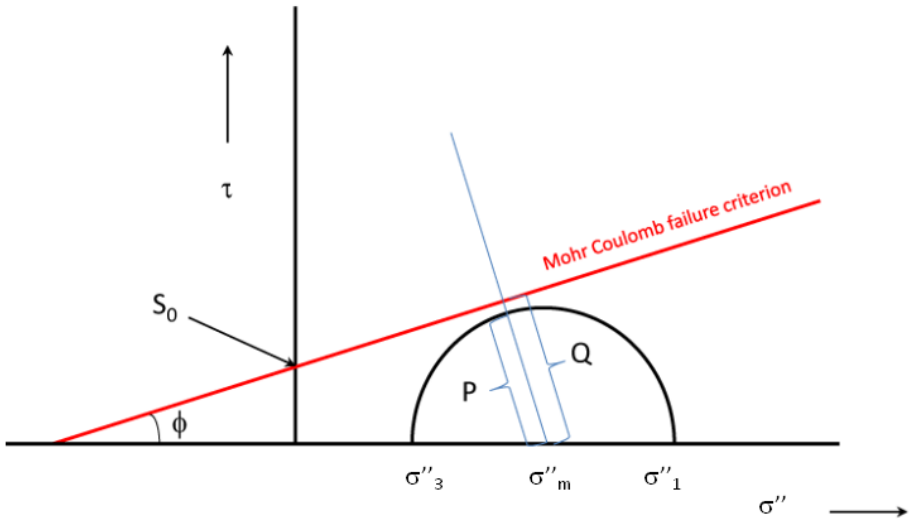

Figure A.2.1 : Mohr diagram in the $\tau - \sigma''$ plane with the normal effective stress σ'' along the horizontal axis and the shear stress τ along the vertical axis. The length of line P is equal to the radius of the Mohr circle with the centre at σ''_m, i.e. $|P| = (\sigma''_1 - \sigma''_3)/2$. The length of line Q is equal to the shortest distance between the centre of the Mohr circle and the Mohr-Coulomb failure line, i.e $|Q| = (\sigma''_m + S_0/\tan\phi)\sin\phi$.

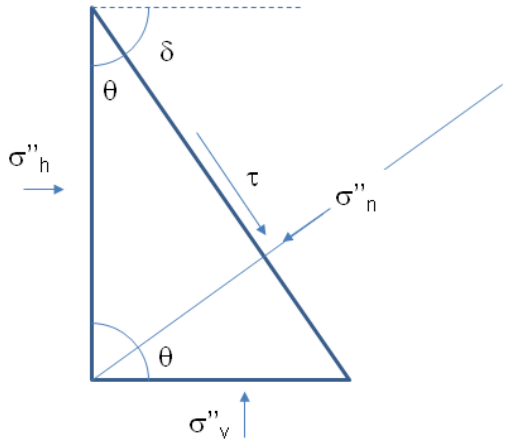

Figure A.2.2 : Relation between the shear and normal effective stresses, τ and σ_n'' along an imaginary plane and the principle horizontal and vertical effective stresses σ_h'' and σ_v''. δ is the dip angle of this plane. The expression for the shear stress can be directly understood from a force balance in the equivalent rotated figure on the right side. To balance the effective vertical stress component, the shear or tangential force on the selected plane must be $F_t = L\tau = (L\sin\theta)(\sigma_v''\cos\theta)$. Hence, $\tau = \sigma_v''\sin\theta\cos\theta$. To balance the same effective vertical stress component, the normal force on the selected plane must be $F_n = L\sigma_n'' = (L\sin\theta)(\sigma_v''\sin\theta)$. Hence, $\sigma_n'' = \sin^2\theta\sigma_v''$. Similar relations hold for the contributions of the horizontal effective stress to the shear and normal effective stresses along the selected plane. Using the equalities $2\cos^2\theta = 1+\cos 2\theta$ and $2\sin^2\theta = 1-\cos 2\theta$, we obtain Eq. (A.2.4).

Appendix A.3 Failure criterion parameters

Considering exceeding the shear capacity utilisation of a fault as a first requirement for a tremor, one may propose to relate the fault failure criterion parameter η to the shear capacity utilisation of a fault, i.e. Eq. (A.2.1). We could write, using the first formulation

of the shear capacity utilisation,

$$\eta_n = f(SCU_n) = f(\bar{\tau}_n/\tau_{MC,n}). \tag{A.3.1}$$

Disregarding stress reduction by tremors, the mean shear stress on the faults $\bar{\tau}_n$ is directly proportional to the presure reduction in the reservoir $p_n - p_0$. In this case, according to Eqs. (2.1.1) and (2.1.2),

$$\bar{\tau}_n = |\tau_0| + c_\tau(p_n - p_0) \quad \text{where} \quad c_\tau = \alpha c_{\sigma_v}. \tag{A.3.2}$$

Inserting $\sigma''_{n,n} = \sigma_{n,0} + \sigma_n - p_n$ into Eq. (A.2.2), we obtain

$$\tau_{MC,n} = S_0 + \tan\phi(\sigma_{n,0} + \sigma_n - p_n). \tag{A.3.3}$$

Using that changes in the normal stress on non-vertical faults are proportional to changes in the compaction pressure, i.e. $\sigma_n = c_{\sigma_n}(p_n - p_0)$,

$$\tau_{MC,n} = S_0 + \tan\phi(\sigma_{n,0} - p_0 - (1 - c_{\sigma_n})(p_n - p_0)). \tag{A.3.4}$$

For a small friction angle ϕ and a reasonable strength of cohesion S_0, τ_{MC} only weakly depends on a change of the normal effective stress on the fault $\sigma''_{n,n} = \sigma_{n,n} - p_n$ and can be assumed to be constant. For small values of S_0, this still holds when $\sigma_n - (p_n - p_0) \ll \sigma_{n,0} - p_0$.

In the region of interest, the strength parameters and the initial conditions in the terms for $\bar{\tau}_n$ and $\tau_{MC,n}$ vary over the faults. To show the effect of variations of these parameters and conditions on variations in values for the shear capacity utilisation, we suppose that these variations are uncorrelated and normally distributed around a mean value m with a standard deviation σ[4]. We exclude variations in the constant p_0. Increasing the pressure drop, we compare the cumulative distribution function (cdf) for failure according to the shear capacity utilisation criterion $SCU > 1$ with the Weibull cumulative probability distribution function for failure. The cdf of the latter is given by

$$F_W((p_n - p_0); k_W, \delta p_{fail}) = 1 - \exp\big(-\eta_n^{k_W}\big) = 1 - \exp\big(-((p_n - p_0)/\delta p_{fail})^{k_W}\big). \tag{A.3.5}$$

[4]According to Hoek (2006), see also Hoek and Brown (1997), the Mohr-Coulomb parameters S_0 and ϕ are correlated. For the failure of rock mass at slopes and around dams and tunnels, they propose to use the practical generalised Hoek-Brown strength criterion based on strength parameters that seem uncorrelated. Values for these parameters follow also from a normal distribution.

The cumulative probability density of the normal or Gaussian distribution function is given by

$$F_N(x; m, \sigma) = \frac{1}{\sqrt{2\pi}} \int_{-\infty}^{x} \exp\left(\frac{(x-m)^2}{2\sigma^2}\right) \quad \text{or} \quad F_N(x; m, \sigma) = \frac{1}{2}\left[1 + \operatorname{erf}\left(\frac{(x-m)}{\sigma\sqrt{2}}\right)\right].$$

m is the mean and σ is the standard deviation. The related probability density function is

$$f_N(x; m, \sigma) = \frac{1}{\sigma\sqrt{2\pi}} \exp\left(-\frac{(x-m)^2}{2\sigma^2}\right).$$

The fit parameter δp_{fail} is a characteristic pressure at which most of the faults slip and is used instead of the fit parameter τ_{fail}. In the following, we use two sets of values for the strength of cohesion S_0 and the friction angle ϕ along the fault. The first values are comparable with those used by van den Bogert (2015) [5], see Table A.3.1 .
The second set of values follow from a frequently used assumption that the strength of cohesion S_0 in the fault is negligible and that the fault friction coefficient $\mu \sim 0.85$ for faults in the upper zone of the earth crust[6]. The related frictional strength is $\tau \sim 0.85\sigma_n$ and related friction angle $\phi \sim 40°$. This extreme value is higher than follows from the residual strength of Slochteren reservoir rock according to experiments in a triaxial apparatus. A friction coefficient $\mu \sim 0.65$ is reported by NAM. Sanz et al. (2015) use a value $\mu \sim 0.65$ to compare the cumulative dissipative fault energy by fault slippage with the cumulative energy of the observed tremors.

We suppose that the faults in the Groningen field have been not exposed to major tectonic activity or excessive loading by the in-situ gas pressure before gas production. While vertical faults are hardly stressed before gas production, the non-vertical faults in the field (and there are many, see Appendix C, Figure C.1.8) will be stressed before gas production. For this reason, we have compared the cdf's for a few initial stresses, $\bar{\tau}_0$.

The cumulative distribution function for failure based on the shear capacity utilisation criterion is calculated for 100 cases for which the reservoir pressure is reduced from 35 MPa to 10 MPa in 25 steps of 1 MPa. The Weibull cdf is fitted to this cdf and the Weibull parameters are derived using the numpy routine $curve\_fit$ in Python^{TM}. This procedure has been repeated about 10 times to estimate the variation in the Weibull parameters derived from this comparison. This is done for various standard deviations σ and for three different values for $\bar{\tau}_0$ and for two sets of strength fault properties, i.e. for $S_0 = 5$ MPa and $\phi = 15°$ and for $S_0 = 0$ MPa and $\phi = 40°$.

We have increased the parameter c_τ from 1 to 2.5 to exceed the shear capacity utilisation for the second set of strength parameters at about the same reservoir pressure as for the first set of parameters. The results are summarised in Table A.3.1 . Using the parameters $\mu = 0.5$ and $c_\tau \sim 1.5$ gives about a similar result as using the parameters $\mu = 0.85$ and $c_\tau \sim 2.5$.

The Weibull cumulative distribution function for failure reasonably fits to the cumulative distribution function for failure based on shear capacity criterion. The differences in the tails are systematic, see Figure A.3.2 . We disregard them because both distri-

[5] Peter van den Bogert uses $S_0 = 7$ MPa and $\phi = 13°$ to ensure that the onset of fault slip is simulated at a realistic reservoir depletion pressure for a wide range of Poisson ratio's. The Poisson ratio has a strong influence on the change in the horizontal stress due to reservoir compaction, see also the results of the so-called Phase 1 study of van den Bogert, van Eijs, and van der Wall.

[6] This follows from Byerlee's law, see e.g. Scholz (2002), §2.2.

bution functions are phenomenological. Also, the uncorrelated normal distributions for the parameters in the expression for the shear capacity utilisation have no physical basis. Further, these differences hardly matter when modelling a fault system producing a moderate number of tremors.
As expected, the value for the Weibull parameter or shape parameter k_W increases for smaller relative standard deviations in the values of the parameters for the shear capacity utilisation. The characteristic pressure for failure δp_{fail} hardly changes. δp_{fail} decreases with increasing initial shear stress $\bar{\tau}_0$. Further, the Weibull shape parameter k_W decreases with increasing initial shear stress $\bar{\tau}_0$ when it becomes a significant factor in the expression for the shear capacity utilisation.

Figure A.3.3 shows the number of failures following from exceeding the shear capacity utilisation criterion and from the Weibull probability distribution for failure when the reservoir pressure decreases. After a smooth onset of the failure rate, the failure rate becomes almost constant when the reservoir pressure continues to decrease.

Table A.3.1 : Relation between the relative standard deviation σ^* in the normal distribution functions for the parameters $\bar{\tau}_0$, c_τ, S_0, ϕ, $\sigma_{n,0}$ and c_{σ_n} and the parameters of the Weibull probability distribution function k_W and δp_{fail} for 3 mean initial shear stresses $\bar{\tau}_0$ and two sets of fault strength parameters. $\sigma^* = \sigma/m$ where m is the mean value of the parameter

$\bar{\tau}_0$	c_τ	S_0	ϕ	$\sigma_{n,0}$	c_{σ_n}	σ^*	k_W	δp_{fail}
MPa	-	MPa	degree	MPa	-	-	-	MPa
0	1	5	15	60	0.5	0.05	10.5±1.2	17
						0.1	5.0±0.4	18±0.5
						0.15	3.3	18
						0.2	2.5	18
2	1	5	15	60	0.5	0.05	9.5±1.0	15
						0.1	4.7±0.5	14
						0.15	3.0	14
						0.2	2.1	15
5	1	5	15	60	0.5	0.05	7.0±0.8	10
						0.1	3.4	10
						0.15	2.2±0.3	11
						0.2	1.8±0.3	11
2	2.5	0	40	60	0.5	0.05	4.7±0.5	17
						0.1	2.6±0.2	18
						0.15	1.8±0.4	17
						0.2	1.3±0.2	20±2

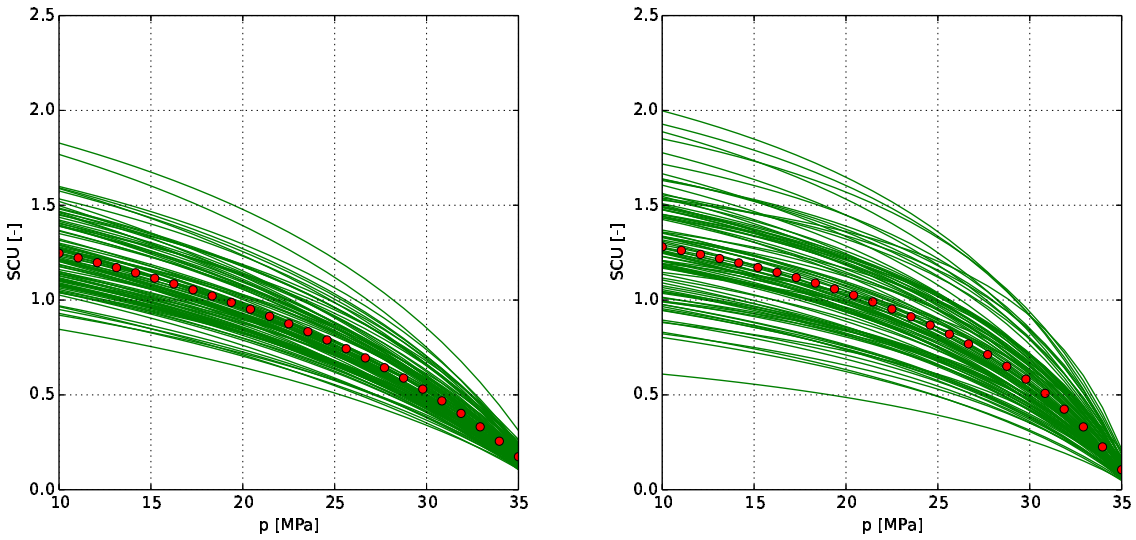

Figure A.3.1 : The shear capacity utilisation versus the reservoir pressure. The initial mean shear stress is $\bar{\tau}_0 = 2$ MPa. The relative standard deviation in the shear capacity utilisation parameter values is $\sigma^* = 0.1$. Left figure for $S_0 = 5$ MPa and $\phi = 15°$. Right figure for $S_0 = 0$ MPa and $\phi = 40°$.

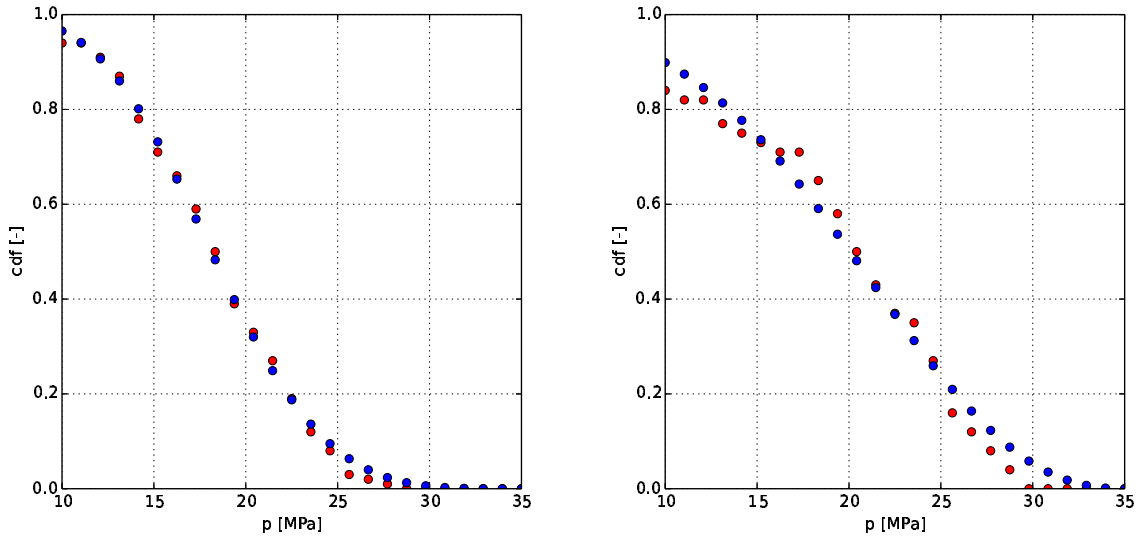

Figure A.3.2 : Cumulative distribution functions for failure according the shear capacity utilisation criterion (red) and according to the Weibull distribution function for failure (blue) versus the reservoir pressure.
The initial mean shear stress is $\bar{\tau}_0 = 2$ MPa. The relative standard deviation in the parameter values determining the shear capacity utilisation is $\sigma^* = 0.1$. Left figure for $S_0 = 5$ MPa and $\phi = 15°$. Right figure for $S_0 = 0$ MPa and $\phi = 40°$.

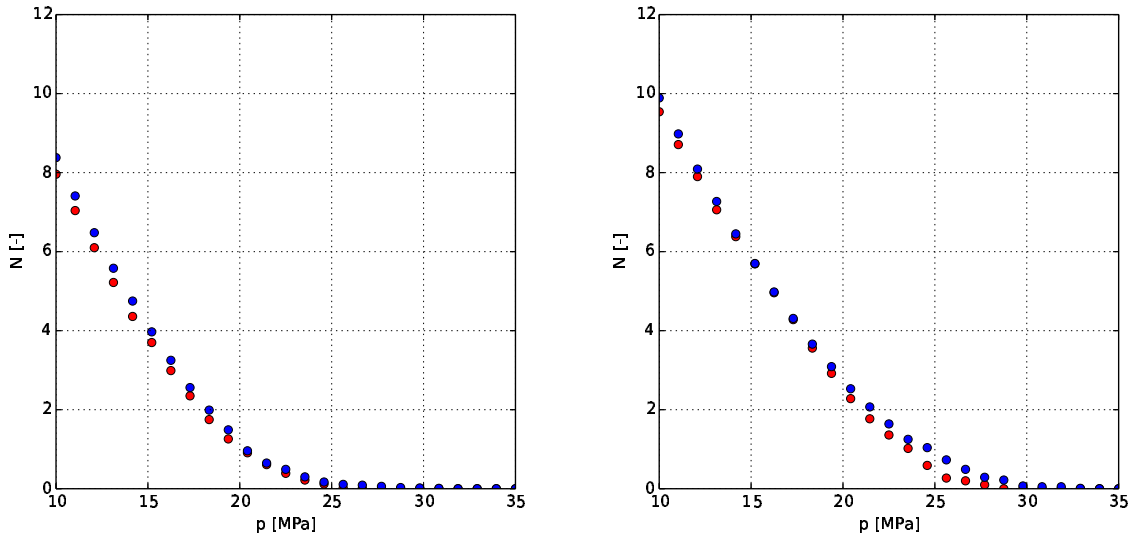

Figure A.3.3 : Number of failures following from exceeding the shear capacity utilisation criterion (red) and from the Weibull probability distribution for failure (blue) versus the reservoir pressure.
The initial mean shear stress is $\bar{\tau}_0 = 2$ MPa. The relative standard deviation in the parameter values determining the shear capacity utilisation is $\sigma^* = 0.1$. Left figure for $S_0 = 5$ MPa and $\phi = 15°$. Right figure for $S_0 = 0$ MPa and $\phi = 40°$.

Appendix B

Deformation around typical reservoir offsets

The work below addresses a few aspects of elastic stress and deformation around a few typical faults in the Groningen reservoir with the purpose to obtain estimates for the constants or fit parameters c_{σ_v} and c_{M0}. The first one, c_{σ_v} couples the effective vertical stress away from the faults to a change in the mean shear stress on the faults. The second one, c_{M0} couples the energy released by the tremors to the mean reduction of the shear stress on the faults. For extensive geomechanical modelling of fault failure, including a-seismic, subsonic or quasi-steady slip along single faults and along faults in the Groningen field, we refer to van den Bogert (2015) and Sanz et al. (2015).

In the model, the reservoir is linear poro-elastic and the overburden and underburden are linear elastic. All rocks are uniform and isotropic. The relevant length scales for stress build-up and failure are the reservoir thickness h_{res} [m], the fault throw t_{res} [m], the fault dip angle δ and the reservoir compaction δh_{res} [m]. The latter is determined by the pressure drop and compaction coefficient. We consider only one reservoir thickness of 200 m and one compaction condition that follows from a reservoir pressure drop of 25 MPa.
The mean depth of the reservoir is 3 km. The domain for the calculation is 6 km in vertical direction and 8 km in horizontal direction. The faults cut the reservoir in the center of the domain. To approximate uniaxial compaction, the mechanical left and right boundary conditions are of the so-called roller type, i.e. they allow only free vertical displacement. Displacement at the upper surface of the domain is free. The displacement at the basement boundary at 6 km depth is for the calculations in §B.1 constrained to zero. For the calculations in §B.2 the basement boundary condition is of roller type, i.e. there is only free displacement in horizontal direction. The domain and boundary conditions are illustrated in Figure B.0.1 .

The computer programme used for the geomechanical calculations is COMSOL^{TM}. The calculations are based on the finite element method. We use the poro-elastic physics mod-

ule from the geomechanics library[1]. The 2 dimensional calculations under a plane strain condition are done for 9 typical faults which are cutting through a compacted reservoir under typical field stress conditions. The names and the mean geometric features of these faults are listed in Table B.0.2 .

For the modelling, we have used rounded values for the rock properties and the reservoir pressures and are comparable with van den Bogert (2015), see Table B.0.1 [2].

[1] COMSOL^{TM} uses the elastic theory convention that strain and stress are negative under compression and shrinkage. Using the geomechanical convention in this report that strain and stress are positive under compression and shrinkage, we have modified the results of the simulator by changing signs where needed.

[2] The mean reservoir depth is 3 km. The values for the gas bulk modulus K_f [Pa], the porosity ϕ [-] and the Biot modulus M [Pa] are not needed for the Monte-Carlo simulations but are used in the stress calculations. The Biot modulus M can be calculated from the other poro-elastic constants as follows, see also Fjaer et al. (2008), §1.6, Eq. 1.157. Using $\alpha = 1 - K/K_s$,

$$M = \frac{1}{\phi/K_f + (\alpha - \phi)/K_s}.$$

Table B.0.1 : Input parameters for modelling. (c.) means calculated from primary input.

Property	Symbol	Unit	Value
field data			
- gravitational constant	g	m/s^2	9.81
- horizontal field stress	$\sigma_{h,0}$	MPa	50/40
- vertical field stress	$\sigma_{v,0}$	MPa	60
- initial stress on the vert. fault	τ_0	MPa	0
- initial reservoir pressure	p_0	MPa	35
- final reservoir pressure	p_1	MPa	10
rock properties			
- bulk density	ρ_s	kg/m^3	2200
- grain modulus	K_s	GPa	22
- Poisson ratio	ν	-	0.25
- Young modulus	E	GPa	10
- shear modulus (c.)	μ	GPa	4
- bulk modulus (c.)	K	GPa	6.7
- Biot constant (c.)	α	-	0.7
- uniaxial compaction coefficient (c.)	C_m	1/bar	8.3 10^{-6}
- uniaxial compaction modulus (c.)	H	GPa	12.0
- porosity	ϕ	-	0.2
- gas bulk modulus (20 MPa, 100 °C)	K_f	GPa	0.02
- Biot modulus (c.)	M	GPa	0.1
- strength of cohesion	S_0	-	5
- friction angle	ϕ	degree	15
- friction coefficient (c.)	μ	-	0.27
reservoir geometry			
- reservoir thickness	h_{res}	m	200
- reservoir throw	t_{res}	m	0, 50, 100
- depth of the centre of the reservoir	z_{res}	km	3
- fault dip angle	δ	degree	90, 80, 70
uniaxial compaction			
- stress path coefficient total stress (c.)	γ	-	0.46
- stress path coefficient effective stress poro-el (c.)	γ'	-	-0.23
- stress path coefficient effective stress failure (c.)	γ''	-	-0.53
- uniaxial reservoir compaction (c.)	δh_{res}	m	-0.29

Table B.0.2 : Nine typical faults around a reservoir offset investigated for stress calculations. The reservoir is in all cases 200 m thick. The mean depth of the reservoir is 3 km. The domain of the calculation is between the free surface and the basement at 6 km depth and two boundaries at 4 km left and 4 km right of the center of the fault, which is at the height of the mean reservoir depth.

Property	Symbol	Unit	fault	fault	fault
.....	.....	.....	.....	.....	.....
name			I-0	I-50	I-100
dip angle	δ	degree	90	90	90
throw	t_{res}	m	0	50	100
.....	.....	.....	.....	.....	.....
name			II-0	II-50	II-100
dip angle	δ	degree	80	80	80
throw	t_{res}	m	0	50	100
.....	.....	.....	.....	.....	.....
name			III-0	III-50	III-100
dip angle	δ	degree	70	70	70
throw	t_{res}	m	0	50	100

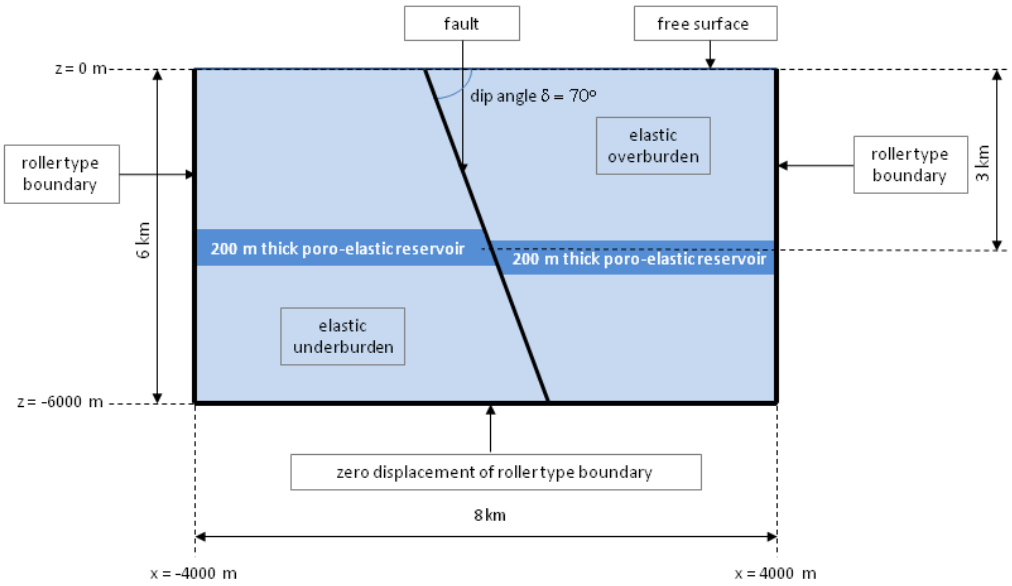

Figure B.0.1 : Domain and boundary conditions of a calculation for fault III-100 with a fault dip angle $\delta = 70°$ and throw $t_{res} = 100$ m. The reservoir thickness is 200 m. for the calculations in §B.1 constrained to zero. For the calculations in §B.2 the basement boundary is of roller type, i.e. there is only free displacement in the horizontal direction. For the last calculations, the gravitational force is active to generate the vertical and horizontal stresses.

Appendix B.1 Deformation after compaction

In this section, we present the mean and maximum changes in the shear and normal stresses and shear capacity utilisation which are cutting through a compacted reservoir under typical field stresses for the faults given in Table B.0.2 . These are one vertical (I) and two non-vertical (II, III) faults with throws of 0, 50 and 100 m. The two non-vertical faults have a dip angle δ of 80 and 70°. The calculations don't include local non-seismic fault slip when the shear capacity of the fault is exceeded. Such calculations can be found in van den Bogert (2015) and Sanz et al. (2015).

The calculations don't include the gravitational force. The field stresses in the reservoir

are added to the results using the superposition principle for linear elastic deformation. The (total) vertical field stress σ_v at reservoir depth is taken 60 MPa. The (total) horizontal stresses σ_H and σ_h are taken equal. We do the calculations for a typical value at the mean reservoir depth of $\sigma_h = 50$ MPa and for a lower bound $\sigma_h = 40$ MPa, referring to van Eijs and Valencia (2014). We disregard variations of these stresses over the reservoir with depth, in contrast to van den Bogert (2015) and Sanz et al. (2015). We note that the Poisson ratio used, in accordance with van den Bogert (2015), may be high compared to values from samples from wells and that the horizontal and vertical field stresses are somewhat low compared to other data used, see also Appendix C. Recognising that the values for the rock properties along the faults in the Groningen field could be quite different, the results should be regarded as indicative.

The mesh around the reservoir offset of the vertical fault is shown in Figure B.1.1 . The rock properties and the other input parameters are given in Table B.0.1 . The uniaxial compaction coefficient is comparable with values derived from the subsidence data in the Groningen field. The calculated compaction in the reservoir for faults with zero throw is equal to the value calculated for uniaxial compaction, i.e. δh_{res} = - 0.29 m.

The pressure in the reservoir decreases from $p_0 = 35$ MPa to $p_1 = 10$ MPa. The initial shear stress on the vertical fault I τ_0 is zero. The initial shear stress on the two non-vertical faults II and III with fault dip angles of 80° and 70° is significant due to the imbalance between the vertical and horizontal field stresses.

The resulting changes in stresses for uniaxial compaction are given in Tables B.1.2 and B.1.3 . These tables show the mean, minimum and maximum stresses along the fault after compaction for the vertical and non-vertical faults with 0, 50 and 100 m fault throws. Figures B.1.2 - B.1.3 show the vertical and horizontal displacements in the whole domain and in the rock volume around the reservoir offset for the vertical fault I-100 with a fault throw of 100 m.
Figures B.1.4 - B.1.6 show the shear stress, the effective normal stresses and the shear capacity utilisation for the faults I-100, II-100 and III-100 versus depth for a horizontal field stress of 40 MPa. The values vary considerably along the fault plane. The effective normal stress is minimal in the reservoir rock. The shear stress peaks at the geometric discontinuities along the faults.
It can be expected that failure starts locally along the fault plane when the reservoir pressure decreases and the shear stress over the fault increases. Whether local failure is followed by seismic fault slip and a significant tremor is another question. The transition from subsonic to sonic (or seismic) slip depend on other factors, such as a drop in the shear stress during rock displacement (or strain weakening).

Around the fault, the overburden, underburden and reservoir rock are pulled into the reservoir when the reservoir pressure decreases. In the right upper part of the reservoir offset, rock is pulled to the right side. In the left lower part of the reservoir offset, rock is

pulled to the left side, see Figure B.1.3 . These forces correspond with similar forces at the edge of a reservoir, see e.g. Fjaer et al. (2008), §12.3 or Mulders (2003), §6.2 Figure 6.1.

Using similar fault strength parameters as van den Bogert (2015) but for a horizontal stress of 40 MPa, the mean and maximum shear capacity utilisation for the non-vertical faults II and III after reservoir compaction are in the range $S\breve{C}U_1 \sim$ 0.5 - 0.9 MPa and $SCU_{1,max} \sim$ 0.5 - 1.5 MPa, see Table B.1.4 . The maximum values indicate that local shear-type failure can be expected at a lower reservoir pressure drop than 25 MPa, in agreement with calculations of van den Bogert (2015). For fault II-100, $SCU_{1,max} > 1$ for $p_0 - p <$ 10 - 15 MPa.

For the parameters given in Table B.0.1 and a horizontal field stress of 40 MPa, fault III is close to shear-type failure before compaction. In this case, local failure is expected at a low reservoir pressure drop but also when relatively little elastic energy is added to the rock surrounding the fault by compaction. For a horizontal field stress of 50 MPa, fault III is before compaction farther away from shear-type failure. A larger reservoir pressure drop is needed to initiate fault failure, see Table B.1.5 .
In this context, we may expect that faults with a small dip angle, such as faults I and II, are more likely candidates to generate a tremor under a low horizontal field stress. Fault III is a more likely candidate to generate a tremor when the horizontal field stress is larger and more elastic energy can be added to the surrounding rock before failure.

For the vertical fault, the absolute values of the mean and peak shear stresses are proportional to the absolute value of the pressure drop in the reservoir during compaction, i.e. $\bar{\tau} \propto \delta p$ and $\tau_{peak} \propto \delta p$. For a pressure drop of 25 MPa and a related uniaxial reservoir compaction $\delta h_{res} \sim$ -0.3 m, the minimal normal effective stress in relation to failure on the fault is for the three faults in the range $\sigma''_{n,1,min}$ = 18 - 23 MPa. The mean values of $\sigma''_{n,1,min}$ are somewhat higher.
After compaction, the maximum shear stresses over the three faults are in the range $\tau_{1,max}$ = 10 - 18 MPa, see Table B.1.1 . The mean shear stress values are 30 - 70% lower. Hence, $c_{\sigma_v} \sim 0.5$ is a reasonable value for the geometric constant relating a change in the effective vertical stress away from the faults to a change in the mean shear stress on the faults.

Table B.1.1 : Changes in the vertical and horizontal stresses in the reservoir following uniaxial compaction for two cases, using the equations given in Appendix A, §A.1.

Property	Symbol	Unit	Before compaction	Change	After compaction
.....	.....	.....	.....	.....	.....
total vertical stress in reservoir	$\sigma_{v,i}$	MPa	60	0	60
eff. vertical stress in reservoir, poro-el	$\sigma'_{v,i}$	MPa	36	17	53
eff. vertical stress in reservoir, failure	$\sigma''_{v,i}$	MPa	25	25	50
total horizontal stress in reservoir	$\sigma_{h,i}$	MPa	50	-12	38
eff. horizontal stress in reservoir, poro-el	$\sigma'_{h,i}$	MPa	26	5	31
eff. horizontal stress in reservoir, failure	$\sigma''_{h,i}$	MPa	15	13	28
.....	.....	.....	.....	.....	.....
total vertical stress in reservoir	$\sigma_{v,i}$	MPa	60	0	60
eff. vertical stress in reservoir, poro-el	$\sigma'_{v,i}$	MPa	36	17	53
eff. vertical stress in reservoir, failure	$\sigma''_{v,i}$	MPa	25	25	50
total horizontal stress in reservoir	$\sigma_{h,i}$	MPa	40	-12	28
eff. horizontal stress in reservoir, poro-el	$\sigma'_{h,i}$	MPa	16	5	21
eff. horizontal stress in reservoir, failure	$\sigma''_{h,i}$	MPa	5	13	18

Table B.1.2 : Initial stresses before compaction and mean, minimal and maximal absolute stresses after compaction and before a-seismic or seismic failure. The vertical stress at reservoir depth is $\sigma_v = 60$ MPa. The horizontal field stress at reservoir depth is $\sigma_h = 50$ MPa.

Property	Symbol	Unit	fault	fault	fault
reservoir pressure before compaction	p_0	MPa	35		
reservoir pressure after compaction	p_1	MPa	10		
.....	.....	.....	.....	.....	.....
			I-0	I-50	I-100
dip angle	δ	degree	90	90	90
throw	t_{res}	m	0	50	100
shear stress before compaction	τ_0	MPa	0	0	0
mean abs. shear stress after compaction	$\breve{\tau}_1$	MPa	0	2.7	3.6
max. abs. shear stress after compaction	$\tau_{1,max}$	MPa	0	9.2	10
normal eff. stress before compaction	$\sigma''_{n,0}$	MPa	15	15	15
mean abs. eff. normal stress after compaction	$\breve{\sigma}''_{n,1}$	MPa	28	31	32
min. abs. eff. normal stress after compaction	$\sigma_{n,1,min}$	MPa	28	28	28
.....	.....	.....	.....	.....	.....
			II-0	II-50	II-100
dip angle	δ	degree	80	80	80
throw	t_{res}	m	0	50	100
shear stress before compaction	τ_0	MPa	1.7	1.7	1.7
mean abs. shear stress after compaction	$\breve{\tau}_1$	MPa	3.7	5.3	5.6
max. abs. shear stress after compaction	$\tau_{1,max}$	MPa	3.7	12	12
normal eff. stress before compaction	$\sigma''_{n,0}$	MPa	15	15	15
mean abs. eff. normal stress after compaction	$\breve{\sigma}''_{n,1}$	MPa	29	31	33
min. abs. eff. normal stress after compaction	$\sigma_{n,1,min}$	MPa	29	36	36
.....	.....	.....	.....	.....	.....
			III-0	III-50	III-100
dip angle	δ	degree	70	70	70
throw	t_{res}	m	0	50	100
shear stress before compaction	τ_0	MPa	3.2	3.2	3.2
mean abs. shear stress after compaction	$\breve{\tau}_1$	MPa	6.9	7.9	7.8
max. abs. shear stress after compaction	$\tau_{1,max}$	MPa	6.9	15	15
normal eff. stress before compaction	$\sigma''_{n,0}$	MPa	16	16	16
mean abs. eff. normal stress after compaction	$\breve{\sigma}''_{n,1}$	MPa	31	33	35
min. abs. eff. normal stress after compaction	$\sigma_{n,1,min}$	MPa	31	41	38

Table B.1.3 : Initial stresses before compaction and mean, minimal and maximal absolute stresses after compaction and before a-seismic or seismic failure. The vertical stress at reservoir depth is $\sigma_v = 60$ MPa. The horizontal field stress at reservoir depth is $\sigma_h = 40$ MPa.

Property	Symbol	Unit	fault	fault	fault
reservoir pressure before compaction	p_0	MPa	35		
reservoir pressure after compaction	p_1	MPa	10		
.....	.....	.....	.....	.....	.....
			I-0	I-50	I-100
dip angle	δ	degree	90	90	90
throw	t_{res}	m	0	50	100
shear stress before compaction	τ_0	MPa	0	0	0
mean abs. shear stress after compaction	$\breve{\tau}_1$	MPa	0	2.7	3.6
max. abs. shear stress after compaction	$\tau_{1,max}$	MPa	0	9.2	10
normal eff. stress before compaction	$\sigma''_{n,0}$	MPa	5.0	5.0	5.0
mean abs. eff. normal stress after compaction	$\breve{\sigma}''_{n,1}$	MPa	18	21	22
min. abs. eff. normal stress after compaction	$\sigma_{n,1,min}$	MPa	18	18	18
.....	.....	.....	.....	.....	.....
			II-0	II-50	II-100
dip angle	δ	degree	80	80	80
throw	t_{res}	m	0	50	100
shear stress before compaction	τ_0	MPa	3.4	3.4	3.4
mean abs. shear stress after compaction	$\breve{\tau}_1$	MPa	5.4	6.9	7.1
max. abs. shear stress after compaction	$\tau_{1,max}$	MPa	5.4	14	14
normal eff. stress before compaction	$\sigma''_{n,0}$	MPa	5.6	5.6	5.6
mean abs. eff. normal stress after compaction	$\breve{\sigma}''_{n,1}$	MPa	19	22	23
min. abs. eff. normal stress after compaction	$\sigma_{n,1,min}$	MPa	19	19	20
.....	.....	.....	.....	.....	.....
			III-0	III-50	III-100
dip angle	δ	degree	70	70	70
throw	t_{res}	m	0	50	100
shear stress before compaction	τ_0	MPa	6.4	6.4	6.4
mean abs. shear stress after compaction	$\breve{\tau}_1$	MPa	10	11	11
max. abs. shear stress after compaction	$\tau_{1,max}$	MPa	10	18	18
normal eff. stress before compaction	$\sigma''_{n,0}$	MPa	7.3	7.3	7.3
mean abs. eff. normal stress after compaction	$\breve{\sigma}''_{n,1}$	MPa	22	25	26
min. abs. eff. normal stress after compaction	$\sigma_{n,1,min}$	MPa	22	23	23

Table B.1.4 : Shear capacity utilisation after compaction and before a-seismic or seismic failure. The horizontal field stress at reservoir depth is $\sigma_h = 40$ MPa.

Property	Symbol	Unit	fault	fault	fault
reservoir pressure before compaction	p_0	MPa	35		
reservoir pressure after compaction	p_1	MPa	10		
.....	.....	.....	.....	.....	.....
			I-0	I-50	I-100
dip angle	δ	degree	90	90	90
throw	t_{res}	m	0	50	100
mean shear capacity utilisation before compaction	$S\breve{C}U_0$	-	0	0	0
mean shear capacity utilisation after compaction	$S\breve{C}U_1$	-	0	0.26	0.33
max. shear capacity utilisation after compaction	$SCU_{1,max}$	-	0	0.9	1.1
.....	.....	.....	.....	.....	.....
			II-0	II-50	II-100
dip angle	δ	degree	80	80	80
throw	t_{res}	m	0	50	100
mean shear capacity utilisation before compaction	$S\breve{C}U_0$	-	0.5	0.5	0.5
mean shear capacity utilisation after compaction	$S\breve{C}U_1$	-	0.5	0.64	0.65
max. shear capacity utilisation after compaction	$SCU_{1,max}$	-	0.5	1.3	1.3
.....	.....	.....	.....	.....	.....
			III-0	III-50	III-100
dip angle	δ	degree	70	70	70
throw	t_{res}	m	0	50	100
mean shear capacity utilisation before compaction	$S\breve{C}U_0$	-	0.92	0.92	0.92
mean shear capacity utilisation after compaction	$S\breve{C}U_1$	-	0.93	0.95	0.92
max. shear capacity utilisation after compaction	$SCU_{1,max}$	-	0.93	1.5	1.5

Table B.1.5 : Shear capacity utilisation after compaction and before a-seismic or seismic failure. The horizontal field stress at reservoir depth is $\sigma_h = 50$ MPa.

Property	Symbol	Unit	fault	fault	fault
reservoir pressure before compaction	p_0	MPa	35		
reservoir pressure after compaction	p_1	MPa	10		
.....	.....	.....	.....	.....	.....
			III-0	III-50	III-100
dip angle	δ	degree	70	70	70
throw	t_{res}	m	0	50	100
mean shear capacity utilisation before compaction	$S\breve{C}U_0$	-	0.34	0.34	0.34
mean shear capacity utilisation after compaction	$S\breve{C}U_1$	-	0.52	0.56	0.56
max. shear capacity utilisation after compaction	$SCU_{1,max}$	-	0.52	1.1	1.1

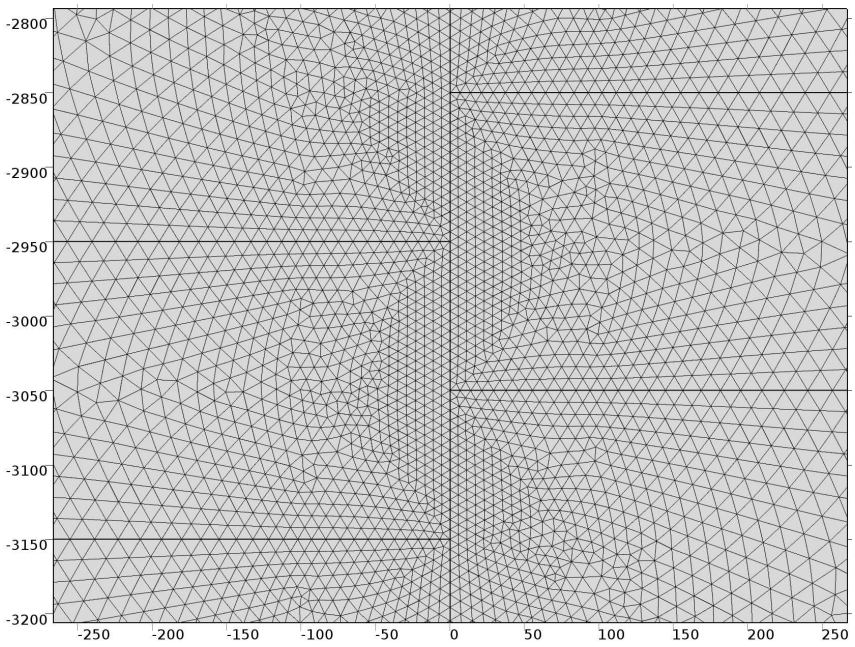

Figure B.1.1 : Mesh around the reservoir offset for the compaction calculations before failure for the vertical fault I-100 with a fault dip angle $\delta = 90°$ and throw $t_{res} = 100$ m. The reservoir thickness is 200 m. The elements along the fault and the reservoir have a size of about 6 m. There are about 37000 domain elements and 950 boundary elements.

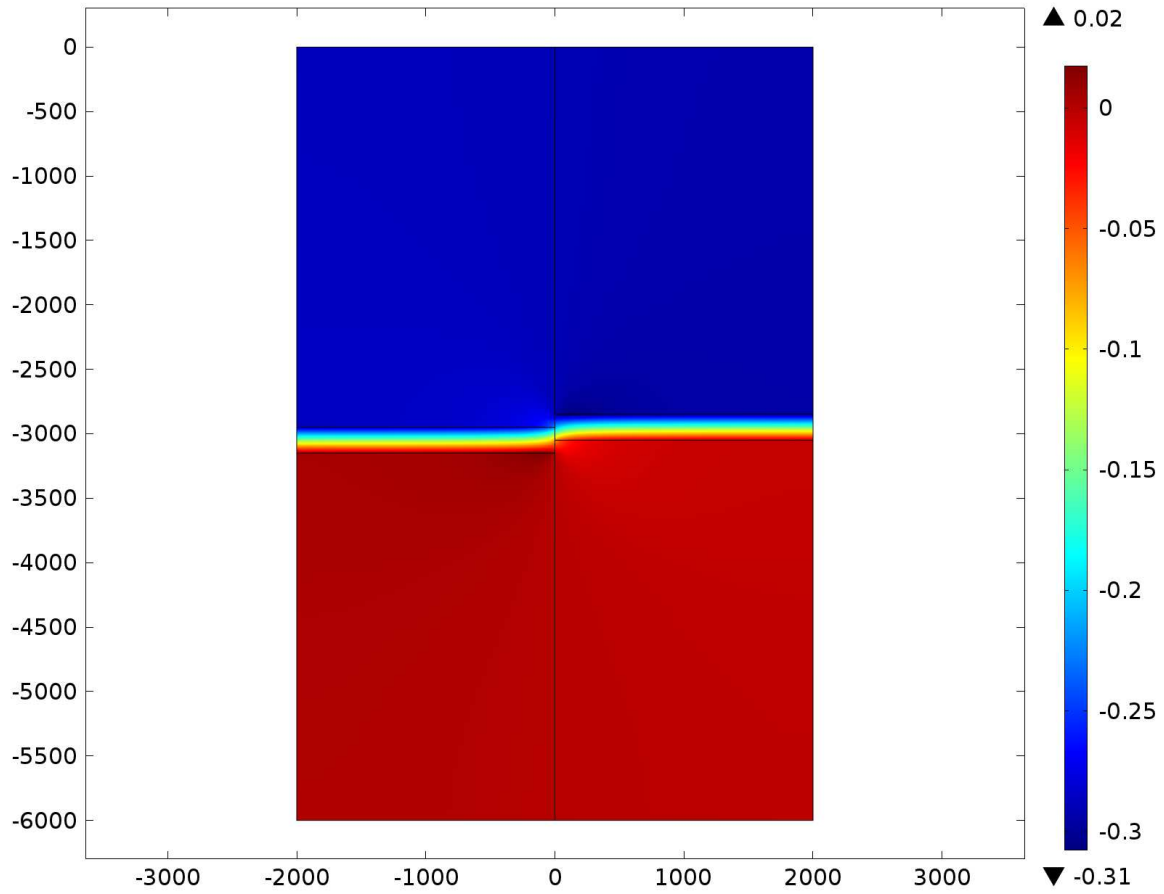

Figure B.1.2 : Vertical rock displacement in meters in the whole domain after compaction and before a-seismic or seismic failure for fault I-100 with a fault dip angle $\delta = 90°$ and throw $t_{res} = 100$ m. The reservoir thickness is 200 m.

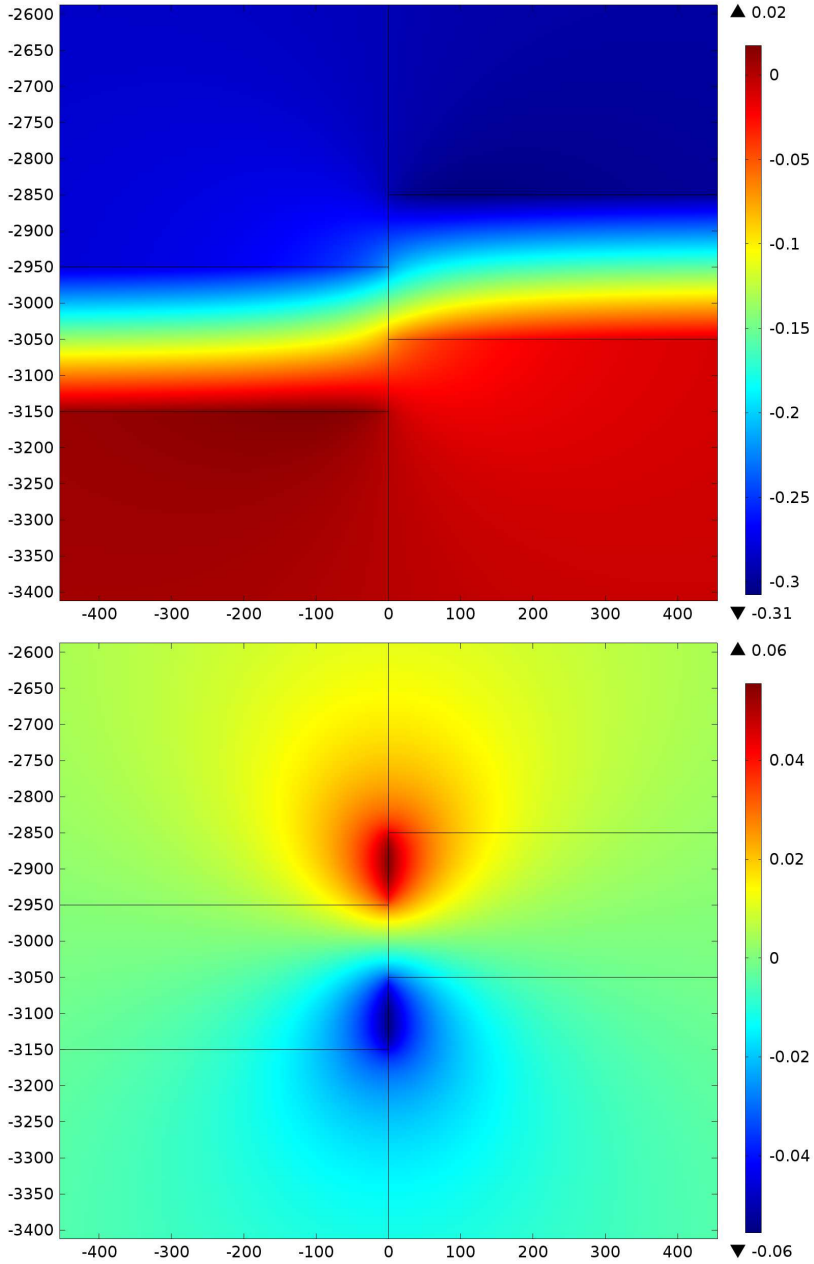

Figure B.1.3 : Vertical (top) and horizontal (bottom) rock displacements in meters around the reservoir offset after compaction and before a-seismic or seismic failure for fault I-100 with a fault dip angle $\delta = 90°$ and throw $t_{res} = 100$ m. The reservoir thickness is 200 m.

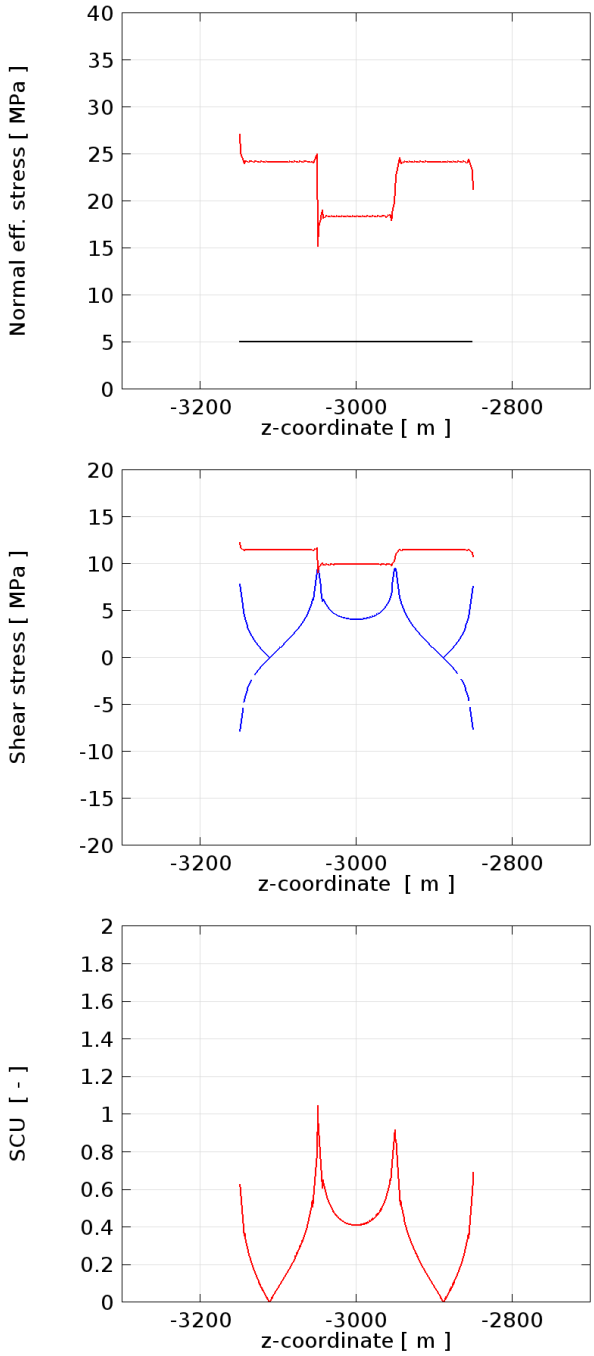

Figure B.1.4 : Stresses and shear capacity utilisation versus depth for fault I-100 with a fault dip angle $\delta = 90°$ and throw $t_{res} = 100$ m after compaction and before failure for a horizontal field stress of 40 MPa.
Top: Normal effective stresses before and after compaction in relation to rock failure, $\sigma''_{n,0}$ (black) and $\sigma''_{n,1}$ (red). Center: shear stress after compaction, τ_1 (dashed/solid blue). The solid blue line is the absolute shear stress. The red line shows the shear stress required for Mohr-Coulomb shear-type failure. Bottom: shear capacity utilisation after compaction, SCU_1.

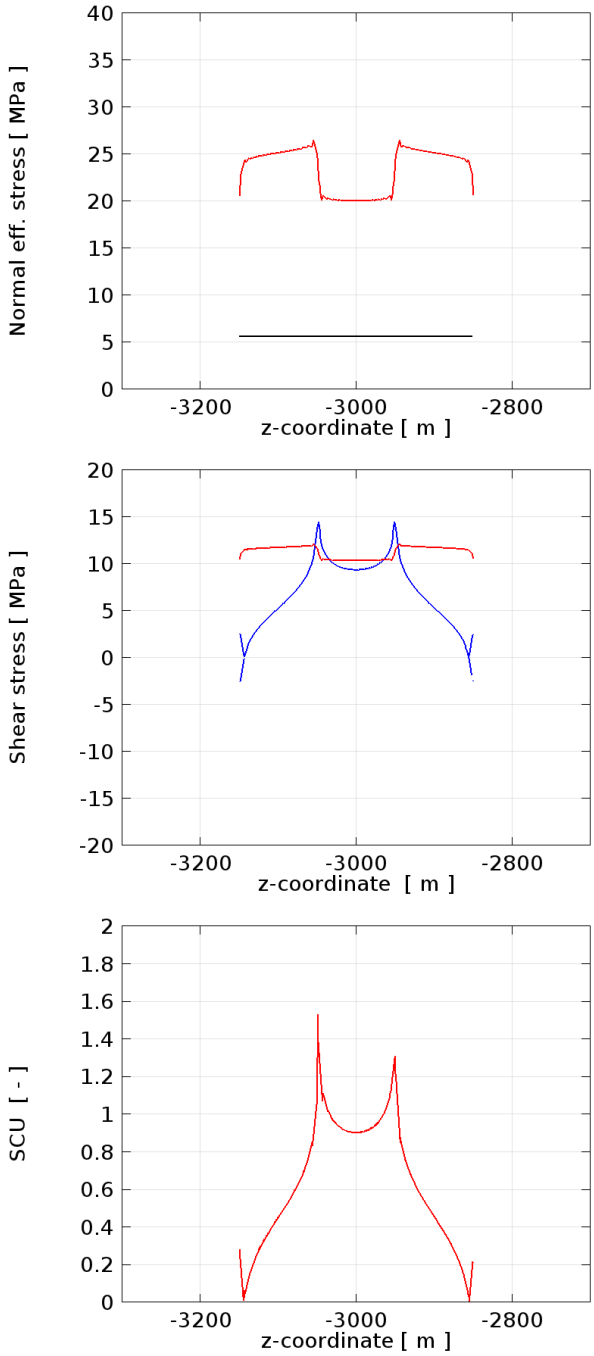

Figure B.1.5 : Stresses and shear capacity utilisation versus depth for fault II-100 with a fault dip angle $\delta = 80°$ and throw $t_{res} = 100$ m after compaction and before failure for a horizontal field stress of $\sigma_h = 40$ MPa.
Top: Normal effective stresses before and after compaction in relation to rock failure, $\sigma''_{n,0}$ (black) and $\sigma''_{n,1}$ (red). Center: shear stress after compaction, τ_1 (dashed/solid blue). The solid blue line is the absolute shear stress. The red line shows the shear stress required for Mohr-Coulomb shear-type failure. Bottom: shear capacity utilisation after compaction, SCU_1.

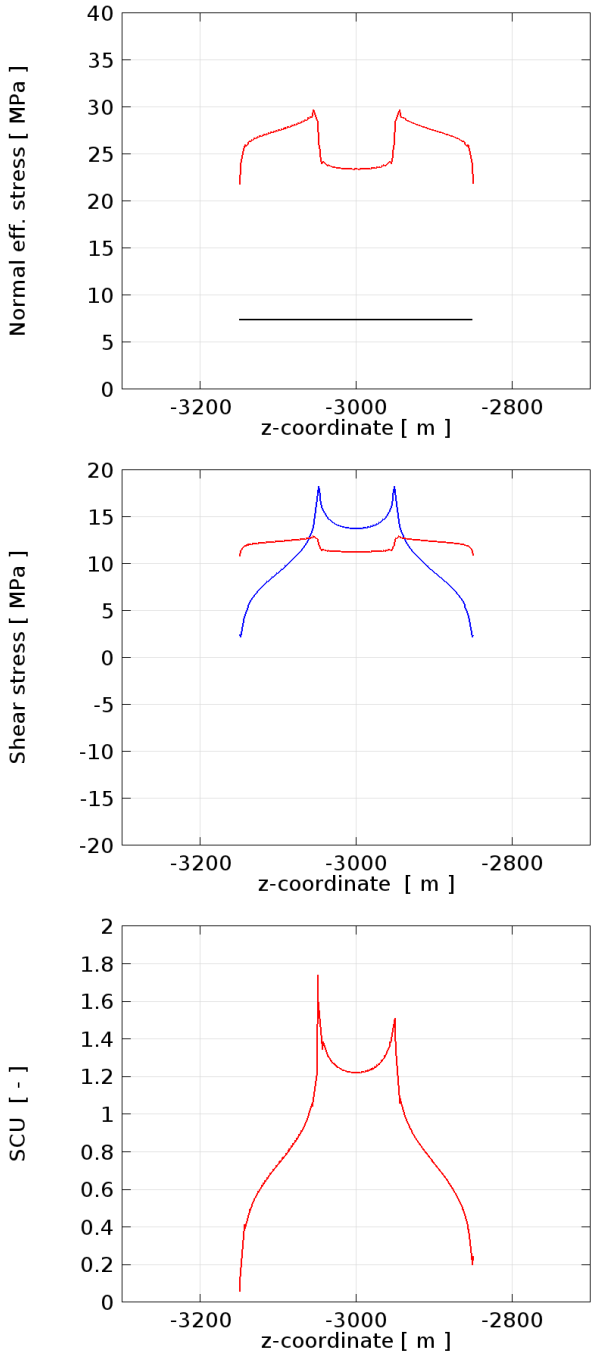

Figure B.1.6 : Stresses and shear capacity utilisation versus depth for fault III-100 with a fault dip angle $\delta = 70°$ and throw $t_{res} = 100$ m after compaction and before failure for a horizontal field stress of $\sigma_h = 40$ MPa.
Top: Normal effective stresses before and after compaction in relation to rock failure, $\sigma''_{n,0}$ (black) and $\sigma''_{n,1}$ (red). Center: shear stress after compaction, τ_1 (dashed/solid blue). The solid blue line is the absolute shear stress. The red line shows the shear stress required for Mohr-Coulomb shear-type failure. Bottom: shear capacity utilisation after compaction, SCU_1.

Appendix B.2 Energy release due to fault failure

The purpose of the work presented in this section is to calculate the liberated energy when the fault around the reservoir offset completely fails, either a-seismically or seismically. The liberated or released energy is used to calculate a typical value for the stress relaxtion parameter c_{M0} in §B.3. First, we show an important relation between slip and shear stress along the fault and the reduction of the gravitational and elastic energy in the surrounding rock.

B.2.1 Theory - elastic media

The relation between the release of gravitational and elastic energy in terms of the expression Eq. (2.2.3) in §2.2 is explained by Aki and Richards (2009), §3.4, Box 3.4. This is done for a case in which the internal energy is given by the free elastic energy density or strain energy density function F'_{el} [J/m^3] and body forces are absent[3]. The resulting formula is of great generality and can be derived when considering a quasi-static deformation from an initial condition (0) to a final condition (1). For convenience, we repeat here the derivation of this relation in the notations of this report and include body forces.

Take that a displacement discontinuity develops over an internal surface Σ contained in an elastic body with volume V, see also Figure B.2.1 . Take that the reference state of zero strain and zero stress are accessible. If the initial stress and strain prior to deformation are σ^0_{ij} and ϵ^0_{ij}, and the rock displacement $\boldsymbol{u}$ is measured from this state, the free elastic energy density in V at condition (1) can be written as

$$F'^1_{el} = \frac{1}{2}\sigma^1_{ij}\epsilon^1_{ij} = \frac{1}{2}\big(\sigma^0_{ij} + \sigma_{ij}\big)\big(\epsilon^0_{ij} + \epsilon_{ij}\big). \tag{B.2.1}$$

σ_{ij} and ϵ_{ij} stand for the changes in the strain and stress with respect to the initial condition(0). The superscripts 0 and 1 refer to the initial and final states. Inserting herein $u_{i,j} = \partial u_i/\partial x_j$, using $\epsilon_{ij} = 1/2(u_{i,j} + u_{j,i})$,

$$F'^1_{el} = \frac{1}{4}\big(\sigma^0_{ij} + \sigma_{ij}\big)\big(\epsilon^0_{ij} + u_{i,j}\big) + \frac{1}{4}\big(\sigma^0_{ij} + \sigma_{ij}\big)\big(\epsilon^0_{ij} + u_{j,i}\big). \tag{B.2.2}$$

or, using the symmetry of σ_{ij},

$$F'^1_{el} = \frac{1}{2}\big(\sigma^0_{ij} + \sigma_{ij}\big)\big(\epsilon^0_{ij} + u_{i,j}\big), \tag{B.2.3}$$

or

$$F'^1_{el} = F'^0_{el} + \frac{1}{2}\big(\sigma^0_{ij} + \sigma_{ij}\big)u_{i,j} + \frac{1}{2}\sigma_{ij}\epsilon^0_{ij}, \tag{B.2.4}$$

[3]The entropy of an elastic body is usually included in specific heat terms when needed. In this case, the strain energy density is equivalent to the free elastic energy density. In the literature, the strain energy function is frequently denoted by the symbol W.

where $F'^0_{el} = \frac{1}{2}\sigma^0_{ij}\epsilon^0_{ij}$. Using $\sigma^1_{ij} = \sigma^0_{ij} + \sigma_{ij}$ and $\sigma_{ij} = c_{ijkl}\epsilon_{kl}$ where c_{ijkl} [Pa] is a fourth order tensor which relates the strain to the stress[4],

$$F'^1_{el} = F'^0_{el} + \frac{1}{2}\sigma^1_{ij}u_{i,j} + \frac{1}{2}c_{ijkl}u_{k,l}\epsilon^0_{ij}. \tag{B.2.5}$$

Using $c_{ijkl} = c_{klij}$, the second term and the third term on the RHS of this expression can be combined. Using $\sigma^0_{kl} = c_{klij}\epsilon^0_{ij}$,

$$F'_{el} = F'^0_{el} + \frac{1}{2}\sigma^1_{ij}u_{i,j} + \frac{1}{2}\sigma^0_{kl}u_{k,l}. \tag{B.2.6}$$

The difference between the elastic energies in the final condition (1) and the initial configuration (0) becomes

$$\Delta F_{el} = \int_V (F'^1_{el} - F'^0_{el})dV \quad = \frac{1}{2}\int_V \big(\sigma^1_{ij} + \sigma^0_{ij}\big)u_{i,j}dV. \tag{B.2.7}$$

According to the equation of motion,

$$\rho\ddot{u}_i = f_i + \sigma_{ij,j}, \tag{B.2.8}$$

where ρ [kg/m^3] is the mass density of the rock and f_i [N/m^3] is the body force per unit volume. Since σ^0_{ij} and σ^1_{ij} are static stress fields, $\sigma_{ij,j} = \partial\sigma_{ij}/\partial x_j = -f_i$. Herewith,

$$\Delta F_{el} = \frac{1}{2}\int_V \big[\big(\sigma^1_{ij} + \sigma^0_{ij}\big)u_i\big]_{,j}dV - \frac{1}{2}\int_V \big(f^1_i + f^0_i\big)u_i dV. \tag{B.2.9}$$

The last term evolves from the body forces. If they are absent, Aki's result is obtained. If the body force is a constant gravitational field, i.e. $f^1_i = f^0_i = \rho g_i$, where g_i is the i^{th} component of the gravitational vector,

$$\Delta F_T = \Delta F_{el} + \Delta F_{grav} = \frac{1}{2}\int_V \big[\big(\sigma^1_{ij} + \sigma^0_{ij}\big)u_i\big)\big]_{,j}dV \quad \text{where} \quad \Delta F_{grav} = \int_V \rho g_i u_i dV. \tag{B.2.10}$$

ΔF_{grav} is the release of gravitational energy when the body is displaced. Regarding the volume V as the interior of the outer surface S and the internal surfaces Σ^- and Σ^+ on both sides of surface Σ of the displacement discontinuity and applying Gauss's divergence theorem, we obtain

$$\Delta F_T = -\frac{1}{2}\int_\Sigma \big(\sigma^1_{ij} + \sigma^0_{ij}\big)[u_i]\nu_j d\Sigma, \tag{B.2.11}$$

under the assumption that on the outer surface S, the displacement is parallel to the surface or zero or the stresses are zero. $[u_i] = u^+_i - u^-_i$ [m] is the i^{th} component of the

[4]This tensor follows from Cauchy's generalisation of Hooke's law. For isotropic media, $c_{ijkl} = \lambda\delta_{ij}\delta_{kl} + \mu(\delta_{ik}\delta_{jl} + \delta_{il}\delta_{jk})$ where λ [Pa] and μ [Pa] are the Lamé constants. The summation convention is used when double indices occur in a term.

discontinuity in the rock displacement $\boldsymbol{u}$ (or slip) at surface Σ. u_i^+ and u_i^- are supposed to take place on the internal surfaces Σ^- and Σ^+ on both sides of surface Σ. Σ^- and Σ^+ are at an incremental distance from Σ. ν_j [-] is the j component of unit vector of surface Σ pointing from Σ^- to Σ^+. In the absence of body forces, this equation is known as the Volterra equation.

The liberated energy $E_T = -\Delta F_T$ supplies the energy to initiate the fracture, the work done on the two surfaces Σ^+ and Σ^- as they grind past each other and the seismic energy which is radiated away from this plane.

If the average of the initial and final stress does not vary strongly over the surface, we can express Eq. (B.2.11) for a tangential slip $[u]$ along a plane surface Σ in terms of the moment tensor $M_0 = \mu \int_\Sigma [u] d\Sigma$ and of the mean shear stress along this plane $\tilde{\tau} = \frac{1}{2}(\tau^0 + \tau^1)$, i.e.

$$E_T = \frac{\tilde{\tau}}{\mu} M_0. \tag{B.2.12}$$

Writing $D = 1/\Sigma \int_\Sigma [u] d\Sigma$ and using now the symbol S for the internal surface Σ, we obtain Eq. (2.2.2) in §2.2, i.e.

$$E_T = \tilde{\tau} D S, \tag{B.2.13}$$

which can be derived from the equations in Udias et al. (2014), §1.5.

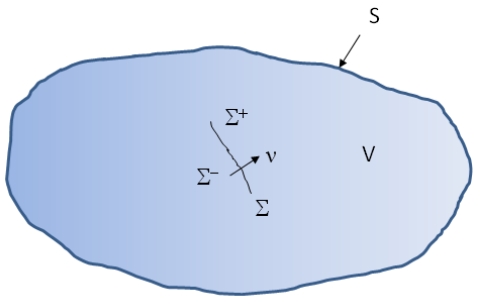

Figure B.2.1 : A finite elastic body with volume V and external surface S and an internal surface Σ which models a buried fault. Across the internal surface Σ displacement discontinuities may arise. The displacement on the Σ^- side of Σ may differ from displacements on the Σ^+ side of Σ. The normal to Σ is $\boldsymbol{\nu}$ which points from Σ^- to Σ^+. The displacement discontinuity is denoted by $[\boldsymbol{u}] = \boldsymbol{u}^+ - \boldsymbol{u}^-$ and where $\boldsymbol{u}$ stands for $\boldsymbol{u}^+ = \boldsymbol{u}|_{\Sigma^+}$ and $\boldsymbol{u}^- = \boldsymbol{u}|_{\Sigma^-}$.

B.2.2 Theory - poro-elastic media

When poro-elastic media are involved, such as the reservoir, the expression for the free energy density of the rock differs from Eq. (B.2.1) and other terms contribute to the total energy release when there is slip. In agreement with Biot (1962), Eq. 3.4, the free energy of an isotropic poro-elastic medium $F'_{el} = F'_{el}(\epsilon_{ik}, \zeta)$ [J/m^3] reads in the notations of this

report as[5]

$$F'_{el} = \frac{1}{2}\big(K + \alpha^2 M\big)\epsilon_{ll}^2 + \mu(\tilde{\epsilon}_{ik})^2 - \alpha M \epsilon_{ll}\zeta + \frac{1}{2}M\zeta^2 \quad \text{where} \quad \tilde{\epsilon}_{ik} = \epsilon_{ik} - \frac{1}{3}\delta_{ik}\epsilon_{ll}. \tag{B.2.14}$$

ζ [m^3/m^3] is the change in fluid volume content per unit volume undeformed rock. The 4 independent poro-elastic constants K, α, M and μ completely determine the poro-elastic behaviour of the rock. K [Pa] is the (drained) bulk modulus of the rock, α [-] is the Biot coefficient or Biot constant, M [Pa] is a poro-elastic constant which is sometimes called the Biot modulus. Since $K + \alpha^2 M$ is equal to the undrained bulk modulus of the rock K_u [Pa], i.e. $K_u = K + \alpha^2 M$, K_u is usually in the expression. μ [Pa] is the shear modulus of the rock. The summation convention is applied to subscripts occurring twice in vector and tensor expressions. A consequence of this notation is that $\epsilon_{ll} = \epsilon_{11} + \epsilon_{22} + \epsilon_{33}$. $\epsilon_{ll} = 1 + \delta V/V_0$ is the volumetric strain of the rock. δV and V_0 are the change in the volume of the rock and the volume of the undeformed rock, respectively.
The pressure change follows from $\delta p \equiv [\partial F'_{el}/\partial\zeta]_\epsilon$. So,

$$\delta p = -\alpha M \epsilon_{ll} + M\zeta. \tag{B.2.15}$$

Vice versa[6],

$$\zeta = \alpha\epsilon_{ll} + \frac{1}{M}\delta p. \tag{B.2.16}$$

[5]Actually, Biot (1962), Eq. 3.4 reads in the notations of this report as

$$F'_{el} = \frac{1}{2}\big(K + \frac{4}{3}\mu + \alpha^2 M\big)\epsilon_{ll}^2 + \frac{1}{2}\mu I_2 - \alpha M\epsilon_{ll}\zeta + \frac{1}{2}M\zeta^2,$$

with

$$I_2 = 4\big(\epsilon_{yz}^2 + \epsilon_{zx}^2 + \epsilon_{xy}^2 - \epsilon_{yy}\epsilon_{zz} - \epsilon_{zz}\epsilon_{xx} - \epsilon_{xx}\epsilon_{yy}\big).$$

We use here the conventions of elasticity theory, i.e. compressive strain and stress are negative. The cartesian coordinate indices (x, y, z) are equivalent notations for the indices (i, j, k). In compact notation, I_2 reads as

$$I_2 = 2\big(\epsilon_{ik}^2 - \epsilon_{ll}^2\big).$$

ϵ_{ik}^2 is the sum of the squares of all strain components and ϵ_{ll}^2 is the square of the sum of the diagonal strain components.

[6]In other terms ζ relates to a change in the porosity of the rock $\delta\phi$ [m^3/m^3] and a change in the fluid pressure δp [Pa] in the rock as

$$\zeta = \delta\phi + \frac{\phi_0}{K_w}\delta p.$$

K_w [Pa] is the bulk modulus of the rock and ϕ_0 [m^3/m^3] is the porosity of the undeformed rock. For $\zeta = 0$, $\delta p = -K_w\delta\phi/\phi_0$. From Eq. (B.2.15), $\delta p = -\alpha M\epsilon_{ll}$. Combining both expressions, we have $\delta\phi = \phi_0\alpha M/K_w\epsilon_{ll}$. From a general relation between the poro-elastic constants,

$$M = \frac{1}{K/K_s(1/K - 1/K_s) + \phi_0(1/K_w - 1/K_s)},$$

we have for a compressible fluid compared to the rock $M \approx K_w/\phi_0$ and $\delta\phi \approx \alpha\epsilon_{ll}$. For incompressible grains, $K/K_s \to 0$ and $\alpha = 1 - K/K_s \to 1$, we obtain $\delta\phi/\phi_0 = \epsilon_{ll}$, as expected.

The components of the stress tensor follow from $\sigma_{ik} \equiv [\partial F'_{el}/\partial \epsilon_{ik}]_\zeta$. Using Eq. (B.2.14),

$$\sigma_{ik} = \big(K + \alpha^2 M\big)\epsilon_{ll}\delta_{ik} + 2\mu\big(\epsilon_{ik} - \frac{1}{3}\delta_{ik}\epsilon_{ll}\big) - \alpha M\zeta\delta_{ik}. \tag{B.2.17}$$

It depends on the fluid pressure changes and fluid motions around the fault during rupture which energy will be released. In the following, we consider first the special or undrained case for which the fluid displacement ζ during fault slip is zero.

We compare again the initial condition (0) and the final condition (1) taking that the reference state of zero strain, zero stress and zero fluid displacement are accessible. We only consider third term in Eq. (B.2.14), recognising that the first two terms in Eq. (B.2.14) lead to the same result as given in Eq. (B.2.7) and that the last term in Eq. (B.2.14) for $\zeta^1 = \zeta^0$ can be disregarded. Herewith, Eq. (B.2.6) can be extended as

$$F'_{el} = F'^0_{el} + \frac{1}{2}\sigma^1_{ij}u_{i,j} + \frac{1}{2}\sigma^0_{kl}u_{k,l} + \alpha M\big(\epsilon^1_{ll} - \epsilon^0_{ll}\big)\zeta^0, \tag{B.2.18}$$

or, using $\delta p = -\alpha M\epsilon_{ll}$ and $\delta p^1 - \delta p^0 = p^1 - p^0$,

$$F'_{el} = F'^0_{el} + \frac{1}{2}\sigma^1_{ij}u_{i,j} + \frac{1}{2}\sigma^0_{kl}u_{k,l} + (p^1 - p^0)\zeta^0. \tag{B.2.19}$$

The last term corresponds to the energy required to increase the pore fluid pressure as a result of the compaction associated with the slip motion.

The second case, we consider is one of constant pore pressure at the initial and final conditions. According to Eq. (B.2.16), we have in this case $\zeta = \alpha\epsilon_{ll}$. Substituting this for ζ into the expression for the free elastic energy, Eq. (B.2.14), we obtain

$$F'_{el} = \frac{1}{2}K\epsilon^2_{ll} + \mu(\tilde{\epsilon}_{ik})^2. \tag{B.2.20}$$

For isotropic rock, this expression for the free elastic energy density is essentially the same as given by Eq. (B.2.1). In the case of a constant fluid pressure, energy stored in the fluid takes no part in the release of energy by slip.

If the pore fluid is a gas with a relatively high compressibility, the Biot modulus M is small compared to K and also in the undrained condition of $\zeta = 0$, the energy contributions due to the fluid and the fluid-rock interactions are small compared to the gravitational and elastic contributions.

B.2.3 Set up of the calculations

The domain and boundary conditions are illustrated in Figure B.2.2 . The input parameters are given in Table B.2.1 . In the following calculations, the gravitational force is used

to generate the vertical and horizontal field stresses. We assume that the deformation energy, added to the rock mass by the gravitational force over geological time, is still in the rock in the form of elastic energy before the gas production and reservoir compaction takes place.
The boundary conditions at the basement and on both the sides of the domain of the calculation are of roller type to ensure that no work is done to the surrounding world when the compaction in the reservoir takes place.

We consider two cases. For the first case, the horizontal stress follows from the vertical stress generated by the weight of the rock and the Poisson ratio of the rock, i.e. $\sigma_h = \nu/(1-\nu)\sigma_v$ and $\sigma_v = -\rho g z$. $\rho = 2200$ kg/m^3 is the mass density of the rock, $g = 9.81$ m/s^2 is the gravitational constant and z is the the z-coordinate. z is zero at the surface. No other horizontal stress has been added. Using $\nu = 0.25$, the horizontal stress is one third of the vertical stress. At the mean reservoir depth of 3 km, $\sigma_v \sim 66$ MPa and $\sigma_h \sim 22$ MPa. This horizontal stress is low compared to the observed ones. For the second case, the horizontal field stress at the reservoir level is about 42 MPa. The rock properties are given in Table B.0.1 .

For the calculations, we have introduced a thin so-called weak zone along the reservoir offset to simulate fault failure, see Figure B.2.2 . This zone including parts of the fault where the reservoir is juxtaposed against the overburden and the underburden. The weak zone has a length $l = (h_{res} + t_{res})/\cos(\delta)$. The gravitational and elastic energy of the rock in the domain are calculated for two conditions. In the first condition, the poro-elastic constants of the rock in the weak zone are the same as in the surrounding reservoir rock. In the second condition, the Young modulus of the rock in the weak zone E_w [Pa] is reduced to a value $E_w/E = 10^{-5}$ times the original value while the bulk modulus K remains the same. The Poisson ratio in the weak zone ν_w becomes

$$\nu_w = \frac{1}{2}\big(1 - \frac{E_w}{3K}\big). \tag{B.2.21}$$

For $E_w/E \to 0$, $\nu_w \to 0.5$. The a-seismic or seismic failure of the fault is mimicked by liquifying the porous rock in the weak zone. The weak zone is allowed to take up all the shear strain while the volumetric strain in the weak zone remains practically the same.

To generate a horizontal stress around the fault in the reservoir of about 40 MPa, we have extended the domain by 50% in the horizontal direction at one side of the original formation with rock with the same density ρ_s and bulk modulus K but with a lower Young modulus and thus a higher Poisson ratio[7]. Under gravitation, this rock pushes to the original formation leading to an increase of the horizontal stress at reservoir depth. Still, no work is done to the surrounding world since this rock is also inside the roller

[7]The elastic properties of this rock at the side of the orignal formation are $K = 6.7$ GPa, $E = 2$ GPa and $\nu = 0.45$. Between 0.5 and 5 km depth, both field stresses increase almost linearly with depth around the fault.

type boundary conditions of the domain of calculation. The reservoir pressure remains constant. This means that if the overall reservoir compaction slightly increases by fault failure and the pore volume decreases, some pore fluid is expelled from the domain.

The slip D [m] along the fault is calculated from displacement differences between corresponding locations on the right and the left side of the weak zone, using the so-called linear extrusion functions[8]. Displacement differences normal to the fault are small compared to displacement differences parallel to the fault, as expected when keeping the bulk modulus K of the rock in the weak zone high and constant.

The liberated gravitational and elastic energy by fault failure has been calculated by two methods. Firstly, by subtracting the total gravitational and elastic energy in the domain of calculation at condition (1) after failure from the value at the initial condition (0). Since both values are practically the same, a fine grid is required. We have repeated a few calculations for various fine grids, two widths of the weak zone, i.e. one of 0.5 m and another of 1 m and several widths of the domains, to be sure that numerical errors can be disregarded. A detail of the fine grid we used is shown in Figure B.2.3 .
Secondly, we have calculated the liberated gravitational and elastic energy from Eq. (B.2.11). The product of the slip D parallel to the fault after failure and the mean shear stress $\tilde{\tau}$ along the fault before failure is integrated over the length of the weak zone. For $E_w/E = 10^{-5}$, the contribution of the shear stress over the fault after failure τ^1 can be disregarded. So, it is sufficient to integrate the product $\tau^0 \times D/2$ over the length of the fault.
For large liberated energies, e.g. for fault III-100, results correspond well, i.e. within $\pm 10\%$. However, for smaller liberated energies the correspondence is not satisfactory due to numerical inaccuracies which become apparent when subtracting the gravitational and elastic energy of both conditions. Tables B.2.2 and B.2.3 show the results using the second method.

[8]The extrusion function maps a variable from one boundary on another boundary, in this case by a linear projection.

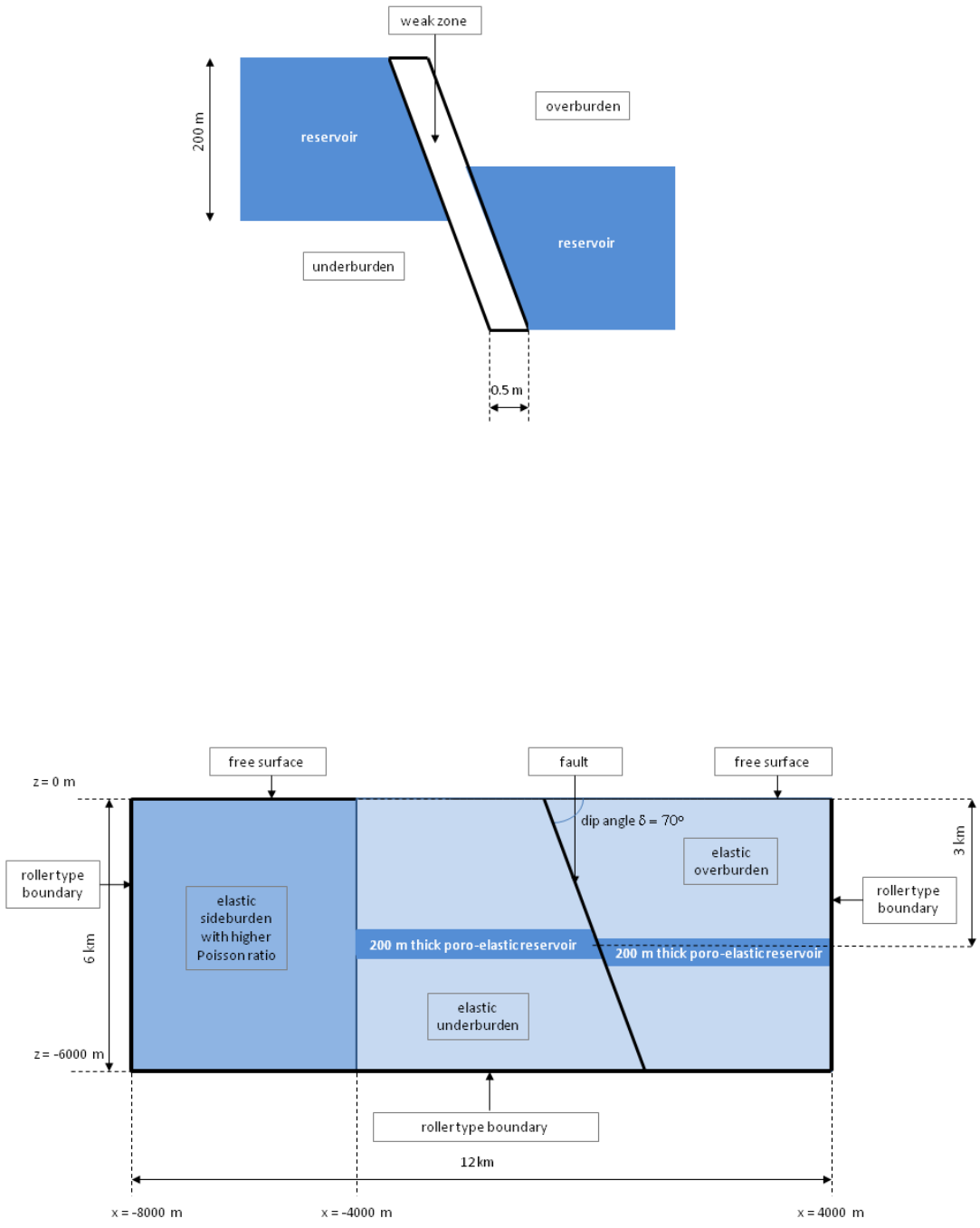

Figure B.2.2 : Weak zone (top) and the domain and boundary conditions (bottom) of a calculation for fault III-100 with a fault dip angle $\delta = 70°$. For clarity, the weak zone is not shown at scale. The gravitational force is used to generate the vertical and horizontal stresses. The side burden is used to increase the horizontal stress in the reservoir to about $\sigma_h = 40$ MPa.

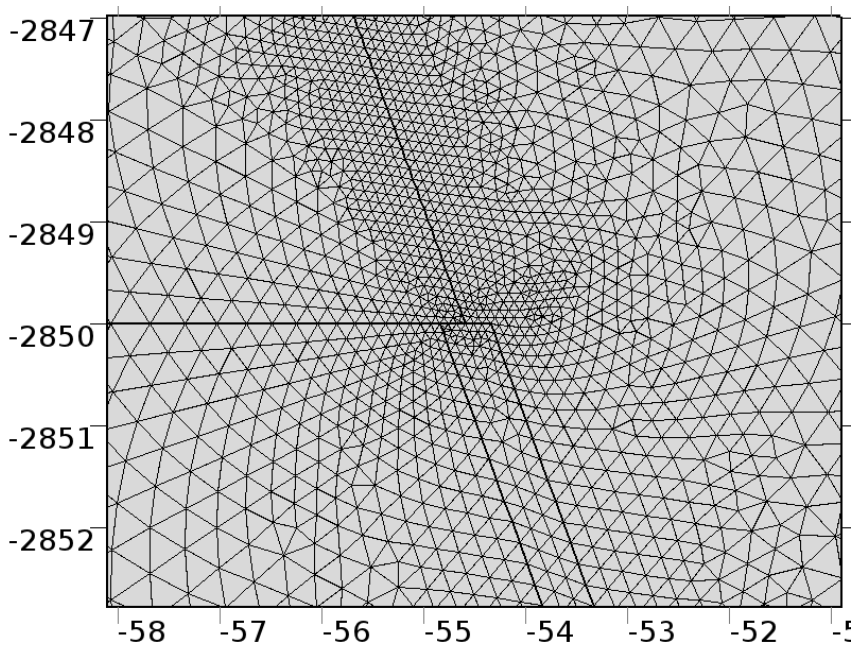

Figure B.2.3 : Detail of mesh around the top of the weak zone along the fault used for the calculations of the gravitational and elastic energies for fault III-100, see §B.2. The width of the weak zone is 0.5 m. The width of the entire domain is 8 km. In the whole domain, there are 136290 elements and 8100 boundary elements. A two times finer grid in the weak zone gives the same results.

B.2.4 Results

The results for the two cases with $\sigma_h \sim 22$ and $\sigma_h \sim 42$ MPa, are shown in Tables B.2.2 and B.2.3 . Figures B.2.4 and B.2.5 show for the fault III-100 for the first case with $\sigma_h \sim$ 22 MPa, the vertical and horizontal displacements, the slip and the stress on the fault before and after failure. Qualitatively similar figures are obtained for the second case[9]. The shear stress along the fault drops to a negligible value after failure. For the first case, the shear stress is significantly larger than for the second case. The latter one is shown in Figure B.1.6 . The profile of the normal effective stress somewhat smears out over the fault plane by failure.

Part of the gravitational and elastic energy which can be released originates from the imbalance of the field stresses along the fault and is already available before compaction takes place[10]. For faults II and III with dip angles of 70° and 80°, the released energy

[9]We show here the figures for the first case because they can be easily compared with results from other geomechanical simulators.

[10]Hence, the change in the energy of the reservoir and surrounding rock is not proportional to the square of the reservoir compaction strain or hange in the reservoir pressure.

strongly increases with the fault dip and with the imbalance between the vertical and horizontal stresses, see Tables B.2.2 and Tables B.2.3 . For the vertical fault an increasing horizontal stress leads to a somewhat larger energy release.
The small amount of liberated energy for fault I-0 in the second case is a result of the field stresses. The principle field stresses around the fault, as set up by the forces from the side burden, are not perfectly parallel and perpendicular to the vertical fault.

The effect of a partial failure of fault can be estimated by representing it by a smaller reduction of the Young modulus in the weak zone. For fault III-100 with a dip angle of 70° and a throw of 100 m and for $E_w/E = 10^{-5}$, 10^{-4}, 10^{-3}, 10^{-2} and 10^{-1}, we obtain E'''_T = 2.2, 2.1, 2.0, 0.8 and 0.1 GJ/m. So, a substantial weakening of the rock along the fault is needed, i.e. $E_w/E < 0.1$, to release a significant amount of gravitational and elastic energy.

The liberated energy roughly increases in proportion to the reduction of the reservoir pressure and the compaction, i.e. $E'''_T \approx E'''_{T,0} - c_{E,p}(p_1 - p_0)$ where $E_{T,0}$ [J] and $c_{E,p}$ [J/Pa] are constants depending on fault geometry and field stresses. At a reservoir pressure drop of 12.5 MPa, for $\sigma_v = 66$ MPa and $\sigma_h = 22$ MPa and for faults II-50 and III-100, E'''_T = 0.40 and 1.6 GJ/m, respectively. For $\sigma_v = 66$ MPa, $\sigma_h = 42$ MPa and for faults II-50 and III-100 these values are $E'''_T = 0.51$ and 1.0 GJ/m, respectively.

For fault III-100, we have calculated the effect of the Poisson ratio of the reservoir rock and the rest of the formation. Keeping the uniaxial compaction coefficient $C_m = 8.3\ 10^{-6}$ bar^{-1} the same, using $\nu = 0.2$, $E = 10.8$ GPa (and herewith $K = 5.0$ GPa and $\alpha = 0.72$), $E'''_T = 1.6$ GPa instead of 2.1 GPa for similar field stresses. For a field stress around the fault of $\sigma_v = 63$ MPa and $\sigma_h = 48$ MPa, the release of gravitational and elastic energy reduces to $E'''_T = 0.8$ GPa.

From the present results, we conclude that the maximum energy released by a complete failure of the fault in the reservoir is of the order of 1 GJ/m. Similar values have been calculated by van Peter den Bogert using Geomec (Diana^{TM}). Part of the energy release follows from a small overall subsidence. This can be easily understood as follows. A failed fault inside a rock increases the mean or apparent Poisson ratio of this rock. Under gravitational forces this lead to more compaction. This amount is about two times more than a small, counter-intuitive, overall increase of the deformation energy in the rock. Although stress relaxes close to the fault it increases farther away from the fault by a small additional compaction.

Considering future production scenarios for the Groningen field, we should recognise that a part of the stress over the non-vertical faults follows from the imbalance between the horizontal and vertical field stresses. In the over- and underburden, these stresses could be released by a rupture process in the reservoir. This is unlikely to happen in the overburden which consists of plastic Zechstein evaporites. However, we cannot rule it out

for the underburden at this stage. Pressure diffusion into the underburden over the gas production time lead to an increase of the effective normal stress on the fault in the underburden. If this process has been significant and if related compaction in this part of the underburden can be disregarded, this process could be beneficial to arrest seismic ruptures in the underburden. Repressurising the reservoir could partly undo this positive effect[11].

[11]This effect depends on the shift and increase of the Mohr stress circle when compared to the Mohr-Coulomb failure criterion.
Taking that the interface between the bottom of the Rotliegend reservoir and the eroded Carboniferous underburden is relatively sharp, the pressure diffusion distance into the underburden can be estimated as follows. The pressure diffusion coefficient in a permeable rock is given by $D_p = kK_f/(\phi\mu)$ [m^2/s] where ϕ [-] and k [m^2] are the porosity and the permeability of the rock, μ [Pa.s] and K_f [Pa] are the typical dynamic viscosity and bulk modulus of the gas at the conditions of interest, see e.g. Dake (1978), §5.1. Using typical values for a organic-rich shale of $\phi = 0.1$ and $k = 10$ nD, and for natural gas at 20 MPa, $\mu = 2\ 10^{-5}$ Pa.s, $K_f = 0.02$ GPa, we obtain $D_p \sim 0.7$ m^2/s. Over a period of 30 years ($\sim 10^9$ s), the distance over which the pressure diffuses into the underburden is $L \sim 10$ m.
This distance could be comparable to the so-called breakdown length of the rupture front or the dimension of the nucleation area for tremors of magnitudes in the range observed. Both are of order $\mu/\Delta\tau_b D_c$ where μ [Pa] is shear modulus, $\Delta\tau_b = \tau_p - \tau_r$ [Pa] is the breakdown strength and D_c [m] is the so-called breakdown displacement, see Ohnaka (2013), §6.4. τ_p is the peak shear strength in the rupture front. τ_r is the residual shear strength in this front when the fault ruptures.
Of course, the permeability of the Carboniferous underburden along a fault zone can be much different. This depends on the fracture networks in this zone which can be non-filled or filled by precipitated minerals from hydrothermal fluids in the past.

Table B.2.1 : Input parameters for modelling. They are the same as shown in Table B.0.1 (c.) means calculated from primary input.

Property	Symbol	Unit	Value
field data			
- gravitational constant	g	m/s^2	9.81
- initial reservoir pressure	p_0	MPa	35
- final reservoir pressure	p_1	MPa	10
rock properties			
- bulk density	ρ_s	kg/m^3	2200
- grain modulus	K_s	GPa	22
- Poisson ratio	ν	-	0.25
- Young modulus	E	GPa	10
- shear modulus (c.)	μ	GPa	4
- bulk modulus (c.)	K	GPa	6.7
- Biot constant (c.)	α	-	0.7
- uniaxial compaction coefficient (c.)	C_m	1/bar	8.3 10^{-6}
- uniaxial compaction modulus (c.)	H	GPa	12.0
- porosity	ϕ	-	0.2
- gas bulk modulus (20 MPa, 100 °C)	K_f	GPa	0.02
- Biot modulus (c.)	M	GPa	0.1
reservoir geometry			
- reservoir thickness	h_{res}	m	200
- reservoir throw	t_{res}	m	0, 50, 100
- depth of the centre of the reservoir	z_{res}	km	3
- fault dip angle	δ	degree	90, 80, 70

Table B.2.2 : Liberated gravitational and elastic energy E'''_T per unit length fault strike in the reservoir and surrounding rock when the fault fails by a-seismic or seismic slip before and after reservoir compaction. Reservoir compaction follows from 25 MPa pressure drop in the reservoir. The field stresses at the mean depth of the reservoir, i.e. at 3 km depth, are $\sigma_v = 66$ MPa and $\sigma_h = 22$ MPa.

Property	Symbol	Unit	fault	fault	fault
reservoir pressure before compaction	p_0	MPa	35		
reservoir pressure after compaction	p_1	MPa	10		
.....	.....	.....	.....	.....	.....
			I-0	I-50	I-100
dip angle	δ	degree	90	90	90
throw	t_{res}	m	0	50	100
liberated energy before compaction	E'''_T	GJ/m	0	0	0
liberated energy after compaction	E'''_T	GJ/m	0	0.029	0.088
.....	.....	.....	.....	.....	.....
			II-0	II-50	II-100
dip angle	δ	degree	80	80	80
throw	t_{res}	m	0	50	100
liberated energy before compaction	E'''_T	GJ/m	0.16	0.24	0.35
liberated energy after compaction	E'''_T	GJ/m	0.26	0.59	0.95
....	.....	.....	.....	.....	.....
			III-0	III-50	III-100
dip angle	δ	degree	70	70	70
throw	t_{res}	m	0	50	100
liberated energy before compaction	E'''_T	GJ/m	0.49	0.77	1.1
liberated energy after compaction	E'''_T	GJ/m	0.81	1.5	2.2

Table B.2.3 : Liberated gravitational and elastic energy E_T''' per unit length fault strike in the reservoir and surrounding rock when the fault fails by a-seismic or seismic slip before and after reservoir compaction. Reservoir compaction follows from 25 MPa pressure drop in the reservoir. The field stresses at the mean depth of the reservoir, i.e. at 3 km depth, are $\sigma_v = 66$ MPa and $\sigma_h = 42$ MPa. The small amount of liberated energy of fault I-0 follows from the field stresses set up by the side burden, see text.

Property	Symbol	Unit	fault	fault	fault
reservoir pressure before compaction	p_0	MPa	35		
reservoir pressure after compaction	p_1	MPa	10		
.....	.....	.....	.....	.....	.....
			I-0	I-50	I-100
dip angle	δ	degree	90	90	90
throw	t_{res}	m	0	50	100
liberated energy before compaction	E_T'''	GJ/m	0	0	0
liberated energy after compaction	E_T'''	GJ/m	0.08	0.27	0.51
.....	.....	.....	.....	.....	.....
			II-0	II-50	II-100
dip angle	δ	degree	80	80	80
throw	t_{res}	m	0	50	100
liberated energy before compaction	E_T'''	GJ/m	0.22	0.33	0.47
liberated energy after compaction	E_T'''	GJ/m	0.32	0.71	1.1
....	.....	.....	.....	.....	.....
			III-0	III-50	III-100
dip angle	δ	degree	70	70	70
throw	t_{res}	m	0	50	100
liberated energy before compaction	E_T'''	GJ/m	0.30	0.47	0.68
liberated energy after compaction	E_T'''	GJ/m	0.52	1.0	1.3

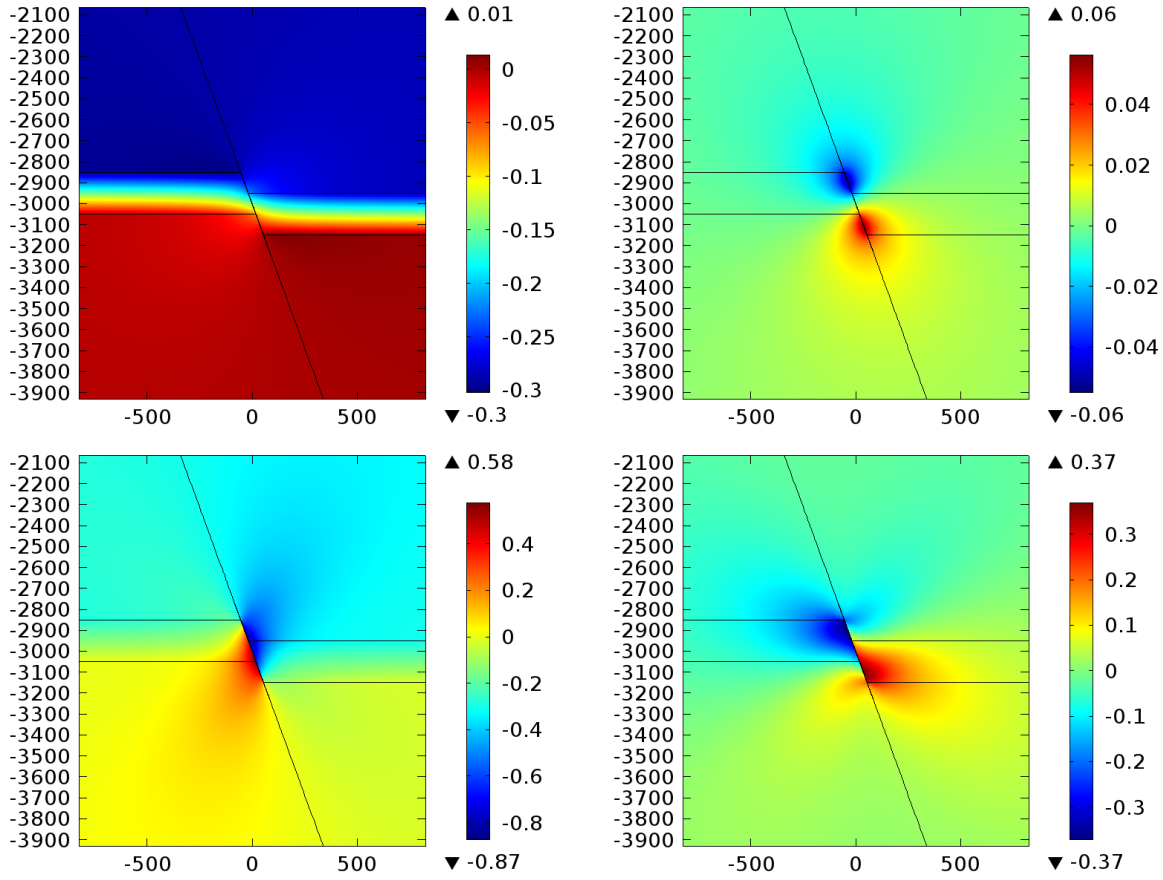

Figure B.2.4 : Vertical (left) and horizontal (right) rock displacements around the reservoir offset by compaction before failure (top) and after failure (bottom) for fault III-100. The field stresses at the mean depth of the reservoir, i.e. at 3 km depth, are $\sigma_v = 66$ MPa and $\sigma_h = 22$ MPa.

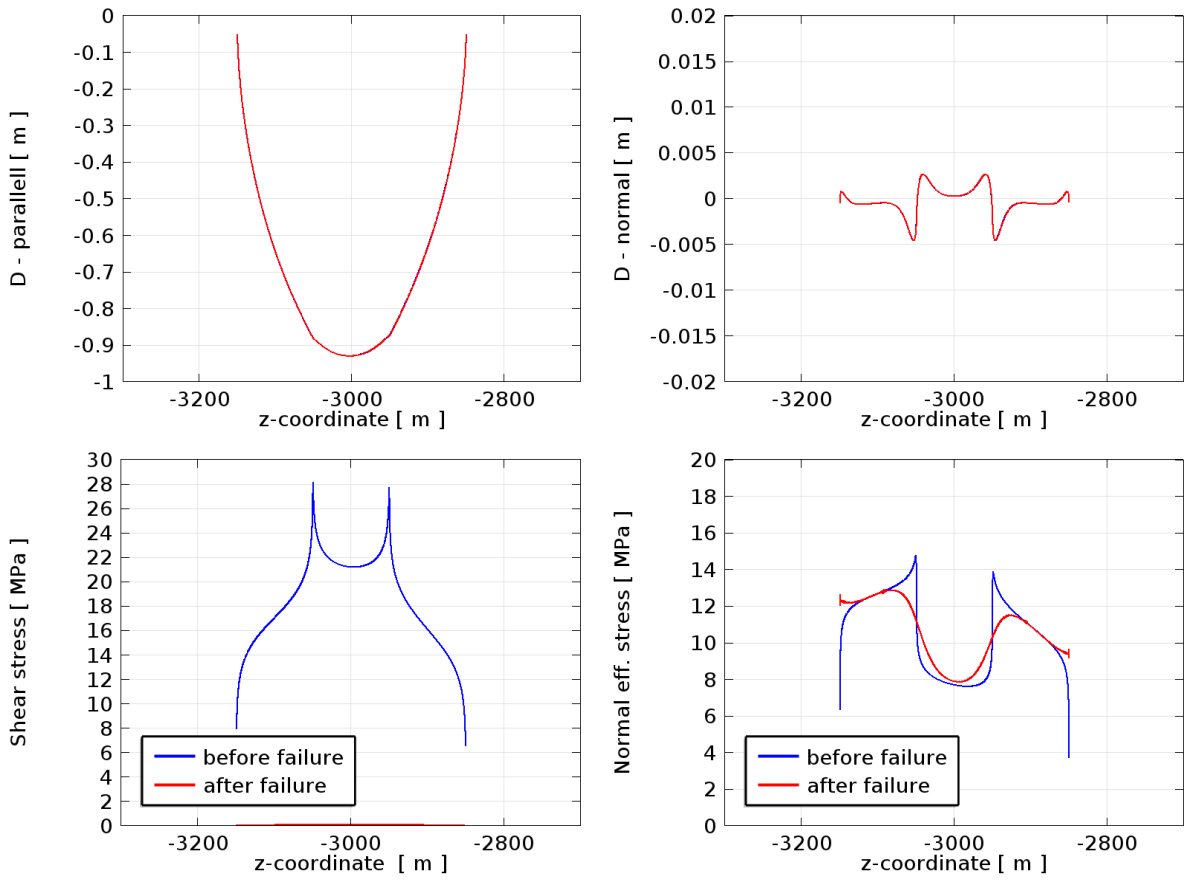

Figure B.2.5 : Top: the slip over the fault plane in terms of the difference between the displacement of corresponding locations at the right side and the left side of the weak zone for fault III-100. Top left: slip parallel to the fault plane. Top right: slip normal to the fault plane. The normal component of the slip is small compared to the parallel component, as expected.
Bottom: shear stress τ (left) and normal effective stress in relation to rock failure σ_n'' (right) along the fault plane before (blue) and after failure (red) for fault III-100. The field stresses at the mean depth of the reservoir, i.e. at 3 km depth, are $\sigma_v = 66$ MPa and $\sigma_h = 22$ MPa.

Appendix B.3 Stress relaxation parameter c_{M0}

B.3.1 Typical constants for the stress relaxation parameter c_{M0}

According to Appendix C, Figures C.1.6 - C.1.9 , a typical fault segment of the identified faults in the Groningen field has a throw of about 20 - 80 m and a dip of 70 - 80 degrees and length of about 0.5 - 2 km. Assuming a horizontal field stress of at least 40 MPa, we expect from Table B.2.3 that the maximum typical energy per unit length fault which could be liberated by a complete failure of the fault in the reservoir after compaction, is of the order $E_T''' \sim 0.5$ GJ/m.

Part of the energy released originates from the imbalance in the field stresses. The other part originates from the stress induced by reservoir compaction and this amount increases roughly linearly with the pressure drop in the reservoir. Using $E_T''' \sim 0.5$ GJ/m, the induced stress increases with $c_{E,p} \sim 0.02$ GJ/m/MPa. In the model, Eqs. (2.1.1) and (2.1.2) relate the pressure drop and the effective vertical stress away from the faults to a change in the mean shear stress on the faults $\bar{\tau}$ by the geometric constant c_{σ_v} and the Biot constant α. Using a value for $c_{\sigma_v} = 0.5$ and $\alpha = 0.7$, see §B.1, the energy which could be liberated relates to the mean shear stress on the faults as

$$E_T''' = E_{T,0}''' + c_E \bar{\tau}. \tag{B.3.1}$$

The constant $c_E = c_{E,p}/(\alpha c_{\sigma_v})$ has a typical value of $c_E \sim 0.06$ GJ/m/MPa or in other units $c_E \sim 60$ m^2.

B.3.2 Reduction of the mean shear stress

The reduction of the mean shear stress over all faults in the region of interest, $\delta\bar{\tau}$ by a tremor with seismic moment M_0 also follows from the following energy balance. Suppose that the energy released by a tremor E_T is small compared to the gravitational and elastic energy in the region of interest which could be librated by fault failure, E [J]. Take that E can be expressed as a function of the mean shear stress along the faults, i.e. $E = E(\bar{\tau})$. In good approximation,

$$E^0 - E^1 \approx E' \delta\bar{\tau}, \tag{B.3.2}$$

where E^0 and E^1 are the gravitational and elastic energy in the region before and after the tremor and $E' = dE/d\bar{\tau}$. Vice versa, using $E_T = E^0 - E^1$,

$$\delta\bar{\tau} = \frac{E_T}{E'}. \tag{B.3.3}$$

Using the relation between the seismic moment and the liberated gravitational and elastic energy, Eq. (2.2.3), i.e. $E_T = \tilde{\tau}/\mu M_0$ and combining this with Eq. (B.3.3), we have

$$\delta\bar{\tau} = \frac{\tilde{\tau}}{\mu E'} M_0. \tag{B.3.4}$$

If $\tilde{\tau} \propto \bar{\tau}$, we see immediately that $\delta\bar{\tau} \propto M_0$ only if $E \propto \bar{\tau}^2$ and herewith $E' \propto \bar{\tau}$. The remaining tasks are to derive

- an estimate for the mean shear stress during rupture $\tilde{\tau}$.
- an estimate for the potential gravitational and elastic energy in the region of interest which can be liberated as a function of the mean shear stress on the faults $\bar{\tau}$, i.e. $E = E(\bar{\tau})$.

A first estimate for a typical reduction of the shear stress on the faults during rupture would be of the order 1 MPa. This value is supported by the analysis of seismic signals by Kraaijpoel and Dost (2013) and an estimate of the seismic efficiency by McGarr (1999), see §2.2.1. For such small stress drops, $\tilde{\tau} \sim \bar{\tau}$.
However, a larger shear stress drop cannot be excluded at this stage. According to Udias et al. (2014), the seismic efficiency can be larger for shallow tectonic earthquakes or for brittle failure. Further, a larger value for the stress drop of 3 MPa is used by to predict ground motions from the tremors in the Groningen area, see Bommer et al. (2015). Finally, small but significant local reductions of normal forces on the fault during rupture can be expected from geomechanical modelling, see §B.1. But, in both cases of a large and a small stress drop, it can be expected that $\tilde{\tau} \propto \bar{\tau}$.

The gravitational and elastic energy that is released in the region of interest by a single tremor, $E^0 - E^1$ relates to the gravitional and elastic energy loss per unit meter fault E_T''' as

$$E_T = LE_T''' . \tag{B.3.5}$$

L [m] is the length of the rupture plane along fault strike. For a complete failure of the fault $\tilde{\tau} \sim \bar{\tau}^0$. In this case, according §B.3 and using Eq. (B.3.1),

$$E'(\bar{\tau}) \equiv \frac{dE}{d\bar{\tau}} \sim L\frac{dE_T'''}{d\bar{\tau}} = Lc_E. \tag{B.3.6}$$

where c_E is approximately constant with a typical value $c_E \sim 60$ m^2 for the faults of interest. E' [m^3] is proportional to $\bar{\tau}$ if L [m] would be proportional to $\bar{\tau}$. Using Eq. (B.3.6), we recast Eq. (B.3.4) as

$$\delta\bar{\tau} = \frac{\tilde{\tau}}{\mu L c_E} M_0, \tag{B.3.7}$$

or, after inserting $\tilde{\tau} = \bar{\tau}^0/2$ for a complete failure of the fault,

$$\delta\bar{\tau} = \frac{\bar{\tau}^0}{2\mu L c_E} M_0. \tag{B.3.8}$$

For the largest tremor with seismic moment $M_{0,max}$, $\delta\bar{\tau} = \bar{\tau}^0/2$ and $L = L_f$. $L_f =$

$c_f S_{area}/D_f$ is the total fault length in the region of interest. D_f [m] is the mean fault distance in this region and c_f [-] is a geometric constant depending on the direction of the faults. S_{area} [m^2] is the area of this region. Inserting this hypothetical case into Eq. (B.3.8),

$$M_{0,max} = 2\mu L_f c_E. \tag{B.3.9}$$

As an example, $L_f \sim 160$ km for a region with a radius of 5 km and a mean fault distance $D_f = 1$ km, using $c_f = 2$. Herewith, $M_{0,max} \sim 8\ 10^{16}$ J.

On the other hand, from Eq. (2.2.1),

$$M_{0,max} = \mu[DS]_{max} = \mu L_f h_{res}|\delta h_{res}|. \tag{B.3.10}$$

Using $S_{max} = L_f h_{res}$ as the maximum fault surface which could rupture in the region of interest and $D_{max} = |\delta h_{res}|$ as the maximum mean slip along the faults, $M_{0,max} = 8\ 10^{16}$ J for $h_{res} = 200$ m and $|\delta h_{res}| = 0.3$ m. We obtain the same result since c_E is about equal to $h_{res}|\delta h_{res}|$.

Inserting $\delta\bar{\tau}^0_{max} = c_{M0} M_{0,max}$, $\delta\bar{\tau}^0_{max} = \bar{\tau}^0$ and $L = L_f$ into Eq. (B.3.8), we obtain

$$c_{M0} = \frac{\bar{\tau}^0}{\mu L_f c_E}. \tag{B.3.11}$$

Inserting herein $L_f = 160$ km, $c_E = 60$ m^2, $\mu = 4$ GPa and $\bar{\tau}^0/2 = 4$ MPa, we obtain $c_{M0} = 2\ 10^{-10}$ Pa/J.

According to Eq. (B.3.11), $c_{M0} \propto 1/L_f \propto 1/R^2_{area}$. In general, c_{M0} is larger for smaller regions. c_{M0} is also larger for a lower fault density or for a lower density of faults which could fail seismically and for a smaller stress reduction over the fault during rupture. In the latter case, the constant c_E has a lower value.

Appendix C

Reservoir and fault data

Appendix C.1 Groningen field

The $\sim$ 40 x 40 km Groningen field is situated on the Groningen Block, east of the Lauwersee Through. The field has numerous faults with various reservoir offsets and fault dips. At the Rotliegend level, they mainly trend NW-SE, see NAM (2013). The faults are limited in vertical extend. Most of them don't continue through the sealing Zechstein evaporites on top of the reservoir. The Rotliegend reservoir block from the early Permian could be seen as a regional high compared to surrounding deeper Rotliegend formations. The reservoir thickness varies gradually from about 100 m in the south-east to about 300 m in the north-west and the reservoir compaction has varied over the period 1964 - 2008 from 0.15 m in the south east of the field to about 0.25 m in the center of the field. The Rotliegend sandstone contains a large number of aeolian and fluvial sand layers of about 0.5 - 1 m thickness each. The porosity varies from about 0.1 along the boundary of the field to about 0.25 in the center.

The mean reservoir depth is about 3 km. The vertical stress about 65 MPa taking a mean mass density of the overburden of $\sim$ 2.2 kg/m^3. The mean horizontal stress at reservoir depth is usually in the range 45 - 60 MPa but could be as low as about 40 MPa, according to van Eijs and Valencia (2014).

The bulk rock densities of the Slochteren reservoir, the Carboniferous underburden and most of the overburden rock are in the range 2150 - 2300 kg/m^3. The Poisson ratio's of these rocks are supposed to be in the range 0.2 - 0.3. The bulk rock densities of the Halite and Anhydrite in the Zechstein caprock are about 2100 and 2900 kg/m^3, respectively. The Poisson ratio's of these rocks are supposed to be 0.35 and 0.25, respectively. The sealing Zechstein formation of evaporites is about 1 km thick.
The Poisson ratio's of reservoir rock from three wells (EKL-12, KPD-12 and ZPD-12) vary between 0.1 - 0.3 and increase somewhat with the porosity. Most values are between 0.1 and 0.25. For a typical porosity of 0.2, the mean value of the Poisson ratio is about 0.2. The Young modulus of the reservoir rock decreases with porosity and varies between

5 and 40 GPa. For a typical porosity of 0.2, the mean Young modulus is about 10 GPa.

The mean uniaxial compression coefficient C_m is of the order 10^{-4} MPa^{-1}. According to NAM (2013), Figures 4.4 and 4.6, the first cycle uniaxial compaction coefficient of core plugs from the Rotliegend sandstone reservoir varies in the range $C_m = 0.5$ - $3\ 10^{-4}$ MPa^{-1}. The second and following cycle values are about a factor two lower. The lower values are for a porosity $\phi = 0.1$. The higher values are for a porosity $\phi = 0.25$. For $\phi = 0.2$, $C_m \sim 1.5\ 10^{-4}$ MPa^{-1}. The apparent C_m values derived from the subsidence data are about a factor 2 smaller, similar to the second cycle values in the laboratory. The apparent values correspond with the general observation that the mechanical Young modulus is roughly two times lower than the acoustic Young modulus related to the sound velocity in the Rotliegend. This value is roughly 20 GPa.

There are several reasons for the difference between the apparent values for C_m in the field and the first cycle laboratory values. One reason is that part of the observed compaction in the laboratory is non-elastic or plastic. This has been shown by recent extensive compaction measurements on a comparable Rotliegend sandstone from the Moddergat field, somewhat north-west of the Groningen field, see Hol et al. (2015). Roughly half of it is due to elastic deformation. The plastic contribution to the deformation decreases with increasing effective stress. The elastic part of the stress path coefficient is comparable with one which we would obtain from the elastic parameters used. Whether part of the non-elastic response is due to core damage at the grain scale when retrieving it from reservoir is still to be sorted out. Since the grains in the rock are not very well cemented, unloading the rock may have an effect on the bulk modulus and/or the Poisson ratio of the rock. Both properties have an effect on the uniaxial compression coefficient. Further, we note that not all the experiments on the reservoir rock have been performed under zero radial strain.

We expect that the effect of reservoir pressure gradients on the mechanical load on the reservoir rock is moderate. The pressure drop was within a few MPa the same over the whole field over a long period and possible pressure gradients can relax over a distance of a few km in a year time[1].

Figure C.1.1 shows a number of the faults in the Groningen field and the circles that bound the regions of interest. The coordinates of the centers of these regions are given in Table 3.3.1 . The data originates from the NAM. It has been derived from seismic data

[1]The gas is extracted from the reservoir at a significant number of gas production clusters distributed over the field. The pressure diffusion coefficient in a permeable rock is given by $D_p = kK_f/(\phi\mu)$ [m^2/s] where ϕ [-] and k [m^2] are the porosity and the permeability of the rock, μ [Pa.s] and K_f [Pa] are the typical dynamic viscosity and bulk modulus of the gas at the conditions of interest, see e.g. Dake (1978), §5.1. Using typical values $\phi = 0.15$, $\mu = 2\ 10^{-5}$ Pa.s, $K_f = 0.02$ GPa and $k = 100$ mD, we obtain $D_p \sim 0.7$ m^2/s. So, the distance over which the pressure diffuses in a year $L \sim 4$ km.
The mean permeability of the reservoir ranges from tens to hundreds mDarcy. Herewith, D_p is in the range 0.1 - 1 m^2/s. Within a period of year $t \sim 3\ 10^7$ s, reservoir pressure gradients relax over a distance of the order $L \sim \sqrt{D_p t}$ or 2 - 5 km.

and presented in the form of an EXCEL spreadsheet. The spreadsheet contains a large number of locations along a large number of 'named' faults with the heights of horizon of the top of the Zechstein formation and the thickness of two layers herein on both sides of the faults as well as the azimuth angle with respect to the north α and the fault dip angle δ. The spacing between two nearby locations along the faults is of the order of 100 m.
This set of faults is not complete. As indicated by Mallik (2015), there could be many more faults that have not been identified yet or captured by this database. On the other hand, many or a significant number of the faults in this database may slip non-seismically or don't slip at all.

Figure C.1.2 shows a scatter plot of the subsidence data of the ground above the field over the period 1972 - 2008 combined with the faults. In this period, the reservoir pressure decreased from about 35 MPa to about 12 MPa, almost uniform over the field. The data in these figures originates from the Nederlandse Aardolie Maatschappij (NAM). The same data has been used by Bierman and Kraaijeveld (2015) to study the compaction of the reservoir. Figure C.1.3 shows a contour plot of the reservoir depth. The reservoir thickness (not shown) gradually increases from 100 m in the south east to about 300 m in the north-west.

Figures C.1.4 and C.1.5 show bird's views of the landscapes of the reservoir depth and the subsidence above the Groningen field over the period 1972 - 2008. The landscapes are constructed using a linear interpolation between the measurement points and constant extrapolation outside the area of measurements. There are significant reservoir offsets along the two gorges in the north-west part of the Groningen 'high'.
The reservoir compaction profile follows about the subsidence profile over the field. Most of the tremors are observed in areas where the compaction is substantial.

In relation to a possible arrest of ruptures by kinks or other geometric discontinuities in the faults shown here, we have first splitted the named faults in the EXCEL spreadsheet from NAM into fault segments. A fault segment is created when the azimuth angle α from one fault location to the other changes more than 0.3 degree/m. Practically all the centers of the fault segments lie on the named faults.
The histograms of these pdf's are shown in Figures C.1.6 - C.1.9 . The data for the horizons and thicknesses of the formations, the azimuth angle and the dip angle have been weighted with the lengths of the fault segments between the locations given. This has been done for the whole field and for regions of interest. For the whole field, the probability density functions of the processed data hardly differs from the raw data.

Since there are no reverse faults, the histogram in Figure C.1.7 shows the pdf for the mean absolute value of the fault throws. Most of the fault segments have lengths in the range 0.3 - 3 km. A substantial number of faults have fault throws in the range 50 - 100 m according to Figure C.1.7 . The fault dip angle somewhat peaks around 80°, see Figure C.1.8 . There is some preference for north-south and east-west directions for the faults,

see the peaks in the histogram of the azimuth angle, see Figure C.1.9 .

In general, the pdf's for regions with many and a few or no tremors do not differ much from the pdf's of the whole field apart from some differences in the dip angle, see Figure C.1.8 . Also, the pdf's do not change much when other criteria are used to define the fault segments (except the pdf for the length of the fault segment, of course).
As shown by Bourne and Oates (2014), reservoir compaction is an important factor to discriminate regions with a few tremors from those with many. However, while the reservoir compaction and porosity in the region around Scheemda are less and could explain why there are hardly tremors, this is not the case for the region around Usquert. In this region, the reservoir compaction is substantial.

Figure C.1.10 shows the histograms for the fault dip and fault throw of fault segments which are closest to the hypocenters of the strongest tremors with $M \geq 2.5$. Following Bourne and Oates (2014), we also include the uncertainty in the location of the tremors. We have added to the X- and Y-coordinates of the locations of the tremors a random number from a normal distribution with a mean and standard deviation of 0 km and 0.5 km, respectively. According to both sets of histograms, strong tremors evolve from areas close to or along fault segments with a throw of about 100 m and a dip angle of about 65°. Repeating this exercise with a lower magnitude limit for the 'strongest' tremors, the peaks in the histograms become less pronounced.

Figure C.1.11 shows the histograms for the fault dip and fault throw of fault segments which are closest to the hypocenters of the first observed tremors in a part of the Groningen field with most tremors. This part of the field is bounded by the X,Y coordinates [240,260,570,600] and is subdivided in square regions of 5×5 km^2. For each region, the first hypocenter of the first tremor is associated with the nearest fault.
The histograms for the fault properties associated with the first tremors with $M \geq 0.5$ hardly differ from those for the fault properties of all tremors, see Figures C.1.7 and C.1.8 .
Recognising that the selected minimum magnitude and the size of square areas are subjective, we have repeated this exercise for $M \geq 0$ and $M \geq 1.0$ and for areas of 2.5×2.5 km^2 in the same part of the Groningen field. Similar histograms are obtained. Comparing the histograms with the field average histograms of all tremors, there is a small tendency that tremors start at faults with a higher dip angle.

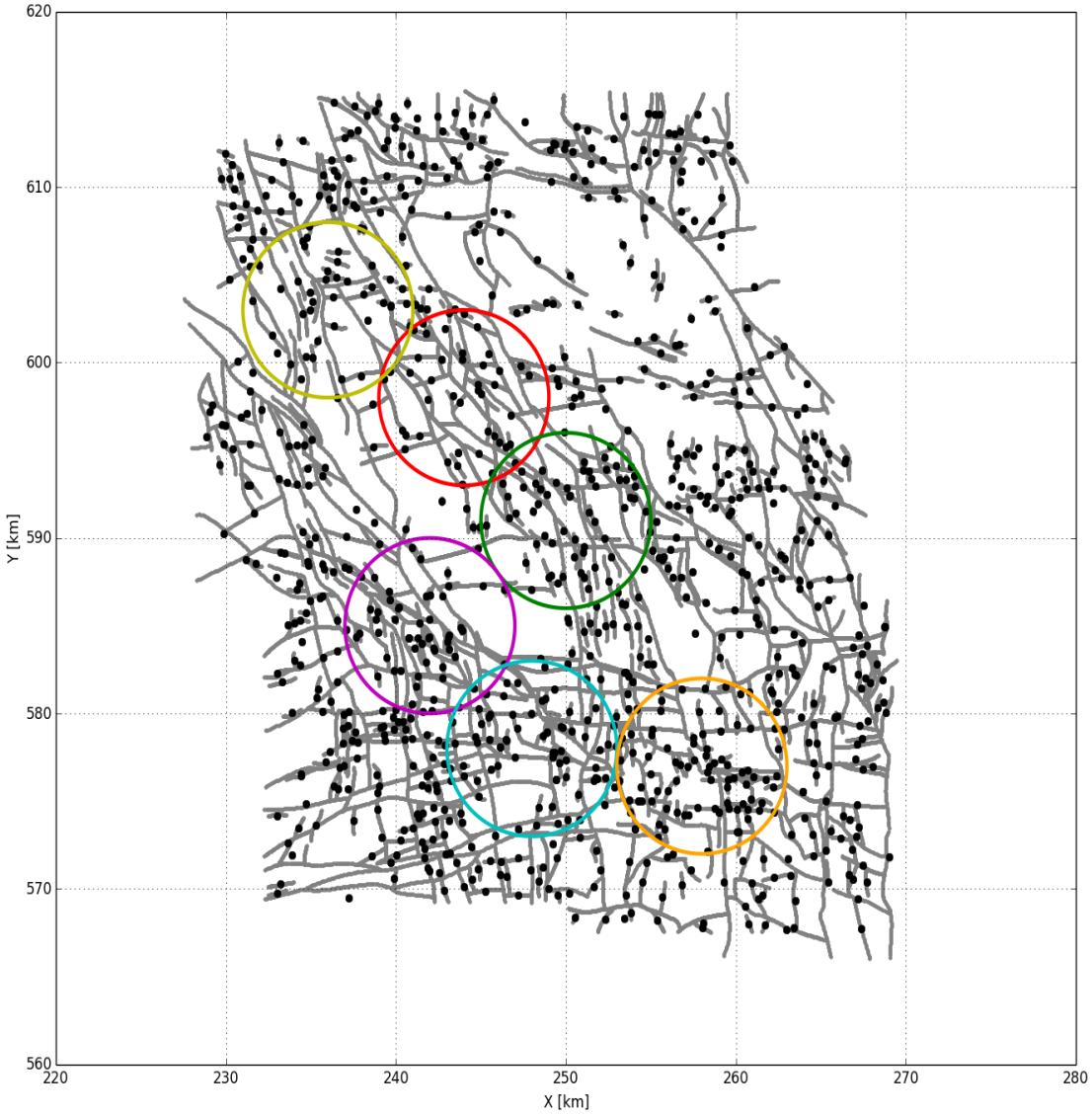

Figure C.1.1 : Faults in the Groningen field according to NAM data (grey lines). Centers of the fault segments in the field (black dots). The circles show the regions of interest around Loppersum (red), Ten Boer (green), Lageland (magenta) and Woudsbloem (cyan) with many tremors and around Scheemda (orange) and Usquert (yellow) with little tremors. The coordinates of the centers of these regions are given in Table 3.3.1 .

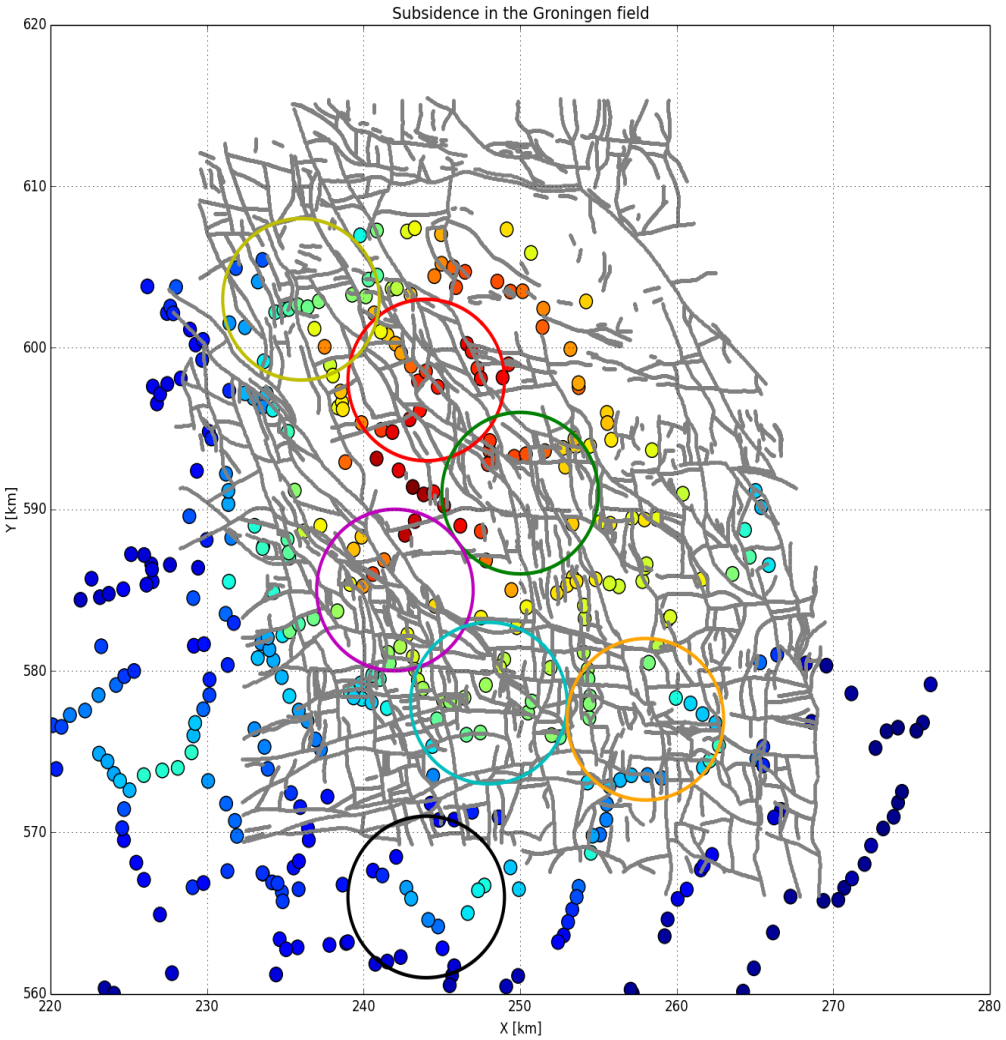

Figure C.1.2 : Faults and subsidence above the Groningen field over the period 1972 - 2008 according to processed ground level measurements of NAM. The circles show the regions of interest around Loppersum (red), Ten Boer (green), Lageland (magenta), Woudsbloem (cyan) and Annerveen (black) with many tremors and around Scheemda (orange) and Usquert (yellow) with little tremors.
The rainbow colour scale for the subsidence data is linear. It ranges from 0 m for dark blue and 0.3 m for red.

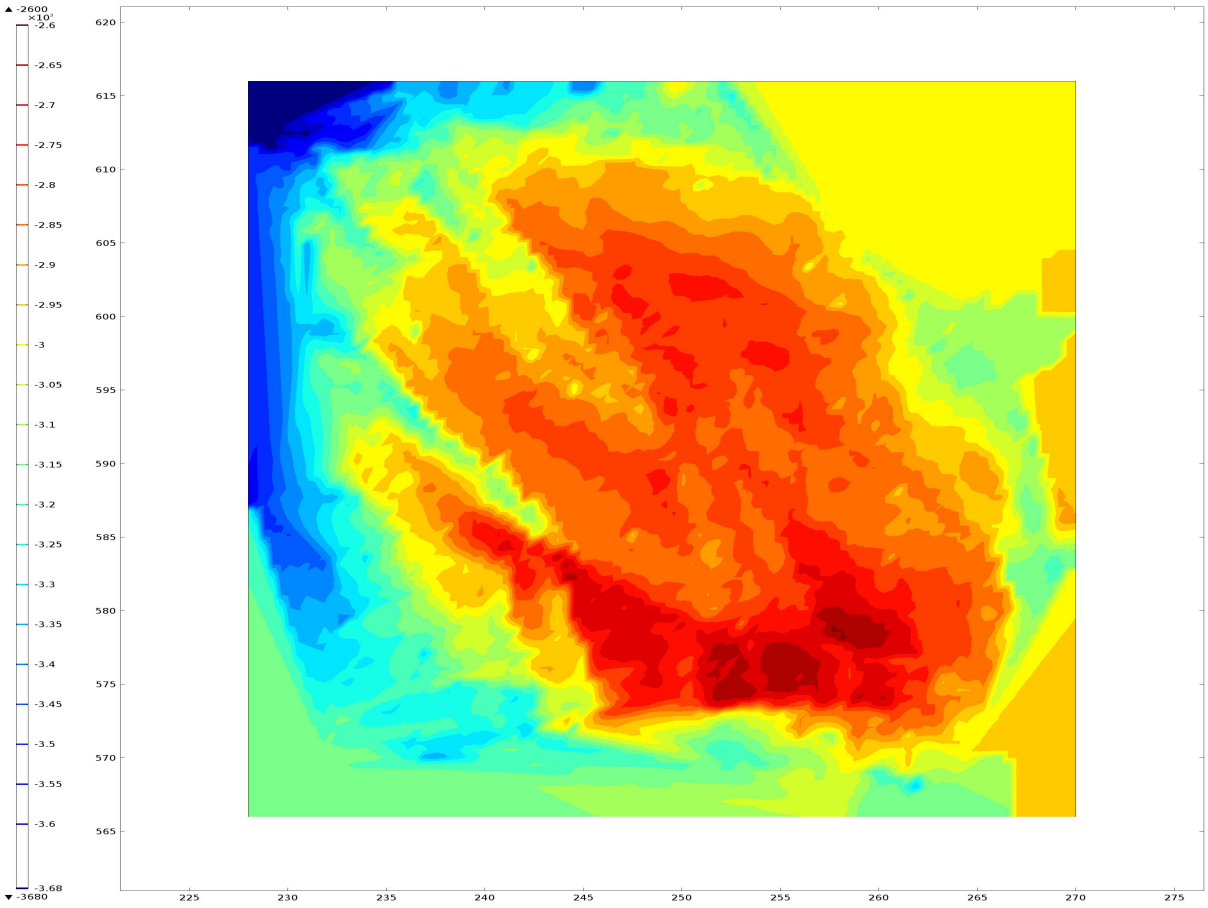

Figure C.1.3 : Contour plot of the depth of the top of the reservoir (top).

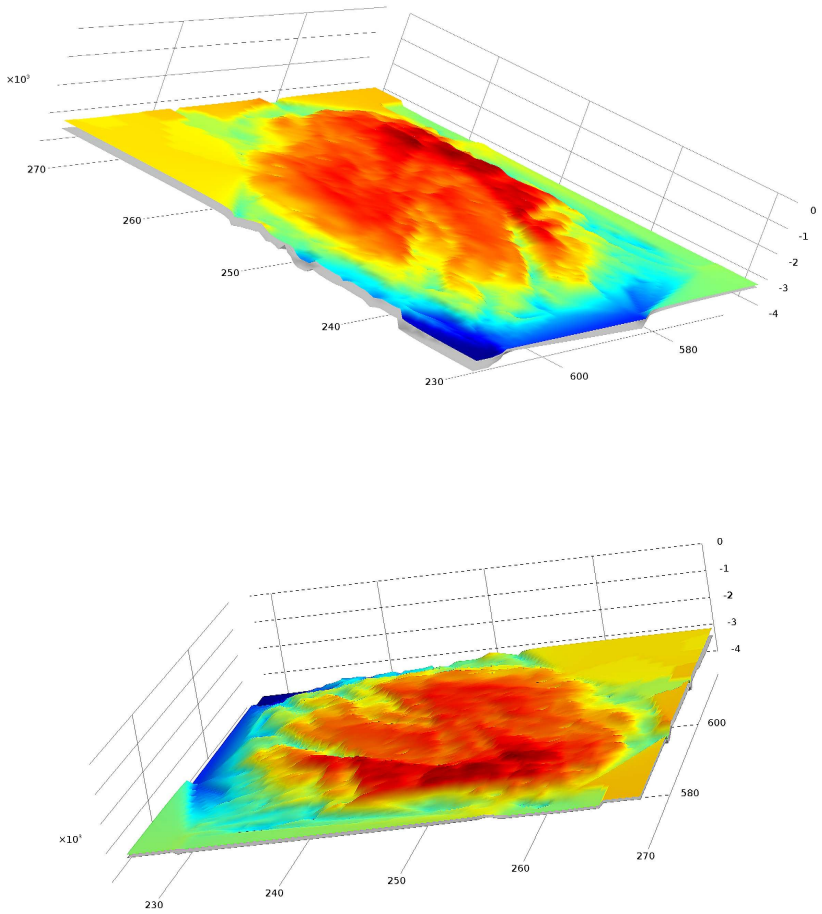

Figure C.1.4 : Bird's view from north-west direction (top) and from south-east direction (bottom) of the depth of the reservoir top of the Groningen field. To approach the real geometry as good as possible, the vertical-to-horizontal aspect ratio is only two times more than in reality (which leads, unfortunately, to a somewhat blurred image). Data from NAM.

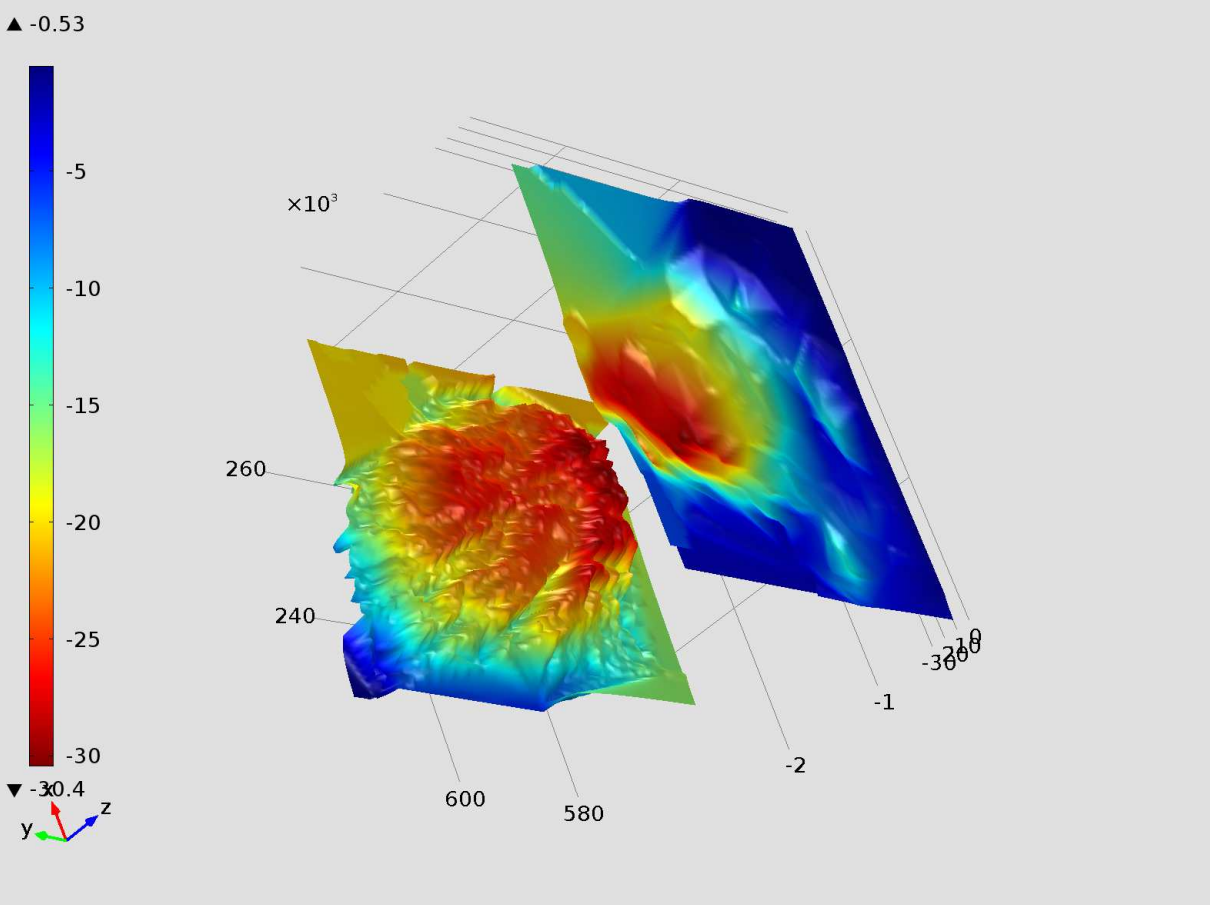

Figure C.1.5 : Bird's view from north-west direction of the subsidence above the Groningen field over the period 1965 - 2008 (top layer) and the depth of the top of the reservoir. The vertical-to-horizontal aspect ratio is exaggerated to highlight height variations in the landscape. The color bar on the left in centimeters holds for the subsidence plane. Data from NAM.

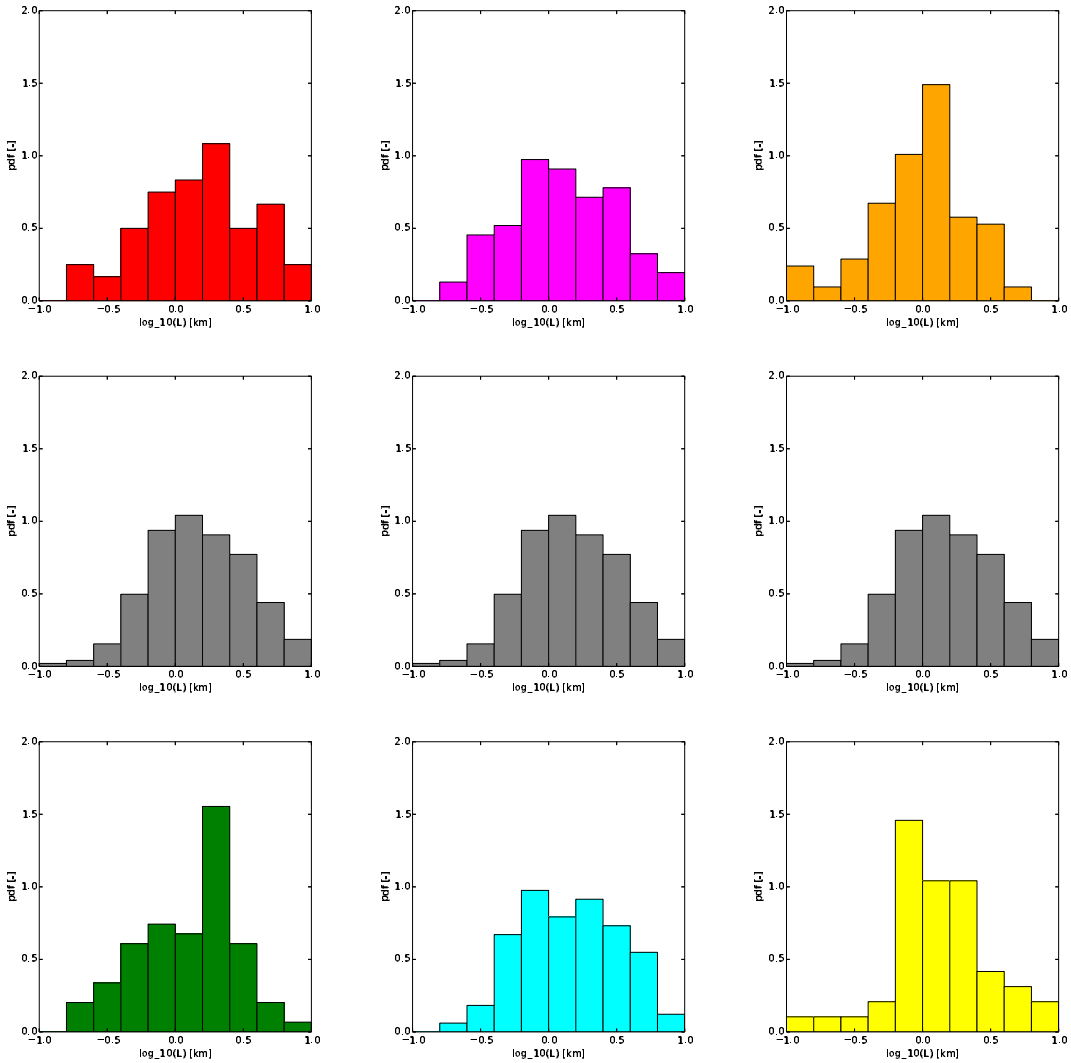

Figure C.1.6 : Histograms of the pdf of the lengths of the fault segments for the whole Groningen field (grey), the selected regions around Loppersum (red), Ten Boer (green), Lageland (magenta) and Woudsbloem (cyan) regions with many tremors and around Scheemda (orange) and Usquert (yellow) with little tremors.

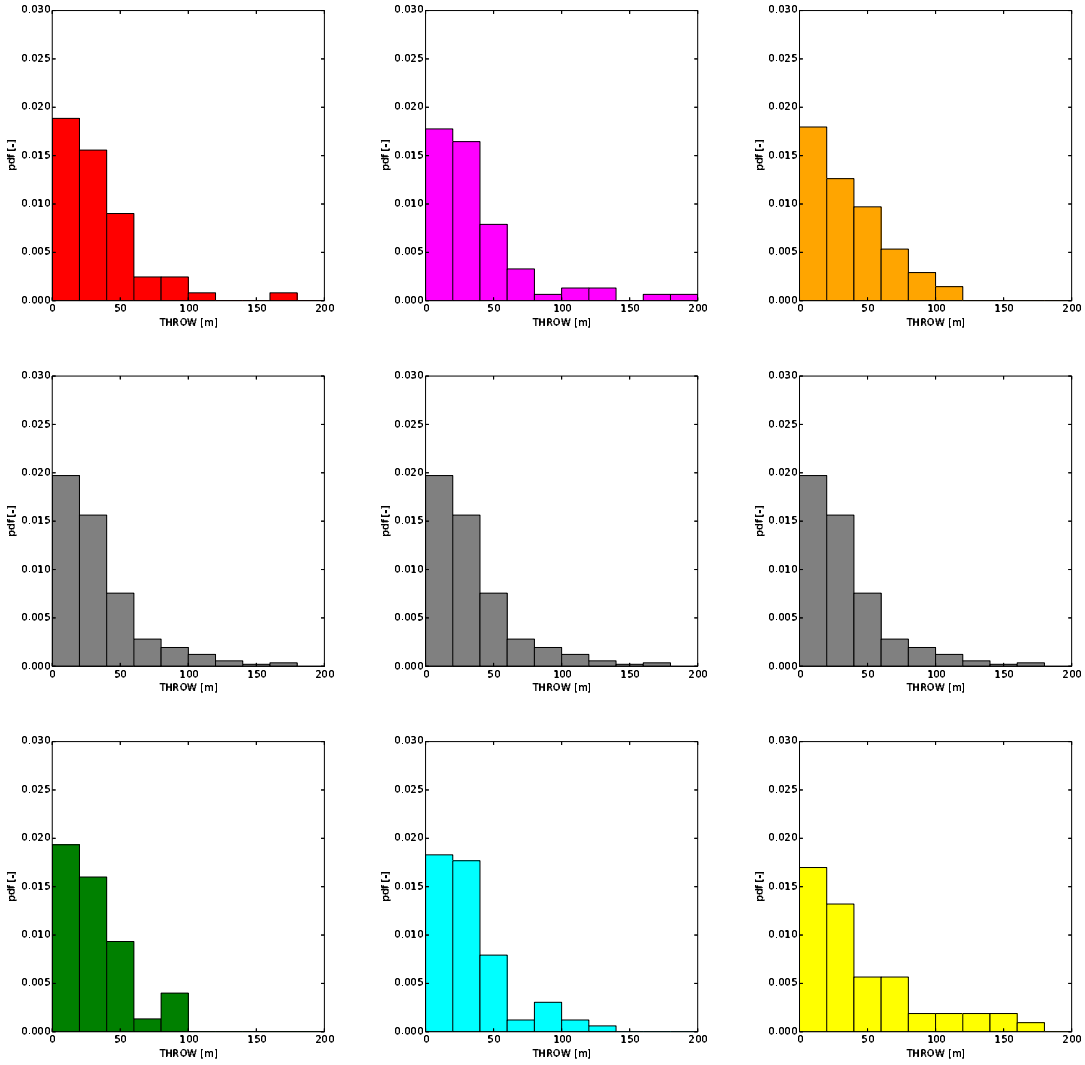

Figure C.1.7 : Histograms of the pdf of the mean absolute fault throw t_{res} of the fault segments for the whole Groningen field (grey), the selected regions around Loppersum (red), Ten Boer (green), Lageland (magenta) and Woudsbloem (cyan) regions with many tremors and around Scheemda (orange) and Usquert (yellow) with little tremors.

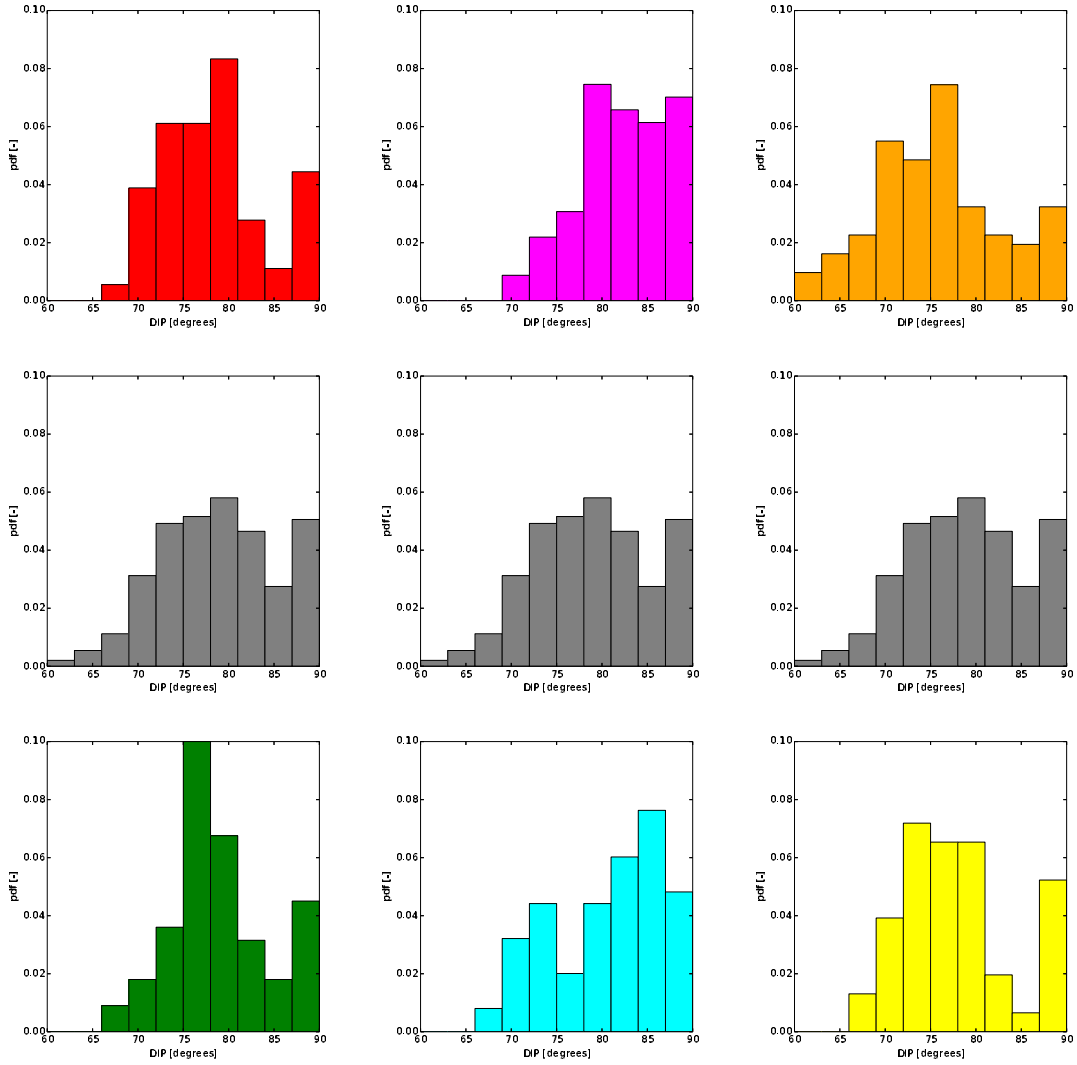

Figure C.1.8 : Histograms of the pdf of the mean dip angle δ of the fault segments for the whole Groningen field (grey), the selected regions around Loppersum (red), Ten Boer (green), Lageland (magenta) and Woudsbloem (cyan) regions with many tremors and around Scheemda (orange) and Usquert (yellow) with little tremors.

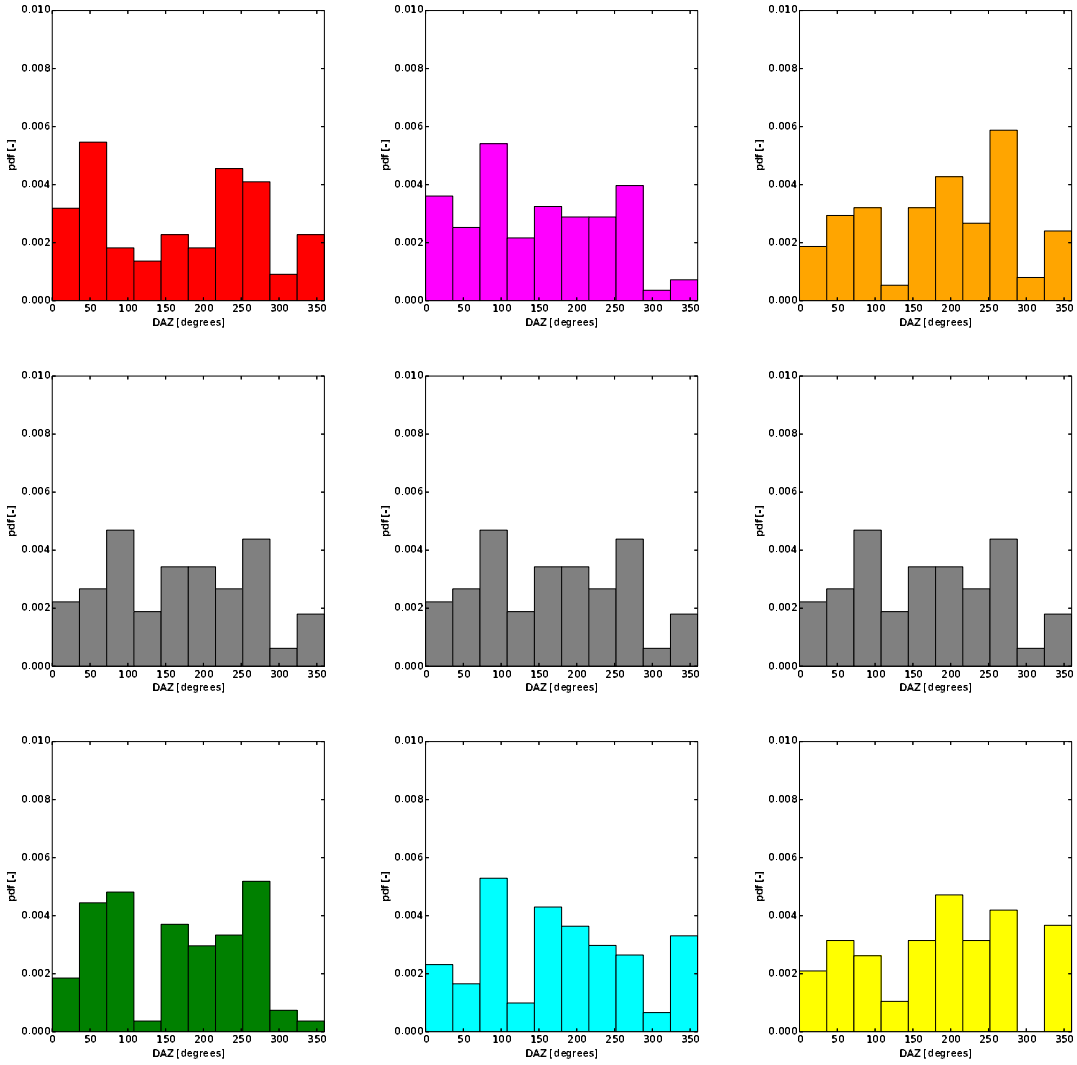

Figure C.1.9 : Histograms of the pdf of the mean azimuth angle α of the fault segments for the whole Groningen field (grey), the selected regions around Loppersum (red), Ten Boer (green), Lageland (magenta) and Woudsbloem (cyan) regions with many tremors and around Scheemda (orange) and Usquert (yellow) with little tremors.

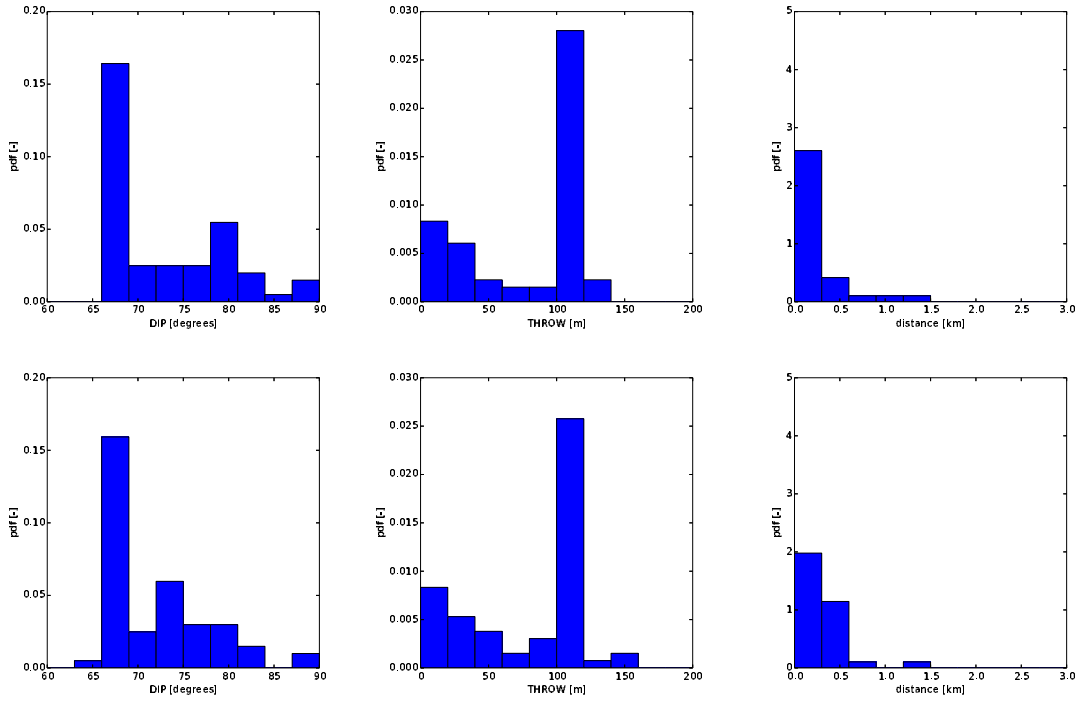

Figure C.1.10 : Histograms of the pdf of the dip angle δ (left) and fault throw t_{res} (center) of the fault segments most close to the hypocenters of the 65 largest tremors with a magnitude $M \geq 2.5$. The right figures show the histogram of the pdf of the distance between the hypocenters of the largest tremors and these fault segments. According to the right figures, most of the hypocenters of these tremors are in a distance less than 0.5 km away from these fault segments. For the top figures, we have used the hypocenter coordinates from the KNMI data, see Appendix D. For the bottom figures, we have added to the coordinates of these hypocenters a random number from a normal distribution, accounting for the uncertainty in the location of the hypocenters.

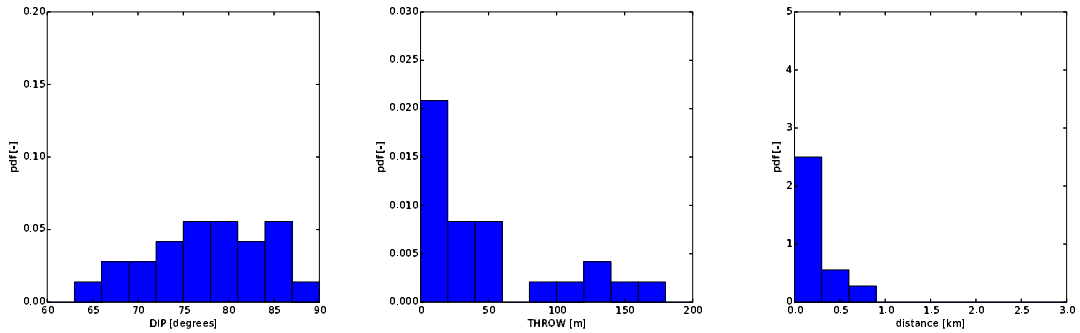

Figure C.1.11 : Histograms of the pdf of the dip angle δ (left) and the fault throw t_{res} (center) of the fault segments most close to the hypocenters of the first tremors with a magnitude $M \geq 0.5$ in 5×5 km^2 square areas in a part of the Groningen field with the most tremors. The right figure shows the histogram of the pdf of the distance between the hypocenters of the first tremors and these faults. This part of the Groningen field is bounded by the X,Y coordinates [240,260,570,600].

Appendix C.2 Annerveen en Eleveld fields

Figures C.2.1 and C.2.2 show the Annerveen and Eleveld fields south of the Groningen field. These figures show several faults along the edges of the reservoir and through the reservoir. So far, we have not used detailed information about these faults. For more data about the Eleveld field, we refer to Roest and Kuilman (1993) and Roest and Kuilman (1994).

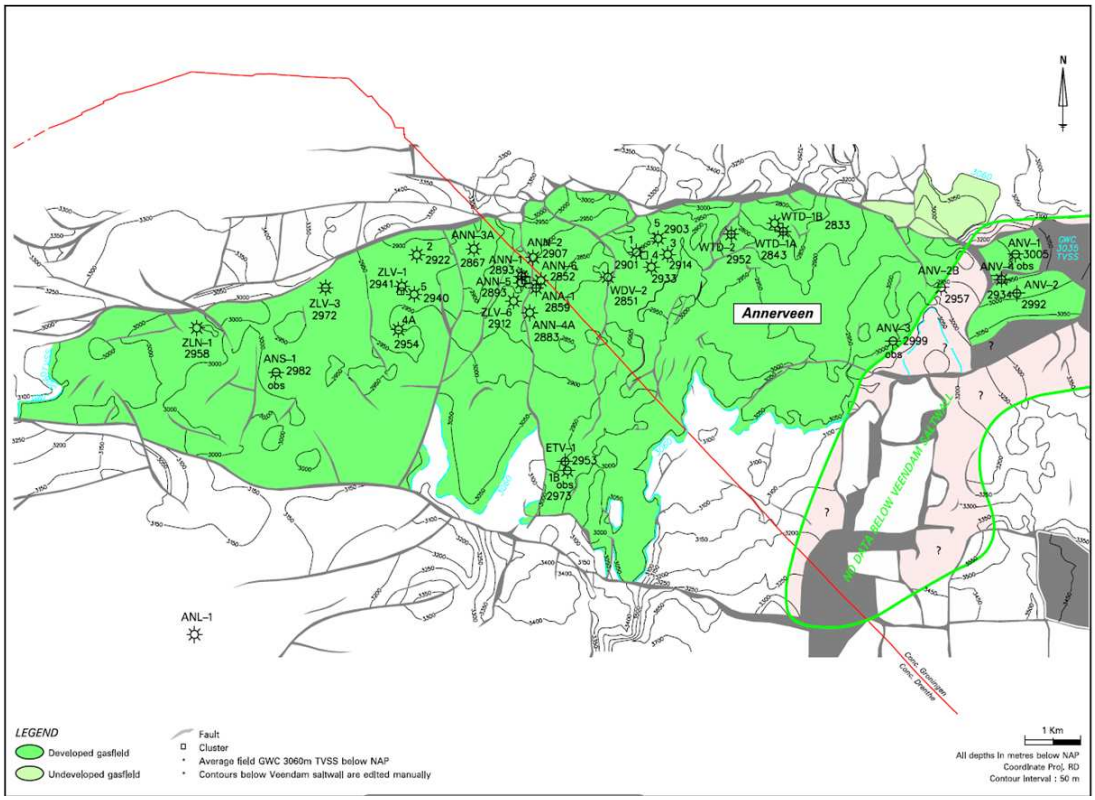

Figure C.2.1 : Annerveen field.

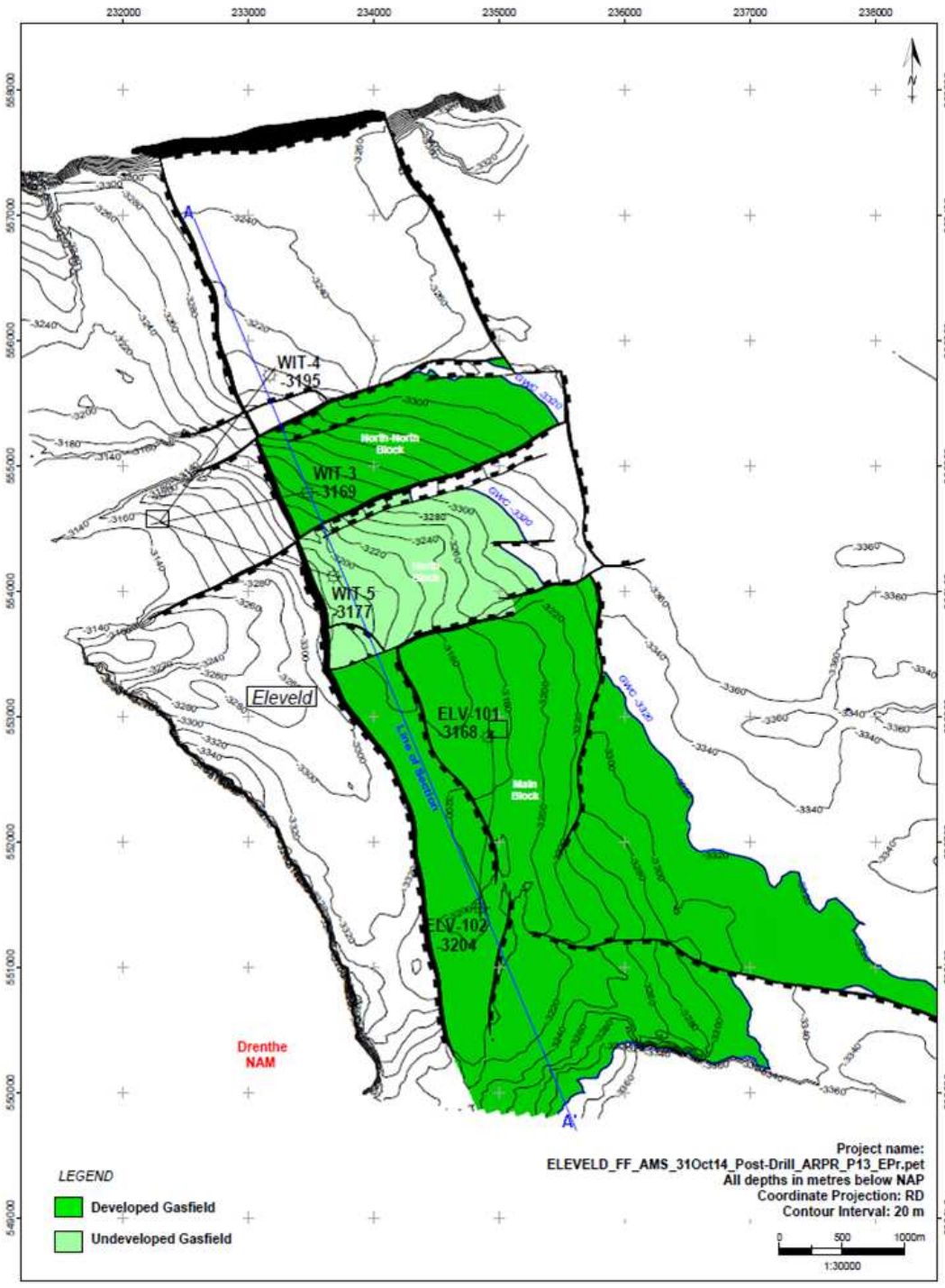

Figure C.2.2 : Eleveld field.

Appendix D

KNMI data about tremors in the Groningen, Annerveen and Eleveld fields

Figures D.0.1 - D.0.2 - D.0.5 show the faults and the hypocenters of the tremors of magnitudes of various ranges on the scale of Richter. The hypocenters of the tremors concentrate in certain regions, such as around Loppersum, Ten Boer, Lageland, Woudsbloem, Annen and Eleveld.
The Annerveen (around Annen) and Eleveld fields are separated from the Groningen field but the reservoirs are also in the Rotliegend rock. We have added these fields to this study because they are in a similar formation as the Groningen field but the reservoir pressure reductions over time have been quite different. In the Eleveld field, tremor rate declined after the reservoir pressure reduction became negligible after early 2005. In the larger west and center part of the Annerveen field, the main reservoir pressure reduction took place before 1995 - 2000. A possible decline of the tremor rate in this field after 2000 is less clear because of the low amount of tremors.
The circles in these figures show the regions of interest with a substantial number of tremors and also two regions around Scheemda and Usquert with almost no tremors. The ratio between weak and strong tremors vary significantly in the regions. Table D.0.1 shows the names, the easting (X) and northing (Y) coordinates of the centers of the regions of interest and the fault density.

Tables D.0.2 - D.0.21 contain the name of the town/village of the hypocenters of the tremors in the Netherlands, the date/time of the tremors, the X and Y [km] coordinates of the hypocenters and the magnitude of the tremors M [Richter] used for the simuations[1]. The elapsed time in terms of days has been calculated from the data by taking that the average year has 365.25 days, starting at 1^{st} of january 1960. These tables originate from tables available from the Koninklijke Nederlands Meteorologisch Instituut in

[1]The table contains also tremor data outside the Groningen, Annerveen and Eleveld fields which is not used.

the Netherlands (KNMI) which can be found on the www.knmi.nl WEB site. For the data in the period from january 2014 to december 2014, the easting and northing X and Y coordinates of the hypocenters of the tremors have been calculated from the longitude and lattitude data provided by the KNMI.

The tables contain about 1000 tremors[2]. Note that the network of seismometers has been designed to detect and locate tremors in the Groningen field above magnitudes of 1.5 and was only fully operational after 1994. This means that not all tremors before 1995 have been captured. Excluding tremors before 1995 and with magnitudes below M = 1.0, about 700 tremors remain. The distribution of tremors is not uniform over the Groningen, Annerveen and Eleveld fields and also the frequency-magnitude relationship derived from this data varies in the regions of interest.

Table D.0.1 : Names and the coordinates of the fields, centers of the regions of interest and the names of a few nearby villages. The mean fault distance D_f is calculated from the area of the region S_{area} [m^2] and the cumulative length of the observed faults L_f [m], i.e. $D_f = c_f S_{area}/L_f$. c_f [-] is a geometric constant depending on the azimuth angle distribution of the faults. For example: for parallel faults, $c_f = 1$ and for faults in the pattern of a square grid, $c_f = 2$. We use $c_f = 2$.

Field	Name region	Nearby Villages	X_{cen} km	Y_{cen} km	D_f km
Groningen	Loppersum	Loppersum	244	598	1.2
	Ten Boer	Garresweer Overschild Steendam	250	591	1.3
	Lageland	Lageland	242	585	1.1
	Woudsbloem	Woudsbloem Hogezand Froombosch	248	578	1.0
	Scheemda	Scheemda	258	577	1.2
	Usquert	Usquert	236	603	1.5
Annerveen	Annerveen	Annen	244	566	NA
Eleveld	Eleveld	Eleveld	235	553	NA

[2]The table has been compared with a recent ArcGIS file used by NAM. The table contains a few tremors less than the ARCGIS file and a few tremors are assigned to other village names.
The small tremors around Midlaren in march 2009 are believed not to be related to reservoir compaction. They originate from a drilling activity.

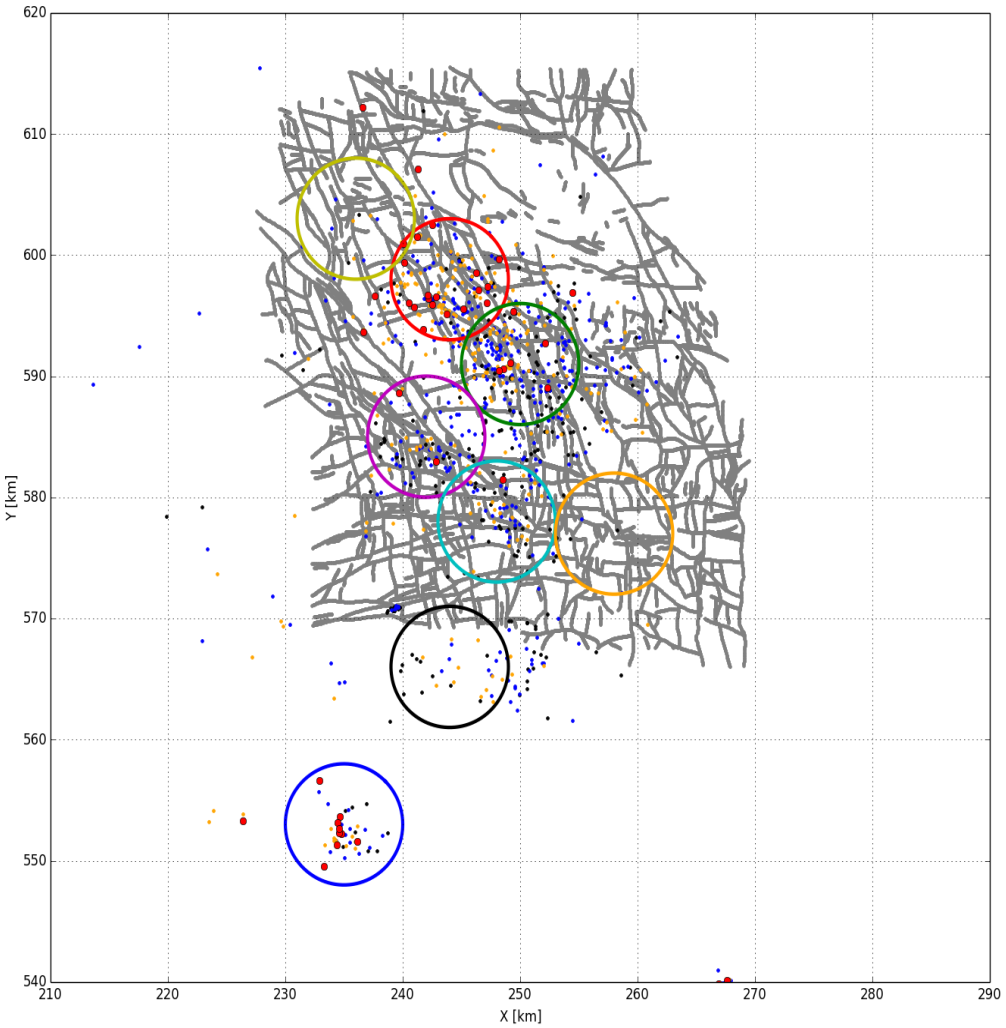

Figure D.0.1 : Faults and hypocenters of tremors in the Groningen field according to KNMI and NAM data. The faults are shown as grey lines. The regions of interest are shown by circles of 5 km radius, Loppersum (red), Ten Boer (green), Lageland (magenta), Woudsbloem (cyan), Scheemda (orange), Usquert (yellow), Annerveen (black) and Eleveld (blue). The hypocenters of the tremors are shown by the coloured dots. The colors correspond to the magnitude of the tremors in the following ranges on the scale of Richter: black for $0.5 \leq M < 1$, blue for $1.0 \leq M < 1.5$, orange for $1.5 \leq M < 2.5$ and red for $2.5 \leq M < 4$. Note that not all faults with throws less than about 80 m and tremors below $M = 1.5$ have been captured.

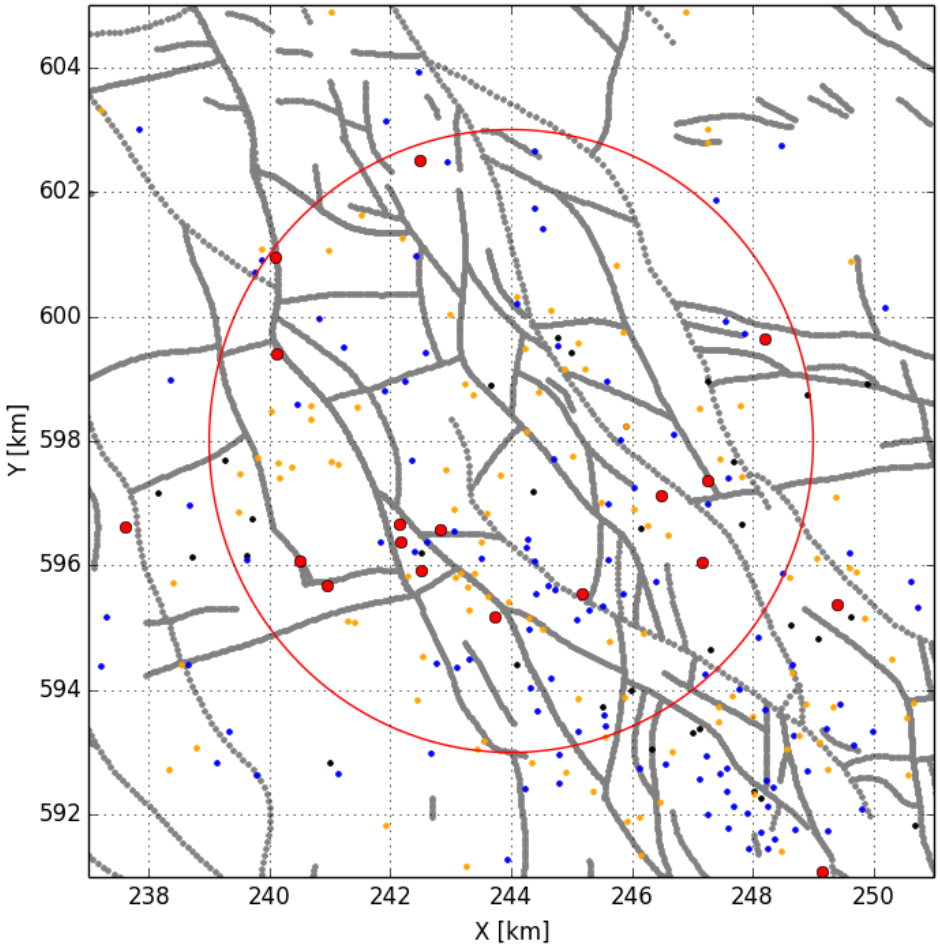

Figure D.0.2 : Faults and hypocenters of tremors around Loppersum according to KNMI and NAM data. The faults are shown as grey lines. The region of interest is shown by the circle of 5 km radius. The hypocenters of the tremors are shown by the coloured dots. The colors correspond to the magnitude of the tremors in the following ranges on the scale of Richter: black for $0.5 \leq M < 1$, blue for $1.0 \leq M < 1.5$, orange for $1.5 \leq M < 2.5$ and red for $2.5 \leq M < 4$. Not all faults with throws less than about 80 m and tremors below $M = 1.5$ have been captured.

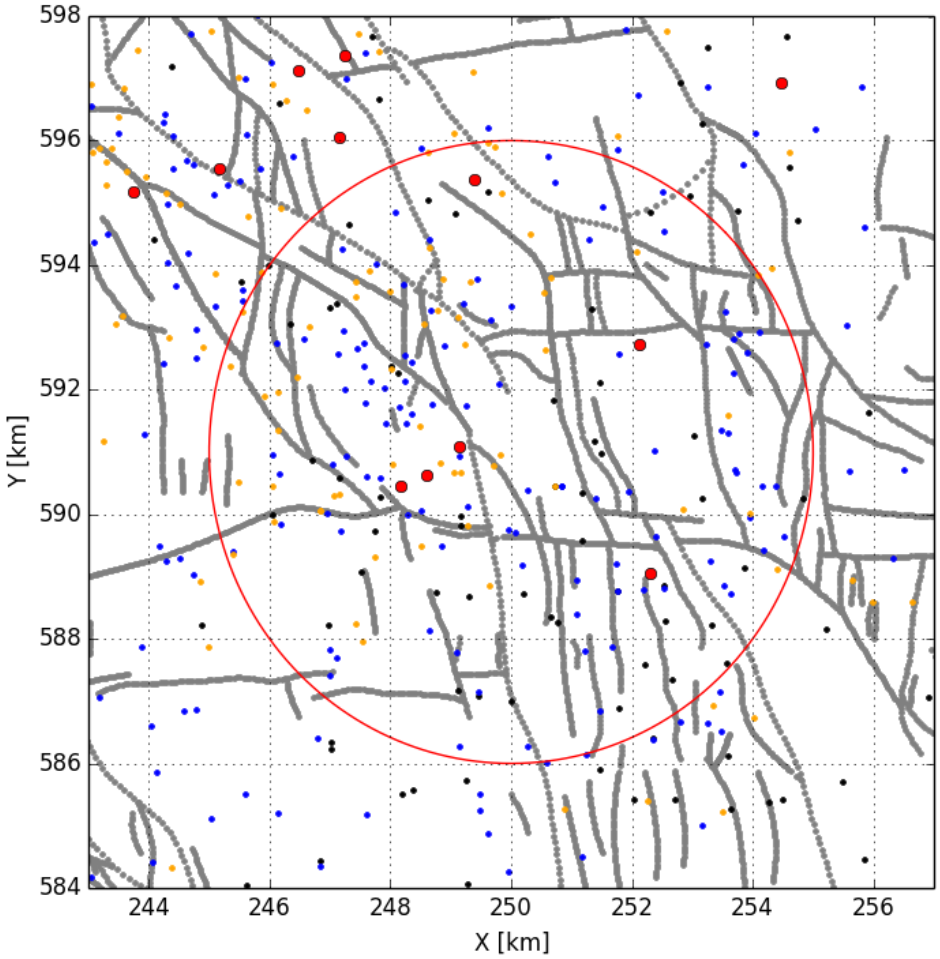

Figure D.0.3 : Faults and hypocenters of tremors around Ten Boer according to KNMI and NAM data. The faults are shown as grey lines. The region of interest is shown by the circle of 5 km radius. The hypocenters of the tremors are shown by the coloured dots. The colors correspond to the magnitude of the tremors in the following ranges on the scale of Richter: black for $0.5 \leq M < 1$, blue for $1.0 \leq M < 1.5$, orange for $1.5 \leq M < 2.5$ and red for $2.5 \leq M < 4$. Not all faults with throws less than about 80 m and tremors below $M = 1.5$ have been captured.

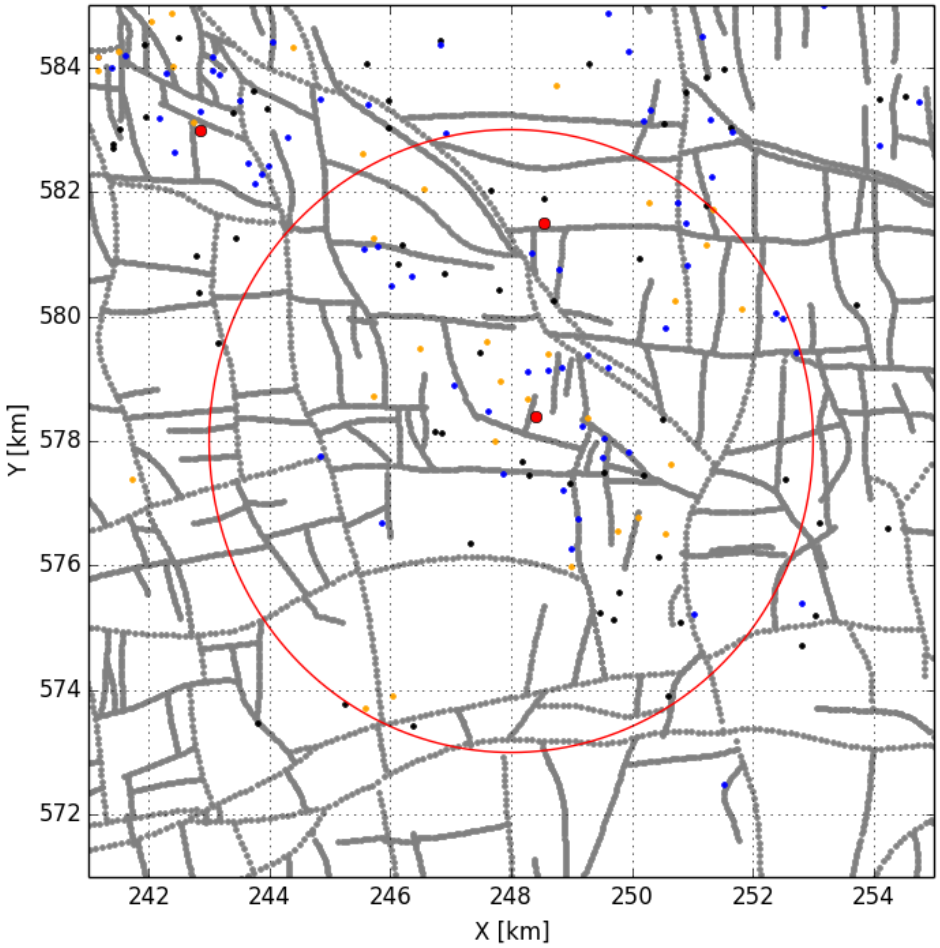

Figure D.0.4 : Faults and hypocenters of tremors around Woudsbloem according to KNMI and NAM data. The faults are shown as grey lines. The region of interest is shown by the circle of 5 km radius. The hypocenters of the tremors are shown by the coloured dots. The colors correspond to the magnitude of the tremors in the following ranges on the scale of Richter: black for $0.5 \leq M < 1$, blue for $1.0 \leq M < 1.5$, orange for $1.5 \leq M < 2.5$ and red for $2.5 \leq M < 4$. Not all faults with throws less than about 80 m and tremors below $M = 1.5$ have been captured.

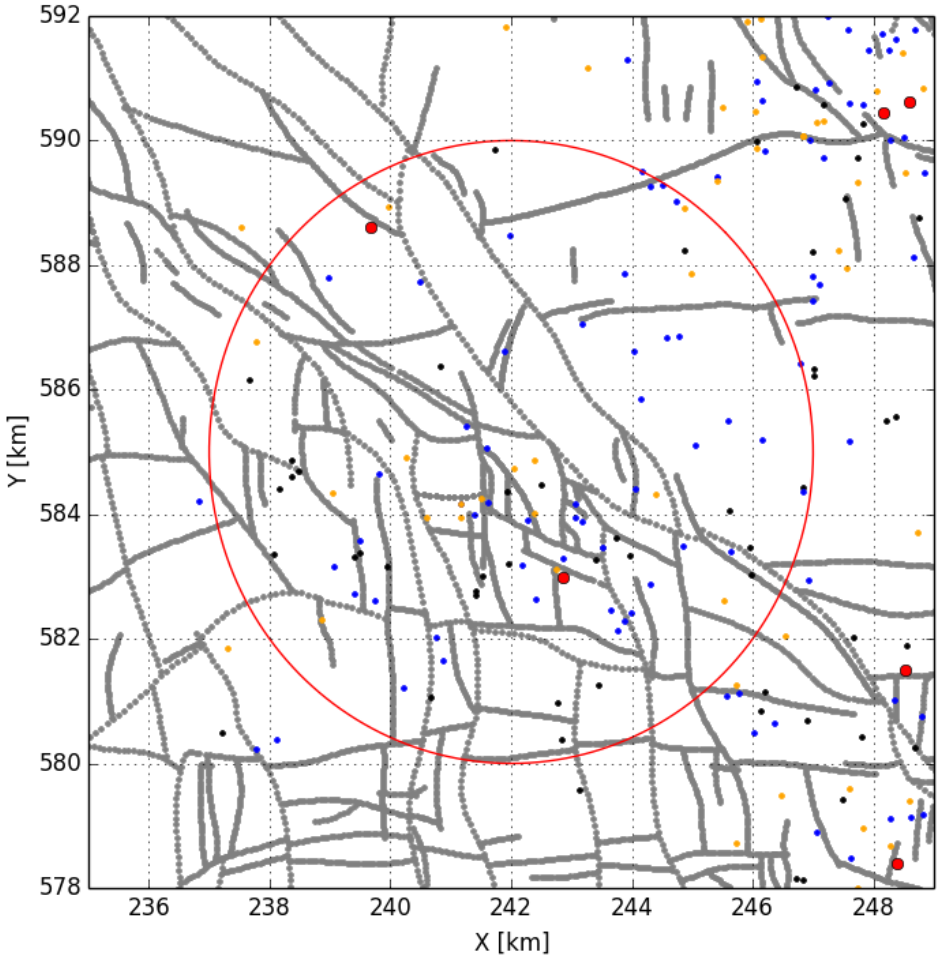

Figure D.0.5 : Faults and hypocenters of tremors around Lageland according to KNMI and NAM data. The faults are shown as grey lines. The region of interest is shown by the circle of 5 km radius. The hypocenters of the tremors are shown by the coloured dots. The colors correspond to the magnitude of the tremors in the following ranges on the scale of Richter: black for $0.5 \leq M < 1$, blue for $1.0 \leq M < 1.5$, orange for $1.5 \leq M < 2.5$ and red for $2.5 \leq M < 4$. Not all faults with throws less than about 80 m and tremors below $M = 1.5$ have been captured.

Table D.0.2 : Observed tremors in the Netherlands.

Location	t	t	X	Y	M
	y/m/d	days	m	m	Richter
Assen	19861226	9887.7	232924	556587	2.8
Hooghalen	19871214	10241.1	233266	549537	2.5
Purmerend	19891201	10958.9	126697	504593	2.7
Emmen	19910215	11399.2	257992	532491	2.2
Geelbroek	19910425	11470.1	234788	552218	2.6
Eleveld	19910808	11574.9	234653	553624	2.7
Middelstum	19911205	11693.7	239503	597465	2.4
Geelbroek	19920523	11863.6	234563	552325	2.6
Geelbroek	19920524	11865.1	233885	552685	1.6
Roswinkel	19920611	11881.6	265802	539341	2.7
Eleveld	19920722	11923.3	234437	553158	2.6
Ten-Boer	19921206	12059.3	245107	593338	1.3
Slochteren	19921211	12064.3	245782	581126	1.4
Noordbroek	19930212	12126.9	253715	590669	1.0
Langelo	19930305	12149.8	227177	566825	1.5
Hoogezand	19930312	12157.1	249789	575582	0.9
Overschild	19930326	12170.7	248848	589495	1.1
Haren	19930505	12211.2	241729	577378	1.5
Ten-Post	19930514	12219.4	248692	591773	1.1
Bedum	19930627	12263.7	239118	592839	1.4
Stedum	19930627	12262.9	239788	592647	1.0
Appingedam	19930710	12276.8	251518	594928	1.4
Loppersum	19930727	12293.4	249625	595169	0.8
Nijenklooster	19930823	12320.4	252297	594851	0.7
Oldenzijl	19930904	12331.3	246682	598117	1.4
Middelstum	19930922	12350.0	240682	598562	2.0
Slochteren	19930925	12352.6	250129	580932	0.9
Slochteren	19931123	12411.7	250699	580256	2.2
Ten-Post	19931222	12441.3	246050	590462	1.6
Winneweer	19940204	12484.3	247581	591790	1.3
Roswinkel	19940205	12485.2	266672	539583	2.9
Garsthuizen	19940228	12508.0	243671	598895	0.6
Steendam	19940302	12511.9	249639	588861	1.5
Eenrum	19940306	12516.0	249431	593774	1.0
't-Zandt	19940314	12524.0	249605	596207	1.3
Zandeweer	19940314	12523.8	240970	601053	1.6
Westerbroek	19940314	12524.5	245866	576693	1.1
Delfzijl	19940324	12534.6	259885	593193	0.8
Steendam	19940404	12544.9	251094	588389	1.3
Kolham	19940507	12578.4	249269	579374	1.0
Hellum	19940510	12581.7	251646	583021	0.8
Weiwerd	19940605	12606.9	259159	590784	1.0
Achterdiep	19940606	12607.3	251022	575217	1.0
Garsthuizen	19940608	12609.7	241142	597625	1.5
De-Klip	19940626	12628.0	252512	595171	1.0
Uithuizermeeden	19940627	12629.0	246885	604892	1.7
Stedum	19940701	12632.6	236660	593651	2.7
't-Zandt	19940719	12651.2	245220	599164	2.0
Middelstum	19940730	12662.3	237609	596616	2.7
Middelstum	19940730	12662.2	234143	598134	1.3
Alkmaar	19940806	12668.2	109221	518630	3.0
Annen	19940816	12678.8	242855	564487	2.3
Warffum	19940907	12699.7	233964	602231	1.4
Emmen	19940909	12701.8	258193	526189	1.7
Alkmaar	19940921	12713.6	109021	519047	3.2
Schoonebeek	19940923	12715.4	255931	521208	1.3

Table D.0.3 : Observed tremors in the Netherlands, continued.

Location	t	t	X	Y	M
	y/m/d	days	m	m	Richter
Schildwolde	19941026	12749.7	245039	585119	1.2
Steendam	19941213	12797.3	250188	589187	1.0
Amsweer	19950124	12838.4	255555	593044	1.3
Annen	19950131	12845.8	244303	564737	2.0
Veendam	19950201	12845.6	247956	566531	1.2
Doekegat	19950321	12896.4	256377	606679	1.1
Loppersum	19950406	12912.0	241030	597677	2.0
Zuidlaren	19950426	12932.1	240799	566992	0.7
Weiwerd	19950515	12951.3	258791	592390	1.8
Boerakker	19950603	12969.6	219873	578443	0.9
Roswinkel	19950620	12986.5	265651	539449	2.7
Veenhuizen	19950715	13012.0	250911	580817	1.0
Meedhuizen	19950721	13018.3	260095	588689	1.1
Wirdumerdraai	19950913	13071.5	244299	594974	1.0
Altena	19951018	13106.5	228887	571840	1.1
Loppersum	19951102	13121.3	243598	596835	1.6
Uithuizerwad	19951104	13122.8	243577	609986	1.8
Steendam	19951120	13139.3	246561	592809	1.1
PolderWormer	19951224	13173.2	118279	502595	2.3
Emmen	19951230	13179.1	266865	540960	1.2
Schaaphok	19960212	13222.1	247021	586231	0.9
Emmen	19960224	13234.4	257635	531315	1.0
Roswinkel	19960225	13235.2	267805	540166	0.9
Eppenhuizen	19960229	13239.3	238401	595721	2.0
Roswinkel	19960306	13246.5	267805	540166	1.6
Eexterveen	19960312	13253.0	248994	564882	1.1
Roswinkel	19960312	13252.5	267631	540117	2.6
Schuilingsoord	19960312	13253.0	239817	565676	0.8
Roswinkel	19960314	13254.6	267947	540136	1.1
Appingedam	19960316	13257.1	252374	591031	1.4
Roswinkel	19960321	13262.1	267278	539619	1.8
Amen	19960401	13271.9	237052	550845	0.6
Nieuw-Annerveen	19960401	13272.1	248986	565289	0.1
Spijkerboor	19960409	13280.2	249561	564429	1.1
Ten-Boer	19960415	13286.0	241727	589862	0.9
Holwierde	19960417	13287.9	254570	597680	0.9
Warffum	19960421	13292.1	235342	599378	0.5
Delfzijl	19960425	13296.2	253242	597486	0.9
Annerveenschekanaal	19960607	13339.3	248278	567242	1.2
Garrelsweer	19960607	13338.6	247685	592143	1.3
Annerveenschekanaal	19960607	13339.4	251744	567013	0.7
Eleveld	19960616	13348.5	234350	551598	1.7
Spijkerboor	19960703	13365.2	249911	563693	0.8
Wachtum	19960804	13397.3	246237	527063	1.6
Weerdinge	19960806	13399.3	258209	530771	1.6
Annen	19960809	13402.2	242193	564031	0.3
Oterdumerwarven	19960809	13401.6	259734	589942	1.6
Geelbroek	19960825	13417.6	234465	551451	1.7
Nieuw-Roden	19960902	13425.9	224175	573700	2.1
Amen	19961016	13469.5	237160	551070	1.3
't-Zandt	19961116	13500.7	246033	597251	1.3
Wachtum	19961117	13500.9	245787	527055	2.2
Leek	19961130	13514.8	223365	575746	1.0
Roswinkel	19961206	13520.2	267220	539807	1.6
Annerveenschekanaal	19961216	13530.4	250651	565823	0.5
Annerveenschekanaal	19961216	13530.5	251085	566481	0.1

Table D.0.4 : Observed tremors in the Netherlands, continued.

Location	t	t	X	Y	M
	y/m/d	days	m	m	Richter
Schaaphok	19961226	13540.8	246898	586824	0.2
Winde	19961228	13542.8	229818	569369	1.9
Roswinkel	19961228	13543.0	266548	539725	2.7
Donderen	19961228	13543.2	229589	569755	1.8
Westeremden	19970108	13553.2	243294	595288	1.5
Geelbroek	19970114	13559.3	234917	551199	0.7
Roswinkel	19970116	13561.3	266708	539807	2.4
Annen	19970124	13569.2	241478	566484	0.6
Zijldijk	19970217	13592.4	245743	600826	1.6
Eleveld	19970217	13592.6	234349	551691	1.2
Roswinkel	19970219	13594.9	266230	539495	3.4
Coevorden	19970226	13601.6	250808	517933	1.2
Pieterzijl	19970302	13608.1	213614	589307	1.3
Zuidlaarderveen	19970308	13613.8	250575	569680	0.8
Zuidlaarderveen	19970308	13614.5	250345	569990	0.0
Woudbloem	19970325	13631.3	245806	585726	0.2
Emmen	19970401	13637.0	255255	532137	1.4
Noordbroek	19970409	13646.0	253708	580187	0.5
Roswinkel	19970417	13653.1	267209	539707	0.8
Schildwolde	19970429	13665.3	249482	585519	1.4
Weiwerd	19970504	13671.2	257813	591386	1.1
Kropswolde	19970504	13671.3	245252	573770	0.8
Roswinkel	19970519	13685.7	267227	539911	1.3
Opwierde	19970606	13703.8	254165	590455	1.2
't-Zandt	19970619	13716.4	245903	598231	1.8
Roswinkel	19970620	13717.4	267351	539413	1.8
Oud-Annerveen	19970621	13718.0	246361	568207	2.0
Roswinkel	19970709	13736.4	267234	539596	1.2
Oud-Annerveen	19970717	13745.0	244085	564455	0.7
Lageland	19970723	13750.4	246150	585195	1.2
Roswinkel	19970818	13776.5	267006	539739	1.6
Roswinkel	19970818	13776.0	267006	539721	2.1
Spijkerboor	19970822	13780.6	250558	564857	0.2
Spijkerboor	19970823	13781.3	250558	564857	0.6
Lageland	19970823	13780.8	241494	584256	1.6
Wirdum	19970913	13801.2	245513	595349	1.1
Annen	19970914	13802.8	245681	562796	0.4
Zandeweer	19971101	13850.9	242558	605164	1.4
Donderen	19971103	13852.8	230374	569489	1.4
Wirdum	19971104	13854.0	248643	594278	1.7
Oud-Annerveen	19971115	13864.2	251026	569429	0.3
Slochteren	19971120	13869.1	248796	580756	1.2
Woudbloem	19971126	13875.1	246913	586062	0.2
Meedhuizen	19971203	13883.2	255641	588947	1.8
Siddeburen	19971203	13883.2	253164	585000	1.3
Zuidlaarderveen	19971207	13887.0	243051	566012	0.3
Termunterzijl	19971223	13902.6	263437	593327	1.3

Table D.0.5 : Observed tremors in the Netherlands, continued.

Location	t	t	X	Y	M
	y/m/d	days	m	m	Richter
Amen	19980108	13918.2	236272	550573	1.2
Geelbroek	19980122	13932.1	232828	555728	1.1
Roswinkel	19980128	13938.8	266449	539541	2.7
Roswinkel	19980128	13938.3	266111	539589	2.0
Woudbloem	19980131	13941.2	245615	584053	0.7
Meedhuizen	19980205	13945.7	258169	590317	1.1
't-Zandt	19980215	13955.8	247251	597367	2.6
Westeremden	19980329	14000.3	244390	596070	1.3
Zeerijp	19980419	14020.3	243958	595412	1.5
Uithuizen	19980419	14021.0	241012	604894	1.6
Veendam	19980428	14029.5	253920	569840	0.4
Scharmer	19980430	14032.0	243138	579574	0.9
Oldenzijl	19980518	14050.1	244378	602655	1.3
Slochteren	19980530	14061.8	247800	580422	0.9
Roswinkel	19980714	14106.8	267235	539540	3.3
Froombosch	19980814	14137.9	249607	579177	1.1
Overschild	19980824	14147.0	249820	590961	2.4
Emmen	19980905	14158.7	255427	529229	1.9
Zeerijp	19981004	14188.8	245593	597001	1.0
Deurze	19981020	14203.9	236875	554682	0.8
Geelbroek	19981101	14215.8	234560	552473	1.3
Oldenzijl	19981212	14257.3	242186	601261	2.0
Slochteren	19981226	14270.9	251338	581716	1.6
Roswinkel	19990111	14286.3	267471	540047	1.1
Zeerijp	19990113	14288.2	247466	597724	2.1
Siddeburen	19990131	14306.8	250915	586215	0.4
Borgercompagnie	19990305	14341.3	249024	569074	1.0
Wirdum	19990306	14343.0	247651	593906	1.6
Roswinkel	19990312	14348.5	267111	539571	1.3
Roswinkel	19990317	14353.5	267124	539482	1.5
Appingedam	19990421	14387.9	251787	592577	1.4
Rottevalle	19990422	14389.4	206154	569561	1.0
Roswinkel	19990506	14403.3	267339	539896	1.4
Stedum	19990508	14405.9	242432	593845	1.6
Roswinkel	19990514	14411.7	267118	539741	1.7
Roswinkel	19990515	14412.3	267118	539741	1.4
Sappemeer	19990521	14418.8	250447	576133	0.7
Steenbergen	19990607	14434.8	222914	568191	1.1
Amen	19990707	14465.2	238264	552071	1.3
Garsthuizen	19990810	14498.6	244091	600201	1.4
Westeremden	19990811	14500.2	242500	596202	0.7
Eexterveen	19990907	14526.2	249319	565388	1.5
Eexterveen	19990907	14525.8	250572	564189	0.5
Schipborg	19991018	14567.7	244162	566330	0.4
Schuilingsoord	19991018	14567.5	241516	564389	0.3
Amen	19991022	14571.9	235929	550994	1.7
Achterdiep	19991208	14618.5	249524	577729	1.1
Schildwolde	19991209	14619.0	249487	585241	1.1
Achterdiep	19991209	14620.0	249179	578242	1.0
Achterdiep	19991210	14620.0	248865	577215	1.4
Westeremden	19991220	14630.7	243042	596898	1.5
Kolham	19991221	14631.7	247049	578905	1.0
Delfzijl	19991224	14634.1	258876	593616	1.8
Roswinkel	19991231	14641.3	266892	539830	2.8
Roswinkel	20000107	14648.2	266557	539711	1.1
Schipborg	20000110	14650.9	239920	566197	0.6
Appingedam	20000212	14683.5	250546	593554	1.7

Table D.0.6 : Observed tremors in the Netherlands, continued.

Location	t	t	X	Y	M
	y/m/d	days	m	m	Richter
Westeremden	20000319	14720.4	242285	595827	1.6
Roswinkel	20000327	14728.3	266667	539825	0.8
Dalen	20000401	14733.1	247108	522666	1.3
Engelbert	20000408	14739.8	238111	580375	1.2
Godlinze	20000408	14740.5	251990	599056	1.1
Ten-Boer	20000414	14746.5	247243	592006	1.2
Garsthuizen	20000516	14778.9	242985	600032	1.9
Annerveenschekanaal	20000609	14801.9	250506	567489	1.1
Loppersum	20000611	14803.8	246602	596483	2.0
Loppersum	20000612	14804.6	245177	595546	2.5
Siddeburen	20000615	14808.4	252303	589063	2.5
Loppersum	20000706	14829.8	245843	595559	1.2
Vries	20000710	14833.2	234583	564697	1.0
Vries	20000713	14836.5	233886	566299	1.1
't-Zandt	20000716	14839.1	247783	598565	1.5
Annerveenschekanaal	20000922	14906.7	250978	566256	1.0
Annerveenschekanaal	20000922	14906.3	249178	566889	2.2
Annerveenschekanaal	20000923	14907.4	248845	566771	1.0
Roswinkel	20001025	14940.1	267125	539463	3.2
Deurze	20001112	14957.1	236981	555054	0.3
Borgercompagnie	20001223	14998.4	250348	569842	0.4
Meedhuizen	20001226	15001.9	256493	590708	1.4
Annerveenschekanaal	20010226	15062.4	251097	565887	0.8
Lageland	20010318	15085.2	242042	584747	1.6
Geelbroek	20010428	15125.3	234236	551764	1.5
Eleveld	20010428	15125.5	234776	552978	1.1
Roswinkel	20010428	15125.9	267233	539615	2.4
Hoornsedijk	20010517	15145.4	236835	576828	1.4
Annen	20010610	15168.1	246567	563203	0.5
Annerveenschekanaal	20010619	15177.4	250971	566608	1.0
Overschild	20010621	15178.9	249158	590670	1.7
Veendam	20010807	15226.2	252605	568663	0.3
Alkmaar	20010909	15258.8	109374	518265	3.5
Alkmaar	20010910	15259.5	109274	518445	3.2
Noordzee	20010912	15261.2	55761	560664	3.1
Bergen-aan-Zee	20011010	15290.0	105011	521739	2.7
Schaaphok	20011010	15290.0	246834	584355	1.0
Schaaphok	20011010	15289.9	246832	584429	0.8
Appingedam	20011112	15322.4	254094	593849	1.5
Woudbloem	20011204	15344.6	248355	580507	0.2
Woudbloem	20011204	15345.3	248355	580507	0.0
Woudbloem	20011204	15345.5	245560	581085	1.0
Slochteren	20011211	15352.1	248551	581902	0.7
Veendam	20011220	15361.5	252195	566818	0.5
Uithuizerwad	20011225	15366.3	243031	609550	1.3
Eexterveen	20011226	15366.6	250015	564104	0.2
Stedum	20020205	15407.1	243555	593197	2.2
Roswinkel	20020214	15416.1	266003	539401	2.1
Appingedam	20020227	15428.4	250732	595339	1.1
Donderen	20020317	15449.7	232409	567889	0.4
Annen	20020414	15476.3	247686	563168	1.9
Bierum	20020510	15503.6	252747	599980	1.7
Geelbroek	20020511	15503.9	235141	551221	1.5
Eleveld	20020522	15514.7	235453	552655	1.0
Smilde	20020628	15551.5	226363	553848	1.8

Table D.0.7 : Observed tremors in the Netherlands, continued.

Location	t	t	X	Y	M
	y/m/d	days	m	m	Richter
Froombosch	20020718	15572.4	248279	578687	1.6
Geelbroek	20020727	15581.2	234126	551632	1.6
Oudemolen	20020805	15589.2	240074	563771	0.9
Luddeweer	20020829	15613.7	245705	585205	0.0
Marinberg	20020905	15619.9	234809	502735	0.9
Veendam	20020906	15620.9	252347	570365	0.6
Annen	20020922	15636.9	241636	563910	0.6
Annen	20020922	15637.2	238885	561486	0.5
Veendam	20021012	15657.5	250575	569680	0.9
Roswinkel	20021014	15659.4	266670	539694	0.9
Spijkerboor	20021019	15664.1	247533	565317	1.3
Coevorden	20021214	15720.4	252648	521865	1.4
Zuidlaren	20021216	15721.8	244133	567906	1.4
Tjuchem	20021217	15723.5	253168	590249	0.9
Spitsbergen	20021218	15723.9	252540	577380	0.8
Roswinkel	20021224	15730.3	266449	539522	1.4
Loppersum	20030101	15737.5	245293	595289	1.0
Smilde	20030113	15749.7	223896	554127	1.7
Overschild	20030118	15754.5	247176	589723	1.0
Winneweer	20030123	15759.8	245912	591906	1.6
Leermens	20030130	15766.4	248613	595817	1.5
Denemarken	20030131	15768.0	248072	583618	0.3
Eleveld	20030202	15769.3	235688	552009	2.0
De-Paauwen	20030206	15773.5	247124	586623	0.3
Zeerijp	20030211	15778.2	247258	596996	1.3
De-Paauwen	20030212	15778.6	250009	586995	0.8
Rottevalle	20030214	15780.8	204107	573360	1.8
Westeremden	20030228	15794.8	244369	597201	0.7
Middelstum	20030303	15801.0	239809	597730	2.2
Hoogezand	20030306	15803.7	246374	573419	0.9
Kantens	20030309	15806.8	238344	598984	1.1
Emmapolder(Eemshaven	20030323	15820.1	247698	608673	1.5
Harkstede	20030329	15826.5	241386	584087	0.4
Oldenklooster	20030401	15828.6	252448	598342	0.3
Loppersum	20030402	15830.2	243623	595517	1.9
Engelbert	20030405	15832.8	237991	580874	0.3
Overschild	20030406	15834.2	248877	588012	0.1
Ruiten	20030406	15834.4	246017	580499	1.0
Ruiten	20030406	15833.9	246904	580683	0.7
Overschild	20030416	15844.0	247522	589079	0.7
Schaaphok	20030418	15845.5	246168	584250	0.0
Schaaphok	20030420	15847.7	245928	585172	0.1
Ten-Boer	20030428	15855.8	244294	589260	1.0
Ten-Boer	20030429	15857.4	244516	589283	1.3
Siddeburen	20030514	15872.8	253587	586121	0.8
Siddeburen	20030514	15872.5	252357	586411	0.8
Annen	20030521	15879.2	247301	565740	1.1
Muntendam	20030523	15881.8	251182	567207	0.6
Siddeburen	20030531	15889.7	254270	585374	0.8
Stedum	20030603	15892.3	241299	595104	1.5
Harkstede	20030606	15894.8	241411	582696	0.7
Froombosch	20030608	15896.6	248605	579139	1.0
Woltersum	20030608	15896.9	244988	587863	1.5
Smilde	20030616	15904.5	223460	553250	2.3
Assen	20030805	15954.7	233628	554703	1.1

Table D.0.8 : Observed tremors in the Netherlands, continued.

Location	t	t	X	Y	M
	y/m/d	days	m	m	Richter
Zeerijp	20030807	15956.4	246266	596643	1.7
Zeerijp	20030807	15957.1	245611	596093	1.3
Veendam	20030820	15970.2	250575	569661	0.5
Kiel-Windeweer	20030825	15974.2	249010	569779	0.7
Kiel-Windeweer	20030825	15975.1	249233	569784	0.9
Uithuizen	20030922	16002.2	241514	601638	2.4
Westeremden	20030927	16006.8	242164	596381	2.7
Roswinkel	20031011	16021.5	267340	539858	1.6
Hoeksmeer	20031024	16034.3	248604	590622	3.0
Hoeksmeer	20031026	16036.3	248362	591619	1.2
Froombosch	20031029	16039.4	248271	579114	1.0
Stedum	20031110	16050.7	241765	593869	3.0
Westeremden	20031110	16050.6	243049	596546	1.4
Stedum	20031116	16057.0	242505	595924	2.7
Garrelsweer	20031226	16097.9	249216	593380	1.4
Spijkerboor	20031226	16097.8	246605	567099	-0.6
Spijkerboor	20031228	16099.3	247061	566607	-0.3
Delfzijl	20031229	16100.3	258266	596144	1.5
Kolham	20040112	16114.3	245716	578732	1.6
Woltersum	20040124	16126.0	243876	587861	1.0
Appingedam	20040130	16132.4	253671	592821	1.2
Veendam	20040307	16169.8	252592	569312	0.2
Meedhuizen	20040308	16170.7	255498	590483	0.4
Veendam	20040316	16178.6	254964	567969	1.0
Wagenborgen	20040321	16183.9	257142	586344	1.4
Steendam	20040326	16188.8	253321	588231	0.5
Eexterveen	20040415	16208.4	249713	562392	1.0
Lageland	20040430	16223.6	243404	583270	0.5
Garnwerd	20040524	16247.4	230801	591940	1.4
Garnwerd	20040529	16252.5	229693	591737	0.8
Garnwerd	20040531	16255.1	230351	592285	0.3
Doodstil	20040610	16264.3	239860	601089	2.1
Geelbroek	20040621	16275.4	234355	551301	2.8
Appingedam	20040727	16312.0	254048	596111	1.2
Kleinemeer	20040821	16336.3	249000	575993	1.8
Geelbroek	20040822	16336.6	235472	551542	1.0
Roswinkel	20040906	16351.2	266895	539700	1.0
Schipborg	20040910	16355.8	240951	564751	0.4
Uithuizen	20040918	16363.3	242470	603938	1.2
Winneweer	20040922	16366.9	245347	592377	1.5
Annerveenschekanaal	20041008	16384.1	251870	566311	1.3
Zeerijp	20041030	16406.3	247583	597411	1.4
Amerbrug	20041031	16407.3	238708	552302	0.9
Overschild	20041113	16419.1	249280	590134	1.2
Borgercompagnie	20041123	16429.2	250888	570762	0.3
Wittewierum	20041124	16430.8	246061	589886	1.9
Froombosch	20041125	16431.2	247485	579414	0.6
Winneweer	20041126	16432.3	244897	592685	1.6
Engelbert	20041216	16452.4	239396	583309	0.8
Wirdum	20050109	16476.2	248875	593781	1.7
Wirdum	20050117	16484.3	249666	593128	1.1
Ten-Boer	20050130	16496.7	241974	588475	1.0
Bedum	20050208	16506.0	238342	592733	2.3
Anreep-(Assen)	20050215	16512.1	236798	552603	1.0

Table D.0.9 : Observed tremors in the Netherlands, continued.

Location	t	t	X	Y	M
	y/m/d	days	m	m	Richter
Zijldijk	20050216	16514.0	248478	602752	1.3
Annen	20050218	16516.0	241140	566664	0.6
Westeremden	20050218	16515.7	244731	595612	1.3
Schaaphok	20050218	16515.8	245960	583467	0.5
Schaaphok	20050218	16515.3	244386	584327	1.6
Hoogezand	20050220	16517.8	249084	577405	0.0
Appingedam	20050225	16523.0	249848	595154	1.6
Schaapbulten	20050301	16529.0	257197	594229	1.2
Wagenborgen	20050308	16536.1	256904	587062	0.9
Oosterwijtwerd	20050310	16538.3	249722	595894	2.0
De-Paauwen	20050321	16549.5	247019	586343	0.9
Amelanderwad	20050321	16548.6	185710	607872	1.8
Overschild	20050402	16560.7	249104	587793	1.2
Overschild	20050418	16576.6	249450	587151	1.0
Tjuchem	20050421	16579.6	254836	590247	0.9
Appingedam	20050422	16580.7	252958	595106	0.8
Vierburen	20050430	16588.7	242362	597683	1.0
Siddeburen	20050517	16605.6	255528	583731	1.0
Noordbroek	20050525	16613.7	252721	579425	1.1
Morra	20050528	16617.1	201630	598727	1.4
Westeremden	20050530	16619.3	243063	595804	2.3
Oosterwijtwerd	20050622	16640.9	250305	594496	1.5
Lageland	20050709	16658.8	241607	584183	1.1
Winneweer	20050717	16667.1	245553	593254	1.8
Harkstede	20050725	16675.3	243441	581267	0.8
Sappemeer	20050805	16684.8	250100	576775	2.2
Garrelsweer	20050910	16720.9	247225	592952	1.2
Eppenhuizen	20051005	16746.6	238535	594406	1.7
Smilde	20051012	16753.2	226372	553273	2.5
Diddingehuizen	20051023	16763.7	240685	598358	1.9
Harkstede	20051111	16782.6	242414	582639	1.4
Harkstede	20060102	16834.6	242279	583917	1.1
Eleveld	20060110	16842.1	234557	552640	2.6
Hoogezand	20060114	16846.7	247189	577424	0.3
Wittewierum	20060118	16850.6	246836	590068	1.5
Overschild	20060118	16850.7	247427	588243	1.6
Loppersum	20060120	16852.0	245073	595137	1.3
Lageland	20060123	16855.9	242389	584012	1.9
Spijk	20060128	16860.1	250193	600133	1.1
Geelbroek	20060129	16861.1	235125	552185	1.1
Siddeburen	20060211	16874.3	252358	586375	1.3
Hoeksmeer	20060212	16875.0	248822	590830	1.5
Wirdumerdraai	20060224	16886.4	248346	592453	1.3
Kropswolde	20060304	16897.8	245588	573702	1.8
Ten-Post	20060321	16914.5	246145	591354	2.4
Overschild	20060323	16916.7	247740	589325	2.2
Roswinkel	20060325	16918.0	266670	539713	2.1
Roswinkel	20060325	16918.0	266558	539673	1.7
Delfzijl	20060405	16928.5	255045	596187	1.4
Steendam	20060412	16935.4	251660	587863	1.2
Garmerwolde	20060413	16937.1	239044	584342	1.5
Garrelsweer	20060416	16939.8	248015	592336	1.9
Garrelsweer	20060416	16939.7	247121	592578	1.1
Stedum	20060419	16942.6	241410	595087	1.6
Loppersum	20060422	16945.5	245874	593890	1.5
Warffum	20060422	16945.9	235552	600105	0.4
Delfzijl	20060423	16946.5	254614	595566	0.9
Warffum	20060423	16947.0	231438	600743	1.1

Table D.0.10 : Observed tremors in the Netherlands, continued.

Location	t	t	X	Y	M
	y/m/d	days	m	m	Richter
Wirdumerdraai	20060502	16956.0	248896	592706	1.0
Wittewierum	20060503	16957.0	246948	590014	1.2
Westeremden	20060507	16960.7	243501	596109	1.4
Lageland	20060522	16976.5	242492	584477	0.9
Schildwolde	20060606	16990.1	249952	584267	1.4
Lageland	20060608	16992.5	241937	584356	0.8
Overschild	20060616	17000.9	247165	590316	1.6
Garrelsweer	20060617	17001.8	247044	590814	1.2
Appingedam	20060617	17001.7	252525	594540	1.4
Garrelsweer	20060623	17007.3	246669	593014	1.7
Oosterwijtwerd	20060624	17008.6	250613	595745	1.2
Godlinze	20060712	17026.9	249884	598922	0.9
Appingedam	20060712	17027.4	253683	592263	1.3
Appingedam	20060716	17030.7	253585	591593	1.5
Westeremden	20060808	17053.0	242159	596659	3.5
Westeremden	20060808	17053.3	242826	596579	2.5
Harkstede	20060811	17056.0	240755	582016	1.1
Westeremden	20060826	17071.6	243172	595881	2.3
Peizermade	20060906	17081.6	230791	578492	1.8
Garsthuizen	20060927	17102.7	241458	598557	1.6
Hoeksmeer	20061006	17112.9	248477	591418	1.6
Emmen	20061015	17121.8	256044	532061	1.6
Garsthuizen	20061023	17129.7	244887	599158	2.3
Delfzijl	20061025	17131.8	257308	594195	1.4
Zandeweer	20061026	17132.1	242413	600968	1.4
Geelbroek	20061104	17140.8	235045	550219	1.3
Schaaphok	20061105	17141.7	248652	588137	1.2
Warfhuizen	20061225	17192.3	222645	595194	1.3
Delfzijl	20070110	17207.7	254609	595807	1.5
Overschild	20070118	17215.5	246983	588216	0.9
Zeerijp	20070126	17223.3	246039	596898	2.3
Zandeweer	20070131	17229.1	240459	598595	1.2
Middelstum	20070204	17231.8	239614	596168	0.6
Harkstede	20070216	17243.7	242739	583110	1.5
Harkstede	20070217	17244.6	242853	582981	2.6
Harkstede	20070217	17244.6	241516	583013	0.9
Krewerd	20070217	17245.1	252810	596939	0.9
Harkstede	20070303	17261.6	243170	583878	1.1
Wirdum	20070311	17269.4	247760	594019	1.1
Schaaphok	20070321	17279.4	244051	584414	1.2
Schipborg	20070329	17287.3	242507	565223	0.7
Lageland	20070330	17288.7	243058	583950	1.2
Harkstede	20070401	17289.8	241958	583207	0.7
Woudbloem	20070413	17301.6	245628	583405	1.3
Stedum	20070514	17333.0	242531	594533	2.0
Westeind	20070519	17338.5	251342	575984	0.4
Zeerijp	20070609	17359.0	245482	597018	2.1
Bedum	20070610	17359.7	236656	593873	1.7
Bedum	20070611	17360.6	239331	593344	1.1
Stedum	20070623	17372.7	242670	592995	1.2
Emmen	20070702	17382.2	255370	532028	1.4
Garsthuizen	20070815	17425.5	244450	598779	1.5
Leermens	20070917	17458.6	249052	596122	1.5
Schildwolde	20070918	17459.5	249288	584068	0.9
Fraamklap	20070928	17468.7	237300	595182	1.2
Froombosch	20070930	17471.3	248600	579399	2.1
Loppersum	20071027	17498.6	245635	594776	2.0
Overschild	20071113	17515.4	250719	590460	1.7

Table D.0.11 : Observed tremors in the Netherlands, continued.

Location	t	t	X	Y	M
	y/m/d	days	m	m	Richter
Vries	20071130	17532.4	234157	563429	1.5
Sauwerd	20071210	17542.9	231490	590559	0.7
Geelbroek	20080102	17565.3	233805	550718	1.4
Nieuw-Annerveen	20080105	17568.2	248433	564982	1.7
Garmerwolde	20080107	17570.2	239818	584652	1.1
Bedum	20080124	17587.1	247593	579602	1.5
Garrelsweer	20080212	17605.8	248014	592372	0.9
Westlaren	20080217	17610.1	241696	566822	1.8
Froombosch	20080219	17612.2	246842	578122	0.9
Onderdendam	20080319	17642.3	233397	596248	1.2
Steendam	20080329	17652.3	251943	590373	1.4
Westeremden	20080331	17654.8	242389	596218	1.2
Eleveld	20080402	17656.4	235919	551569	1.9
Eleveld	20080402	17655.9	236143	551628	2.5
Meedhuizen	20080407	17661.5	255605	590689	1.2
Tjuchem	20080411	17665.0	254186	589416	1.1
Westerdijkshorn	20080415	17669.0	232907	592252	0.9
Nieuw-Annerveen	20080422	17676.3	247645	565282	1.8
Siddeburen	20080428	17681.8	253242	586652	1.3
Onderdendam	20080505	17690.1	235090	594551	1.0
Ten-Post	20080509	17693.3	244179	589499	1.3
Loppersum	20080510	17694.5	244316	594046	1.2
Garsthuizen	20080518	17702.3	244215	599480	2.2
Loppersum	20080519	17703.7	245097	593857	1.9
Usquert	20080530	17714.7	237831	603001	1.3
Garrelsweer	20080601	17716.4	247909	592037	1.3
Garrelsweer	20080610	17725.4	248127	592263	0.9
Noordzee	20080615	17729.6	85916	542205	2.1
Siddeburen	20080622	17737.2	252043	585422	0.9
Veendam	20080623	17738.2	253248	569993	1.1
Holwierde	20080710	17756.0	254475	596918	2.5
Engelbert	20080723	17769.0	240213	581209	1.2
Emmen	20080805	17780.6	257632	531426	2.0
Loppersum	20080823	17798.9	244088	594413	0.9
Eleveld	20080826	17802.1	234122	551854	2.3
Westerwijtwerd	20080914	17820.4	237203	594383	1.1
Eexterveen	20080915	17821.6	249909	563768	1.0
Lageland	20080920	17826.6	243054	584173	1.3
Warffum	20080929	17835.7	235780	599738	1.8
Noordzee	20081011	17848.3	86333	523931	2.6
Schildwolde	20081026	17862.4	249606	584873	1.1
Geelbroek	20081026	17862.8	233346	551341	1.7
Stedum	20081029	17866.2	243089	594376	1.4
Westeremden	20081030	17866.5	243740	595168	3.2
Garsthuizen	20081107	17874.1	244647	600100	2.2
Spijkerboor	20081110	17877.7	247166	566942	0.7
Eexterveen	20081116	17883.5	249139	563160	1.2
Tetjehorn	20081210	17908.2	251082	588946	1.1
Onderdendam	20081215	17912.3	235750	594952	1.5
Oldenzijl	20081223	17921.1	242940	602480	1.4
Vries	20081224	17921.6	235029	564760	1.2
Zuidlaren	20090101	17928.8	244126	568277	1.5
Delfzijl	20090101	17929.4	255856	594609	1.2
Loppersum	20090101	17929.6	247118	598533	1.7
Westeremden	20090108	17936.4	243496	596387	1.7
Westeremden	20090109	17937.1	243287	595660	1.9
Marsum	20090115	17943.0	253836	595606	1.0

Table D.0.12 : Observed tremors in the Netherlands, continued.

Location	t	t	X	Y	M
	y/m/d	days	m	m	Richter
Sappemeer	20090117	17945.3	249097	576755	1.1
Westeremden	20090201	17959.3	245024	597769	2.2
Appingedam	20090203	17961.2	254114	592922	1.2
Garsthuizen	20090204	17962.1	245101	599571	1.7
Delfzijl	20090205	17964.1	257304	594417	1.1
Overschild	20090216	17974.7	249153	590930	1.4
Midlaren	20090222	17980.8	239282	570749	0.8
Tripscompagnie	20090223	17981.6	251523	572481	1.0
Midlaren	20090226	17984.7	239503	570846	0.5
Midlaren	20090226	17984.4	239281	570786	1.1
Midlaren	20090305	17994.2	239281	570824	0.8
Midlaren	20090312	18000.8	239172	570636	0.6
Midlaren	20090312	18000.9	239172	570655	0.5
Midlaren	20090312	18001.2	239284	570619	0.8
Midlaren	20090312	18001.4	239284	570619	0.6
Delfzijl	20090313	18002.4	255809	596853	1.2
Midlaren	20090314	18002.9	239614	570904	1.0
Midlaren	20090314	18003.3	239059	570727	1.0
Midlaren	20090314	18003.5	238616	570515	0.5
Midlaren	20090317	18005.6	239610	571145	0.4
Midlaren	20090317	18005.9	239389	570993	0.5
Midlaren	20090317	18006.0	239392	570844	1.4
Midlaren	20090317	18005.8	239390	570955	1.1
Midlaren	20090317	18005.6	239616	570774	0.5
Midlaren	20090317	18006.3	239725	570906	0.5
Midlaren	20090317	18005.8	239169	570822	0.6
Midlaren	20090317	18006.1	239390	570937	0.9
Midlaren	20090317	18006.2	239389	570993	0.9
Midlaren	20090317	18005.9	239278	570953	0.9
Midlaren	20090317	18005.9	239388	571085	1.0
Midlaren	20090317	18006.4	239390	570974	1.0
Midlaren	20090317	18005.6	239389	570993	1.0
Midlaren	20090317	18006.0	239502	570920	0.7
Midlaren	20090317	18005.9	239502	570939	0.7
Midlaren	20090317	18006.1	239612	571014	1.1
Midlaren	20090317	18006.4	239615	570830	0.8
Midlaren	20090318	18007.0	239725	570924	0.9
Midlaren	20090318	18006.6	239503	570846	0.9
Midlaren	20090318	18007.3	239613	570941	0.6
Midlaren	20090320	18009.4	238946	570836	0.5
Midlaren	20090320	18009.4	239169	570803	0.6
Midlaren	20090320	18009.2	239278	570972	0.5
Midlaren	20090320	18009.0	239389	570993	0.6
Midlaren	20090320	18008.7	239835	571018	0.4
Midlaren	20090320	18009.5	238726	570609	0.5
Midlaren	20090321	18010.3	239386	571196	0.2
Midlaren	20090321	18010.1	239613	570978	0.5
Midlaren	20090322	18010.7	239390	570955	1.2
Midlaren	20090322	18011.1	239391	570900	0.6
Hoeksmeer	20090327	18015.7	249797	592092	1.0

Table D.0.13 : Observed tremors in the Netherlands, continued.

Location	t	t	X	Y	M
	y/m/d	days	m	m	Richter
Huizinge	20090414	18034.0	240955	595673	2.6
't-Zandt	20090414	18033.9	247689	597672	0.9
Appingedam	20090416	18035.9	252118	592732	2.6
Wirdumerpolder	20090420	18039.5	249712	590774	1.5
Harkstede	20090501	18051.2	243976	582428	1.2
't-Zand	20090504	18054.0	247805	597433	1.8
't-Zand	20090507	18057.0	247535	599932	1.4
Winneweer	20090507	18057.1	244339	592841	1.6
Lageland	20090507	18057.0	244135	585862	1.2
Zeerijp	20090508	18058.4	246479	597129	3.0
Kropswolde	20090508	18058.3	243807	573465	0.9
Annerveenschekanaal	20090522	18072.0	251982	566313	1.3
Meedhuizen	20090526	18076.0	257809	591553	1.3
Meedhuizen	20090526	18076.2	257669	592904	1.3
Siddeburen	20090601	18081.4	254530	583525	0.9
Overschild	20090615	18095.7	250067	589705	1.0
Winneweer	20090705	18115.7	246133	591966	1.8
Schildwolde	20090705	18115.6	251647	582965	1.2
Noordzee	20090714	18124.5	82174	532114	2.7
Wittewierum	20090722	18132.4	246836	590068	1.7
Middelbert	20090819	18159.9	238060	583360	0.7
Steendam	20090914	18185.6	252198	588782	1.3
Eekwerderdraai	20090929	18200.4	249229	592731	1.6
Westenesch	20091102	18234.7	254531	534515	1.4
Hoogezand	20091118	18250.5	246030	573914	1.6
Annerveenschekanaal	20091119	18251.9	250765	565715	1.1
Assen	20091119	18251.5	235648	554420	0.9
Winneweer	20091120	18252.5	245550	593439	1.2
De-Hoeve	20091126	18258.3	203834	545075	2.8
Laskwerd	20091202	18264.7	251390	590251	1.1
Wittewierum	20091204	18266.6	245404	589355	2.3
Doekegat	20091207	18270.4	257010	608177	1.3
Woudbloem	20091221	18283.6	245531	582624	1.5
Garrelsweer	20091223	18285.9	246462	592195	1.5
Woudbloem	20091225	18287.7	245969	583021	0.7
Winneweer	20100109	18302.3	240018	598476	1.7
Hoeksmeer	20100114	18307.6	250275	590395	1.2
Oud-Annerveen	20100211	18335.0	247387	567077	0.3
Froombosch	20100217	18341.4	248827	579181	1.2
Overschild	20100219	18343.0	249286	589819	1.8
Eenum	20100304	18358.7	248501	595870	1.4
Froombosch	20100331	18385.6	247828	578957	2.4
Middelstum	20100403	18388.0	239616	596094	1.4
Eekwerderdraai	20100425	18409.7	249109	593173	1.6
Zuidbroek	20100425	18409.4	252803	575401	1.0
Spijk	20100503	18417.7	249624	600882	2.3
Oosternieland	20100505	18419.7	247258	602784	1.6
Waddenzee	20100507	18422.5	236566	612181	2.5
Tjuchem	20100508	18422.9	253531	588847	1.0
Wagenborgen	20100509	18424.2	257717	585484	1.7
Tjuchem	20100521	18435.9	253858	589132	0.9
Schildwolde	20100526	18440.8	251516	583963	0.9
Lageland	20100530	18444.8	241162	584175	1.5
Lageland	20100530	18445.7	241162	584175	1.2

Table D.0.14 : Observed tremors in the Netherlands, continued.

Location	t	t	X	Y	M
	y/m/d	days	m	m	Richter
Noordbroek	20100608	18454.0	252487	579977	1.0
Hoogezand	20100609	18454.6	247735	578010	2.0
Middelbert	20100610	18455.3	239406	582735	1.1
Krewerd	20100616	18462.1	252571	597750	1.5
Luddeweer	20100621	18466.6	245588	585500	1.3
Groningen	20100621	18466.5	237307	581845	1.5
Wildervank	20100621	18466.8	251986	566110	1.7
Schildwolde	20100704	18480.3	249255	585737	0.8
Woltersum	20100724	18500.2	244857	588917	1.8
Uithuizermeeden	20100814	18520.3	242496	602509	2.5
Slochteren	20100829	18535.6	251238	581157	1.6
Zandeweer	20100831	18537.6	241219	599518	1.4
Schildwolde	20100903	18539.7	250197	583140	1.0
Slochteren	20101006	18573.8	247658	582033	0.9
Kolham	20101022	18589.2	244842	577769	1.0
Appingedam	20101031	18598.9	253898	592601	1.0
Westeremden	20101115	18613.3	242608	596389	1.4
Delfzijl	20101124	18621.5	259527	589233	0.6
Warfum	20101202	18630.5	234257	604629	1.2
Appingedam	20101207	18634.8	253229	592718	1.2
Winneweer	20101208	18636.3	244781	592961	1.1
Termunterzijl	20101230	18658.2	262725	595334	0.9
Hoeksmeer	20110106	18664.5	247826	590588	1.3
Nieuwolda	20110107	18665.5	260391	585337	1.7
Annen	20110116	18675.1	247108	564140	1.8
Westerwijtwerd	20110119	18677.8	238780	593075	2.4
Hoogezand	20110122	18681.1	248995	576271	1.1
Lellens	20110128	18686.4	243259	591170	1.5
Kroddeburen	20110130	18688.3	243923	591293	1.4
Luddeweer	20110208	18696.6	246795	586413	1.3
Appingedam	20110311	18730.4	253454	587157	1.4
Overschild	20110313	18732.7	247544	587949	1.5
Achterdiep	20110314	18734.0	250198	577464	0.8
Nieuwe	20110319	18738.5	258595	565301	0.9
Schildwolde	20110326	18746.0	250585	586023	1.2
Loppersum	20110326	18745.5	244521	594978	1.5
Sappemeer	20110328	18747.7	249770	576546	2.0
Eemshaven	20110408	18758.3	251709	607455	1.3
Gieterveen	20110412	18762.0	252297	561756	0.9
Overschild	20110413	18763.2	249175	589817	0.9
Slochteren	20110415	18764.6	251816	580111	1.5
Ommelanderwijk	20110420	18770.2	256431	567220	0.8
Tussenklappen	20110424	18774.5	253030	575202	0.5
Steendam	20110428	18777.5	252403	589640	1.4
Winneweer	20110428	18777.9	244235	592431	1.4
Meeden	20110502	18782.4	258671	572148	1.2
Scheemda	20110505	18785.0	258226	577314	0.8
Wirdum	20110507	18787.5	247200	594268	1.1
Overschild	20110508	18788.2	249309	588688	0.9
Holwierde	20110510	18790.6	253255	596856	1.0
Klein Harkstede	20110510	18790.8	239743	582611	1.2
Froombosch	20110512	18792.8	246481	579487	1.8
Hellum	20110512	18792.7	251172	584495	1.1
Noordzee	20110514	18794.5	89783	627902	2.5
Garrelsweer	20110518	18798.4	247106	593395	0.8
Siddeburen	20110518	18798.8	252266	585408	1.9

Table D.0.15 : Observed tremors in the Netherlands, continued.

Location	t	t	X	Y	M
	y/m/d	days	m	m	Richter
Bocht-van-Wattum	20110519	18799.9	255086	604834	0.9
Krewerd	20110519	18799.2	251905	597775	1.2
Kolhol	20110519	18799.1	247386	601877	1.4
Sappemeer	20110523	18803.0	250802	575101	0.9
Overschild	20110523	18803.1	246990	587827	1.2
Oosternieland	20110526	18806.1	247254	603007	1.9
Waterhuizen	20110527	18807.3	239158	577852	1.7
Garsthuizen	20110602	18812.6	244769	599528	1.0
Steendam	20110602	18812.5	250649	588362	0.8
Haren	20110605	18816.2	236829	577199	1.5
Rottumerplaat	20110605	18816.2	227776	615471	1.4
Thesinge	20110610	18821.3	238984	587809	1.0
Noordbroek	20110618	18829.1	252374	580048	1.3
Schuilingsoord	20110619	18829.4	243281	565664	1.1
Schuilingsoord	20110619	18829.4	243163	565977	0.3
Wirdum	20110623	18833.7	247437	593493	1.7
Westeremden	20110624	18834.6	244692	597708	1.1
Wittewierum	20110627	18837.7	245403	589411	1.0
Garrelsweer	20110627	18838.1	249151	591078	3.2
Appingedam	20110627	18837.9	247604	590603	1.4
Appingedam	20110627	18837.7	249249	591748	1.1
Noordzee	20110705	18846.3	80509	548239	2.5
Slochteren	20110723	18864.3	247597	585185	1.2
Tjuchem	20110727	18868.1	254515	589647	1.2
Schaapbulten	20110727	18867.9	259402	589843	1.2
Zandeweer	20110727	18868.2	239756	600716	1.1
Loppersum	20110729	18870.4	244296	595159	1.8
Godlinze	20110801	18872.4	248889	598753	0.9
Schuilingsoord	20110802	18873.6	244728	565950	1.6
Hoeksmeer	20110817	18888.3	248254	591450	1.0
Woltersum	20110818	18889.9	244743	589027	1.3
Noordwolde	20110820	18891.4	237524	588619	1.5
Sappemeer	20110823	18894.9	250551	576506	1.6
Garsthuizen	20110831	18902.5	241898	598807	1.1
Uithuizen	20110831	18902.4	241305	607070	2.5
Stedum	20110904	18905.8	241006	592836	0.8
Oosterwijtwerd	20110906	18908.7	249399	595368	2.5
Woltersum	20110907	18909.6	246998	587419	1.4
Eekwerderdraai	20110915	18917.5	250652	593798	1.6
Eleveld	20110922	18924.3	235092	554151	0.9
Westeremden	20110925	18927.0	244272	596420	1.0
Garsthuizen	20110925	18927.0	244240	598144	2.0
Noordzee	20111004	18936.5	79336	537685	2.6
Siddeburen	20111008	18940.7	253347	586932	1.9
Noordzee	20111009	18942.0	54789	589160	3.1
Ten-Boer	20111009	18941.2	239964	588940	1.5
Farmsum	20111024	18956.3	260106	593253	1.3
Oosterwijtwerd	20111104	18966.7	249610	595966	1.5
Harkstede	20111106	18969.2	241409	582770	0.7
Eexterveen	20111107	18970.3	249564	564299	1.0
Garmerwolde	20111107	18969.8	241591	585073	1.2
Nieuwolda	20111109	18972.1	259810	586457	1.6
Eleveld	20111115	18978.4	235906	552348	0.9
Weiwerd	20111115	18977.6	260277	590511	1.5
Froombosch	20111118	18981.5	247573	580659	0.2
Appingedam	20111127	18990.5	250564	592645	1.7
Lakswerd	20111204	18997.1	250830	590462	1.3
Tripscompagnie	20111220	19013.3	250603	573910	0.9
Noordzee	20111220	19013.2	80825	532209	2.2
Engelbert	20111223	19016.1	237780	580239	1.1
Middelstum	20111230	19023.7	239491	596853	2.2
Middelstum	20120106	19029.5	240143	597643	1.9

Table D.0.16 : Observed tremors in the Netherlands, continued.

Location	t	t	X	Y	M
	y/m/d	days	m	m	Richter
Thesinge	20120107	19031.2	237778	586769	1.6
Wirdum	20120116	19040.2	248663	593276	1.3
Zevenhuizen	20120121	19045.2	241387	583994	1.1
Winneweer	20120124	19047.9	246118	592745	1.3
Nieuwe Pekela	20120127	19051.4	260850	569486	1.6
Zeerijp	20120128	19051.7	246156	596604	0.9
Lellens	20120130	19054.1	245494	590526	1.5
Tjuchem	20120131	19054.7	253953	589950	1.4
Sappemeer	20120201	19055.4	249686	575135	0.9
Westeremden	20120204	19058.8	243809	597451	1.8
Eenum	20120205	19059.3	248641	594407	1.4
Meedhuizen	20120205	19059.5	255982	588601	1.5
Tjuchem	20120207	19061.7	253714	590724	1.4
Noordzee	20120212	19066.0	86204	522783	1.3
Noordzee	20120212	19066.6	83425	533097	1.7
Stedum	20120216	19070.1	241913	591832	1.9
Westeremden	20120217	19071.0	242920	597546	1.7
Nieuwediep	20120217	19071.8	254425	561577	1.0
Siddeburen	20120219	19073.0	254019	586742	1.8
Garmerwolde	20120304	19088.5	238153	584419	0.9
Hellum	20120307	19091.9	254754	583455	1.3
Garrelsweer	20120307	19092.2	250830	590462	1.0
Overschild	20120308	19093.1	249116	587181	0.5
Hoogezand	20120308	19092.6	247321	576350	0.9
Noordzee	20120316	19100.8	102668	523951	1.0
Meedhuizen	20120318	19103.2	255918	591642	0.9
Woudbloem	20120323	19108.2	245894	581072	0.4
Winneweer	20120327	19112.2	244789	592516	1.0
Wagenborgen	20120331	19115.7	257046	585636	1.6
Tjuchem	20120404	19118.9	253951	590006	1.7
Garrelsweer	20120407	19122.7	249047	590667	1.5
Steendam	20120413	19128.3	251791	586882	0.7
Uithuizen(Wad)	20120414	19129.1	241771	611883	0.9
Wirdum	20120416	19130.9	248241	592136	1.1
Loppersum	20120418	19133.2	244619	595685	1.2
Groet-(Noordzee)	20120418	19133.2	103455	523739	1.8
Krewerd	20120421	19136.5	251255	596963	0.3
Sappemeer	20120425	19140.3	250640	577639	2.0
Steendam	20120506	19151.3	250762	588271	0.8
Siddeburen	20120510	19155.6	254491	585416	0.8
Appingedam	20120511	19156.9	254743	594716	0.9
Appingedam	20120513	19158.7	251486	590976	0.9
Siddeburen	20120515	19160.9	255487	585696	0.8
Siddeburen	20120517	19162.2	252711	585417	0.9
Huizinge	20120524	19170.0	240366	597592	1.5
Overschild	20120528	19173.4	250197	588724	0.6
Sappemeer	20120602	19178.6	250514	578360	0.7
Kolham	20120608	19183.8	246730	578156	0.9
Wagenborgen	20120614	19190.0	257367	586218	1.7
Siddeburen	20120615	19190.7	253494	585229	1.5
Wirdum	20120621	19197.3	247991	593579	1.7
Oosterwijtwerd	20120621	19197.4	249995	593340	1.1
Lellens	20120622	19198.5	246158	590649	1.4
Lellens	20120622	19198.5	246059	589998	0.8
Zuidbroek	20120627	19203.2	252817	574715	0.5
Zuidbroek	20120627	19203.3	252930	574624	0.3
Eexterzandvoort	20120627	19203.0	247133	562824	0.4
Eexterzandvoort	20120627	19202.7	247133	562860	0.2

Table D.0.17 : Observed tremors in the Netherlands, continued.

Location	t	t	X	Y	M
	y/m/d	days	m	m	Richter
Overschild	20120703	19209.8	247104	587699	1.1
Overschild	20120707	19213.1	249172	589965	0.8
Eenum	20120707	19213.9	247303	594659	0.7
Lettelbert	20120710	19216.1	222871	579208	0.9
Steendam	20120712	19218.7	252531	588808	1.0
Wirdum	20120716	19223.0	246996	593318	0.6
Sappemeer	20120719	19225.6	249528	577506	0.9
Garrelsweer	20120725	19231.1	250719	590460	0.8
Stedum	20120727	19233.6	241121	592652	1.2
Westeremden	20120730	19237.0	244399	595551	1.3
Wirdum	20120730	19236.5	248211	593694	1.0
Hoogezand	20120730	19237.1	248303	577463	0.5
Eenum	20120801	19237.6	249077	594824	0.7
Harkstede	20120808	19244.6	240661	581069	0.8
Haren	20120809	19246.3	236928	577943	1.5
Garrelsweer	20120814	19251.3	248138	591726	1.0
Leermens	20120815	19252.0	249365	597093	2.4
Zeerijp	20120816	19253.1	245796	598026	1.2
Huizinge	20120816	19252.8	240504	596073	3.6
Middelstum	20120817	19254.2	239255	597683	0.6
Siddeburen	20120817	19254.0	255847	584461	0.8
Appingedam	20120823	19260.2	251371	591178	0.7
Appingedam	20120828	19265.5	251464	592107	0.9
Middelstum	20120923	19290.3	238727	596135	0.9
Schildwolde	20120928	19295.4	251328	582253	1.2
Woudbloem	20120930	19297.9	246121	580854	0.6
Amen	20120930	19297.8	237837	550785	0.7
Nieuw-Annerveen	20121007	19305.1	247565	563630	1.0
Steendam	20121013	19310.6	252530	588864	0.9
Oudwoude	20121016	19314.3	204713	590189	1.1
Wirdum	20121023	19320.4	247569	592383	1.3
Garmerwolde	20121027	19325.2	236821	584211	1.0
Garrelsweer	20121030	19328.2	246710	590864	0.7
Oldenzijl	20121113	19341.7	241930	603130	1.0
Steendam	20121114	19342.7	251753	588773	0.9
Overschild	20121117	19345.5	248503	590063	1.1
Tjuchem	20121118	19346.0	255213	588159	0.7
Appingedam	20121122	19350.5	253781	592896	1.1
Froombosch	20121127	19355.0	248346	581008	1.4
Froombosch	20121127	19355.4	247780	581479	0.4
Steendam	20121130	19358.3	251458	586838	1.0
Steendam	20121130	19358.1	251250	586147	1.1
Steendam	20121130	19357.9	252222	587577	0.9
Loppersum	20121217	19376.1	244434	593678	1.2
Zuidbroek	20121220	19378.4	253111	576687	0.6
t-Zandt	20121225	19383.9	247871	599735	1.2
Garrelsweer	20130105	19394.1	250691	591832	0.9
Noordzee	20130105	19394.7	78889	537877	2.6
Lauwerzijl	20130109	19397.7	217574	592454	1.2
Delfzijl	20130111	19399.8	259701	596509	1.4
Usquert	20130111	19400.3	235728	602817	1.8
Steendam	20130111	19399.9	252672	587345	0.8
Zuidbroek	20130112	19401.3	254228	576599	0.6
Krewerd	20130112	19401.4	253156	596278	0.9
Steendam	20130112	19401.2	252541	588288	0.9
Zandeweer	20130118	19407.3	239864	600903	1.3
Overschild	20130119	19408.2	248515	589488	2.4
Froombosch	20130127	19416.1	247615	578471	1.2

Table D.0.18 : Observed tremors in the Netherlands, continued.

Location	t	t	X	Y	M
	y/m/d	days	m	m	Richter
Meedhuizen	20130128	19417.5	256649	588596	1.5
Lageland	20130203	19422.9	242847	583297	1.4
Froombosch	20130204	19424.0	248694	580253	0.9
Garmerwolde	20130205	19424.7	238857	582317	1.5
Zandeweer	20130207	19426.5	240112	599405	2.7
Zandeweer	20130207	19427.1	240085	600945	3.2
t-Zandt	20130209	19428.2	246230	598516	2.7
Tjuchem	20130210	19429.4	252838	590075	1.5
Tjuchem	20130210	19429.1	254387	590460	1.1
Garrelsweer	20130211	19430.3	248045	590797	2.0
Garrelsweer	20130211	19430.3	247054	590295	1.8
Woudbloem	20130211	19430.5	246544	582048	1.8
Losdorp	20130213	19432.6	251995	598815	1.8
Wirdum	20130215	19434.7	248774	593278	2.0
Borgsweer	20130216	19435.5	261965	594593	0.8
Steendam	20130216	19435.4	251477	585912	0.8
Nieuwolda	20130218	19437.3	260784	587666	1.9
Leermens	20130218	19437.3	247820	596673	0.7
t-Zandt	20130221	19440.6	245903	598231	0.7
Garrelsweer	20130225	19444.6	247921	591462	1.0
Froombosch	20130227	19447.0	247239	580634	0.4
Middelstum	20130302	19451.9	239715	596745	0.7
Bergen	20130306	19456.4	109369	517690	0.7
Steendam	20130313	19463.1	251181	589579	0.8
Farmsum	20130314	19464.2	258556	592997	1.0
Eemshaven	20130316	19466.3	248214	610576	2.0
Lageland	20130329	19479.3	243731	583629	0.9
Hellum	20130402	19482.4	254101	582737	1.1
Garsthuizen	20130415	19495.7	244993	599421	0.9
Sappemeer	20130423	19503.4	249461	575242	0.6
Sappemeer	20130423	19503.1	248974	577328	0.5
Zeerijp	20130427	19508.0	246394	595736	1.0
Loppersum	20130428	19508.1	244647	594183	1.3
Zevenhuizen	20130429	19509.1	239956	583152	0.8
Woltersum	20130430	19510.5	244870	588232	0.7
Garmerwolde	20130501	19511.9	238367	584868	0.9
Eenum	20130502	19512.5	248628	595057	0.7
Steendam	20130510	19520.6	252797	586662	1.4
Wagenborgen	20130513	19523.7	257383	585495	1.1
Appingedam	20130519	19529.5	253036	591267	0.8
Hoogezand	20130522	19533.4	247857	577474	1.2
Overschild	20130522	19532.7	249955	589758	1.2
Stedum	20130524	19534.8	242754	594444	1.2
Harkstede	20130525	19535.5	242181	583192	1.1
Stedum	20130525	19536.0	243309	594492	1.0
Usquert	20130525	19535.7	236273	603364	0.9
Geelbroek	20130525	19535.8	234452	552268	1.1
Steendam	20130530	19540.9	251744	589200	1.2
Steendam	20130531	19541.6	251753	588773	1.0
Appingedam	20130603	19544.2	253552	593244	1.2
Garrelsweer	20130605	19545.9	247832	590273	0.7
Garmerwolde	20130605	19546.1	238372	584609	0.9
Borgsweer	20130607	19548.1	261521	589555	1.3
Harkstede	20130608	19549.5	242778	580977	0.7
Oosterwijtwerd	20130614	19555.9	251329	593292	0.7
Hellum	20130614	19555.2	254086	583497	0.6
Lageland	20130618	19559.6	243959	583336	0.7
Appingedam	20130623	19564.8	253591	591315	1.1
Westerwijtwerd	20130627	19568.8	238646	594408	1.3
Schildwolde	20130630	19571.2	250532	583091	0.8
Winneweer	20130630	19571.1	246335	593046	0.8
Loppersum	20130630	19571.2	245983	594003	0.7

Table D.0.19 : Observed tremors in the Netherlands, continued.

Location	t	t	X	Y	M
	y/m/d	days	m	m	Richter
Garrelsweer	20130702	19573.8	248163	590446	3.0
Toornwerd	20130703	19575.2	238154	597163	0.9
Sauwerd	20130708	19579.9	231920	591457	1.6
Appingedam	20130713	19584.6	253740	594862	0.9
Eenum	20130714	19585.7	248077	594841	1.1
Oosterwijtwerd	20130720	19592.0	249321	593734	2.4
Wirdum	20130720	19591.6	247432	593735	1.9
Steendam	20130721	19593.3	251216	587816	1.3
Overschild	20130721	19592.6	247732	589733	0.7
Garmerwolde	20130726	19597.5	238482	584703	0.9
Slochteren	20130730	19601.9	251226	581788	0.7
Harkstede	20130731	19602.7	243868	582277	1.0
Hoogezand	20130807	19608.9	248188	577666	0.6
Overschild	20130807	19609.6	249451	587077	0.9
Schildwolde	20130808	19609.9	249134	586272	1.0
Amelanderwad	20130809	19610.9	189928	606324	1.8
Garmerwolde	20130814	19616.2	239503	583589	1.1
Lageland	20130816	19618.7	242373	584866	2.1
Overschild	20130821	19622.9	248751	588752	0.9
Wirdum	20130825	19627.3	247453	592659	1.3
Appingedam	20130827	19629.6	253479	591351	1.1
Westeremden	20130901	19633.8	243394	595885	1.5
Zeerijp	20130904	19636.3	247166	596048	2.8
Steendam	20130918	19650.9	251166	590339	0.9
Zevenhuizen	20130922	19654.9	240258	584920	1.7
Zevenhuizen	20130922	19654.6	241251	585420	1.0
Zevenhuizen	20130922	19654.8	240609	583943	1.6
Paterswolde	20130924	19656.8	243932	566696	1.1
Overschild	20130925	19657.2	248282	590003	1.1
Tjuchem	20130925	19657.6	253300	589250	1.2
Eppenhuizen	20130928	19661.1	244089	600312	1.9
Harkstede	20130929	19662.1	240873	581648	1.2
Harkstede	20130930	19662.4	243642	582458	1.2
Harkstede	20131001	19664.2	243759	582145	1.1
Lageland	20131001	19663.9	243512	583477	1.2
Wirdum	20131002	19665.4	248233	592563	1.4
Wirdum	20131002	19665.5	248556	593051	1.9
Borgsweer	20131002	19665.6	263365	591582	0.9
Wirdum	20131003	19665.8	247562	592753	1.2
Garsthuizen	20131010	19673.5	243227	598924	1.5
Castricum	20131022	19684.9	100794	507281	2.5
Woltersum	20131023	19685.9	244784	586857	1.1
Castricum	20131023	19685.7	100573	507710	2.0
Siddeburen	20131023	19686.0	253467	586508	1.1
Noordzee	20131027	19690.6	98092	508202	1.8
Noordzee	20131105	19698.9	97085	509030	1.7
Tjuchem	20131107	19700.2	254414	589125	1.5
Annen	20131109	19702.6	246672	563575	2.4
Garrelsweer	20131110	19704.0	247264	590930	1.2
Stedum	20131115	19708.3	243446	593047	1.6
Loppersum	20131118	19711.8	245546	593605	1.4
Appingedam	20131126	19719.2	252088	594216	2.0
Noordzee	20131128	19721.8	98105	509334	1.7
Noordzee	20131128	19721.1	98219	509406	1.4
Lageland	20131206	19730.2	244302	582879	1.3
Meedhuizen	20131208	19732.4	257302	589297	1.1

Table D.0.20 : Observed tremors in the Netherlands, continued.

Location	t	t	X	Y	M
	y/m/d	days	m	m	Richter
Slochteren	20131220	19744.3	250897	581503	1.3
Schildwolde	20131222	19746.0	250305	583309	1.0
Huizinge	20131223	19747.0	241831	596375	1.2
Woudbloem	20140102	19756.7	246348	580636	1.4
Garmerwolde	20140104	19758.7	239065	583155	1.1
Rottum	20140109	19763.6	236670	599568	1.0
Garrelsweer	20140112	19766.1	247160	590575	0.9
Nieuwolda	20140116	19770.8	260759	588834	1.2
Zuidwolde	20140121	19775.0	233760	587665	1.0
Garsthuizen	20140123	19777.3	244767	599657	0.6
Noordbroek	20140123	19777.1	255197	578233	1.1
Zevenhuizen	20140126	19780.5	241166	583953	1.5
Loppersum	20140203	19787.8	246188	594916	1.5
Luddeweer	20140205	19789.5	248368	585572	0.9
Geelbroek	20140205	19790.2	234326	553064	2.0
Froombosch	20140206	19791.1	248396	578393	1.3
Meedhuizen	20140211	19795.4	259382	590770	0.8
Leermens	20140213	19797.5	248201	599634	3.0
Winneweer	20140217	19801.6	245519	593735	0.8
Westerwijtwerd	20140218	19802.6	240154	597408	1.7
Woltersum	20140228	19812.6	246055	590953	1.2
Annerveenschekanaal	20140304	19819.0	251420	568470	1.1
Annerveenschekanaal	20140304	19819.0	251286	569361	0.8
Annerveenschekanaal	20140304	19818.9	251286	569138	0.8
Zeerijp	20140310	19825.0	247262	598966	0.9
Schildwolde	20140311	19826.2	250883	585276	2.3
Froombosch	20140311	19826.2	250749	581826	1.1
Eleveld	20140312	19826.8	235325	554224	1.3
Appingedam	20140314	19829.7	251286	594403	1.0
Waterhuizen	20140314	19829.0	239483	583384	0.8
Appingedam	20140315	19830.6	254303	593958	1.9
Rottum	20140318	19833.7	237203	603307	2.1
Slochteren	20140321	19836.5	251286	583162	1.1
Sappemeer	20140323	19838.2	249274	578376	1.6
Siddeburen	20140327	19842.2	253633	588727	1.4
Eemshaven	20140328	19843.7	246591	613324	1.3
Borgsweer	20140330	19845.7	262351	591287	1.4
Zevenhuizen	20140331	19846.6	240824	586389	0.7
Sappemeer	20140402	19847.5	249542	578042	1.2
Sappemeer	20140402	19847.5	249944	577819	1.1
Sappemeer	20140403	19848.3	250548	579823	1.0
Zevenhuizen	20140404	19849.6	240489	587725	1.2
Meedhuizen	20140409	19854.4	256315	589283	1.1
Loppersum	20140417	19863.1	244244	596295	1.3
Zeerijp	20140420	19865.6	245586	598966	1.4
Schildwolde	20140426	19871.6	250280	586278	1.3
Westerbroek	20140427	19873.2	242836	580379	0.5
Woudbloem	20140512	19888.6	244848	583496	1.3
Westerwijtwerd	20140513	19889.4	238678	596963	1.4
Kolham	20140517	19892.8	245720	581270	1.6
Meedhuizen	20140519	19895.4	258796	590730	1.0
Kolham	20140612	19919.0	246189	581158	0.8
Woudbloem	20140612	19918.4	246927	582939	1.2
Westeremden	20140616	19922.8	243373	598744	1.8
Slochteren	20140629	19935.7	250883	583607	0.7

Table D.0.21 : Observed tremors in the Netherlands, continued.

Location	t	t	X	Y	M
	y/m/d	days	m	m	Richter
Meedhuizen	20140702	19938.9	257254	590508	1.3
Slochteren	20140702	19939.3	248737	583718	2.1
Haren	20140706	19942.7	237203	580491	0.9
Zevenhuizen	20140707	19944.4	241897	586612	1.2
Woltersum	20140707	19944.5	246189	589840	1.0
Lageland	20140708	19945.0	243171	587057	1.2
Slochteren	20140715	19952.2	251219	583830	0.7
Siddeburen	20140722	19959.3	253566	587614	0.9
Oosterwijtwerd	20140809	19976.7	251755	595850	1.3
Oosterwijtwerd	20140809	19976.7	251755	596073	2.0
Garsthuizen	20140819	19986.8	244379	601749	1.2
Garsthuizen	20140821	19988.5	244513	601415	1.2
Slochteren	20140825	19992.4	248201	585499	0.8
Garmerwolde	20140901	19998.5	237673	586167	0.5
Froombosch	20140901	19998.7	248536	581492	2.6
Froombosch	20140901	19998.8	250280	581826	1.6
Lageland	20140923	20021.1	244043	586612	1.4
Lageland	20140923	20021.2	244580	586835	1.0
Huizinge	20140924	20022.4	242233	598966	1.0
Meedhuizen	20140925	20023.3	258595	590619	1.5
Ten-Boer	20140930	20027.9	239684	588615	2.8
Zeerijp	20141021	20049.2	245854	599745	1.5
Zandeweer	20141105	20063.4	241227	601526	2.9
Amen	20141111	20069.9	236130	552888	2.0
Hellum	20141116	20074.3	253633	585276	0.9
Woudbloem	20141116	20075.1	246860	585276	0.6
Huizinge	20141122	20080.5	242568	599412	1.3
Oosterwijtwerd	20141129	20088.2	252090	596740	1.0
Huizinge	20141130	20088.4	240824	599968	1.4
Noordbroek	20141203	20091.9	251621	581047	1.0

Bibliographic Information

Classification	Restricted
Report number	SR.15.11335
Title	Induced seismicity in the Groningen field - statistical assessment of tremors along faults in a compacting reservoir
Sub title	
Author(s)	H.M. Wentinck
Keywords	earthquake, tremor, seismic moment, fault slip, shear capacity utilisation, Mohr-Coulomb failure, fault, reservoir compaction, Groningen field, statistics, Weibull, Pareto, Poisson probability distribution
Date of Issue	June 2015
US Export Control	Non US - Non Controlled
WBSE Code	ZZPT/015242/010302
Reviewed by	C. Harris, P.A.J. van den Bogert and R.M.H.E. van Eijs
Approved by	S.J. Bourne
Sponsoring Company / Customer	Shell Global Solutions
Spons/Cust Address	Kesslerpark 1, 2288 GS Rijswijk, NL
Issuing Company	Shell Global Solutions International B.V., Rijswijk P.O. Box 60 2280 AB Rijswijk The Netherlands

Report distribution

Electronic distribution (PDF)

Name, Company, Ref. Ind.

PT Information Services, PTT/TIKE, PT-Information-Services@Shell.com

Cid Alfaro, Marcela V GSNL-PTI/RC
Bierman, Stijn M GSNL-PTD/TASE
Busch, Andreas GSNL-PTI/RC
van den Bogert, Peter AJ GSNL-PTU/E/Q
de Borst, Karin GSNL-PTI/RC
Bourne, Stephen J GSNL-PTI/RC
Doornhof, Dirk NAM-PTU/E/Q
Droujinine, Alexander GSNL-PTI/ET
van Eijs, Rob MHE PTU/E/Q
van Elk, Jan F NAM-UIO/T/DL
van Es, Rob GSNL-PTN/EN
van Gent, Heijn W GSNL-PTI/EG
Harris, Christopher GSNL-PTI/RC
Hindriks, Kees OH GSNL-PTI/RC
Hol, Sander GSNL-PTI/RF
Kampman, Niko JS GSNL-PTI/RC
Kraaijeveld, Famke GSNL-PTI/RC
ten Kroode, Fons PE GSNL-PTI/ET
Mallik, Jyotirmoy NAM-PTU/E/F
Marcelis, Fons HM GSNL-PTI/RF
Maron, Karel P NAM-UIO/T/DL
van der Molen, Ide NAM-PTU/E/F
Mossop, Antony P NAM-PTU/E/Q
Oates, Steve J GSNL-PTU/E/S
Paleja, Rakesh J GSUK-PTD/TASE
Romijn, Remco NAM-UIO/T/DL
Schutjens, Peter PTIN-PTU/E/Q
Visser, Clemens A NAM-UIO/T/DG
van der Wal, Onno NAM-PTU/E/Q
Warners, Karin N GSNL PTI/EG
Wentinck, Rick M GSNL-PTI/RC
Wong, Sau-Wai SIEP-PTI/U